

Interlaminar Toughening of Fiber Reinforced Polymers

Dakai Bian

**Submitted in partial fulfillment of the
requirement for the degree
of Doctor of Philosophy
in the Graduate School of Arts and Sciences**

COLUMBIA UNIVERSITY

2018

© 2017

Dakai Bian

All rights reserved

Abstract

Interlaminar Toughening of Fiber Reinforced Polymers

Dakai Bian

Modification in the resin-rich region between plies, also known as the interlaminar region, was investigated to increase the toughness of laminate composites structures. To achieve suitable modifications, the complexities of the physical and chemical processes during the resin curing procedure must be studied. This includes analyses of the interactions among the co-dependent microstructure, process parameters, and material responses. This dissertation seeks to investigate these interactions via a series of experimental and numerical analyses of the geometric- and temperature-based effects on locally interleaving toughening methods and further interlaminar synergistic toughening without interleaf.

Two major weaknesses in composite materials are the brittle resin-rich interlaminar region which forms between the fiber plies after resin infusion, and the ply dropoff region which introduces stress concentration under loads. To address these weaknesses and increase the delamination resistance of the composite specimens, a dual bonding process was explored to alleviate the dropoff effect and toughen the interlaminar region. Hot melt bonding was investigated by applying clamping pressure to ductile thermoplastic interleaf and fiber fabric at an elevated temperature, while diffusion bonding between thermoplastic interleaf and thermoset resin is performed during the resin infusion. This method increased the fracture energy level and thus delamination resistance in the interlaminar region because of deep interleaf penetration into fiber bundles which helped confining crack propagation in the toughened area.

The diffusion and precipitation between thermosets and thermoplastics also improved the delamination resistance by forming a semi-interpenetration networks. This phenomenon was investigated in concoctions of low-concentration polystyrene additive modified epoxy system, which facilitates diffusion and precipitation without increasing the viscosity of the system. Additionally, chemical reaction induced phase separation, concentration of polystyrene, and various curing temperatures are used to evaluate their effects on diffusion and precipitation. These effects were directly investigated by performing attenuated total reflection Fourier transform infrared spectroscopy (ATR-FTIR). The diffusivity and curing kinetics experiments are performed to quantify the diffusivity coefficient of epoxy, hardener and thermoplastics, as well as the reaction rate constant of curing epoxy at various temperatures. Finally, mechanical testing and fracture surface imaging were used to quantify the improvements and characterize the toughening mechanism.

Further improvement on delamination resistance was studied through the synergistic effect of combining different modification methods without the interleaf. Polysulfone molecules are end-capped with epoxide groups. Fiber surface is functionalized with amino groups to generate micro-mechanical interlocks. The interaction between two individual modifications chemically links the modified semi-interpenetration networks to the improved interfacial strength between fiber and epoxy to. The impact of the additive on the crosslinking density was examined through glass transition temperatures, and the chemical modification was characterized by Raman spectroscopy. Mode I and II fracture tests were performed to quantify the improvement of delamination resistance under pure opening and shear loads. The mechanism of synergistic effect was explained based on the fracture surface morphology and the interactions between the modification methods.

Table of Contents

List of figures	vi
Acknowledgements	xx
Chapter 1: Introduction	1
1.1 fiber reinforced polymers.....	1
1.2 development and challenges of fiber reinforced polymers in wind energy.....	12
1.3 literature reviews of methods to improve fiber reinforced polymer	14
1.4 Fundamental theory of bonding between materials	22
1.4.1 Adsorption Theory	22
1.4.2 Mechanical interlocking theory	23
1.4.3 Electric theory	24
1.4.4 Diffusion theory	24
1.5 Mechanism of melt bonding	25
1.6 Interphase formation in polymers	26
1.7 Experiment procedures and characterization methods	28
1.7.1 Vacuum assisted resin transfer molding	28
1.7.2 Mechanical testing	36
1.7.3 Attenuated Total Reflective Fourier Transfer Infrared Spectra (ATR-FTIR)	40
1.7.4 Solubility determination by viscometry	42
1.8 Organization and objectives of dissertation	43

Chapter 2: Effect of Deep Penetration of Interleaf on Delamination Resistance in GFRP

2.1 Introduction	46
2.2 Background	48
2.2.1 Loading conditions at the drop-off structure	48
2.2.2 Crack initiation and propagation	51
2.2.3 Viscosity effect and interleaf flow analysis	52
2.3 Experiment procedures	54
2.3.1 Materials and specimens	55
2.3.2 Testing procedures	56
2.4 Results and discussion	57
2.4.1 Penetration analysis	57
2.4.2 Stress-strain and Toughness Behavior	62
2.4.3 Crack path microscopy	65
2.4.4 Fracture Surface Morphology	69
2.4.5 Influence of Interlayer Thickness	70
2.5 Conclusion	71
2.6 Acknowledgement	74

Chapter 3: Interlaminar Toughening of GFRP, Part 1: Bonding Improvement through Diffusion and Precipitation

3.1 Introduction	75
3.2 Background	77

3.2.1	Polymer compatibility	77
3.2.2	Diffusion process in thermoplastic-rich region	79
3.2.3	Precipitation process in the epoxy-rich region	81
3.2.4	Factors influence the diffusion and precipitation process	82
3.2.5	Crack propagation in the semi-interpenetration network	83
3.3	Experiment materials and procedures	84
3.4	Results and discussion	86
3.4.1	Compatibility of thermoplastics and epoxy	86
3.4.2	Temperature and Additive Concentration Dependent Diffusion/precipitation Process	88
3.4.3	Geometry Influence on the Diffusion and Precipitation Process	96
3.4.4	Stress-strain and Toughness Behavior	98
3.4.5	Crack propagation location and toughening mechanism	100
3.5	Conclusion	102
3.6	Acknowledgement	103
Chapter 4: Interlaminar Toughening of GFRP, Part 2: Characterization and Numerical Simulation of Curing Kinetics		
4.1	Introduction	104
4.2	Background	106
4.2.1	Chemical reactions of the curing process	106
4.2.2	Diffusion and precipitation process considering the curing kinetics	107

4.2.3	Attenuated Total Reflectance – Fourier Transform Infrared Spectroscopy	108
4.3	Experiment materials and procedures	110
4.4	Numerical Simulation	111
4.4.1	Diffusivity of species in the epoxy system	111
4.4.2	Curing kinetics of the epoxy system	112
4.5	Results and discussion	114
4.5.1	Diffusivity determination of the epoxy system	115
4.5.2	Curing kinetics of epoxy system	120
4.5.3	Diffusion and Precipitation Process Simulation without Fibers	123
4.5.4	Diffusion and Precipitation Process Including Fibers	129
4.6	Conclusion	135
4.7	Acknowledgement	135
Chapter 5: Interlaminar toughening of fiber reinforced polymers by synergistic modification of resin and fiber		
5.1	Introduction	136
5.2	Background	139
5.2.1	Chemical reactions between curing epoxy, polysulfone and glass fiber	139
5.2.2	Potential synergistic effect	141
5.3	Numerical simulation	144
5.3.1	Simulating crack growth in composites using XFEM	145
5.3.2	Interface modeling	146

5.4 Experiment materials and procedures	147
5.5 Results and discussion	148
5.5.1 Viscosity behavior of the epoxy system	148
5.5.2 Chemical and morphology determination of modified epoxy system	149
5.5.3 Glass transition temperatures of the epoxy system	151
5.5.4 Phase separation of PSU in the cured epoxy system	153
5.5.5 Mode I fracture test	157
5.5.6 Mode II fracture test	161
5.5.7 Mode I and II simulation	165
5.6 Conclusion	169
5.7 Acknowledgement	170
Chapter 6: Conclusions	171
6.1 Effect of deep interleaf penetration on delamination resistance	171
6.2 Interlaminar toughening by diffusion and precipitation	172
6.3 Effect of curing kinetics on interlaminar toughening	174
6.4 Interlaminar toughening by synergistic modification of resin and fiber	175
6.5 Future work	176
References	179
Appendix	207
Publications under candidature	214

List of Figures

Chapter 1

Fig. 1 Reconstruction of an ancient bow. This is a horn, bamboo, sinew composite [3].	2
Fig. 2 Schematic diagram showing the development of metals, polymers, composites and ceramics [4].	3
Fig. 3 The 1953 Cheverolet Corvette was largely fiberglass and manufactured using new, more efficient molding techniques [5].	4
Fig. 4 Fiber prepreg (left) and fiber preform (right). Prepreg is pre-impregnated with resin. Preform is dry fiber fabric [6].	6
Fig. 5 Open molding methods includes hand layup (left) and spray-up (right) [8].	7
Fig. 6 The TORRESLAYUP is an 11 axes Gantry CNC tape layer machine, that has been specially designed for high speed tape laying of compound contoured aircraft structural components. [9].	8
Fig. 7 Closed molding methods includes vacuum bag molding (left), vacuum infusion (mid) and resin transfer molding (right) [8]	9
Fig. 8 Capital expenditure across processes [10]	11
Fig. 9 Vacuum infusion is widely chosen to produce the wind turbine blade [11].	12
Fig. 10 Image of offshore wind turbines [14]	14
Fig. 11 Molecular structure of octaglycidyl polyhedral oligomeric silsesquioxane [22]	16
Fig. 12 Typical hybrid system with liquid rubber particles and nanosilica particles [39]	17
Fig. 13 Aligned carbon nanotubes (A-CNTs) bridge ply interfaces in laminated composites [39]	18

Fig. 14 Z-pinning method used to improve the bonding between two plies. Crack need to break the z-pins to propagate through the laminate interface [42]	20
Fig. 15 Stitching method used to improve the composites structures. The stitches increases more resin rich region in the composites structure [41].	20
Fig. 16 Ionomer can generate a mixed interphase between epoxy matrix and ionomer interleaf due to the reactive chemical properties [45]	22
Fig. 17 chain entanglement between adhesive and substrate through mutual diffusion [54]	25
Fig. 18 (a) Electrical tape taped along the edges of the clean surface. (b) Rexco Partall Paste wax. (c) Fiber Glast Liquid wax. (d) Yellow sealant tape surround the waxed surface.	29
Fig. 19 Preparation before resin infusion	30
Fig. 20 Preparation of spiral tubes	31
Fig. 21 Tubing connection between vacuum chamber and spiral tubes	32
Fig. 22 resin infuse from left to right with the help of the vacuum pump	33
Fig. 23 Dissolved gas separate out from the resin in the vacuum chamber	34
Fig. 24 Resin infusion process. The speed of infusion is monitored every minute.	36
Fig. 25 Experiment setup for the mixed mode failure. The stain gauge is used to measure the strain change on the drop-off region, and the extensometer is used to record the displacement change on the core layers.	37
Fig. 26 Experiment setup for Mode I fracture test. The Teflon film was pre-inserted in the laminate as the crack initiator.	39
Fig. 27 Experiment setup for Mode II fracture test.	40

Fig. 28 Sample set-up for diffusivity determination	42
---	----

Chapter 2

Fig. 1 (a) MTS System Corp. used their special testing system to test the wind turbine blade to failure under the flap-wise loads. When the blade is in operation, the centrifugal forces will occur due to turbine rotation [15]. (b) Schematic of the specimen under external loads: interleaf is inserted between the external drop-off layer and the core layers. (c) Free body diagrams of the drop-off region and interleaf: applied force and moment equilibrium about Point O, both normal and shear stresses exist in the drop-off region and interleaf.49

Fig. 2 (a) Illustration of the interlaminar shear and normal stress distribution along X-direction on the upper surface of the interleaf: the trends of the shear stress and normal stress are based on the analysis of the force and moment equilibrium for the external drop off layer [18]. For the lower surface of the interleaf, the stresses are of the same magnitudes but opposite directions. Peak stresses occur close to the terminated surface. (b) Considering both normal and shear interlaminar stresses near or on the terminated surface of the interleaf, a crack is more likely to initiate near point A and C.50

Fig. 3 (a) Schematic of the crack path under low penetration condition: crack initiates near the boundary of the pure interleaf region and the large plastic zone ahead of the crack tip reaches the interface between interleaf/fiber and epoxy/fiber, indicating that the crack migrates to this weak interface from Point 1 to Point 2 with the decreasing plastic zone size due to the rigid fiber. (b) Schematic of the crack path under high penetration condition: After crack initiates, the plastic zone only reaches the mixed region of interleaf and fiber (Point 1). The decreasing plastic zone size

arrests the crack propagating in the middle of the mixed region (Point 2), where the delamination resistance is much larger than the interface between interleaf/fiber and epoxy/fiber.	52
Fig.4 Polysulfone (PSU) viscosity versus temperature [23].	53
Fig. 5 3D schematic diagram describing the mechanical test setup. The strain gauge is placed on the top surface of the external drop off layer and 0.4 inch away from the edge of the drop-off layer. A 2"×1" interleaf is inserted underneath the external drop off layer and hot melt-bonded before VARTM. Far field load is in-plane tensile load. Note the coordinate system.	55
Fig. 6 Y-Z cross section (parallel to the drop-off edge) of the specimen with melt-bonded 254μm thick PSU at 280°C. Xylene etched surface shows low penetration of the PSU interleaf into the fiber bundles. Penetration boundary is indicated by the white lines. The average penetration depth is 32.5μm, and the average remaining interleaf thickness is 168μm. Due to the low melt bonding temperature and high viscosity, a limited amount of the interleaf penetrates into the fiber bundles.	58
Fig. 7 Y-Z cross section of the specimen with melt-bonded 254μm thick PSU at 320°C. Xylene etched surface shows high penetration of the PSU interlayer. The average penetration depth is 103.6μm and the average interleaf thickness after melt bonding is 83μm. Larger penetration depths form a thick mixed region of interlayer and fiber bundles.	59
Fig. 8 Experiment results for 254μm thick PSU interleaf penetration depths from 280°C to 380°C. The error bars represent standard errors. The trend of the penetration correlates well with the decreasing viscosity temperature.	60
Fig. 9 Predicted and experimental penetration depths increase with the melt bonding temperature.	

The trend is primarily due to the decreasing viscosity of the PSU interleaf material with temperature.....61

Fig. 10 Representative strain-stress curves obtained from the strain gauge mounted on the drop-off layer in uniaxial tensile tests: reference specimen (without interleaf), interleaved specimens under low/high melt bonding temperatures. The reference specimen shows the highest stiffness while specimens with interleaf are much tougher.62

Fig. 11 Toughness of 254 μ m thick PSU interleaved specimens from 280°C to 380°C. The error bars represent standard errors. The horizontal line represents the average toughness of the specimen without interlayer. The trend correlates well with the trend of the penetration depth (Fig. 8), indicating that the penetration depth directly influences the toughness.63

Fig. 12 Y-Z cross section (parallel to the drop-off edge) of the fractured specimen with melt-bonded 254 μ m thick PSU at 280°C. The white line indicates the penetration boundary. There are two kinds of the crack locations due to the thin penetration depth. Region A shows the crack is near the interface between the pure interleaf and the matrix. Region B shows the crack is near the interface between the interleaf/fiber and epoxy/fiber. The crack reaches the weak interface between interleaf and epoxy under low penetration condition.65

Fig. 13 X-Z cross section (perpendicular to the drop-off edge) of the fractured specimen with melt-bonded 254 μ m thick PSU at 280°C. It shows the crack locates at the interface between interleaf and epoxy/fiber or at the interface between interleaf/fiber and epoxy/fiber. Due to the low penetration depth, the crack always propagates along the weak interface between interleaf and epoxy. Less broken fiber, less bridged fiber and bridged PSU are found compared to the specimen

under the high melt bonding temperature.	67
Fig. 14 Y-Z cross section of the fractured specimen with melt-bonded 254μm thick PSU at 320°C. The white line indicates the penetration boundary. At this melt bonding temperature, the average penetration depth is 106μm. The crack propagates through the middle of the penetration region without reaching the weak interface between interleaf and epoxy.	68
Fig. 15 X-Z cross section of the fractured specimen with melt-bonded 254μm thick PSU at 320°C. The thickness of the interleaf after the melt bonding reduced to about 63μm. The crack propagates through the penetration region of interleaf and fibers. The zone is about 106μm wide as per Fig. 14 under this melt bonding temperature. More broken fibers and bridged fibers result in high toughness.	69
Fig. 16 (a) SEM image of the delamination fracture surface of the specimen with melt-bonded 254μm thick PSU at 280°C. The large clean region indicates brittle adhesion failure, which is caused by the crack propagating through the interface between interleaf and epoxy. The rough region indicates the crack goes through the penetration region, where part of the interleaf underwent plastic shear deformation. Fewer broken fibers and pulled out fibers are found for this condition. (b) SEM image for the delamination fracture surface of the specimen with melt-bonded 254μm thick PSU at 320°C. The much rougher surface indicates more ductile fracture has taken place. Plastic shear deformation of the interleaf can be seen around fiber beams. More broken fibers and pulled out fibers are seen for this condition due to the increased delamination resistance.	72

Fig. 17 Toughness of the specimens vs. interleaf thickness under different melt bonding temperatures. The error bars represent standard errors. The sharp increasing toughness from 25 μm to 127 μm is due to more participated thermoplastic interleaf in plastic deformation. After the peak point, the toughness decreases with interleaf thickness. It is because the influence of the mismatch of the drop-off structure and materials is magnified and induces adhesive failure, which reduces the toughness. For the specimens melt bonded at the higher temperature, which has a higher penetration depth and thus the better bonding quality, some toughness is preserved even the interleaf gets overly thick.....73

Chapter 3

Fig. 1 Phase diagram of nucleation growth (NG) and spinodal decomposition (SD). The system can lower its free energy by separating into two phases with an interphase between c^- and c^+ . Within the range of c^-/c_s and c^+/c_{s+} , phase separation is due to nucleation and growth. Within the range of c_s^- and c_{s+} , phase separation is due to spinodal decomposition.77

Fig. 2 (a) Schematic of semi-interpenetration network. Semi-interpenetration network is formed by the entanglement between the long-chain thermoplastic molecules and crosslinked thermosets. (b) Schematic of crack propagation in the diffusion and precipitation region. When the crack propagates, it needs to break the semi-interpenetration network structure.80

Fig. 3 Vacuum assisted resin transfer molding experiment setup. The entire process is under high vacuum, which provides the lowest porosity in the final specimen.84

Fig. 4 Experimentally determined intrinsic viscosity of PSU, PEI and PC by using eq.3.86

Fig. 5 Average diffusion depths of the specimens (a) with 0% and 5% polystyrene modified epoxy cured from room temperature to 120°C (b) with 0% to 5% polystyrene modified epoxy cured at 80°C and 120°C.	89
Fig. 6 Polysulfone (PSU) thermoplastic diffusion and precipitation region with 5% PS modified epoxy cured at 120°C is measured from optical microscopy imaging of the thermoplastic (TP)-thermoset (TS) interface. The thermoset diffusion into thermoplastic is characterized by a gradient island-shaped phases and the thermoplastic precipitation region is characterized by the dispersed PSU in the epoxy after curing.	91
Fig. 7 Polysulfone (PSU) thermoplastic diffusion and precipitation region with 5% PS modified epoxy cured at 80°C is measured from optical microscopy imaging of the thermoplastic (TP)-thermoset (TS) interface.	91
Fig. 8 Polysulfone (PSU) thermoplastic diffusion and precipitation region with non-modified epoxy cured at 120°C is measured from optical microscopy imaging of the thermoplastic (TP)-thermoset (TS) interface.	92
Fig. 9 Average precipitation depths of the specimens (a) with 0% and 5% polystyrene modified epoxy cured from room temperature to 120°C. (b) with 0% to 5% polystyrene modified epoxy cured at 80°C and 120°C.	93
Fig. 10 EDX line scan across TS-TP interface of the specimen (a) under 5% PS modified epoxy cured at 80°C. (b) under 5% PS modified epoxy cured at 120°C. The dash lines indicate the diffusion and precipitation region.	94
Fig. 11 Polysulfone (PSU) thermoplastic diffusion and precipitation region in the fiber matrix with	

5% PS modified epoxy curing at 120°C. The dash line represents the boundary of TS-TP interface. Arrows represent the locations where there are precipitates.	95
Fig. 12 Polysulfone (PSU) thermoplastic diffusion and precipitation region in the fiber matrix with 5% PS modified epoxy curing at 80°C. The dash line represents the boundary of TS-TP interface. Arrows represent the locations where there are precipitates.	96
Fig. 13 Polysulfone (PSU) thermoplastic diffusion and precipitation region in the fiber matrix with non-modified epoxy curing at 120°C. The dash line represents the boundary of TS-TP interface.	98
Fig. 14 Representative strain-stress curves obtained from the strain gauge mounted on the drop-off layer in uniaxial tensile tests: reference specimen (without interleaf), interleaved specimens with 5% PS modified epoxy cured at 80°C and 120°C.	99
Fig. 15 Toughness of PSU interleaved specimens from 0.5 to 5% PS modified epoxy cured at 80°C and 120°C. The error bars represent standard errors.	99
Fig. 16 SEM image of the fracture surface of (a) the reference specimen without interleaf. (b) the interleaved specimen with diffusion and precipitation. (c) High resolution close up of the fracture surface.	102

Chapter 4

Fig.1 The three main chemical reactions during curing process of the epoxy. a) Primary amine from hardener has open-ring reaction with epoxide group and generates secondary amine. b) Secondary amine reacts with the epoxide group and generates tertiary amine. c) Etherification reaction [15].	105
--	-----

Fig. 2 ATR-FTIR spectra of RIMH 137 curing agent, RIMR 135 resin and PSU. Peaks monitored during diffusion experiments: 915 cm^{-1} (epoxide deformation) and 1036 cm^{-1} (aromatic deformation) in RIMR 135; 2916 cm^{-1} (C-H stretching of diamine) for RIMH 137; 1151 cm^{-1} (S=O stretching) for PSU.	108
Fig. 3 FTIR experiment setup for determination of diffusivity and curing kinetics.	110
Fig. 4 (a) Typical FTIR spectra of 1151 cm^{-1} peak (S=O stretching) decreases with the increasing time observed in the experiment. The diffusivity and reaction rate are both obtained by monitoring the absorbance changes of characteristic peaks with time. (b) Multiple peaks fit around 1151 cm^{-1} peak during diffusivity determination experiment	115
Fig. 5 Diffusivity determination of PSU into epoxy from 60°C to 120°C. Normalized absorbance data were obtained from ATR-FTIR experiments. Least square fitting curves were based on Eq.4 for each conditions.	118
Fig. 6 Diffusivity determination of epoxy into PSU from 60°C to 120°C. Normalized absorbance data were obtained from ATR-FTIR experiments. Least square fitting curves were based on Eq.4 for each conditions.	118
Fig. 7 Diffusivity determination of PSU to hardener from 60°C to 120°C. Normalized absorbance data were obtained from ATR-FTIR experiments. Least square fitting curves were based on Eq.4 for each conditions.	119
Fig. 8 Diffusivity determination of hardener to PSU from 60°C to 120°C. Normalized absorbance data were obtained from ATR-FTIR experiments. Least square fitting curves were based on Eq.4 for each conditions.	120

Fig. 9 Diffusivity determination of PSU into 5% PS modified epoxy from 60°C to 120°C. Normalized absorbance data were obtained from ATR-FTIR experiments. Least square fitting curves were based on Eq.4 for each conditions.	121
Fig. 10 Degree of curing vs curing time of modified and non-modified epoxy curing at a) 80°C b) 120°C	122
Fig. 11 Diffusion and precipitation process simulation of the 5% PS modified epoxy cured at a) 80°C b) 120°C. Concentration map of PSU is not shown. The line plots represent the concentration of epoxy and PSU along the dash line (I).	125
Fig. 12 EDX line scan across the interface of 5% PS modified specimen without fibers cured at a) 80°C b) 120°C. The dash lines represent the width of the diffusion and precipitation region.	128
Fig. 13 Diffusion and precipitation depth results from experiments and simulations from 25°C to 120°C. The error bars represent standard deviation.	129
Fig. 14 Diffusion and precipitation simulation of the 5% PS modified epoxy with fibers cured at 80°C. Concentration map of PSU is not shown. Line plots represents the concentration along line (I) and line (II) in the concentration map.	131
Fig. 15 Diffusion and precipitation simulation of the 5% PS modified epoxy with fibers cured at 120°C. Concentration map of PSU is not shown. Line plots represents the concentration along line (I) and line (II) in the concentration map.	132
Fig. 16 EDX element mapping of the 5% PS modified specimen cured at 120°C. Sulfur, nitrogen and silicon were traced to represent PSU, cured epoxy and fibers.	134
Fig. 17 EDX element mapping of the 5% PS modified specimen cured at 80°C. Sulfur, nitrogen	

and silicon were traced to represent PSU, cured epoxy and fibers.134

Chapter 5

Fig.1 Chemical reactions in epoxy curing [17] and modification process [10] [13]. a) Primary amine from hardener has open-ring reaction with epoxide group from epoxy and generates secondary amine. b) Secondary amine reacts with the epoxide group. c) Etherification reaction. d) Amino-group grafting onto glass fiber surface. e) Epoxide group end-capped PSU.138

Fig. 2 Bonding in the cured epoxy matrix. The physical bonding here is due to the entanglement of long-chain thermoplastics with the crosslinked thermosets epoxy, which is known as semi-interpenetration network. The chemical bonding due to the modifications are among glass fiber surface to PSU, glass fiber surface to curing epoxy, and PSU to curing epoxy.139

Fig. 3 Schematic of crack propagation between glass fiber surface and cured epoxy under different conditions. (a) With no modifications, the crack lies on the interface between non-treated glass fiber surface and epoxy. Weak intermolecular forces are the only major factors holding two materials together. (b) Under Mode I fracture, the crack propagates through the interface between chemical treated glass fiber and modified epoxy. The surface of treated glass fiber becomes rough. The increased contact area not only improves the adhesion strength but also generates micromechanical interlocks. (c) Under Mode II fracture, the crack propagates through the interlaminar region with crack bridging phenomenon.141

Fig.4 (a) Viscosity for epoxy with various concentrations of modified PSU from room temperature to 120°C. (b) Curing kinetics of neat epoxy under 80 and 120°C.144

Fig. 5 Raman spectroscopy for (a) PSU and (b) Epoxide end-capped PSU. The new peak appeared

~1240 cm^{-1} was the evidence of the epoxide ring grafting onto the polymer chain	150
Fig. 6 Raman spectroscopy for (a) non-modified glass fiber surface and (b) chemically treated glass fiber surface. The peak appeared ~995 cm^{-1} is the evidence of the amino functionality group.	152
Fig. 7 SEM images of glass fiber surface morphology (a) before chemical treatment, (b) after chemical treatment, and (c) after chemical treatment at high magnification	154
Fig. 8 Glass transition temperatures of cured epoxy with different concentrations of modified polysulfone. Error bars represent the standard errors. The advantage of bonding between additives and epoxy can compensate for the influence of additive at low additive concentration, leading to increased glass transition temperature.	155
Fig. 9 Optical microscopy of phase morphology in the cured epoxy etched by methyl chloride to remove the PSU-rich region (a) with 0.5 wt% PSU, and (b) with 5 wt% PSU. The holes on the surface were due to the removal of PSU, which were highlighted with arrows.	156
Fig. 10 Mode I critical energy release rate of the specimen with different concentrations of modified PSU. Error bars represent the standard errors.	157
Fig. 11 Synergistic study of Mode I fracture test. Specimens with individual modification method were compared to the specimens with combined modification methods. Slight synergistic effect from two individual modifications methods were found in Mode I fracture test.	158
Fig. 12 SEM images of mode I fracture surface morphology of (a) 2% PSU with non-modified glass fiber, (b) 0% PSU with modified glass fiber and (c) 2% PSU with modified glass fiber.	159
Fig. 13 Mode II critical energy release rate of the specimen with different concentrations of	

modified PSU. Error bars represent the standard errors.	162
Fig. 14 Synergistic study of Mode II fracture test. Specimens with individual modification methods were compared to the ones with combined modification methods. The further improvement of delamination in Mode II was considered due to the more modified epoxy resin participating in the plastic deformation.	163
Fig. 15 SEM images of mode II fracture surface morphology of (a) 0% PSU with modified glass fiber, (b) 2% PSU with non-modified glass fiber and (c) 2% PSU with modified glass fiber	164
Fig. 16 Simulation of Mode I fracture. Specimen was 160mm in length, 4.15mm in thickness. The left end was under a displacement loading. Initially the pre-crack was 60mm in length and placed 5 microns above the middle of the interlaminar region. The contour map in magnified regions represented the status of crack. Value of 1 (red) in that element represented total fracture and value of 0 (blue) in that element represented zero fracture. The value in between indicated there still existed traction on the crack surface, which were considered as partial fracture. The crack growth matched the previous crack propagation analysis for Mode I in Fig. 3b.	166
Fig. 17 Mode I simulation results vs experiment results.	167
Fig. 18 Simulation of Mode II fracture. The shear deformation was represented by the misalignment of the cells along the pre-defined interlaminar region. The contour map in magnified region represented the status of crack.	168
Fig. 19 Mode II simulation results vs experiments results. The overestimation of the simulation results after the crack initiation was mainly because the crack bridging phenomenon dissipated more energy than single crack growth modelled in the simulation.	169

Acknowledgements

The research done in order to complete this thesis would without any doubts not be possible without the help and contributions of many peoples whose assistance I would like to acknowledge. First, I would like to acknowledge my advisor Prof. Y. Lawrence Yao for his advises, guidance, and patience during my entire doctoral studies. I am very grateful to Prof. Yao for offering me a position in the Advanced Manufacturing Lab and providing me financial support. Prof. Yao taught me many invaluable lessons not only of how to perform high quality research, but also of how to become a more effective person in my life.

Many thanks to the researchers who were willing to allow me to use resources of their laboratories, including Prof. Ah-Hyung Park, Prof. Robert Farrauto, Dr. Tong Wang, Shuoxun Wang, Daniel Eida, Ming Gao, Siwei Ma and Chao Wang. I am very pleased to acknowledge colleagues from Advanced Manufacturing Lab, and particularly Dr. Grant Brandal, Dr. Hongliang Wang, Dr. Panjawat Kongsuwan as friends and colleagues.

Last, and far from least, many thanks for the support in many ways are owed to my family who always stands by me.

Chapter 1: Introduction

1.1 fiber reinforced polymers

Fiber reinforced polymers are a category of composites materials that specifically use fibers to improve the mechanical properties of polymer composites. The polymers without fiber reinforcement are known as matrix materials, which are typically polyester, vinyl ester, polyurethane, and epoxy. These matrix materials are common thermoset resins, they are relatively high in strength, but are brittle in nature. Polyester resin is easy to use and is the least expensive resin available, but it is sensitive to UV degradation and only has moderate mechanical properties. Vinyl ester resin has very high chemical/environmental resistance, but it is sensitive to heat and costs more than polyester resin. Polyurethane resin has higher mechanical and chemical resistance properties than vinyl ester resin, but it costs 1.5 times more than vinyl ester. Epoxies have high mechanical and thermal properties, high moisture resistance, and long working time. However, it is the most expensive of the four resins thus it is generally used in circumstances requiring high mechanical performance such as aerospace and wind energy industries. Fibers are used to reinforce the matrix, resulting in composites with much stronger and stiffer mechanical properties. The extent to which strength and elasticity are enhanced in a fiber reinforced polymers is attributed to the matrix and fiber properties, in addition to the volume fraction, length and orientation of the fiber. The common fiber types in today's industries include aramid fiber, glass fiber, carbon fiber, and basalt fiber. Among the various fibers, glass fiber is most widely used given cost and performance considerations [1, 2].

Fiber reinforced polymers are considered advanced composites materials in aerospace and military applications. However, the first composites can be traced back to 3400 B.C. One of the earliest uses of composites materials was utilized by the ancient Mesopotamians; they glued wood strips at different angles to create plywood. Archeologists have also found natural composite building materials used in Egypt and Mesopotamia. The ancient builders and artisans used straw to reinforce mud bricks, pottery, and boats around 1500 B.C. In about 1200 AD, the Mongols invented the first composite bows made from a combination of wood, bamboo, bone, cattle tendons, horns, and silk bonded with natural pine resin. The bows were small, very powerful, and extremely accurate. Composite Mongolian bows were the most feared weapons on earth until the invention effective firearms in the 14th century (Fig.1).



Fig. 1 Reconstruction of an ancient bow. This is a horn, bamboo, sinew composite [3].

In the later 19th century and early 20th century, revolutionary advancements in chemistry were made. Polymerization allowed a new synthetic resin to transform from a liquid to a solid with crosslinked structure, and more plastics materials such as vinyl, polystyrene and polyester were developed (Fig. 2). As important as these innovations were, reinforcement was needed to improve strength and rigidity. The 1930s were perhaps the most important decade for the composites industry. In 1935, Owens Corning launched the fiber reinforce polymer (FRP) industry by introducing the first glass fiber. In 1936, unsaturated polyester resins were patented. Because of their curing properties, they would become the dominant choice of resins in manufacturing today. In 1938, other higher performance resin systems like epoxies also became available. In World War II, the need from the industry brought fiber reinforce polymers from research into production. Glass fiber composites showed not only strong strength to weight ratio, but also high transparency to the radio frequency. Thus FRPs were adopted for the radar domes and other electronic equipment.

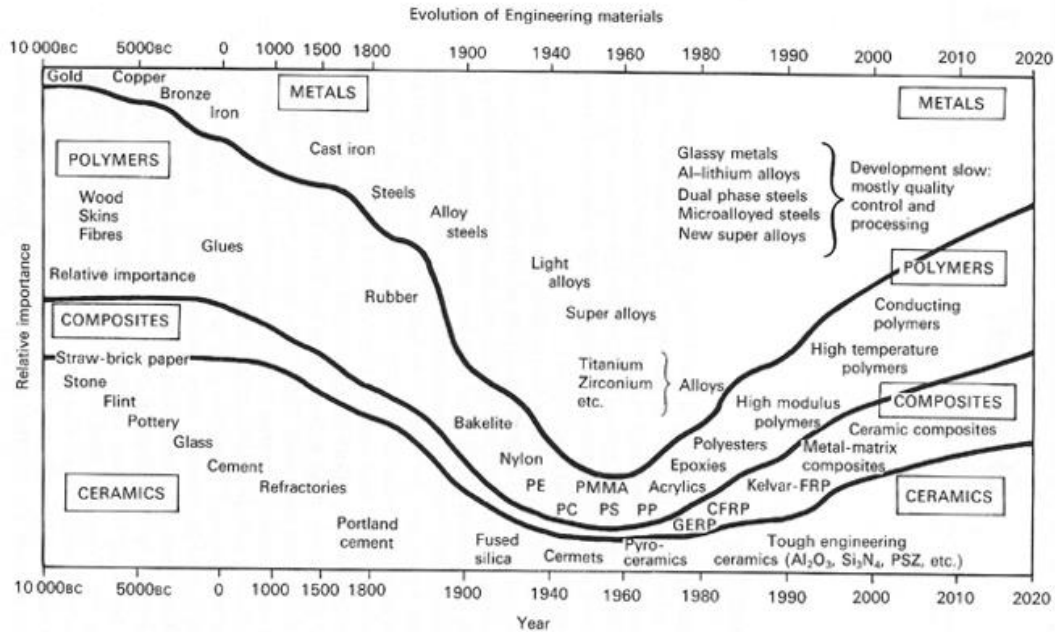


Fig. 2 Schematic diagram showing the development of metals, polymers, composites and ceramics [4].

The FRP for structure usage was not fully commercialized until after the war. By 1947 a fully composite body automobile had been made and tested. This car was reasonably successful and it led to the development of the 1953 Corvette (Fig. 3), which was made using fiberglass preforms impregnated with resin and molded in matched metal dies. During this period, several methods for molding were developed. In 1960s, carbon and boron fibers were developed. Graphite fibers were used only in polymer matrices at this time. The use of graphite as reinforcement for metal matrices was not possible because of the reactivity of carbon with metals such as aluminum and magnesium, It took the invention of air-stable coatings for carbon fibers to prevent reactions between carbon and metal before graphite-aluminum and graphite-magnesium composites became a reality [4]. Progress in advanced fibers led to breakthroughs in aerospace components, structural and personal

armor, sporting equipment, medical devices, and many other applications. New and improved resins continued to expand the composites market, especially into applications requiring higher temperature ranges and corrosive resistance.



Fig. 3 The 1953 Cheverolet Corvette was largely fiberglass and manufactured using new, more efficient molding techniques [5].

There are composites made of short fibers, chopped fibers and long fibers for different proposes. In this study, we focus on long fiber reinforced polymer since it is used in wind energy and aerospace applications. Before the manufacturing process, fiber fabrics are normally categorized into two types: fiber prepreg and fiber preform (shown in Fig. 4[6]). Prepreg is the common term for a reinforcing fabric which has been pre-impregnated with a resin system. This resin system already includes the proper curing agent, which means the prepreg is partially cured. As a result, the prepreg is ready to lay into the mold without the addition of any more resin. Pressure and heat must be used to fully cure the resin. Fiber perform is a dry reinforcing fabric

with no resin It is used in resin transfer molding which will be explained later. There are many advantages in using prepregs. Prepreg can provide maximum strength properties and uniform thickness. Every part that comes out of the mold will have neither resin-rich area nor dry spots. Moreover, using prepreg produces less waste since the resin is already in the fiber structures. Nevertheless, prepreg is pricy. When the cost of resin, cure, fabric and time is added up, prepregs cost more than preforms [6]. As a comparison, the dry preforms and resins used in RTM are generally less expensive than prepreg material and can be stored at room temperature [7].

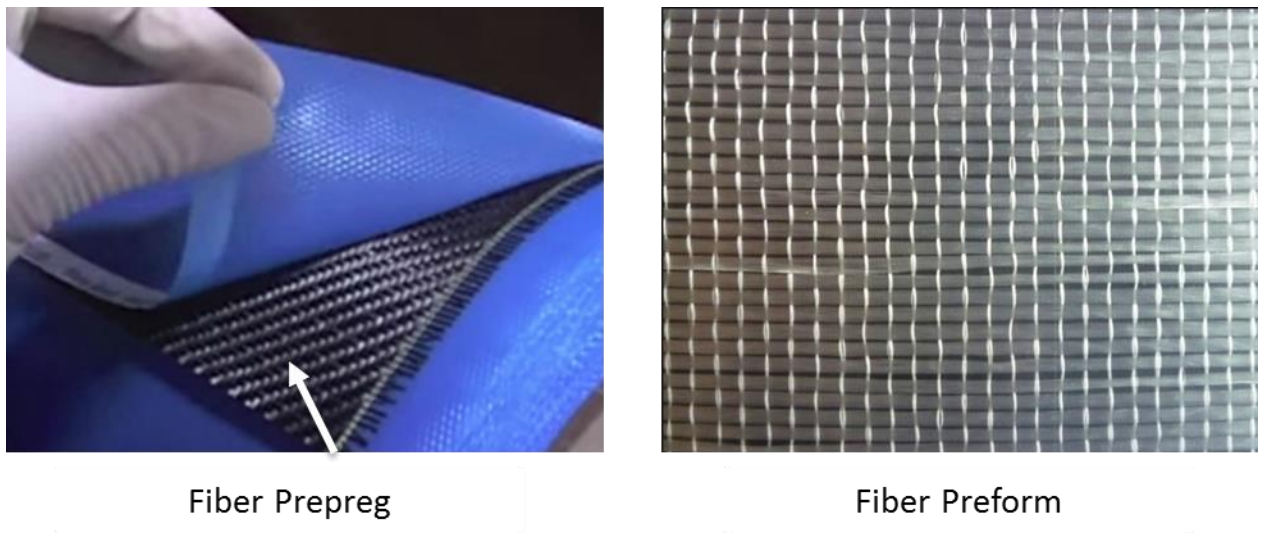


Fig. 4 Fiber prepreg (left) and fiber preform (right). Prepreg is pre-impregnated with resin.

Preform is dry fiber fabric [6].

There are mainly three types of composites manufacturing processes: open molding, closed molding and cast polymer molding. There are a variety of process methods within these categories and each with its own benefits [8].

Open molding (Fig. 5) refers to the process in which composite materials (resin and fibers)

are placed on an open mold where they are cured or hardened while being exposed to the air. Tooling cost for open molds is often inexpensive, making this technique useful for prototyping and short production runs. Open molding utilizes different processes, including hand lay-up and spray-up. Hand lay-up method is the most common and least expensive open-molding method as it requires very few tools. This process is used to make both large and small items including boats, tanks and showers. Spray-up method uses short fibers in resin which is deposited onto a molding surface. Compared with hand-up, this method is more automated and is used to produce large quantities [8].

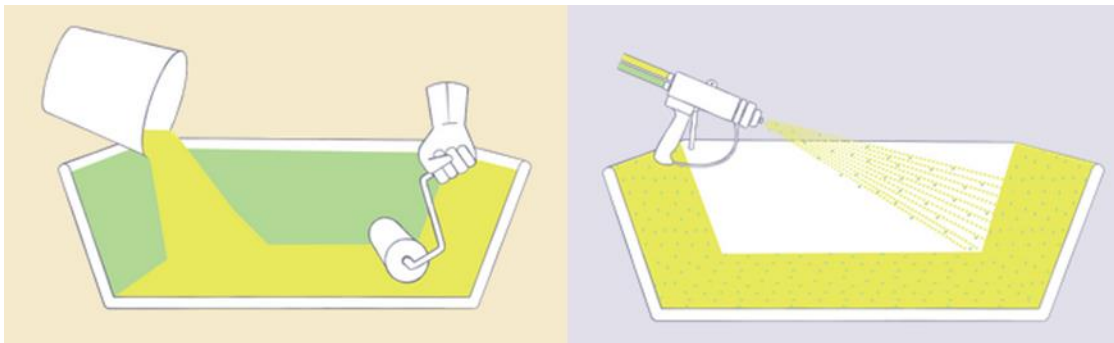


Fig. 5 Open molding methods includes hand layup (left) and spray-up (right) [8].

In the recent years, new technologies based on the open molding method have been developed to produce strong aerospace components in a fast speed. The new methods include automated tape laying (ATL) and automated fiber placement (AFP) as shown in Fig. 6 [9]. The fiber placement process automatically places multiple individual prepreg tows onto a mandrel at high speed by a numerically controlled, articulating robotic placement head. Advantages of fiber placement include processing speed, reduced material scrap and labor costs, parts consolidation and improved

part-to-part uniformity. Often, the process is used to produce large thermoset parts with complex shapes. Automated tape laying (ATL) is an even speedier automated process in which prepreg tape, rather than single tows, is laid down continuously to form parts. ATL is often used for parts with highly complex contours or angles. Tape layup is versatile, allowing breaks and direction changes in the process. It can also be adapted for both thermoset and thermoplastic materials. ATL and AFP grew out of the machine tool industry and they are being extensively used in the manufacturing of fuselage, wingskin panels, wingbox, tail and other structures on the forthcoming Boeing 787 Dreamliner and the Airbus A350 XWB. These open molding technologies are also used extensively to produce parts for the F-35 Lightning II fighter jet, the V-22 Osprey tiltrotor troop transport, and a variety of other aircrafts [7].



Fig. 6 The TORRESLAYUP is an 11 axes Gantry CNC tape layer machine that has been specially designed for high speed tape laying of compound contoured aircraft structural components. [9]

Closed molding (Fig. 7) refers to the process in which composite materials are processed and cured inside a vacuum bag or a two-sided mold, sealed off from the atmosphere. Closed molding may be considered for two cases: when a two-sided finish is needed, and if high production volumes are required. Closed-molding processes are usually automated and require special equipment, so they're mainly used in large plants that produce huge volumes of material—up to 500,000 parts a year. This category includes but is not limited to vacuum bag molding, vacuum infusion process, and resin transfer molding. Vacuum bag molding is designed to improve the mechanical properties of laminate composite. A vacuum is created to force out trapped air and excess resin, thus compacting the laminate. High-fiber concentration provides better adhesion (between layers of sandwich construction). In addition, vacuum bag molding helps eliminate excess resin that builds up when structures are made using (open-molding) hand lay-up techniques. Vacuum infusion process uses vacuum pressure to drive resin into a laminate, it is typically used to manufacture very large structures. Vacuum infusion produces strong, lightweight laminates and offers substantial emissions reductions (compared to open-molding processing and wet lay-up vacuum bagging). This process uses the same low-cost tooling as open molding and requires minimal equipment. Resin transfer molding can produce complex parts with smooth finishes on all surfaces [8].

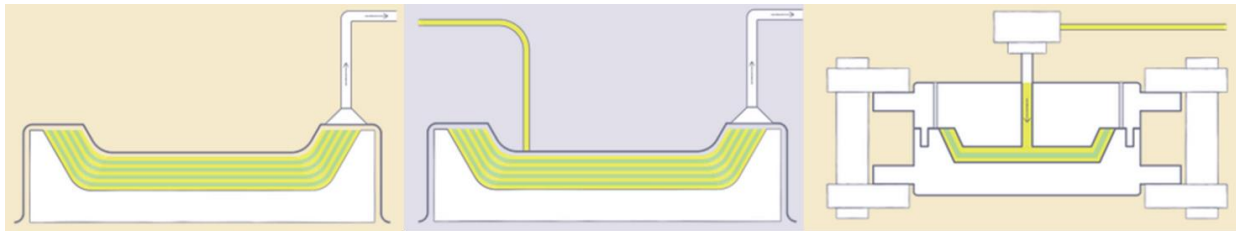


Fig. 7 Closed molding methods includes vacuum bag molding (left), vacuum infusion (mid)

and resin transfer molding (right) [8].

In order to produce more complex shape parts and high mechanical property laminate structure with lower cost than prepreg method, combinations of methods have been developed. These techniques includes vacuum assisted resin transfer molding (VARTM) and controlled atmospheric pressure resin infusion (CARPI) [7]. The Boeing Co. (Chicago, Ill.) and NASA, as well as small fabricating firms are using these methods to produce aerospace-quality laminates [8].

Because present research is collaborated with GE Global Research Center, the application of fiber reinforced polymers in wind energy is especially focused. The manufacturing of wind turbine rotor blades uses two different technologies: vacuum infusion and the prepreg process. Vacuum infusion is more frequent used, it contributes to about 65% of wind energy installations in Europe (162,087 t), while prepreg is used in the remaining 35% (87,278 t) [11]. The main reason that using vacuum infusion is the preferred method in producing wind turbine blade is mainly due to the cost. One report from Lockheed Martin in 2014 indicated that VARTM has incomparable advantage in the cost compared to any tape laying methods currently using in the industries as shown in the Fig. 8 [11].

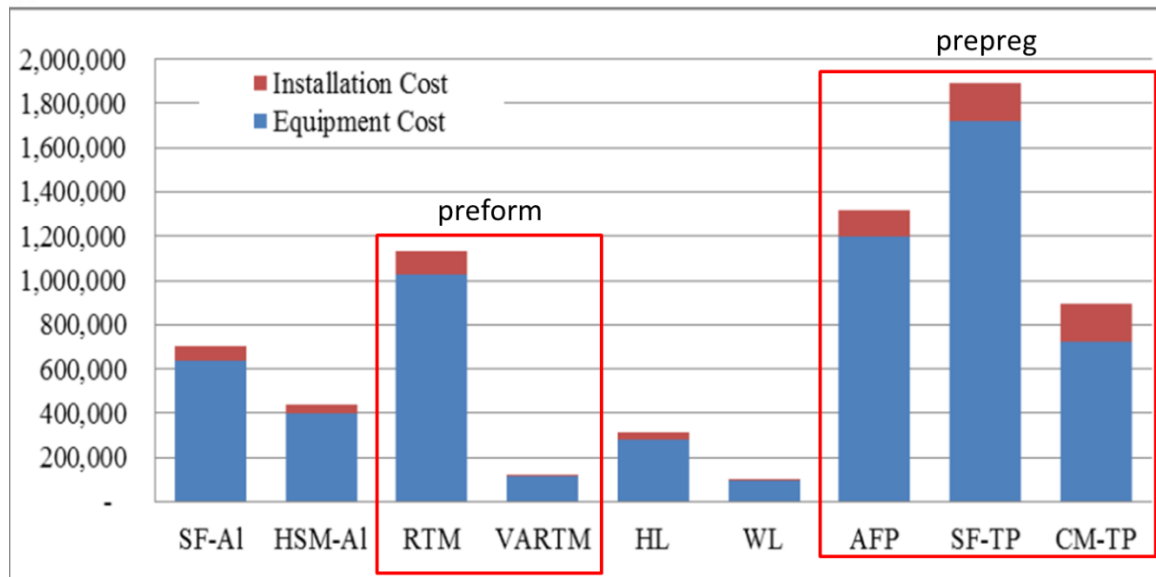


Fig. 8 Capital expenditure across processes [11]

Material technology has developed alongside blade producers' growing preference for resin infusion manufacture. Now that it is possible to achieve a smooth, fair mold surface with high vacuum integrity with composite tooling, infusion is rapidly becoming the process of choice for significant series production of wind turbine blade as shown in Fig. 9 [12]. Most turbine makers are globalizing their operations at a rapid pace. Germany's Siemens Wind Power opened a wind blade plant in Fort Madison, Iowa, last year. Meanwhile, Denmark's Vestas announced plans in August to build a blade plant in Brighton, Colo., to supplement its Existing plant in Windsor, Colorado. The two facilities are expected to produce 3600 blades/year [13].

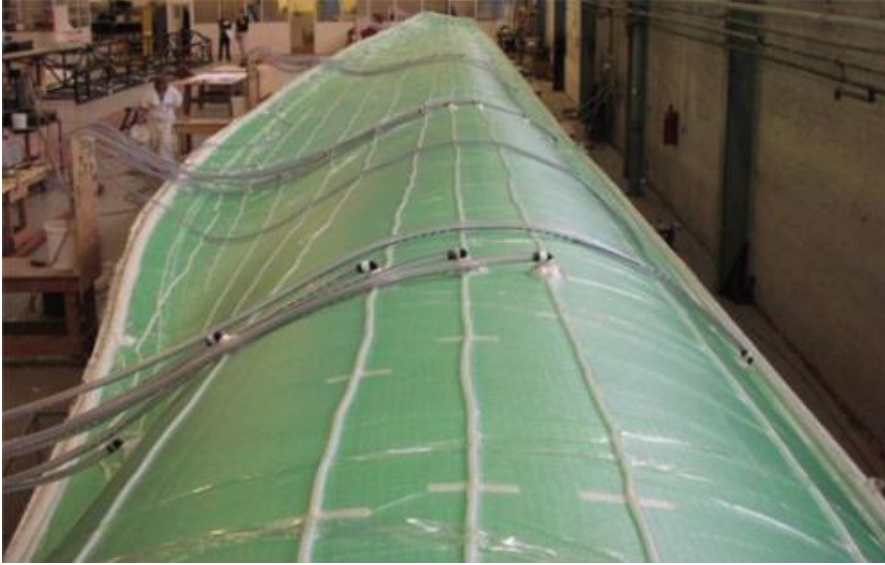


Fig. 9 Vacuum infusion is widely chosen to produce the wind turbine blade [12].

1.2 Development and challenges of fiber reinforced polymers in wind energy

Fiber reinforced polymers are becoming a widely used materials in different industries. The general global applications can be summarized in six categories: marine transportation components, architectural cladding components, aerospace transportation and weapons components, automotive components, energy sector components (wind turbines), and static structural components (buildings/bridges). Since our research is based on the wind turbine blade structure, wind energy related fiber reinforced polymers is discussed this thesis.

The first wind turbine blade used for the electric power generation was built by the S. Morgan-Smith in Vermont, USA, in 1941. The first turbine had two blades which were 53.3 in length and it was able to generate 1.25MW power. The blades were made of steel, and one of the blades failed after only several hundred hours. It became evident that the proper choice of materials is important, and the limitations of metals as a blade materials was were exposed at the beginning wind energy

development. In 1956, Gedser wind turbine was built by Johannes at Gedser coast, which had wooden ribs supporting the aluminum shells and steel spars. It ran for 11 years without problems, however, the blade was only 24m. After the 1970s, most of wind turbine blades were produced with composites materials.

The current trend in wind energy technology is aimed at developing dedicated offshore wind power systems. It is expected that these remotely deployed turbines will be equipped with rotor blades with a length in excess of 100 meters (Fig. 10). Whether such large blades can be manufactured with the current structural design is doubtful and spar-rib-skin structures are suggested as alternative design. Due to the increasing costs of fossil fuels and the increasing efficiency of wind turbines in the last decade, wind energy has become increasingly cost-efficient [14]. With the current growth rate of installed power (annual growth rate worldwide: 25%), which forecasts that in 2020 12% of the global electricity will be produced by wind turbines (23% by 2040), wind energy is well on its way of becoming one of our mainstream sources of energy. In order to keep up this high growth rate, the wind energy market is currently facing a transformation from onshore energy production to offshore installation of so-called wind farms. Remote deployment of a turbine in such a harsh environment makes operation and maintenance difficult and expensive, which brings up the need for dedicated offshore wind power systems. In order to maintain a continuous reduction in costs per kWh (40% cost reduction compared to 2002 is envisaged in 2020 [15]), technological developments predominantly aim at increasing the (rated) power output per turbine (currently 3.5 MW, near future 6-10 [14]). In order to extract more power from the wind, such multi-MW size turbines require larger blades to increase the rotor swept area.

Therefore, it is expected that the maximum blade length will increase from 65 m (2006) to over 100 m in the next decades [16]. Not being bound by noise pollution regulations and having to deal less with aesthetical issues, offshore turbines seem to be well suited for these super-sized blades. However, it is feared that soon the limit of the current blade technology is reached and that new and improved materials and more efficient blade designs are necessary to overcome what has truly become a technological challenge: manufacturing of large wind turbine blades [17, 18].



Fig. 10 Image of offshore wind turbines [19]

1.3 literature reviews of methods to improve fiber reinforced polymer

Fiber reinforced polymers are usually used as laminate composites, the composites are prone to delamination due to the poor through thickness strength. Thus, great efforts have been made to improve the fracture toughness and delamination resistance of fiber reinforced polymers, especially the ones involving irregular shapes.

Many researchers have been studying to improve the composite performance.

Some researchers tried to functionalize the modifier. The smallest known silica particles POSS and tetraethylenepentamine were chemically grafting onto carbon fibers. The POSS grafting improved the fiber surface interfacial adhesion and amino-group in tetraethylenepentamine was able to create strong bonding to the epoxy resin as shown in Fig. 11 [20]. Some used amino end-capped aromatic liquid crystalline copolyesteramide as toughener. This thermoplastic main-chain liquid-crystalline polymer can form a thermally stable network and the secondary amino groups from liquid crystalline copolyesteramide can react with the epoxide group in resin, leading to strong bonding between thermosets and thermoplastics [21]. Similar work has been made on polyethersulfone. A hydroxyl terminated polyethersulfone has been developed and co-cured with N, N'-bismaleimido-4,4'-diphenyl methane in the epoxy system. The results indicated that thermal stability, glass transition temperature increased but the impact strength decreased [22]. A phosphorous-modified polysulfone was used as a combined flame retardant and toughness modifier to combine both desirable functions in a single compound [23]. Mechanical properties of bismaleimides modified polysulfone epoxy matrices was also studied but due to the viscosity consideration, the fiber was not included and the polysulfone was grafted with an epoxide group [24]. Besides grafting epoxide group, synthesis of polyarylene ether sulfone was grafted with pendant amines on its main chain to produce the chemical reactivity with the epoxy [25].

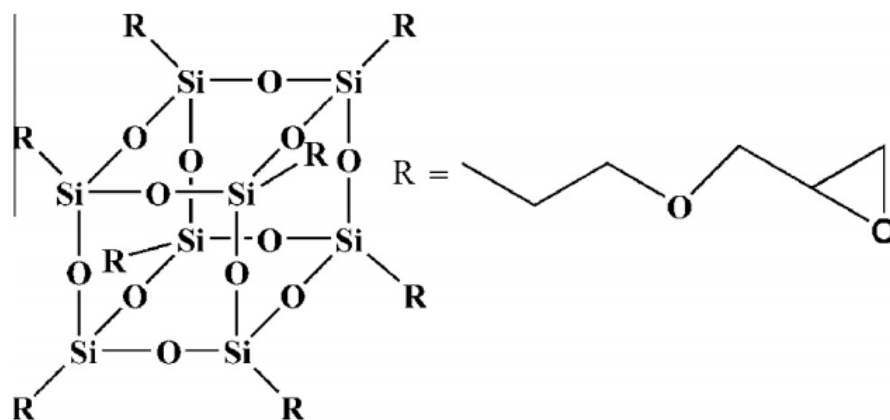


Fig. 11 Molecular structure of octaglycidyl polyhedral oligomeric silsesquioxane [22]

The advantages of grafting and co-polymerization are obvious: it can provide strong chemical bonding; implementation of low concentrated thermoplastic may still have low viscosity which is enough for resin infusion; alkali treatment can improve the mechanical properties without damaging the base glass fiber [20]. However, the downsides of this method is also significant: acid or strong oxidant treatment on fibers may damage the fibers and influence the mechanical behavior and viscosity of the epoxy will increase based on how much modifiers in the system.

Others were trying to add two more modifiers in the same epoxy system to overcome and compensate the loss of strength due to the ductile toughener. An epoxy resin modified with reactive liquid rubber and silica nanoparticles was studied as demonstrated in Fig. 10. Acrylonitrile rubber was used and cyclohexyldiamine was chosen as the hardener. Gic of the unmodified polymer was increased from 609J/m to 1223J/m by 4.6 wt% reactive rubber and increased further to 2059J/m by 4.1 wt% reactive rubber and 2 wt% nanosilica [26, 27].

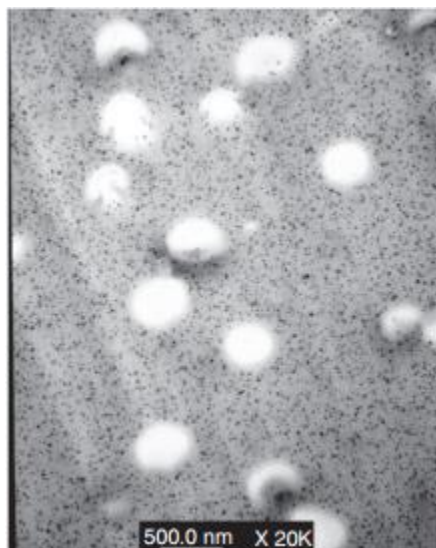


Fig. 12 Typical hybrid system with liquid rubber particles and nanosilica particles [29]

Caccavale et al. studied the same resin but used polyamine hardener. In his study, 7.3 wt% rubber modification only partially compensated by the addition of 3.7 wt% nanosilica but the toughness was still 6% lower than that of nonmodified epoxy system and the glass transition temperature was dropped by 19K [28]. Tsau et al. studied the same liquid reactive rubber acrylonitrile but used isophorone diamine as the hardener. The modulus of the unmodified system was lowered by 10 wt% of rubber from 3.25 GPa to 2.63 GPa, and brought back to 3.18 GPa by the addition of 10 wt% nanosilica. G_{ic} was increased by 516% (1170J/m) but the hybrid system achieved only 930J/m, indicating there was no synergistic effect [29]. Sun et al. studied SC-79 epoxy resin system and used nanosilica and alumina or carbon nanofibers as the third modifier. The modulus of the matrix improved by 40% with 10 wt% nanosilica, however alumina or carbon nanofibers shows no further improvements [30]. Carboxy-terminated polyurethane-co-polyether block copolymer was used as an elastomer toughener with nanosilica. It showed that 9 wt% elastomer and 9 wt%

nanosilica was the best mixture but there was no synergistic effect of the two modifiers [31]. In another study, amino-functional reactive liquid rubbers showed synergistic improvement by 80% to 300%. The long flexible rubber molecules randomly crosslinked into polymer matrix was concluded as the major reason to make the toughening more efficient [32, 33]. Core-shell elastomers was another modifier widely studied to toughen the epoxy matrix, but the hybrid system with nanosilica indicated the additive behavior not synergistic effect [34-36]. The hybrid system provides the feasibility of resin infusion because the nano-size particle can penetrate into close meshed fabrics and nanosilica only increase the resin viscosity only slightly at higher concentrations. The main disadvantages of this method were the reduced strength and modulus due to rubber molecules and lower glass transition temperature of the cured epoxy system, indicating low crosslinking density.

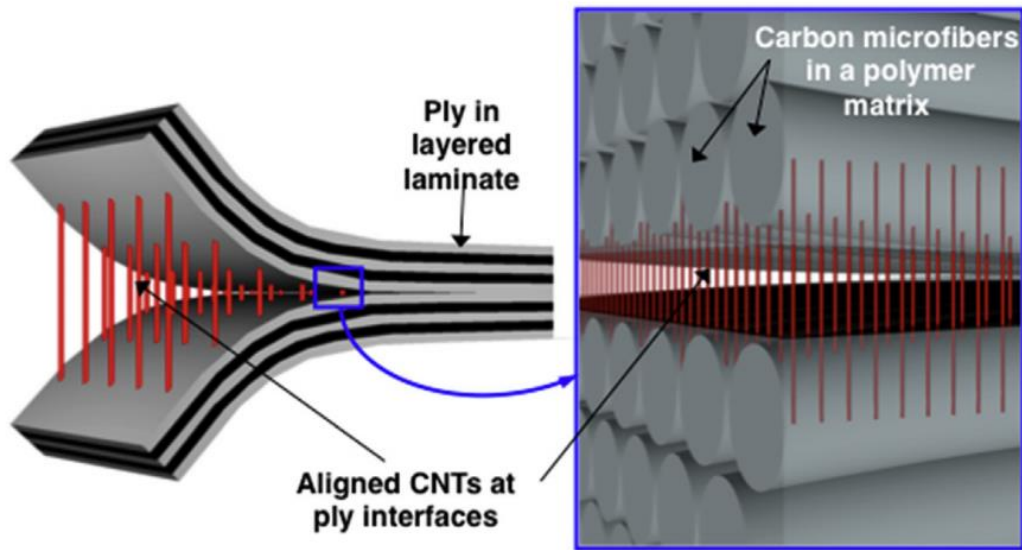


Fig. 13 Aligned carbon nanotubes (A-CNTs) bridge ply interfaces in laminated composites [39]

Tackifier was one other method to improve the composites delamination resistance. Recently,

electrospun was used to generate a membrane on the fiber fabric laminate. Some electrospun polycaprolactone on both sides of the fiber mats, which generated good adhesion of deposited nanofibers on the glass fiber mats, as well as the inherent tough and ductile polycaprolactone nanofibers. The crack was observed partially through the nanofiber toughened interlayer, resulting in increased toughness [37]. This method was considered better than film due to the better interfacial compatibility and the way in which the nanofibers were arranged into the laminate had a major effect on the improved toughness [38]. Aligned carbon nanotubes are developed to place between the fiber fabrics to overcome the problem of forming clusters as an additives. The aligned carbon nanotube increased the interlaminar toughness by hot pressing into the prepreg [39]. Epoxy-based functionalization of carbon nanotube enhanced the interface adhesion between carbon nanotube and resin matrix with preferred orientation [40]. The limitation of this method was the penetration depth of the carbon nanotube was limited to the fiber fabric surface.

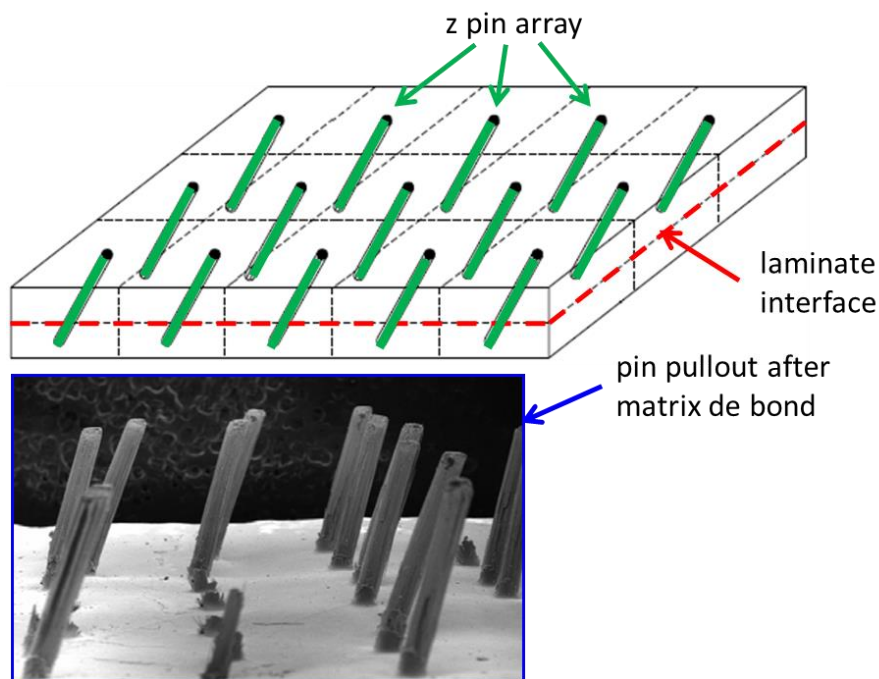


Fig. 14 Z-pinning method used to improve the bonding between two plies. Crack need to break the z-pins to propagate through the laminate interface [42]

Some other researchers try to improve the design of composite structure near the drop-off. Some extend alternating laminates beyond the ply drop to decrease the severity of the dropoff layer. Also some other researchers directly drive fiber into the adjacent layer, which is known as z-pinning [42] or stitching method [41] as shown in Fig. 14 and Fig. 15. However, this method will disrupt the fiber structure and introduce resin rich region, which is a weak region in the composites.

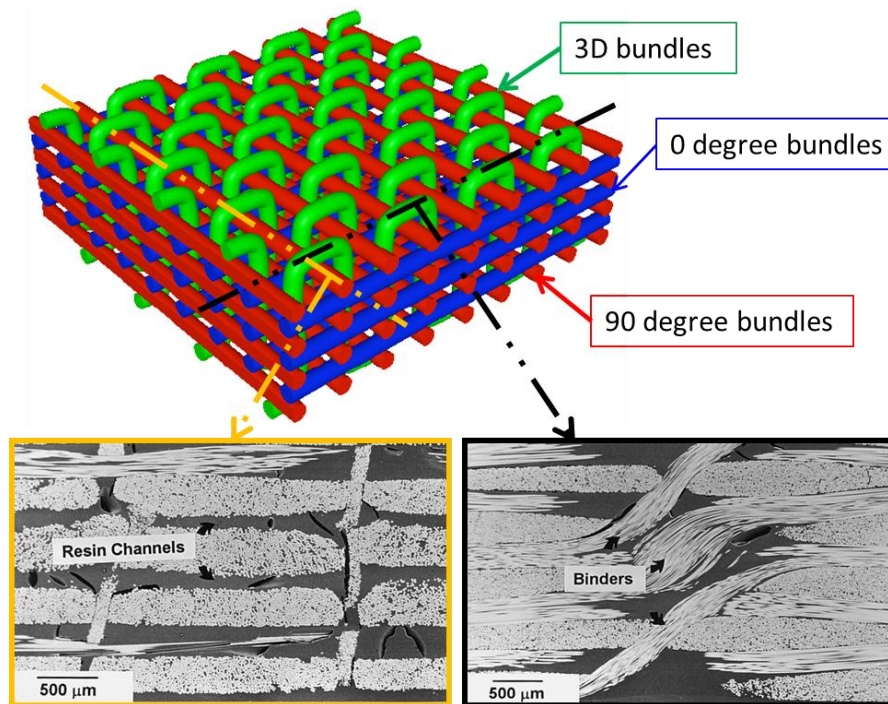


Fig. 15 Stitching method used to improve the composites structures. The stitches increases more resin rich region in the composites structure [41].

Since the thermoset epoxy resin is brittle in nature, it is of high strength but low toughness,

which means it requires small amount of fracture energy for crack to initiate and propagate. Using additive method will increase the viscosity of the epoxy system due to the ductile long chain molecule, researchers tried to insert a ductile material between the up and bottom fiber fabrics at the position the crack most likely to occur. This method is also known as interleaf or interleaving. The interleaf is normally a thermoplastic film or veil or membrane. The most challenge is to overcome the low adhesion between the interleaf material and the epoxy matrix since it will lead to the poor interface bonding. It indicated that both high toughness and adhesion strength are required for the interleaf material [43]. One of the new approaches taken by Hojo, et al [44-46] involves a new type of thermoplastic, ionomer, which is a polymer partially ionized by the metallic ion, used as interleaf. Because of its active chemical property, it has good adhesion to epoxy resin that creates a thin layer which is a mixture of fiber, resin and the ionomer (Fig. 16). In this case, the matrix and interleaf has higher bonding strength; when a crack propagates, it needs more energy to go through the plies. However, the thickness of the mixed zone is only around one to two fiber diameters and the plastic zone ahead of the crack can still reach the interface between the interleaf and epoxy, and thus limit the fracture toughness improvement.

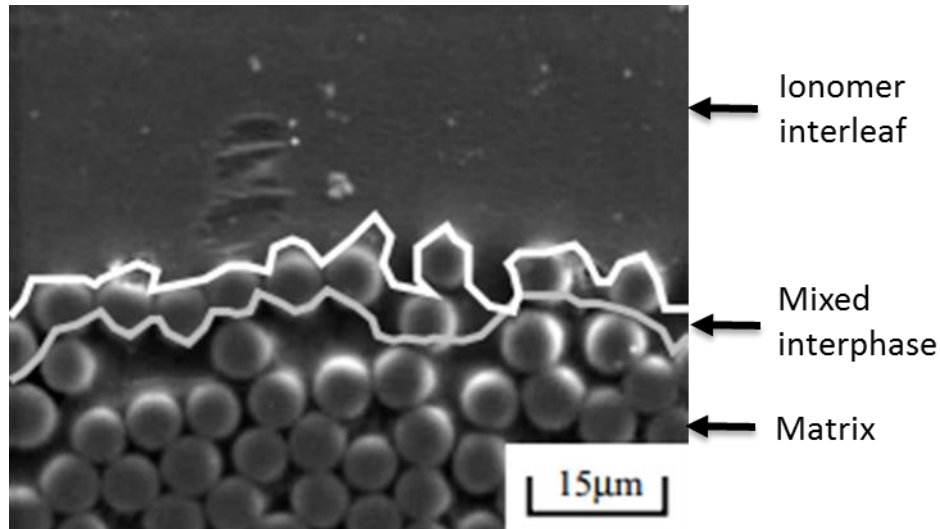


Fig. 16 Ionomer can generate a mixed interphase between epoxy matrix and ionomer interleaf due to the reactive chemical properties [45]

1.4 Fundamental theory of bonding between materials

The bonding mechanism between thermosets and thermoplastics or between polymers and substrates is complicated because there are several intrinsic forces that may operate across the interface. There are four main mechanisms of adhesion that have been proposed, which are adsorption theory, mechanical interlocking theory, electronic theory and diffusion theory. Adsorption theory has the widest applicability, but the other three also may exist in some specific conditions. No one theory is applicable to all systems. It is more likely that the bonding is based on the contribution of one or more mechanisms.

1.4.1 Adsorption Theory

Adsorption theory states that adhesion results due to the interatomic and intermolecular forces that are established between the atoms and molecules in the surfaces of the adhesive and substrate

[47]. Van de Waals forces are the most common atomic forces, however hydrogen forces are also included in this category. These forces are referred to as secondary bonds. The fact that the presence of polar groups on the surface often increases adhesion is given as evidence for this theory. Molecular forces such as ionic, covalent and metallic interfacial bonds, called primary bonds, can also be formed between the adhesive and substrate by chemical reaction. One criticism of the chemical reaction theory is that since reaction is not confined to the interface the theory relies on interfacial reaction to explain the response of a system of materials in which volume deformations are occurring.

1.4.2 Mechanical interlocking theory

The theory of mechanical interlocking proposes that mechanical keying of the adhesive in the irregularities of the substrate surface is the major source of adhesion. Interlocking plays a direct role in joining porous materials such as paper, cloth and wood [48]. However, because high strength joints are achievable with smooth adherents such as glass, surface roughness is not a general requirement for joint strength. The bonding due to mechanical interlocks is directly linked to the porosity and surface roughness of the substrate with the degree of adhesion that can be obtained. Any type of material if it is observed at the microscopic level, has a surface composed of valleys and ridges, the surface topography allows the adhesive to penetrate and fill the valleys, resulting in anchorage areas between the adhesive and substrate. Apart from the roughness and porosity of the substrate surface, to generate adhesion anchor points, it is necessary that the adhesive has a good filling power, the adhesive can penetrate into the valleys and pores substrate surface, the adhesive filling power is directly related to its viscosity. Mechanical adhesion theory

does not account for the incompatibility that may exist between the adhesive and the substrate, it only takes into account the topography of the substrate and adhesive filling power, and so this theory cannot explain the adhesion between surfaces with low roughness or smooth, nor the lack of adhesion between rough substrates incompatible with adhesive.

1.4.3 Electric theory

The electronic theory of adhesion was initially proposed by Deryaguin and coworkers [49]. According to this theory, the joint is a capacitor which becomes charged due to the contact of two different substances. Adhesives and substrates may have different electron band structures and there is likely to be some electron transfer on contact. This results in the formation of a layer of electric charge at the interface. The main evidence for this view is that electrical discharges and sometimes electron emission can occur when one strips pressure-sensitive adhesive tape from a substrate. There are several criticisms of this theory. The electrical phenomena occurs when the joint is broken, thus the phenomena of fracture is used to explain adhesion. Failure and joining phenomena may not be related as the chemical and rheological states of the adhesive are often different in the two instances. Furthermore, there is no decrease in joint strength in environments of increased humidity and conductive materials form joints.

1.4.4 Diffusion theory

The diffusion theory is often used to explain the adhesion of polymers. The theory states that the intrinsic adhesion of polymers to themselves and to each other is due to mutual diffusion of polymer molecules across the interface. The adhesion strongly depends upon the extent to which polymer segments can mix and entangle across an interface [50]. This requires that the

macromolecules possess sufficient mobility and compatibility. The solubility parameter is the index of compatibility of two components.

Voyutskii [51] was an early advocate of the diffusion theory. In his work he found a correlation between joint strength and contact time, temperature, polymer type, molecular weight and viscosity. He argued that functional dependence of joint strength on some of these parameters is similar to that expected for a diffusion process. Direct evidence of interdiffusion exists as radiometric studies have demonstrated the presence of macromolecular diffusion [48]. More recent evidence has been reported by several researchers [52, 53] that have used neutron reflectivity to show that molecular diffusion across the interface creates entanglements between the polymer chains, as a result of these penetrations anchorage areas and adhesion points take place (Fig. 17). The mobility and degree of penetration of the polymers is determined directly by their molecular weight, so that the molecules with low molecular weights have high mobility compared to long chain large molecular weight polymers. This theory usually can be used to explain the phenomenon of adhesion between polymeric materials, plastic welding, etc.

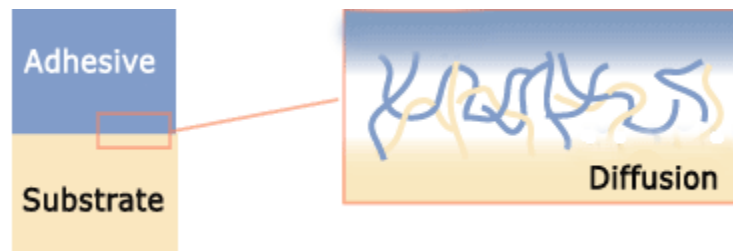


Fig.17 chain entanglement between adhesive and substrate through mutual diffusion [54]

1.5 Mechanism of melt bonding

In the previous section, the method that using toughener to toughen the composite structure has a common limitation that the interface between the toughener and the epoxy resin is weak,

which means the major bonding between the toughener and epoxy is based on intermolecular forces. Although the interleaf is of high ductility, the in-active interaction between interleaf and epoxy will let the weak interface keep in the interlaminar region, thus crack can easily migrate to this interface and the purpose of interleaving methods cannot be fully realized.

In this study, the interleaf material was chosen from high performance industry thermoplastics, which are of high glass transition temperature and strong fracture toughness. In order to prevent the crack migrates to the interface between interleaf and matrix, the thermoplastic interleaf is preheated above the glass transition temperature to increase the mobility of the molecule. Significant reduction of viscosity makes the interleaf possible to flow into the fiber fabric with the help of applied pressure. The deep interleaf penetration into the fiber fabrics makes the interlaminar region as a thermoplastic rich region, in which the crack is arrested and the ductility of thermoplastics leads to the capability of undergoing large plastic deformation when crack propagates. Thus, the fracture energy is increased and delamination resistance is improved.

1.6 Interphase formation in polymers

Interphases between polymer and polymer are important in determining the polymer macroscopic properties. It plays a significant role in many process such as crack healing, welding, adhesion etc. The interphase generate a unique structures in the polymer system and this region often controls the overall mechanical properties of the materials [55-58]. Due to the inhomogeneous phase in the interphase region, it may therefore be more susceptible to have the different properties than either of the bulk phases. Thus, understanding the structure and properties

of the interphase is essential to improve the macroscopic behavior of the composite. Especially the interpenetration of the polymers plays major contributions to the bonding between two materials.

Historically, the most widely studied polymer-polymer interfaces are those between two fully polymerized thermoplastic polymers. Interphase formation at a thermoplastic-thermoplastic interface involves the interaction of the polymer chains. This primarily arises from polymer chain dynamics through Rouse relaxation and motion, reptation, and Fickian diffusion [59-64]. If the chains across the interphase are incompatible they may move away from each other, creating voids at the expense of free energy, and incurring a loss of configurational entropy. The compromising structure attained at equilibrium is the interphase, and it is typically several nanometers thick (1-20 nm) depending on the compatibility of the polymers. Hence the extent of interdiffusion is directly related to the thermodynamic interaction parameter for the polymer system [64]. More compatible polymers display larger interphase thicknesses, typically several hundred nanometers. Optimum properties are, however, obtained for interdiffusion distances on the order of the radius of gyration of the shorter chains, typically 10 nm. In comparison, interphase sizes at compatible interfaces between low molecular weight monomers and fully polymerized thermoplastics can be even larger, on the order of microns. Polymer-polymer interphase formation may also involve other mechanisms like adsorption [65-67] or phase separation [68] in addition to the interdiffusion of polymer macromolecules at the interface. For the present study the polymer-polymer interphase formation, due primarily to diffusion mechanisms, will be examined. Specifically diffusion of compatible low-molecular weight thermosetting species into fully polymerized thermoplastic polymer, and subsequent entanglement upon curing will be studied. This is considered in the

next section.

1.7 Experiment procedures and characterization methods

1.7.1 Vacuum assisted resin transfer molding

All the test specimens in this thesis were produced by improved homemade vacuum assisted resin transfer molding. The process is under high vacuum environment in order to minimize the porosity in the epoxy matrix and debulking process is included to increase the fiber volume fraction and provide the even thickness through the specimen.

The detailed vacuum assisted resin transfer molding procedure is listed below.

Step 1: Panel cleaning

In the first step, the aluminum panel is cleaned to remove the residue from the previous test. This is done by gently scraping the top surface of the aluminum panel using the center section of a razor blade. Afterwards, the panel surface is polished using Kim wipes and acetone until further cleaning does not create any black stains on the Kim wipes (Fig. 18a).

Step 2: Panel Preparation

Electrical tape is taped along the edges of the right side of the panel (Fig. 18a). The region that is enclosed by the electrical tape is waxed using the Rexco Partall Paste that is shown below (Fig. 18b).

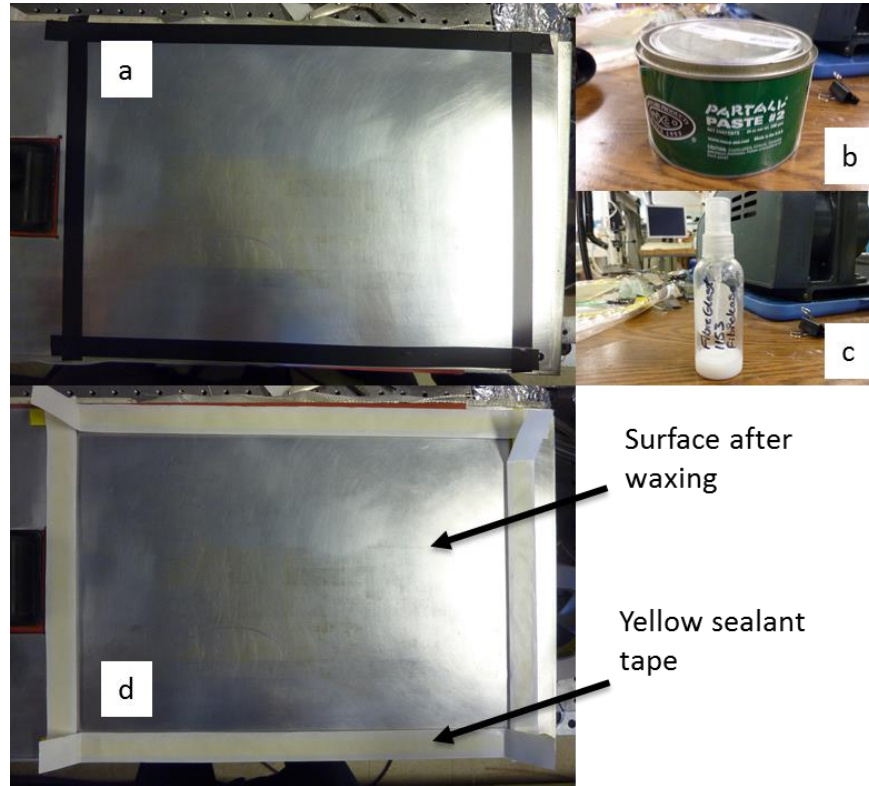


Fig. 18 (a) Electrical tape taped along the edges of the clean surface. (b) Rexco Partall Paste wax. (c) Fiber Glast Liquid wax. (d) Yellow sealant tape surround the waxed surface.

The wax is distributed evenly on the panel surface using Kim wipes. After the application, the coat is allowed to dry for one minute. After one minute has passed, the panel surface is gently wiped using the white cloth to remove excess wax from the surface. This waxing procedure is repeated a total of 4 times. After the completion of four cycles, 4-5 squeezes of Fiber Glast Liquid Wax are sprayed on the panel surface and distributed with a Kim wipe (Fig. 18c).

In the last step of the panel preparation, the electrical tape is replaced by yellow sealant tape. It needs to be made sure to overlap the tape at the corners in order to create a good vacuum seal (Fig. 18d).

Step 3: Component Assembly

To perform the VARTM process and produce a composite panel, the following components are necessary: fiberglass fabric, separation media, distribution media, and plastic foil (Fig. 19).

A full-scale composite panel requires three core fiberglass fabric layers with dimensions 12" by 8" as well as one drop-off layer with dimensions 6" by 8". The fiberglass layers are stacked on the top of each other and placed directly onto the panel surface. Next, a sheet of separation media is cut to a length of 13" and a width of 9". The sheet is placed on the top of the fiberglass layers. Furthermore, a 12" by 8" sheet of distribution media is cut and placed on the top of the separation media. Finally, plastic foil is cut to dimensions of 20" by 15". This foil is eventually placed on the top of the entire assembly and used as a vacuum bag.

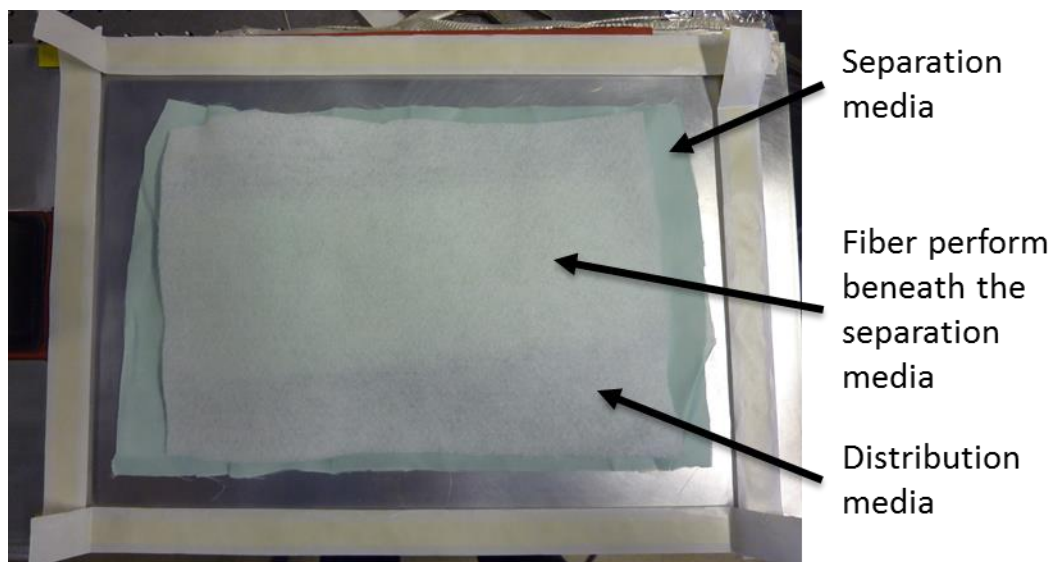


Fig. 19 Preparation before resin infusion

Step 4: Tube connections

Two spiral tubes (Fig. 20) are cut to a length that is equivalent to the width of the composite

panel. It is important to round the edges of the tube segments, since a failure of doing so may tear holes in the vacuum bag. The spiral tubes are afterwards wrapped in separation media, and the ends of the separation media are taped to the spiral tubes using electrical tape.



Fig. 20 Preparation of spiral tubes

One of these tube segments is connected to 3/8" outer diameter clear PVC tubing, which is afterwards connected to the vacuum chamber (Fig. 21). The PVC tube is pressed onto the yellow sealant tape, and a separate piece of yellow sealant tape is pressed on the top of the PVC tube to completely seal the entire area around the PVC tube. The second spiral tube segment is also connected to a 3/8" diameter PVC tube, which in return is connected to the resin trap. Again it needs to be made sure that the PVC tube is properly embedded in yellow sealant tape at the location where the tube exits the aluminum panel.

Step 5: Vacuum bag sealing

At this stage, the left-most yellow sealant tape segment is exposed, and the left edge of the plastic foil (vacuum bag) is pressed onto the tape. Afterwards, the paper cover is removed from

the top and bottom yellow sealant tape segments, and the plastic foil is pressed onto the tape starting from the left and ending at the right end. While the foil is pressed onto the tape, it needs to be kept in tension to minimize the formation of wrinkles that could cause an air-leak.

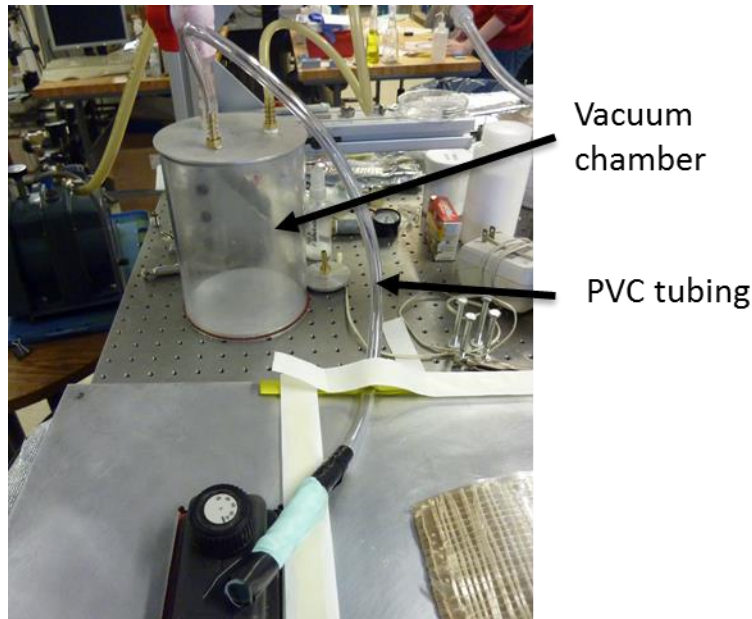


Fig.21 Tubing connection between vacuum chamber and spiral tubes

Once the right end is reached, the yellow sealant tape on the right side is exposed, and the plastic foil is pressed onto the tape to completely seal the rectangular area on the aluminum panel. In order to create a perfect seal, the vacuum bag needs to be pressed onto the yellow sealant tape repeatedly until the sealant tape flattens out and fills even the smallest gaps. Once a good seal is established, the input tube (left tube) is clamped, and valve between the vent (right tube) and the vacuum pump is opened (Fig. 22). If the panel is sealed, the vacuum pump will cease to make pumping sounds after a few seconds. If there is a leak on the other hand, the vacuum pump continues to pump air out of the testing area, and the yellow tape needs to be pressed more firmly

onto the aluminum panel. After achieving a good vacuum, a vacuum check is performed by closing the valve between the vent and the vacuum pump for 15 minutes. If the pump does not make any pumping sound after re-opening the valve after 15 minutes, the next step may be performed.

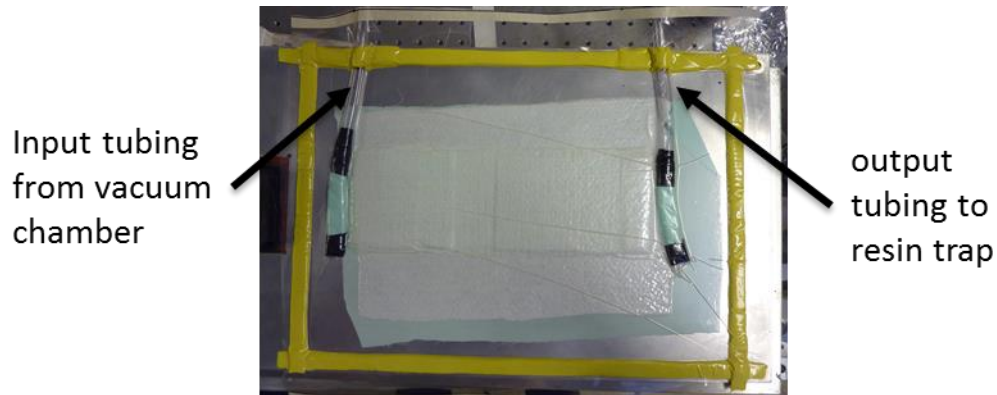


Fig. 22 resin infuse from left to right with the help of the vacuum pump

Step 6: Debulking

In the next step, the fiberglass layers are debulked by releasing and re-applying the vacuum 50 times. To prepare the debulking process, clamps are applied both at the inlet and the vent while keeping the valve between the vacuum pump and the vent opened. One debulking cycle consists of two steps. In the first step, the vacuum is released by un-clamping the inlet clamp and letting air flow into the vacuum bag. In the second step, the vacuum is re-applied by tightening the inlet clamp and releasing the vent clamp.

Step 7: Resin Preparation

After completing the debulking step, the resin can be prepared. The resin consists of two components, which are the epoxy and the hardener. The two components are mixed at a ratio based on the recommendation from the company. For a full-scale composite panel, 250.8 grams of epoxy

are mixed with 74 grams of hardener. Separate beakers are used to measure the weight of both components on the digital scale, whereby special care needs to be taken that the beakers are cleaned properly beforehand (clean with soap and methanol, blow dry with dried air afterwards). The hardener is poured into the beaker with the epoxy, and the resulting resin is stirred for 5 minutes until no more strings can be seen in the resin.

Step 8: Resin Degasification

The beaker with the resin is placed inside the vacuum chamber. An approximately 12" long 3/8" soft PVC tube is press-fit into the outlet hose of the vacuum chamber and sealed with yellow sealant tape. The other end of the PVC tube is placed inside the beaker, and the vacuum chamber is closed. Next, the tube that is connected to the outlet of the vacuum chamber is closed using a vise grip, and the valve that connects the vacuum chamber with the ambient is closed. To create a vacuum inside the chamber and thereby degasify the resin, the chamber inlet valve that connects to the vacuum pump is gradually opened. At some point during the degasifying process, the resin starts forming a foam layer as can be seen in the Fig. 23.

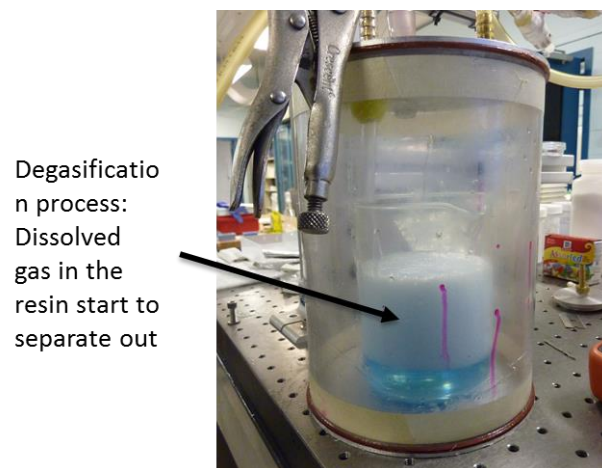


Fig. 23 Dissolved gas separate out from the resin in the vacuum chamber

The foam layer increases in thickness during the degasifying process. To prevent the foam from spilling into the chamber, the input valve that connects the chamber with the vacuum pump needs to be momentarily closed. Once the foam has settled, the valve can be opened again to finish the degasification process. When the degasification is finished, the input valve is closed to perform a vacuum check. In most cases, the vacuum is not perfect, and very soon the pressure in the chamber rises and pushes the resin out of the outlet tube. However, since the pressure in the chamber will eventually be increased anyways during the infusion, it is not problematic if the vacuum chamber has a slight leak. As long as no bubbles can be seen in the resin at the exit of the vacuum chamber, the degasification process was successful.

Step 9: Resin infusion

At this stage, the set-up is ready for the infusion of the resin into the vacuum bag. In order to infuse the resin, the vise grips are removed at both the inflow and the vent. Additionally, the valve between the vacuum pump and the vacuum chamber is closed, and the valve at the vent is opened such that vacuum pressure is maintained at the vent. Afterwards, the valve that connects the vacuum chamber to the ambient is briefly opened to slightly increase the pressure gradient between the inflow and the vent. Due to the pressure gradient, the resin starts flowing into the vacuum bag. While the resin infuses the vacuum bag, the position of the resin is marked after every minute until the resin has reached the vent (Fig.24). Once the entire vacuum bag is full of resin and the resin starts filling the resin trap, the infusion can be stopped by clamping the inflow tube and the vent tube with vise grips. All the valves to the vacuum pump are closed, and the valve that connects the

vacuum tube to the ambient is opened. The inflow tube is cut just above the barbed fitting of the vacuum chamber, and the vent tube is cut just beneath the barbed fitting that connects to the resin trap. It is important to put a cup underneath the resin trap, since the resin will pour out once the tube is cut.

Resin
infusion
from left to
right

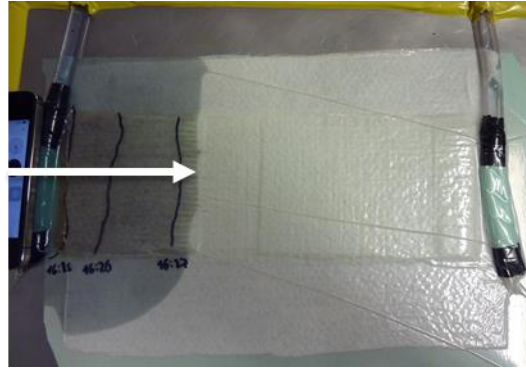


Fig. 24 Resin infusion process. The speed of infusion is monitored every minute.

Step 10: Curing

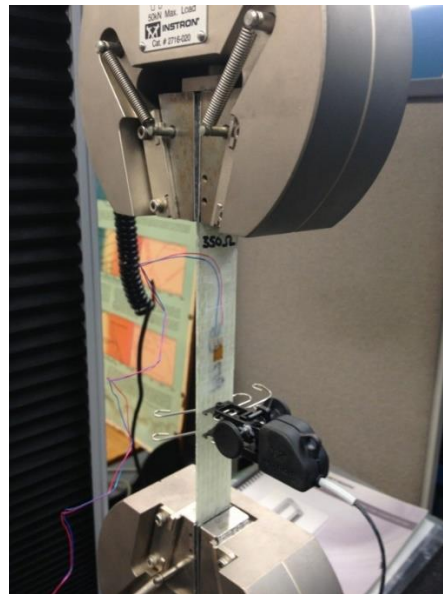
After completing the infusion and disconnecting the vacuum bag setup, the resin is cured with a heating panel that is located underneath the aluminum panel. If the panel contains an interlayer, the temperature is raised to 110°C. Without interlayer, the panel is heated to 80°C. In both cases the panel is cured for a total of 5 hours. A thermocouple is taped onto the top surface of the composite panel and connected to a multimeter to monitor the panel temperature.

1.7.2 Mechanical testing

In this thesis, three different types of mechanical testing have been done. They are uniaxial tensile test of laminate with external drop-off layer (mixed mode failure), standard mode I (Open

mode failure) and mode II (shear mode failure) fracture tests.

Mixed mode failure test is used to simulate the loading conditions in reality. For example, the complex interplay of the forces acting on the wind turbine blade induces both normal and shear stresses in the structure. Modified ASTM-D3039 test on Instron 5569a Universal Testing Machine was performed. Fig. 25 shows the experiment setup for the mixed mode failure test. The 11” long and 1” wide specimens were loaded along the length direction of the specimen. An Omega 0.6mm grid and 120 Ω strain gauge was mounted onto the drop-off ply, such that the edge of the strain gauge was at a distance of 0.4” from the drop-off. Additionally, the displacements of the core plies were measured using an Instron 2630-103 clip-on strain gauge extensometer. The specimens were loaded until the drop-off layer was entirely delaminated, i.e. until the strain at the strain gauge dropped to zero.



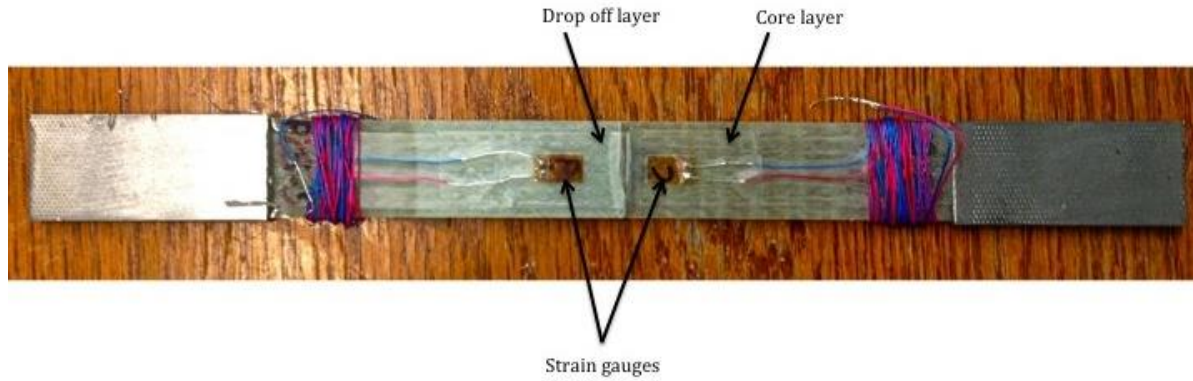


Fig. 25 Experiment setup for the mixed mode failure. The strain gauge is used to measure the strain change on the drop-off region, and the extensometer is used to record the displacement change on the core layers.

Mode I is the fracture mode in which the delamination faces open away from each other. Mode I interlaminar fracture toughness test quantifies the delamination growth by a slow and stable extension. The composite samples are made as double cantilever beams which contain nonadhesive inserts (Fig. 26). The inserts separate the double cantilever beams and help initiate delamination along the midplane of the composite samples. Forces are applied to the specimen via loading blocks bonded to the edges of the specimens with the inserts, and the load and delamination length are recorded. A modified beam theory method is used to express the strain energy G_{Ic} release rate of a double cantilever beam clamped at the delamination front [69]. Per ASTM standards, the dimension of the specimens must be at least 125 mm (5.0 in.) long and from 20 to 25 mm (0.8 to 1.0 in.) wide. The strain rate of the operating machine must be at a constant rate from 0.5 to 5.0 mm/min (0.02 to 0.20 in/min).

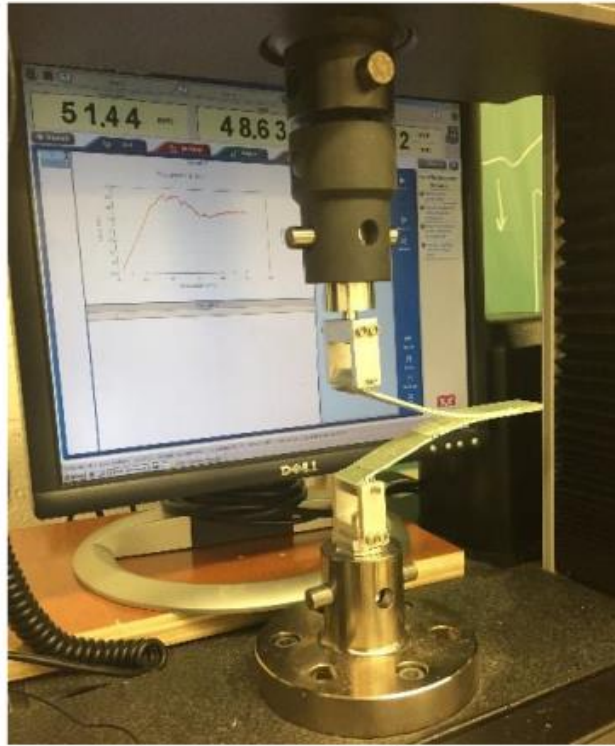


Fig. 26 Experiment setup for Mode I fracture test. The Teflon film was pre-inserted in the laminate as the crack initiator.

Mode II test is performed with compression of the composite rather than extension. The specimen being tested is supported by two cylinders beneath it, and is compressed by a cylinder above the sample and in between the supports as shown in the Fig. 27 [70]. Per ASTM standards, the loading roller must have a radius in the range of 4.7 to 9.6 mm [0.185 to 0.378 in.]. The support rollers must have the same radius in the range of 3.0 to 6.4 mm [0.118 to 0.250 in.]. Loading for all fracture tests must be performed in displacement control at a rate of 0.5 mm/min [0.02 in./min].

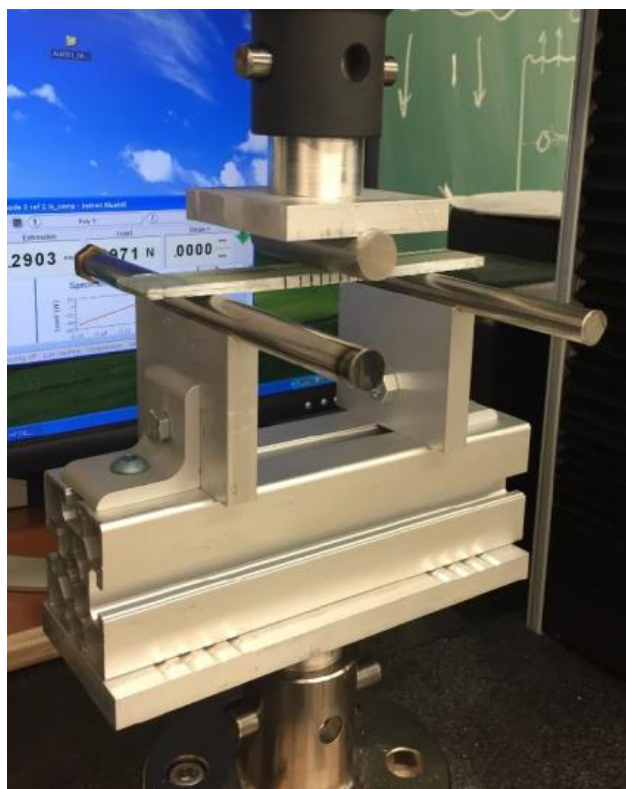


Fig. 27 Experiment setup for Mode II fracture test.

1.7.3 Attenuated Total Reflective Fourier Transfer Infrared Spectra (ATR-FTIR)

Fourier Transform Infrared Spectroscopy-Attenuated Total Reflectance is an internal reflection technique in which an optically dense medium (the internal reflection element-IRE) is used as a waveguide to obtain an infrared spectrum. Since the IRE is an optically dense medium, IR totally reflects above the critical angle at the crystal/sample interface, and an evanescent wave forms at interface, decaying exponentially from the surface through the penetration depth of the infrared. FTIR is an important technique to analyze the molecule structure of the compounds. Molecules have bonds that continually vibrate and move such as stretching vibration or bending vibration. Excited vibrational state can be reached when the specific frequency satisfies the energy

difference between the ground and excited state. In reality, the incident infrared light sets the electrons in the atoms of the interface material into oscillation and the summation of the re-radiation of the electrons is the reflected light. In the molecular level, atom arrangement leads to the incident light reaching different penetration depth based on the wavelength of the light. If the sample absorbs the lights in infrared region, the evanescent wave interacts with the materials. Thus, the infrared spectrum of the sample is obtained by detecting the attenuated radiation [71].

The penetration depth is defined as the distance at which the electric field formed by the evanescent wave diminishes by a factor of 1/e:

$$d_p = \frac{\lambda}{2\pi n_2 (\sin^2 \theta - (\frac{n_1}{n_2})^2)^{0.5}} \quad (1)$$

Where λ is the wavelength of light in vacuum, θ is the angle of incidence, n_1 and n_2 are the refractive indices of the IR crystal and the sample respectively.

If the sample absorbs in the inferred, the wave interacts with the material causing the attenuation of the total reflection of the propagating beam inside the IR crystal

$$A = \int_0^\infty aSC(z) \exp(-\frac{2z}{d_p}) dz \quad (2)$$

Where z is the distance from the surface, a is the oscillator strength, $C(z)$ is the concentration, S is the cross sectional area. This expression represents a weighted average of the concentration of the absorbing species.

In this study, ATR-FTIR is used to determine the diffusivity of thermosets and thermoplastics during the curing process. Thermoplastic, polysulfone in this study, is dissolved in A thin film of thermoplastic is coated onto the crystal by using spin coater. The thickness of the coating film is examined by optical profiler and microscopy. The epoxy, hardener are transferred to the surface of

the film. Specific peaks are monitored with time to measure the change of the absorbance, leading to the change of species concentrations in the infrared penetration region as shown in the Fig. 28 [72].

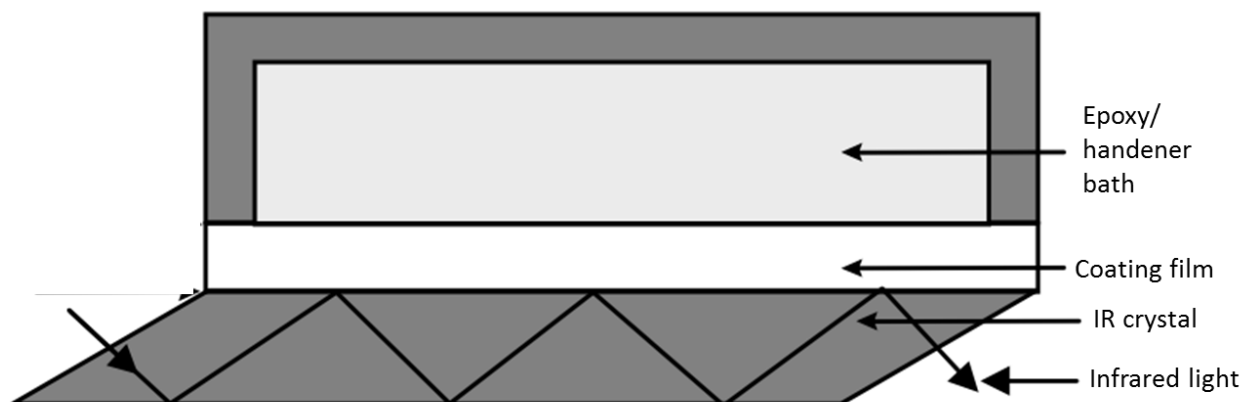


Fig. 28 Sample set-up for diffusivity determination

1.7.4 Solubility determination by viscometry

Solubility parameters of high molecular weight polymers is usually used to predict the compatibility between polymers and solvents, which is of great importance to choose the suitable solvent for the polymers. The solubility of low molecular weight compounds normally is determined by the heat of evaporation. However, high molecular weight polymer has strong intermolecular forces, thus it is difficult to vaporize the polymer before it starts to degradation. As a result, the heat of vaporization method is not suitable for determine the solubility of polymers, viscometry is an alternative way for polymers.

In the suitable solvents, the interaction between the polymer molecules and solvent molecules is positive, which means the polymer molecule chains are able to relax, thus the most compatible

solvents should have the most similar solubility parameters as the polymer since they have close intermolecular forces which are hydrogen bonding, polar forces and dispersion forces. This can be revealed by the relationship between the intrinsic viscosity of the solution and the solvents solubility. Choosing solvents with different solubility which are compatible with the polymer can calculate the viscosity by using viscometry. The polymer solubility is close to the maximum point of viscosity corresponding solution solubility [73].

1.8 Organization and objectives of dissertation

Increasing the toughness of glass fiber reinforced polymers via deep interleaf penetration is presented in Chapter 2. By heating the thermoplastic interleaf above the glass transition temperature, the interleaf softens and is able to flow into the fiber bundles. Additionally, applied pressure through the clamp ensures that the interleaf penetrate deep into the fiber bundles. A physical based model is developed to determine the penetration depth reached in the fibers and to help guide the selection of processing conditions. The width of the penetration region is analyzed with optical microscopy. Quantification of the composite toughness is carried out by uniaxial tensile testing of the specimens to the point of fracture. The melt bonding temperature is found to have significant influence on the interleaf penetration depth, and samples with deep interleaf penetration are consistently found to be stronger.

The pairing of thermosets epoxy and thermoplastic polymers may lead to many subsequent interactions, and as such, delamination resistance improved due to the diffusion and precipitation between thermosets and thermoplastics is investigated in Chapter 3. Viscometry, optical

microscopy, uniaxial tensile test, and electron microscopy are performed to investigate the interactions between thermoplastic and epoxy. The viscometry testing enables determination of the solubility between polymers, as a result the compatibility between the epoxy and thermoplastics can be predicted. A polystyrene modified epoxy is used to promote diffusion and precipitation through reducing the curing reaction rate. In the modified system, the diffusion and precipitation depth increased significantly even with obstructing fiber structures.

Detailed study on the diffusion and precipitation process is discussed in the Chapter 4. Quantification of the diffusivity in the epoxy system is carried out by ATR-FTIR experiments. The FTIR spectra reveals the mass transportation and chemical reaction between thermosets and thermoplastics at the molecular level. Comparison of the spectra peak changes of epoxy and hardener on the PSU shows that the epoxy monomers diffuse faster than the hardener into PSU, and PSU diffuses much slower than epoxy and hardener. Curing reaction rate determination shows that low concentration polystyrene modified epoxy system has significantly reduced epoxy crosslinking speed. A physical based model which couples both curing kinetics and diffusion/precipitation processes is developed to help understand the complex physical chemical process and guide the selection of processing condition.

The development and characterization of a synergistic toughening mechanism on fiber reinforced polymers without using interleaf are described in Chapter 5. The synergistic effect of the two modification methods, surface functionalization of fibers and epoxide end-capped polysulfone modified epoxy, further improves the delamination resistance. The interactions between the two modification methods enable forming of micro-mechanical interlocks on the fiber

surface and strong chemical bonding between modified fiber and epoxy. Furthermore, the formed chemical bonds connect the thermoplastic additive into the crosslinked thermoset networks, compensating for the loss of crosslinking density due to the additive. The crack growth in the interlaminar region is simulated with extended finite element method for a direct comparison of experimental and numerical results in Mode I and II fracture test.

Chapter 2: Effect of Deep Penetration of Interleaf on Delamination Resistance in GFRP

2.1 Introduction

Fiber-Reinforced Polymer (FRP) composites have been widely used. The applications of the composites span automotive, marine and aerospace industries. These industries are dedicated to increase the use of FRP in their products in an effort to decrease weight and increase energy efficiency.

As glass fiber reinforced polymer (GFRP) is often used as laminated structures, the composites are prone to delamination when loaded due to their poor through thickness strength. For some specific product structures like turbine blades, the tapered shape leads to stress concentration at the areas where there is a drop-off laminar, causing catastrophic failure. Efforts have been made to improve the fracture toughness and delamination resistance of GFRP structures especially the ones involving drop-offs.

Some researchers strived to improve the delamination resistance and toughness by increasing the ductility of the entire matrix. From Leach and Moore's research [1], the thermoplastic (TP) matrix, polyether ether ketone (PEEK) significantly increases the delamination resistance and toughness, however, the major disadvantage of Carbon Fiber(CF)/PEEK is also obvious; it requires high temperature and pressure during the molding process due to the higher viscosity of thermoplastics, and thus increases the cost and implementation difficulties [2]. Some other researchers [3] enhance the composites toughness by improving the design of composite structures, such as "feathering", which includes extending alternating laminates beyond the ply-drop to decrease the severity of the drop-off layer, as well as "z-spiking", in which the stitches of the drop-

off layer are removed and the fiber bundles are directly driven into the fiber bundles of the adjacent core layer, the delamination resistance increased; however it is not easy to control the distance between drop offs during fabrication procedure and may disrupt the fiber structure and create resin-rich zones.

Another method is to locally toughen the composites and modify the resin-rich layer in between the plies, known as interleaving, in which a ductile material is inserted between the plies. From Ozdil and Carlsson's research [4], the tested thermoplastic- interleaved composites showed that the low adhesion between the interleaf material and the matrix caused the poor interface adhesion and toughness. The results indicate that both high toughness and adhesion strength are required for the interleaf material. Many approaches have been attempted to achieve this purpose such like incorporating nylon particles [5], modified powder/spray tackifier [6], nanofibers [7-10] and TP/Carbon fiber veil [11], but the adhesive failure between the interleaf and matrix still remains. One of the new approaches taken by Hojo, et al [12-14] involves a new type of thermoplastic, ionomer, which is a polymer partially ionized by the metallic ion, used as interleaf. Because of its active chemical property, it has good adhesion to epoxy resin that creates a thin layer which is a mixture of fiber, resin and the ionomer. In this case, the matrix and interleaf has higher bonding strength; when a crack propagates, it needs more energy to go through the plies. However, the thickness of the mixed zone is only around one to two fiber diameters and the plastic zone ahead of the crack can still reach the interface between the interleaf and epoxy, and thus limit the fracture toughness improvement. If a thermoplastic interleaf penetrates much deeper into the fiber bundles, such a plastic zone ahead of a crack is more likely to remain within the penetrated

region without reaching the interface of the interleaf material and epoxy and as a result, more fracture energy is required for delamination to occur.

In the present study, a hot-melt bonding process of a TP interleaf is investigated. The relationship between the bonding temperature and the penetration depth of the interleaf into fiber bundles was investigated. Inter-laminar mixed-mode fracture properties of the interleaved GFRP were studied as a function of the penetration depth. The dependence of crack path and propagation behavior as well as crack arrest and toughening mechanism on the penetration depth were investigated and discussed.

2.2 Background

2.2.1 Loading Conditions at the Drop-off Structure

GFRP are widely used due to their high strength, light weight and low cost. One of the important applications is the wind turbine blade. In service, the blade is subjected to complex loadings induced by the turbine rotation and variable wind loadings [16]. The loads in the flap-wise direction and centrifugal forces are two important factors that may lead to failure of the blade, as indicated by arrows in Fig. 1(a). Due to aerodynamic requirements and weight constraints, geometric properties are required to vary along the length of the wind turbine blade, and ply drop-offs are introduced by piling up hundreds of plies at the root but only a few at the tip (Fig. 1a). The drop off plies cannot carry any load at the termination location, and thus the far field load carried by the drop off plies needs to be transferred to the adjacent continuous plies via interlaminar stresses [17]. An interleaf is also shown at the drop off site.

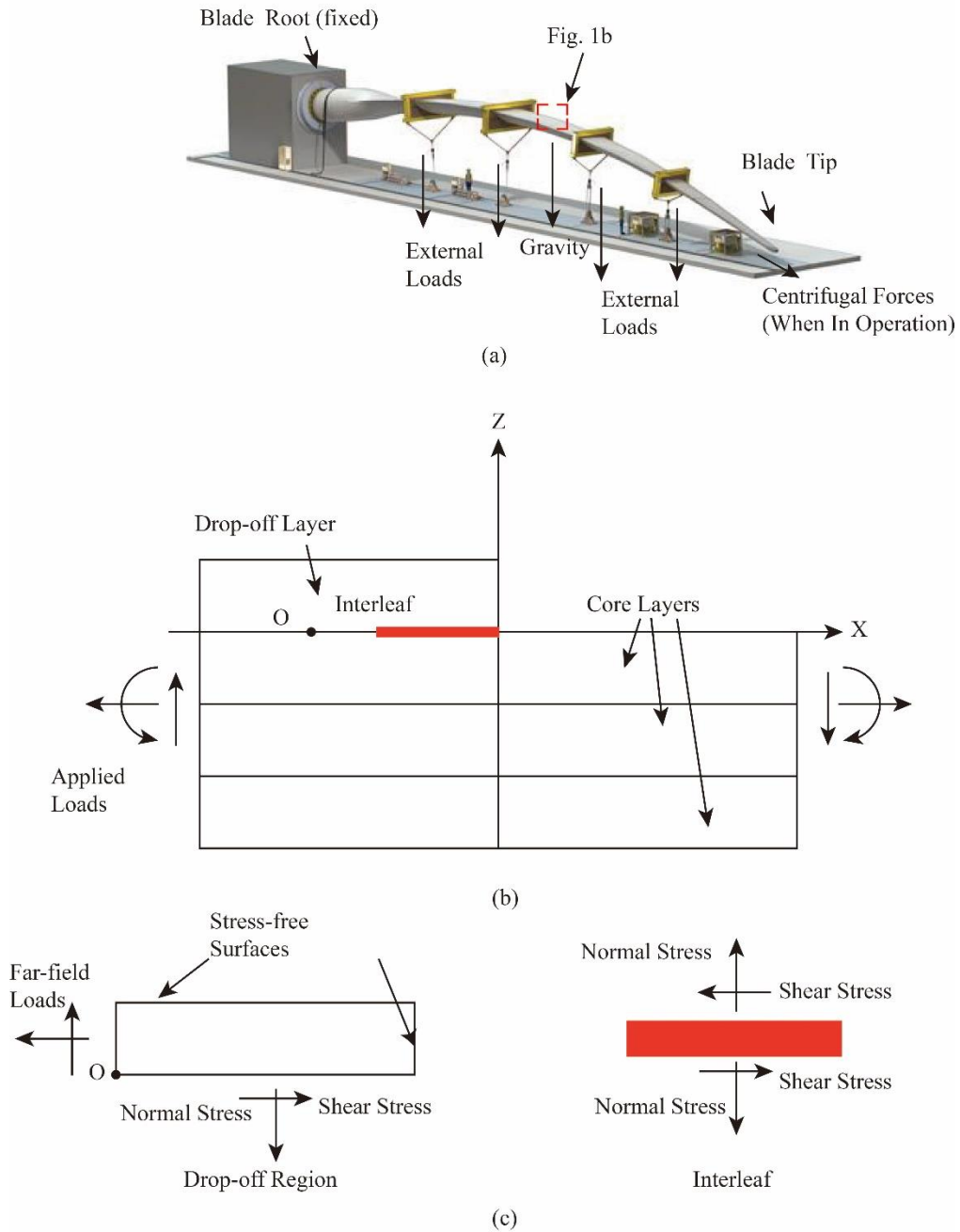


Fig. 1 (a) MTS System Corp. used their special testing system to test the wind turbine blade to failure under the flap-wise loads. When the blade is in operation, the centrifugal forces will occur due to turbine rotation [15]. (b) Schematic of the specimen under external loads: interleaf is inserted between the external drop-off layer and the core layers. (c) Free body diagrams of the drop-off region and interleaf: applied force and moment equilibrium about Point O, both normal and shear stresses exist in the drop-off region and interleaf.

Free body diagrams of the external drop-off layer and the interleaf are shown in Fig. 1 b&c. The

applied loads can be either in-plane or bending loads or both. As required by the force equilibrium on the drop off structure, the interlaminar shear stress must exist along the lower surface, equal to and opposite to the net far-field loads. Normal Stress exists due to the moment equilibrium about point O and its integral along x-direction equal to and opposite to the applied load in the z-direction. The free body diagram of the thin interleaf beneath the drop off ply is determined the same way.

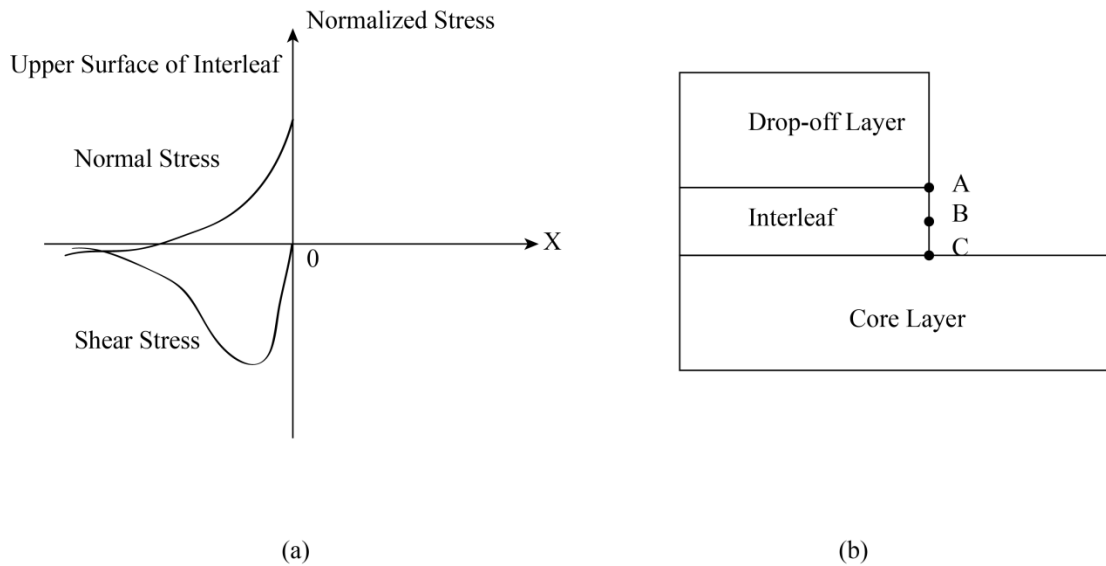


Fig. 2 (a) Illustration of the interlaminar shear and normal stress distribution along X-direction on the upper surface of the interleaf: the trends of the shear stress and normal stress are based on the analysis of the force and moment equilibrium for the external drop off layer [18]. For the lower surface of the interleaf, the stresses are of the same magnitudes but opposite directions.

Peak stresses occur close to the terminated surface. (b) Considering both normal and shear interlaminar stresses near or on the terminated surface of the interleaf, a crack is more likely to initiate near point A and C.

The drop-off structure has the following force distribution. The peak interlaminar normal stress is at the terminated surface and the peak interlaminar shear stress occurs slightly before the terminated surface and shrinks to zero at the terminated surface both under in-plane loads and bending loads [17-18] and illustrated in Fig. 2a. The corresponding interlaminar stress distribution

on the interleaf is determined by the principle of action and reaction. It is observed that the peak interlaminar stress can be reduced significantly by inserting an interleaf of lower stiffness and the interlaminar stress is relieved if a tough interleaf is presented to undergo the necessary plastic deformation, which helps to absorb more incident energy [19].

2.2.2 Crack Initiation and Propagation

By using Quadratic Stress Criterion for initiation of delamination [20],

$$\left(\frac{\sigma_s}{Z_s}\right)^2 + \left(\frac{\sigma_n}{Z_n}\right)^2 > 1 \quad (1)$$

where σ_s is the interlaminar shear stress, Z_s is the interlaminar shear strength, σ_n is the interlaminar normal stress and Z_n is the interlaminar normal strength, the crack will initiate near point A or point C (Fig. 2b), which means the crack is more likely to initiate at the interfaces. Under the in-plane loading condition, for the external drop-off ply, the crack is influenced by both Mode I (opening) and Mode II (shear) fracture. After the crack initiates, it propagates essentially in the weakest region within the crack tip plastic zone [21]. For the brittle materials with high yield strength, near the tip, the stress reaches the ideal strength, which is large enough to break the bond and allow the crack to spread. For more ductile materials, the stress still rises as the crack tip is approached, but when it exceeds the yield strength, the materials yield, and then a plastic zone forms at the crack tip and relieves the stress.

The main purpose of inserting a thermoplastic interleaf into the resin-rich zone is to toughen this brittle region and increase the delamination resistance by absorbing more energy when crack propagates. However, due to the low bonding energy between the interleaf material and epoxy, the crack tip plastic zone can still reach this interface and propagates along it even if the interleaf

migrates a little (one to two fiber diameters) into the matrix as ionomer described in the previous section (Fig.3a). Thus, the hot-melt bonding method is introduced to increase the penetration depth. It is believed that with deeper penetration (5 to 6 fiber diameters) of the interleaf into the fiber bundles, the plastic zone ahead of the crack tip is more likely to remain within the penetrated zone and thus not reach the interface between interleaf and epoxy; as a result, the crack propagates within the penetration region and consumes more fracture energy (Fig.3b).

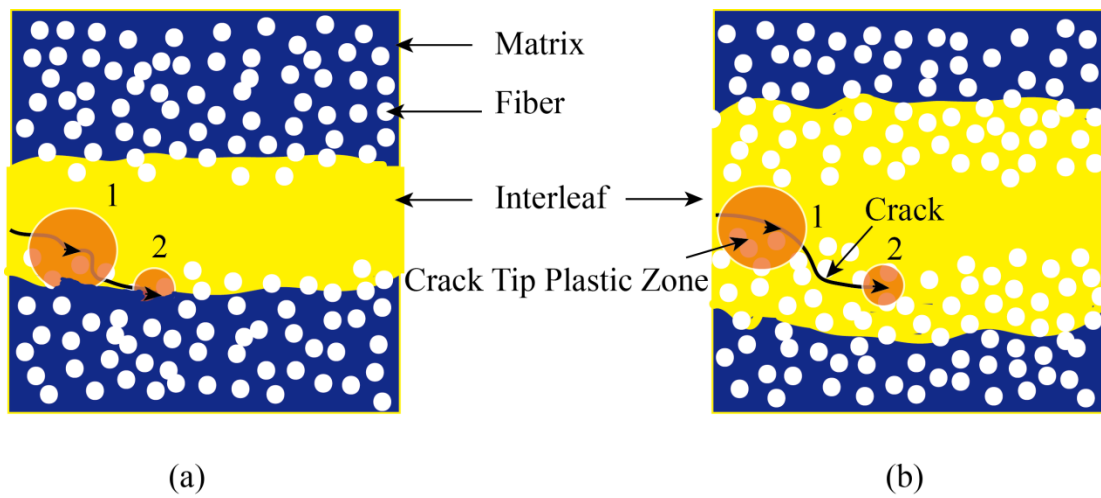


Fig. 3 (a) Schematic of the crack path under low penetration condition: crack initiates near the boundary of the pure interleaf region and the large plastic zone ahead of the crack tip reaches the interface between interleaf/fiber and epoxy/fiber, indicating that the crack migrates to this weak interface from Point 1 to Point 2 with the decreasing plastic zone size due to the rigid fiber. (b) Schematic of the crack path under high penetration condition: After crack initiates, the plastic zone only reaches the mixed region of interleaf and fiber (Point 1). The decreasing plastic zone size arrests the crack propagating in the middle of the mixed region (Point 2), where the delamination resistance is much larger than the interface between interleaf/fiber and epoxy/fiber.

2.2.3 Viscosity Effect and Interleaf Flow Analysis

It is believed that melt bonding leads to a deeper interleaf penetration into the fiber bundles, which can keep the crack inside of the mixed zone. The heating temperature is increased above the glass transition temperature of the thermoplastic interleaf material to soften the interleaf,

decreasing the viscosity and thus facilitating its flow into the fiber bundles. Due to the fact that the heating temperatures are much higher than the glass transition temperature of the thermoplastic, the temperature dependent viscosity η of the thermoplastic material can be modelled by a modified Arrhenius equation with glass transition temperature T_g as shown below [22]:

$$\eta(T) = A \exp\left(\frac{B}{T-T_g}\right) \quad (2)$$

When heated above the glass transition temperature, the viscosity will rapidly decrease. In this case, the temperature dependent viscosity of PSU is shown in the Fig.4 [23].

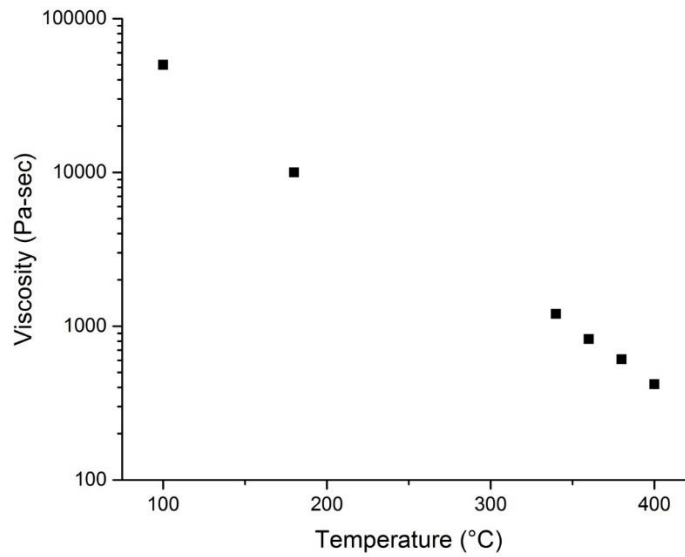


Fig.4 Polysulfone (PSU) viscosity versus temperature [23].

With the above knowledge, a model to predict the penetration depth is developed. The fiber fabric is considered as a porous flat plate with rectangular channels evenly distributed along the surface. An interleaf is pressed with an externally applied pressure and the only movement is in the penetration direction (z-direction). Further assuming the interleaf undergoes incompressible

creeping flow and from Poiseuille's law, the average velocity through the section of the interleaf, which has not penetrated into the porous structure in z-direction yet, is:

$$-\frac{dz_i}{dt} = \frac{L^2}{12 \times \eta} \times \frac{P - P_1}{z_i} \quad (3)$$

where z_i is the thickness of the interleaf not penetrating into the fabric yet, L is the length of the interleaf, η is the flow viscosity, P is the pressure on the thin interleaf in z-direction and P_1 is the pressure on the interface between the interleaf and porous structure. The average velocity of the penetrated interleaf along the channels in the porous structure in z-direction is:

$$\frac{dz_p}{dt} = \frac{d^2 \times P_1}{12 \times \eta \times z_p} \quad (4)$$

where z_p is the penetration depth and d is width of the above mentioned rectangular channels.

From mass conservation, the reduction of interleaf equals the amount of interleaf that penetrates into the porous structure:

$$-\frac{dz_i}{dt} \times L = \frac{dz_p}{dt} \times (1 - f) \times L \quad (5)$$

where f is the fiber volume fraction.

By rearranging the above equations and integrating, the final penetration depth is

$$\frac{1}{2} \left\{ z_o^2 - [z_o + (f - 1) \times z_p]^2 \right\} = \frac{t \times L^2 \times P_a}{12 \times \eta} \left\{ 1 - (1 - f) \times \frac{z_p}{z_o} \right\} - \frac{L^2 \times z_p^2}{2 \times d^2} \quad (6)$$

where z_o is the original thickness of the interleaf, t is dwell time, P_a is the applied pressure from clamps.

2.3 Experiment Procedures

The main objective of the experiments was to investigate the dependence of the hot melt-bonding performance, in particular, the interleaf penetration depth, on the processing temperature.

The melt-bonding temperature was varied between 280°C and 380°C. The effect of the interleaf thickness was also considered, with the interleaf thickness varied from 0.005” to 0.02”. This section describes the specimen preparation procedure as well as the employed test and characterization methods.

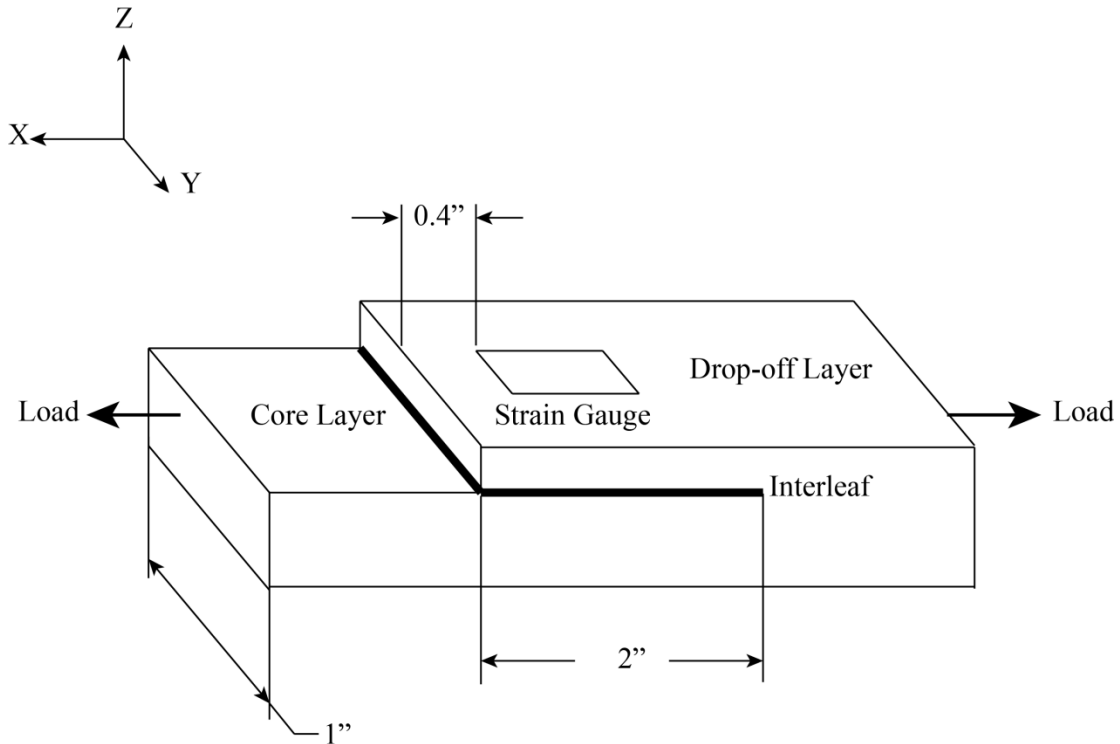


Fig. 5 3D schematic diagram describing the mechanical test setup. The strain gauge is placed on the top surface of the external drop off layer and 0.4 inch away from the edge of the drop-off layer. A 2"×1" interleaf is inserted underneath the external drop off layer and hot melt-bonded before VARTM. Far field load is in-plane tensile load. Note the coordinate system.

2.3.1 Materials and Specimens

The test specimens were fabricated using Saertex 970g/m² glass fiber fabric. The specimens consisted of three core plies of dimensions 11" by 1", as well as one drop-off ply of dimensions 5.5" by 1". The drop-off ply was placed on the top of the three core plies, such that the edge of the

drop-off ply was located at the center of the specimen. A 2" by 1" polysulfone (PSU) Udel/Thermalux interleaf of a thickness ranging from 0.005" to 0.02" was inserted between the drop-off ply and the adjacent core ply, such that the edge of the interleaf matched up with the edge of the drop-off ply. The assembly was then clamped between aluminum plates over a length of 2" from each side of the drop-off, whereby a uniform pressure of 0.493MPa was applied. The clamped specimens were then melt-bonded in a Carbolite CTF tube furnace at temperatures ranging from 280°C to 380°C. The melt-bonded specimens were subsequently processed using the controlled atmospheric pressure resin infusion (CAPRI) method that was patented by the Boeing Corporation [24]. The CAPRI process was chosen over the vacuum-assisted resin transfer molding (VARTM) process since it allowed producing specimens with a higher fiber volume fraction and a lower thickness gradient [25]. The specimens were sealed in a Fibre Glast Stretchlon 800 Bagging Film along with Fibre Glast 582-B Nylon Release Peel Ply (separation media) and Fibre Glast 579-C Breather/Bleeder cloth (distribution media). Once a vacuum was established, the specimens were debulked 75 times by releasing and re-applying the vacuum. Afterwards, the epoxy resin was prepared by mixing Momentive Epikote Resin MGS RIMR 135 with Momentive Epikote Curing Agent MGS RIMR 137 at a ratio of 3.39:1. Prior to the infusion, the resin was degasified in a vacuum chamber to remove the excess air that was introduced during mixing. During the infusion, a partial vacuum was maintained at the resin inlet to reduce the pressure gradient between the resin inlet and the vent. Once the entire vacuum bag was infused by the resin, the composite panel was cured at 110°C for 5 hours.

2.3.2 Testing Procedure

The complex interplay of the forces acting inside the turbine blade causes the drop-off plies to be subjected to both normal stresses and shearing stresses and thus prone to the mixed mode fracture failure. To simulate the real-life situations, this study employed tensile strength tests as per ASTM-D3039 on an Instron 5569a Universal Testing Machine. The 11” long and 1” wide specimens were loaded along the length direction of the specimen as shown in Fig.5. An Omega 0.6mm grid and 120 Ω strain gauge was mounted onto the drop-off ply, such that the edge of the strain gauge was at a distance of 0.4” from the drop-off. Additionally, the displacements of the core plies were measured using an Instron 2630-103 clip-on strain gauge extensometer. The specimens were loaded until the drop-off layer was entirely delaminated, i.e. until the strain at the strain gauge dropped to zero.

For the post-test analysis, the specimens were cross-sectioned along and perpendicular to the length direction. The cross sections were etched by Xylene before imaging. An Olympus BX60 differential interference contrast (DIC) microscope was used to visualize the fracture paths and a Hitachi S-4700 scanning electron microscope (SEM) was used to analyze the fracture surface morphology.

2.4 Results and Discussion

2.4.1 Penetration Analysis

Specimens were treated under different temperature conditions with the same pressure. After the hot-melt bonding process, the resin transfer molding was carried out to produce the composites. Each specimen was cut by a diamond saw and the cross section was polished for the optical

microscopy.

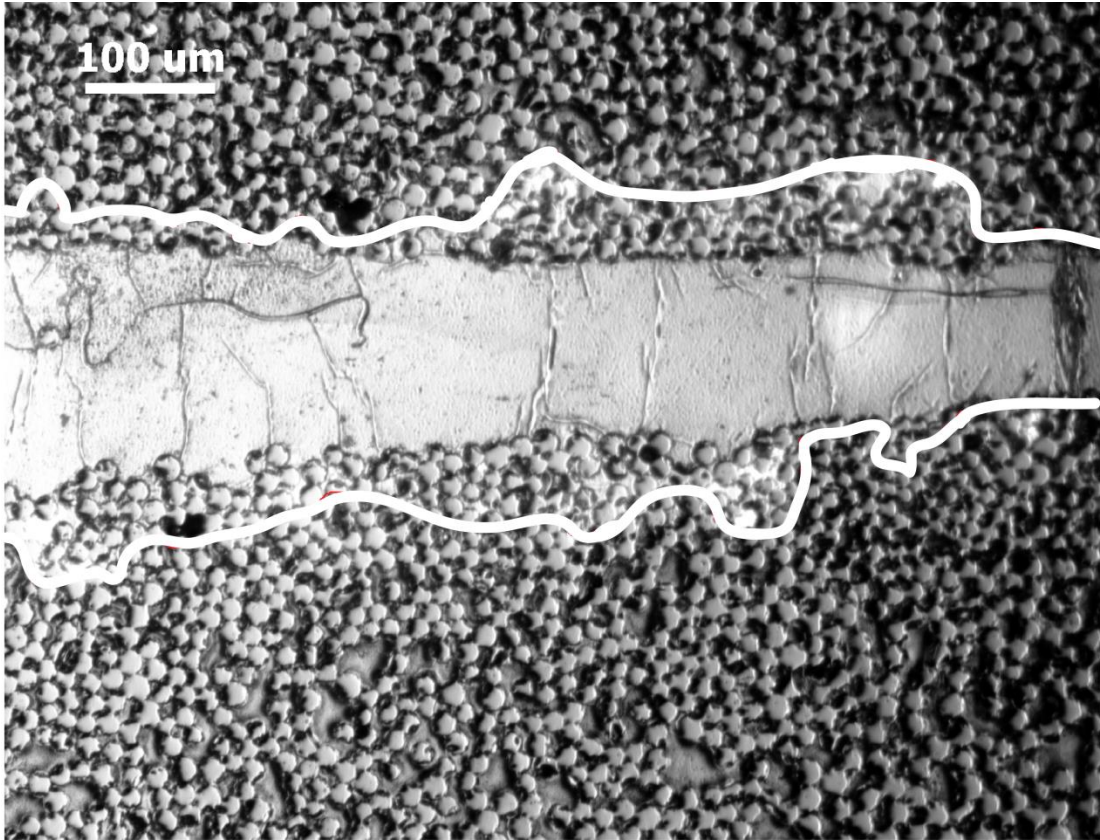


Fig. 6 Y-Z cross section (parallel to the drop-off edge) of the specimen with melt-bonded 254 μm thick PSU at 280°C. Xylene etched surface shows low penetration of the PSU interleaf into the fiber bundles. Penetration boundary is indicated by the white lines. The average penetration depth is 32.5 μm , and the average remaining interleaf thickness is 168 μm . Due to the low melt bonding temperature and high viscosity, a limited amount of the interleaf penetrates into the fiber bundles.

Fig.6 showed a cross section perpendicular to the drop-off edge, that is, the Y-Z plane, and the penetration depth under a lower temperature (280°C). The grey circles were glass fibers; and the darker area surrounding the fibers was epoxy. The brighter area between the upper and lower plies was the thermoplastic interleaf, which penetrated into the fiber bundles. The penetration depth was determined by the color difference observed under optical microscopy. The extent of the penetration is highlighted by curved white lines. As seen, the penetration depth varied from 10

to $60\mu\text{m}$, and the average penetration under this temperature is $32.5\mu\text{m}$.

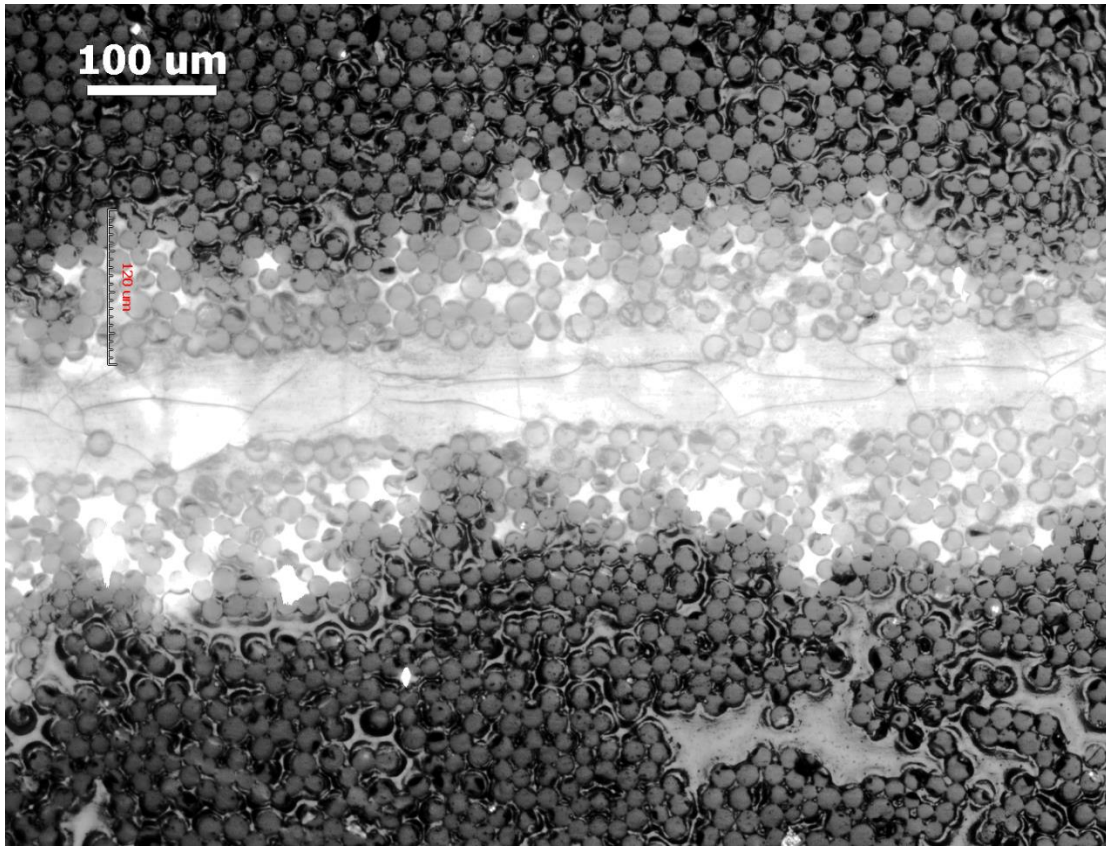


Fig. 7 Y-Z cross section of the specimen with melt-bonded $254\mu\text{m}$ thick PSU at 320°C . Xylene etched surface shows high penetration of the PSU interlayer. The average penetration depth is $103.6\mu\text{m}$ and the average interleaf thickness after melt bonding is $83\mu\text{m}$. Larger penetration depths form a thick mixed region of interlayer and fiber bundles.

In comparison, Fig.7 showed the penetration under a higher temperature (320°C). The thickness of the interleaf was reduced more and the penetration depth increased significantly. For this case, the penetration of the interleaf ranges from 60 to $150\mu\text{m}$ and the average depth is $103.6\mu\text{m}$.

The depth of penetration under temperatures from 280°C to 380°C was observed by optical microscopy and calculated by averaging the data from 12 randomly picked locations. The

standard error was calculated to show the variation. From Fig.8, the penetration depth generally increased with the melt-bonding temperature. The penetration depth rose sharply from 280°C to 340°C and leveled off from 340°C to 380°C. This is primarily because the viscosity of PSU thermoplastic sharply dropped from 2,969 Pa·s at 280°C to about 1,207 Pa·s at 340°C. The reduction becomes much milder above 340°C (Fig. 9).

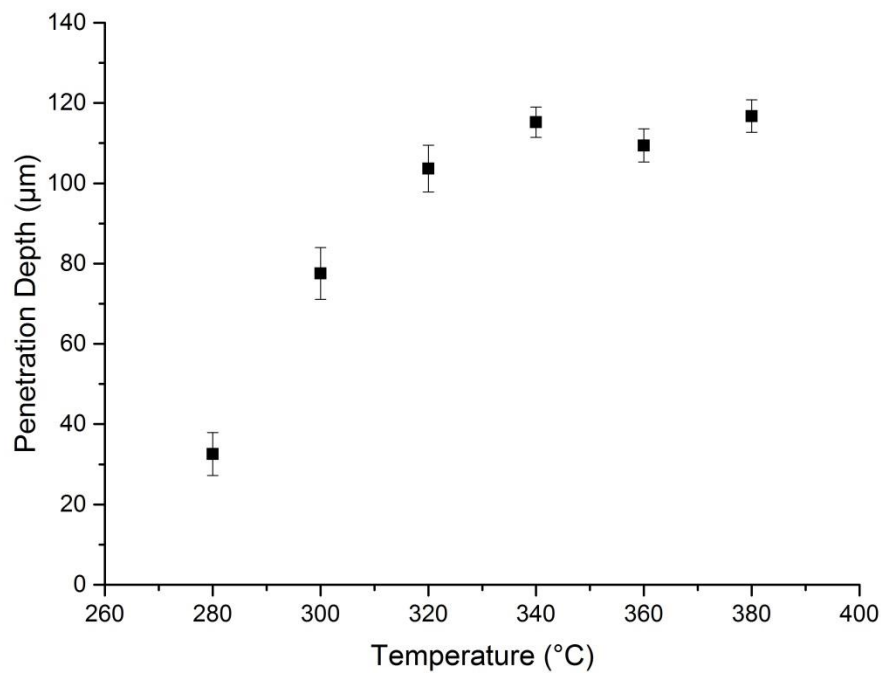


Fig. 8 Experiment results for 254μm thick PSU interleaf penetration depths from 280°C to 380°C. The error bars represent standard errors. The trend of the penetration correlates well with the decreasing viscosity temperature.

By using the method in the background, the predicted penetration depths were superposed in Fig.9 and to compare with the experimental results. Similar to the experimental results, the predicted curve increased with temperature. It, however, overestimated the depth at lower and higher temperatures. The over estimation of the prediction depth at the lower temperature was

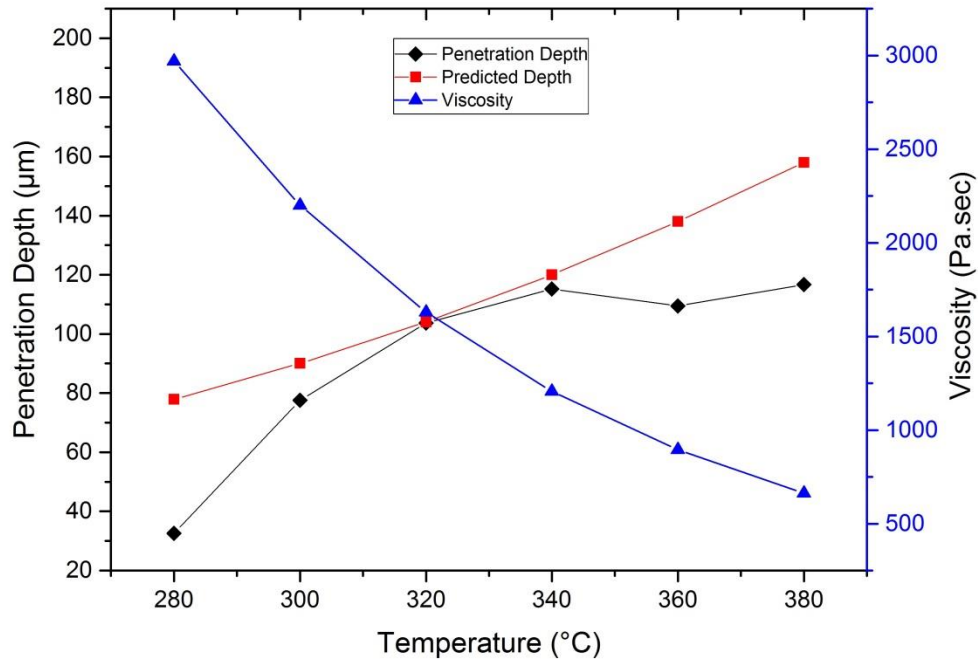


Fig. 9 Predicted and experimental penetration depths increase with the melt bonding temperature. The trend is primarily due to the decreasing viscosity of the PSU interleaf material with temperature.

likely because the model assumed the penetration channels in the porous structure have the constant rectangular cross-section. In reality, the channel resembles an hourglass in shape. When the temperature was low, the viscosity of the thermoplastic interleaf was high and the narrow gap generated greater resistance to the penetration, resulting higher predicted values. A possible improvement is to model the hourglass shape explicitly. When the temperature was high, the thermoplastic interleaf material can penetrate more easily due to the reduced viscosity. However, the thickness reduction of the interleaf was more significant because it was not only related to the penetration depth but also to the flow movement in the X-Y plane now and thus the assumption that the effect of the applied pressure only depended on the thickness reduction by interleaf

penetration likely caused the over estimation at higher temperatures. A possible improvement is to use time and temperature dependent pressure..

2.4.2 Stress-strain and Toughness Behavior

Uniaxial tensile tests were carried out. The specimens were loaded until the drop-off region was totally delaminated and thus the value of the strain gauge returned to zero. Fig.10 shows the stress and strain curves of the drop-off layer under three conditions and there were measured by a strain gauge shown in Fig. 5. The curve marked “reference” referred to the case no interleaf was introduced. It had the lowest slope among all the curves because the pure epoxy specimen was of

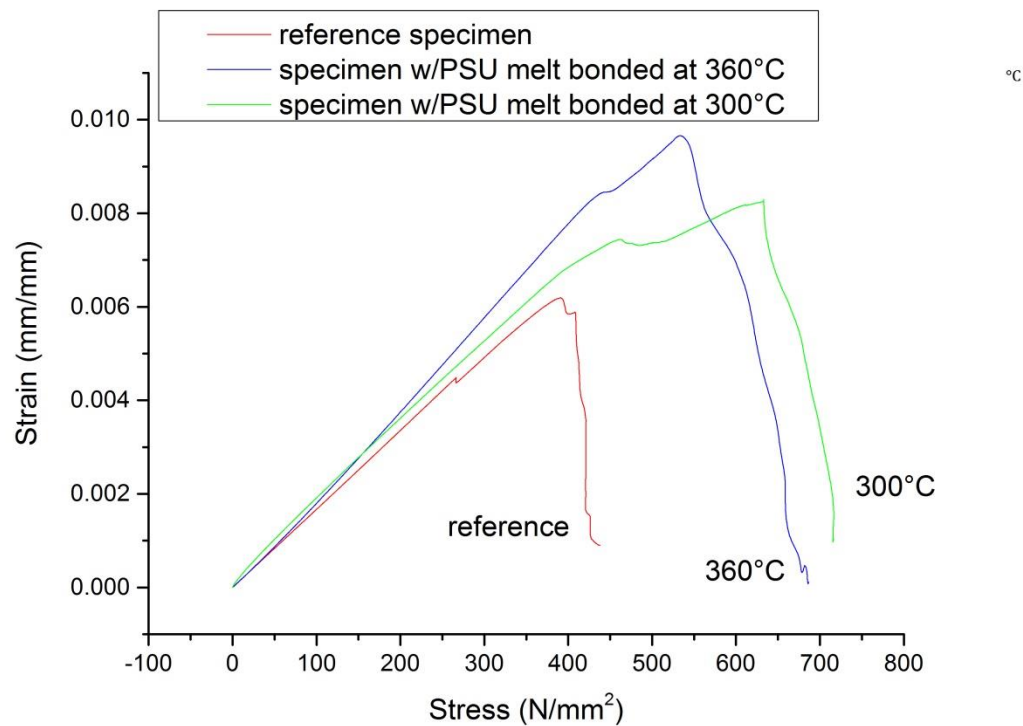


Fig. 10 Representative strain-stress curves obtained from the strain gauge mounted on the drop-off layer in uniaxial tensile tests: reference specimen (without interleaf), interleaved specimens under low/high melt bonding temperatures. The reference specimen shows the highest stiffness while specimens with interleaf are much tougher.

higher stiffness. As a result, the reference specimen began to fail at a low strain (about 0.6%). The curves whose slopes were higher than the reference specimen were the specimens with melt-bonded interleaf at 300°C and 360°C, respectively. As the figure showed, because of the inserted interleaf, the interlaminar layer connecting the drop off layer to the core plies became less stiff. For the curve marked 300°C, it did not fail until the strain reached 0.8% due to its modestly increased penetration depth (Fig. 8). For the curve marked 360°C, the strain went up about 1% before it began to fail due to markedly increased penetration depth. The reference specimen also showed a sharper drop when it started to fail than the two specimens with interleaf.

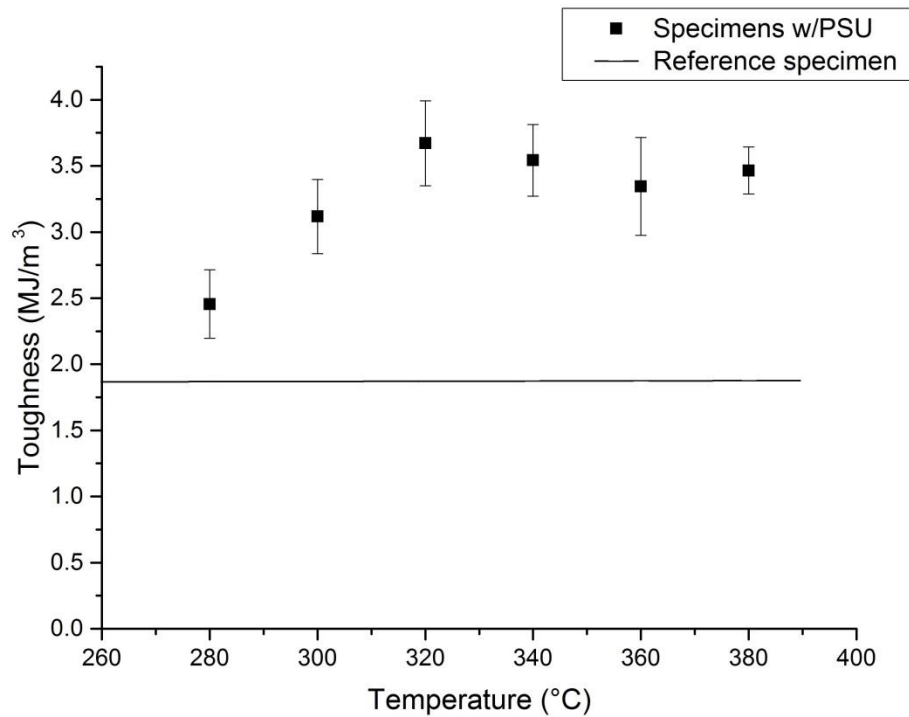


Fig. 11 Toughness of 254μm thick PSU interleaved specimens from 280°C to 380°C. The error bars represent standard errors. The horizontal line represents the average toughness of the specimen without interlayer. The trend correlates well with the trend of the penetration depth (Fig. 8), indicating that the penetration depth directly influences the toughness.

The toughness was calculated by integrating the area under the stress strain curve. It measured the energy required for a crack to initiate and propagate. For the brittle materials such non-modified fiber reinforced polymers, the failure may vary from specimen to specimen, which was mainly related to the physical flaws present in the surface or body of the specimen, leading to different maximum stress that samples could stand. The Weibull distribution is often used to describe the strength of fibers and FRP composites [27]:

$$P(\sigma) = 1 - e^{-\left(\frac{\sigma}{\sigma_0}\right)^m} \quad (7)$$

Where σ is the tensile strength, σ_0 is the averaged tensile strength of specimens, and m is the Weibull modulus. The cumulative probability density function P is estimated as [27]:

$$P = \frac{i}{N+1} \quad (8)$$

Where i is the current test number, N is the total number of specimens.

The parameter m in Eq. 7 describes the tail shape of the distribution. If m is large, the tail will be small, which means the specimen performances are more constant. In this study, the calculated m value for three reference specimens is 31.5 based on the tensile strength of 384, 490, 438 MPa. The m value is close to 25.4 obtained from literature [27], indicating the more constant failure performance of the specimens. Thus, the same method was applied to non-modified reference specimen to calculate the toughness in this study.

In Fig. 11, the toughness of reference specimens is represented by a horizontal line. For each melt bonding temperature, six specimens were tested to validate the data repeatability. Each average toughness and their standard error were represented by a symbol and an error bar. As shown in the figure, the toughness of the specimens had a sharp increase and a peak at the melt

bonding temperature of 320°C, before it leveled off. The trend resembled that of the penetration depth seen in Fig. 8 and provided strong evidence that deep penetration of the interleaf into the fiber bundles led to the increased toughness and thus the improved delamination resistance. At its peak, the toughness was almost twice as high as the reference specimen which has no interleaf.

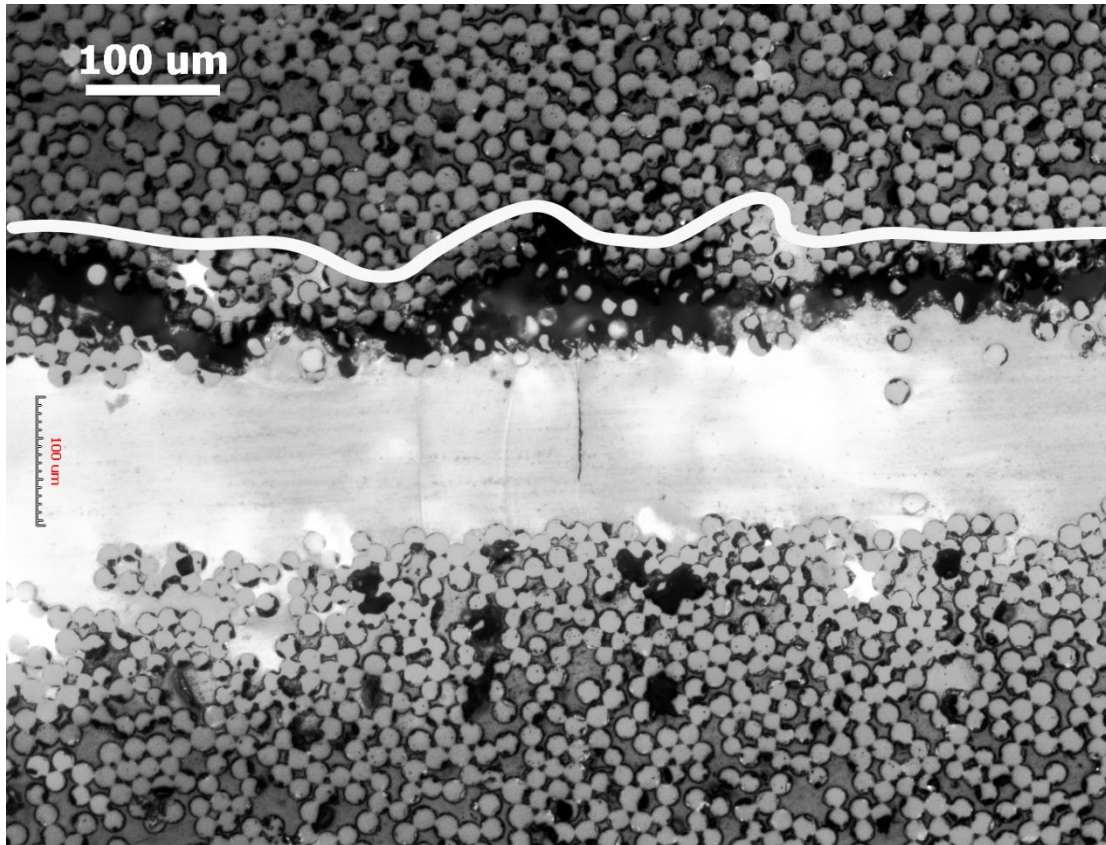


Fig. 12 Y-Z cross section (parallel to the drop-off edge) of the fractured specimen with melt-bonded 254μm thick PSU at 280°C. The white line indicates the penetration boundary. There are two kinds of the crack locations due to the thin penetration depth. Region A shows the crack is near the interface between the pure interleaf and the matrix. Region B shows the crack is near the interface between the interleaf/fiber and epoxy/fiber. The crack reaches the weak interface between interleaf and epoxy under low penetration condition.

2.4.3 Crack Path Microscopy

After mechanical tensile tests, all the specimens were cross sectioned and polished to observe the crack morphology. As the crack went into the drop-off region, the crack propagated near the

lower interface between interleaf and matrix. Shown in Fig.12 was the Y-Z view of the specimen with 254 μ m PSU melt-bonded under 280°C. The dark gully was the crack created after the tensile test. The location of the crack in this figure was mainly located on the interface between the interleaf and the matrix (Region A); it was occasionally located inside the fiber bundles where the interleaf penetration is slightly deeper (Region B). The X-Z view of the crack propagation was shown in Fig.13. As seen from the image, the crack path was mainly along the interface between resin and interleaf, due to the low melt-bonded temperature, the penetration depth was only around 30 μ m, as a result, the crack went slightly into the penetration zone (Region B) or the interface between interleaf and matrix (Region A). In the figure, a few broken fibers were observed, which was another factor leading to the high crack propagation resistance. However, under the low melt bonding temperature, this kind of broken fibers was not commonly seen.

Figs.14 and 15 showed the cross section views of the specimen melt-bonded with 254 μ m PSU thermoplastic interleaf under a higher melt bonding temperature (320°C). As shown in the Y-Z view in Fig.14, the crack was located in the region, where the interleaf penetrated into the fiber bundles. Compared with Fig.12, it was easily observed that the larger penetration depth here, caused by the high melt-bonding temperature, confined the crack entirely within this region, whose toughness has increased due to the penetrated thermoplastic interleaf. From Fig.15, the X-Z plane image also indicated that the crack propagated not through the interface between the interleaf and fiber bundles. As the penetration depth under 320°C was 106 μ m, the crack resided around the central part of the penetration region. Contrary to Fig. 13, Fig.15 showed more broken fiber beams and more bridged fibers pulled out from the matrix, which led to a higher delamination resistance.

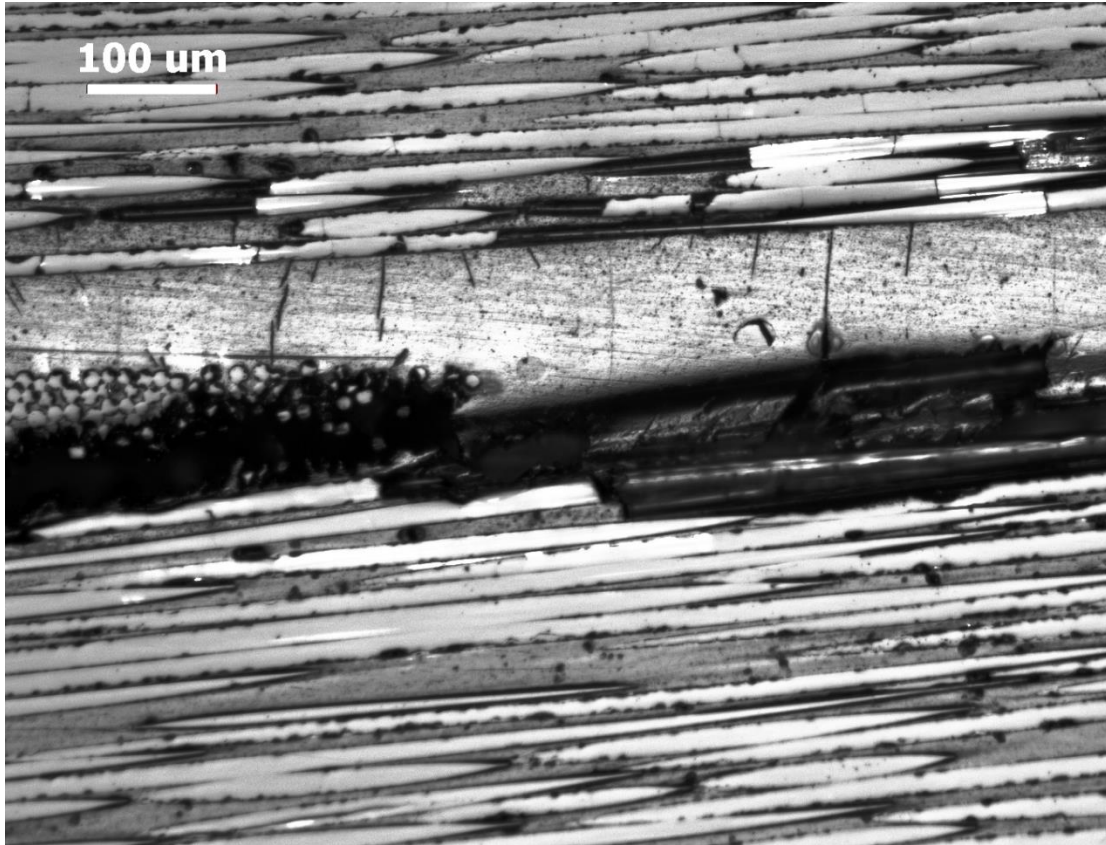


Fig. 13 X-Z cross section (perpendicular to the drop-off edge) of the fractured specimen with melt-bonded 254 μm thick PSU at 280°C. It shows the crack locates at the interface between interleaf and epoxy/fiber or at the interface between interleaf/fiber and epoxy/fiber. Due to the low penetration depth, the crack always propagates along the weak interface between interleaf and epoxy. Less broken fiber, less bridged fiber and bridged PSU are found compared to the specimen under the high melt bonding temperature.

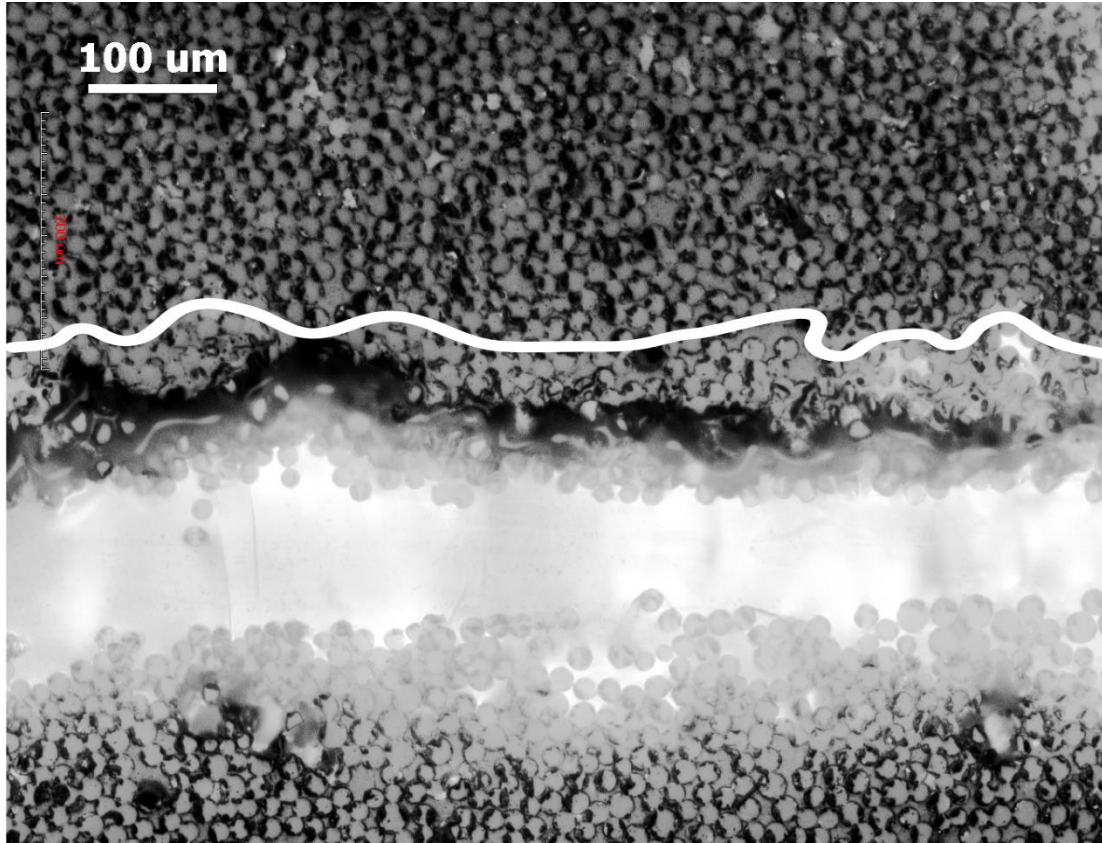


Fig. 14 Y-Z cross section of the fractured specimen with melt-bonded 254 μm thick PSU at 320°C. The white line indicates the penetration boundary. At this melt bonding temperature, the average penetration depth is 106 μm . The crack propagates through the middle of the penetration region without reaching the weak interface between interleaf and epoxy.

These results confirmed our hypothesis indicated in Fig. 3. When the interleaf penetration was low, the plastic zone ahead the crack tip was more likely to reach the interface of the interleaf and the epoxy. As the stiffness of the epoxy was higher than that of the TP interleaf, one did not benefit from the full plastic zone, which absorbed more energy, as part of the zone cannot develop within the epoxy zone (Fig. 3a). When the penetration depth was high, as the strength of the interface between the PSU interleaf and penetration region was still lower than the stress ahead of the crack tip, the crack also went to the penetration region, however, it is more likely to remain within the

region as it is larger now (Fig. 3b). As a result, the penetration region localized and arrested the crack and the high toughness of the penetration region required more energy for the crack to propagate.

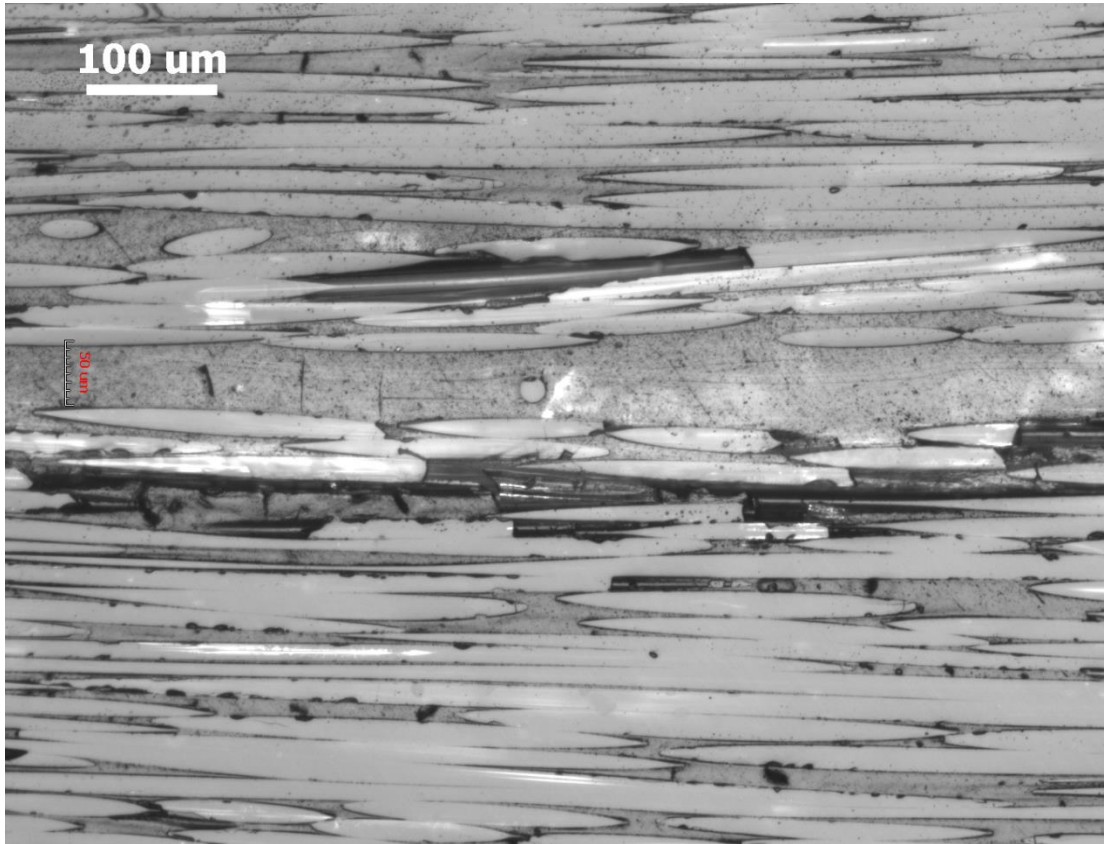


Fig. 15 X-Z cross section of the fractured specimen with melt-bonded 254 μm thick PSU at 320°C. The thickness of the interleaf after the melt bonding reduced to about 63 μm . The crack propagates through the penetration region of interleaf and fibers. The zone is about 106 μm wide as per Fig. 14 under this melt bonding temperature. More broken fibers and bridged fibers result in high toughness.

2.4.4 Fracture Surface Morphology

Fracture surfaces of the specimens after mechanical tensile tests were observed via scanning electron microscopy. Fig.16a showed the typical fracture surface of the specimen with 254 μm thick interleaf melt-bonded at 280°C. From the figure, it showed two kinds of fracture surface. The

first kind was clean where fewer broken fiber beams were found on the surface: individual fiber beam was seen with very few particles on its surface; clean and clear river lines between the fibers indicated there was no plastic shear deformation; fewer pulled-out fibers were found on this type of surface. It was obvious that this fracture surface was the interface between interleaf and fiber or between epoxy and fiber, which was the weak region in the structure and led to the low fracture toughness. The other kind showed rougher surface: the brighter lumps showed large shear deformation, which improved the toughness, however, there was not much torn interleaf remaining on the surface. The crack of both kinds mainly went through the interface between interleaf and fiber or epoxy and fiber, which led to adhesive failure. For the PSU interleaved specimen melt-bonded at 320°C (Fig. 16b), more broken fibers and pulled-out fibers were observed throughout the fracture surface. Most debonded fibers were not clean with small particles or lumps of the “torn resin” attached on the fiber, which indicated large plastic deformation. Because of the high penetration depth, the mixed region with fiber beams, thermoplastic and thermoset resin was deep into the fiber matrix, which led to the phenomenon that even the fibers below the contact interface between thermoplastic and fiber bundles were also pulled out from the matrix. More participated pulled out fibers and broken fibers directly increased the toughness and thus delamination resistance. The present results indicated that high toughness interleaf and high penetration into the fiber bundles were both the key factors to improve the toughness of the composites, avoid the adhesion failure and enhance the bonding quality.

2.4.5 Influence of Interlayer Thickness

The thickness of interlayer may influence the toughness of the specimens. The specimens with

interlayer thickness from 25 μm to 508 μm were tested under two different temperatures (280°C and 320°C) to investigate the crack resistance behavior. As shown in Fig.17, under the lower melt bonding temperature, the toughness of the specimen had a significant increasing when the interlayer thickness increased from 25 μm to 127 μm . However, it decreased after 127 μm . The low toughness with the 25 μm thick interleaf was likely due to the inadequately participated interleaf in plastic deformation because the interleaf was thin. When the thickness increased to 127 μm , the toughness increased. But when the thickness increased further, the influence of stress concentration could be magnified [26] and thus the toughness reduced. Under the higher melt bonding temperature (320°C), the trend was similar except with thicker interleafs, the toughness reduction was not as pronounced. This was likely due to the fact that the interlayer went deeper into the fiber bundles to offset the stress concentration effect mentioned above.

2.5 Conclusion

The effect of the interleaf deep penetration on the mixed-mode delamination resistance was investigated for the PSU thermoplastic interleaved GFRP. The penetration depth increased with the hot-melting bonding temperature to a certain value and then leveled off. This is mainly due to the PSU viscosity behavior, which decreases quickly to around that value and then decreases slowly. As compared with the GFRP without interleaf, the fracture toughness increased by a factor of two with the penetration depth of the 254 μm PSU thermoplastic interleaf into the fiber bundles reached 100 μm under melt-bonding temperature of 320°C, and increased 2.5 times with 127 μm PSU thermoplastic interleaf under melt-bonding temperature of 320°C. This is mainly

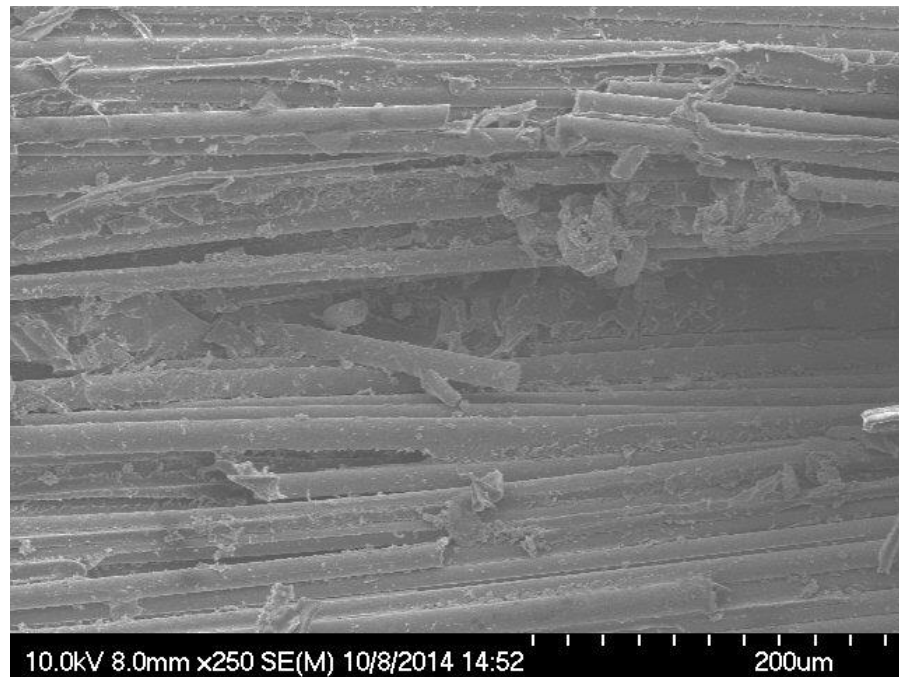
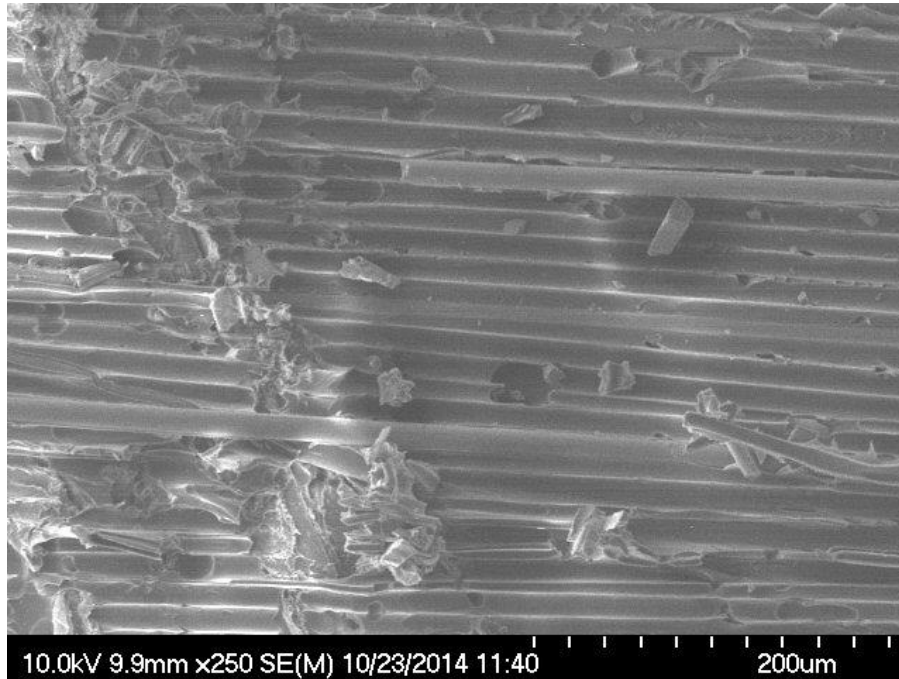


Fig. 16 (a) SEM image of the delamination fracture surface of the specimen with melt-bonded 254 μ m thick PSU at 280°C. The large clean region indicates brittle adhesion failure, which is caused by the crack propagating through the interface between interleaf and epoxy. The rough region indicates the crack goes through the penetration region, where part of the interleaf underwent plastic shear deformation. Fewer broken fibers and pulled out fibers are found for this condition. (b) SEM image for the delamination fracture surface of the specimen with melt-bonded 254 μ m thick PSU at 320°C. The much rougher surface indicates more ductile fracture

has taken place. Plastic shear deformation of the interleaf can be seen around fiber beams. More broken fibers and pulled out fibers are seen for this condition due to the increased delamination resistance.

because the deep penetration zone of improved ductility confines the plastic zone ahead of the crack tip within its boundaries and thus requires more fracture energy for the crack to propagate. Pulled-out and broken fibers were also responsible for the increased toughness. In the case where the penetration is shallow, the plastic zone is likely to reach the interface of the interleaf of the epoxy matrix and thus the benefit of increase toughness due to interleaving cannot be fully realized.

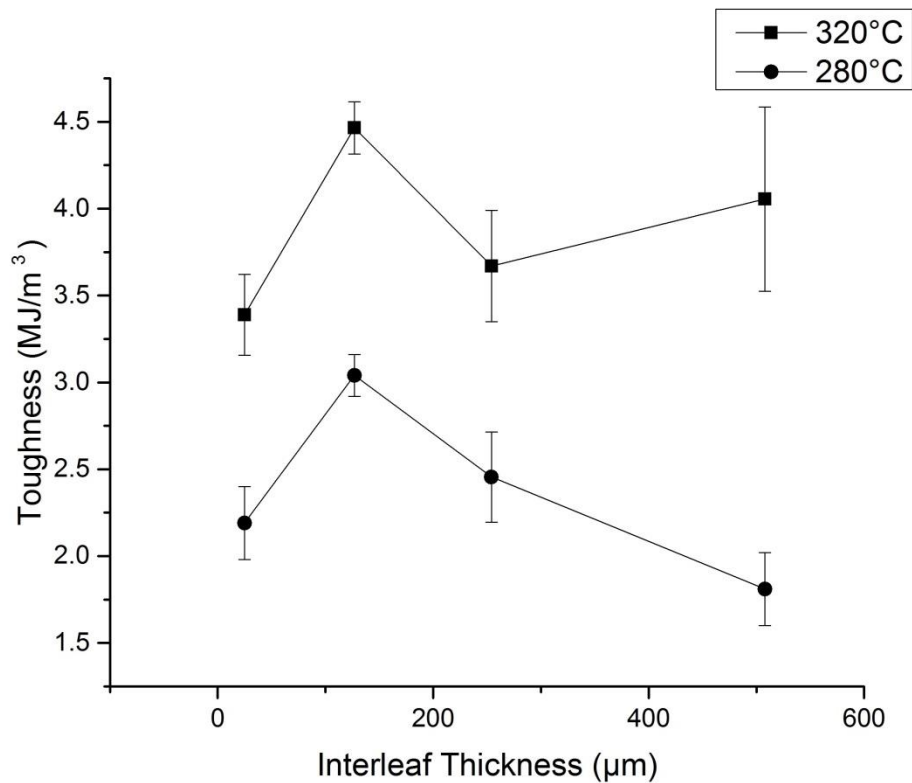


Fig. 17 Toughness of the specimens vs. interleaf thickness under different melt bonding temperatures. The error bars represent standard errors. The sharp increasing toughness from 25μm to 127μm is due to more participated thermoplastic interleaf in plastic deformation. After the peak point, the toughness decreases with interleaf thickness. It is because the influence of the mismatch of the drop-off structure and materials is magnified and induces adhesive failure,

which reduces the toughness. For the specimens melt bonded at the higher temperature, which has a higher penetration depth and thus the better bonding quality, some toughness is preserved even the interleaf gets overly thick.

2.6 Acknowledgement

This research was supported by National Science Foundation under award CMMI-1363328. Authors would also like to thank Paul Ubrich from Momentive Specialty Chemicals Inc. for providing us experiment materials.

Chapter 3: Interlaminar Toughening of GFRP, Part 1: Bonding Improvement through Diffusion and Precipitation

3.1 Introduction

Glass Fiber Reinforced Polymer (GFRP) composites have been widely used as laminated structures in automotive, marine, and aerospace industries due to unique properties such as reduced weight, high strength, and increased energy efficiency compared to traditional metal materials. However, their poor through thickness strength leads to delamination, which can cause catastrophic failure. Thus, preventing laminar from delamination always plays an important role in design and test of the GFRP.

In the past decades, many researchers have been working on finding methods for toughening laminate composites. Some of them used different thermoplastic materials as modifiers. Shetty et al. used 0 to 10 wt% of polycarbonate (PC) to toughen the epoxy resin [1]. Zhang et al. studied the effect of polyetherketone cardo (PEK-C) thickness on the fracture toughness [2]. Xu et al. found moderate increase in the fracture toughness by using polyphthalazinone ether sulfone ketone (PPESK) [3]. Martines et al. blended polysulfone (PSU) with the epoxy under at different weight fractions and curing temperatures [4]. Blanco et al. studied the amine-ended polyethersulfone (PES) influence on the thermomechanical properties of the epoxy [5] and Heitzmann et al. studied the influence of different cure cycles of polyetherimide (PEI) [6]. Other researchers used different methods to achieve composite toughening. Huade et al. used laser to bond layer of fabric by fusing a dense glass bead [7-8]. Groleau et al. used the blends with nylon particles [9]. Hillermeier et al.

studied the effect of modified powder/spray tackifier on the fracture toughness [10]. Li et al. toughened the composite using electrospun nanofibers [11] and Kuwata et al. investigated the toughness of composites by using interleaved TP veil [12]. The above results indicate that both high toughness and adhesion strength are required for the interleaved material [13]. However, most thermoplastics are not likely to be compatible with thermosetting epoxies due to the low reactivity, small surface energies, and weak polarities. Thus, adhesion failure between the interleaved material and matrix still remains.

A strong thermoplastic-thermoset interface is vital to guarantee bonding quality and improve toughness behavior, especially at drop off regions which induce stress concentration [14]. Good adhesion can be realized if two polymers are compatible and their molecules diffuse sufficient distance to generate a gradient interphase, leading to entanglements between the long chain thermoplastics (TP) and cross-linked thermosets (TS). The formation of the entangled long chain TP in crosslinked TS is known as semi-interpenetration network (semi-IPN).

A dual bonding process was introduced in the previous work [14] and present study focused on the effect of diffusion and precipitation. The present study introduces PSU interleaved glass fiber reinforced composites cured with PS modified epoxy to overcome the limitation of polymer diffusion. Compatibility of polymers was determined experimentally by using viscometry. Diffusion and precipitation regions between the thermosets system and inserted PSU film was examined by optical microscopy and scanning electron microscopy. Single external drop-off specimen tensile tests were performed to simulate real loading conditions. Crack initiation and

propagation was observed by microscopy. Fracture surface morphology and toughening mechanism were studied.

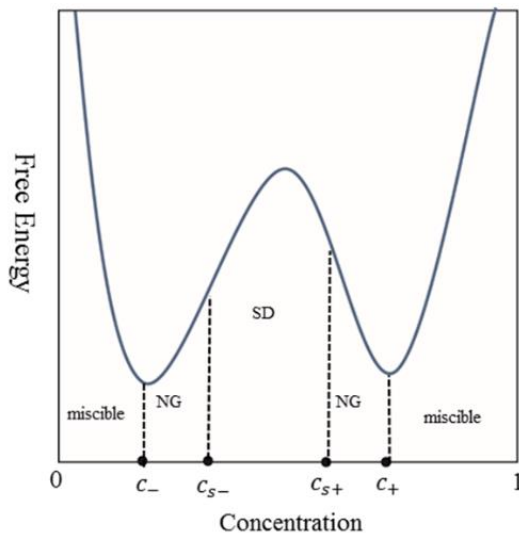


Fig.1 Phase diagram of nucleation growth (NG) and spinodal decomposition (SD). The system can lower its free energy by separating into two phases with an interphase between c_- and c_+ . Within the range of c_-/c_{s-} and c_+/c_{s+} , phase separation is due to nucleation and growth. Within the range of c_{s-} and c_{s+} , phase separation is due to spinodal decomposition.

3.2 Background

3.2.1 Polymer Compatibility

Compatibility between polymers is determined by the solubility of the solute and solvent. The key factor leading to diffusion and precipitation is the ability of solvent molecules to overcome the intermolecular forces of the solute and occupy spaces within the solute molecules. Only polymers that have similar intermolecular forces are likely to be miscible. If the intermolecular forces are

sufficiently different, the strongly attracted molecules will gather together and exclude the weakly attracted molecules. The Hildebrand solubility parameter is the reflection of the degree of intermolecular forces holding the polymer molecules together and is used to predict the compatibility of polymers. The limitation of Hildebrand solubility parameter is that it is not suitable for some polar polymers especially with hydrogen bonds. This solubility parameter is an important reference for choosing a proper solvent or polymer because it is a prediction of compatibility. Usually, heat of vaporization can be measured directly to determine the solubility of a polymer with low molecular weight (MW). However, due to the huge molecular interaction of TPs, it is difficult to gasify a polymer with high MW. Thus, viscometry is introduced in this study to determine the solubility parameter of polymers. The intrinsic viscosity of the solution is related with the degree of solvent's solubility: the solubility of the polymer is the same as the solubility of the solvent when the intrinsic viscosity of the solution reaches maximum value [15],

$$[\eta] = [\eta]_{max} \cdot e^{V \cdot (\delta - \delta_p)^2} \quad (1)$$

when $[\eta] = [\eta]_{max}$, $\delta = \delta_p$. For this equation, η is the intrinsic viscosity, V is the molar volume of the solvent, δ is the solubility parameter of the solvent and δ_p is the solubility parameter of the polymer. Polymers sometimes cannot be dissolved in a pure solvent, so mixed solvent is used to find the proper solvent for specific polymer. The solubility parameter for the mixed solvent can be approximated by

$$\delta_{mixed} = \phi_1 \delta_1 + \phi_2 \delta_2 \quad (2)$$

where ϕ is the volume fraction of the component in the solution, 1 and 2 stand for two different solvents. In a binary solvents system, as long as the solubility of the test polymer is within the range of the two solvents, the volume fraction of the solvents can be adjusted to make the solubility of the solution close to the solubility of the test polymer. Thus the limitation of Eq. 2 is that the solvents should be compatible with each other and the solubility of the test polymer should be in the range between those of the two solvents. The intrinsic viscosity is determined by the experimentally measured viscosity of the solution

$$[\eta_s] = \frac{1}{C} \sqrt{2 \left(\frac{\eta_s - \eta_0}{\eta_0} - \ln \left(\frac{\eta_s}{\eta_0} \right) \right)} \quad (3)$$

where C is the concentration of the solute in the solution, η_0 is the viscosity of the solution without dissolved polymer, and η_s is the viscosity of the solution with dissolved polymer.

3.2.2 Diffusion Process in Thermoplastic-rich Region

From the macroscopic perspective, a diffusion process is the thermal motion of species. It explains the net flux of species from a region of higher concentration to one of lower concentration resulting in a gradual mixing of material. However, this process is different for the epoxy system due to the spontaneous curing during the diffusion. As the TPs begin to encounter the initial liquid phase epoxy, it becomes softened by the TS epoxy. The entangled long chain structures in the TP become swollen, which increases the free space within the TP region. Then the curing epoxy molecules fill the free space in the TP and keep swelling the long chain structure. In the diffusion process, the elevated temperature reduces the viscosity of both the TP

and TS. Under high curing temperature, the diffused TS in the TP rich region remain as an unstable single phase solution at the early stage of curing process. With the processing of the curing reaction, low MW TSs connect with each other through branching and crosslinking, leading to a significant increase of the viscosity and reduction of solubility [16]. This system can lower its free energy by separating into two phases to maintain stability as illustrated in Fig. 1, which shows the typical free energy trends with concentration of solute. In the diffusion region, the concentration difference of solute and solvent is small and the spinodal decomposition (SD) dominates the phase separation. During SD, large clusters form due to high concentration of the penetrating species [17-18]. When the large clusters form, the epoxy is not fully cured. The undergoing curing process generates secondary networks within and around the clusters. These networks are also an important factor that leads to improved toughness [19].

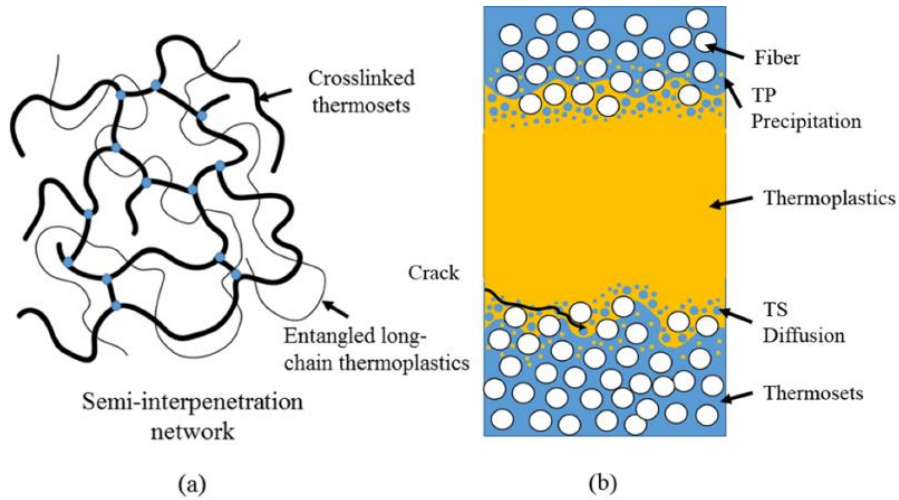


Fig.2 (a) Schematic of semi-interpenetration network. Semi-interpenetration network is formed by the entanglement between the long-chain thermoplastic molecules and crosslinked thermosets. (b) Schematic of crack propagation in

the diffusion and precipitation region. When the crack propagates, it needs to break the semi-interpenetration network structure.

3.2.3 Precipitation Process in the Epoxy-rich Region

As the epoxy begins to diffuse into the TP-rich region, the TP molecules simultaneously start to flow into the epoxy-rich region. At the initial stage of curing, the uncured small molecular weight epoxy prepolymer is compatible with the thermoplastic and has high mobility. The contact between the uncured epoxy and thermoplastic leads to swelling effect, which the amorphous entangled thermoplastics molecules start to undergo chain relaxation. The surface of the thermoplastics generates more free spaces and the mobility of the long chain thermoplastics increases. Thus, the uncured epoxy molecules fill into these free spaces in the TP-rich region and keep swelling the TP beneath the surface, and on the other hand, the long chain TP flow in the uncured epoxy region due to the increased mobility due to the swelling effect. Due to the elevated temperature and chain relaxation of TPs, the mobility of the TPs increases and the swollen long chains transfer to the liquid epoxy region. With the increasing time, the liquid phase epoxy start to cure, turning into gel and finally into cured solid phase epoxy. Since the cross-linked structures are gradually generated during the curing process, the diffusion and precipitation process is coupled with curing reaction which reduces the mobility of the species. At a certain degree of curing, the diffusion and precipitation process ceases. The long chain TP molecules entangle with the cured cross-linked TS structure along the interface between the TP and TS. In the precipitation region, the concentration difference of solute and solvent is significant due to the low mobility of

long chain TP. As can be seen from Fig. 1, the nucleation growth (NG) dominates the phase separation, in which part of solute molecules separate out and cling together to form clusters. From Bernard et al.'s work, morphologies in epoxy-amine/TP blends depend on the TP concentration [16]. The blends containing less than 10 wt% of TP exhibit precipitation with dispersed TP-rich particles in an epoxy-rich matrix. The blends above 20 wt% of TP exhibit diffusion with dispersed-epoxy-amine rich particles in a TP-rich matrix. The sharp interface is located between precipitation and diffusion regions where the spinodal decomposition is the dominant mechanism for the phase separation. The distance of this gradient interphase is believed as one of the major reasons for the improved toughness.

3.2.4 Factors Influence the Diffusion and Precipitation Process

The diffusion and precipitation process in the epoxy system is complicated because it includes both physical and chemical reactions. Both curing reaction and the diffusivity of epoxy and TP are highly dependent on the processing temperature, which is the most important factor. At low processing temperature, the high viscosity of the epoxy and TP has the minimum mobility even if the time before gelation is longer due to the reduction of curing reaction rate. Therefore the diffusion and precipitation process is limited because the species are not able to transport enough distance with low mobility within the time period that diffusion and precipitation can occur. At high processing temperature, the time before gelation is shortened but the mobility of the system is significantly enlarged. Compared to the case at low processing temperature, the species under high processing temperature are able to transport relatively larger distance during the shortened

diffusion and precipitation process. In order to achieve maximum diffusion and precipitation region, it would be better if the curing reaction rate can be reduced at high processing temperature. Thus, PS is used to modify the epoxy because PS additive can be dissolved into the epoxy but not react with it [20]. Also with the low concentration of the PS additive ($< 5\%$), the viscosity and glass transition temperature of the modified epoxy shows almost the same performance as the non-modified epoxy [20]. However, with the PS additive, the curing reaction rate reduces significantly due to the dilute effect. Thus the time before gelation is more than that of the non-modified epoxy, which makes the diffusion and precipitation process take longer [20].

3.2.5 Crack Propagation in the Semi-interpenetration Network

In order to study the mechanical behavior, crack propagation needs to be studied since it directly relates to the fracture energy. The crack initiates near the interfaces under the in-plane loading conditions. After the crack initiates, it propagates essentially in the weakest region within the crack tip yield zone [21-22]. When the stress at the crack tip reaches the yield strength, it becomes large enough to break the bond and allow the crack to spread if the material is brittle. On the other hand, the stress for ductile materials will be relieved by the formation of plastic zone at the crack tip.

The main purpose of interleaving is to toughen the resin-rich region between the plies and improve the delamination resistance by absorbing more energy when a crack spreads. However, due to the dissimilar materials, the crack can still reach the interface between the inserted TP and epoxy matrix, and propagate along the interface. With the modified epoxy, as can be seen from Fig. 2a, the diffusion and precipitation process generates semi-IPN through the interface between TP and

epoxy matrix. The diffusion region is TP-rich region, which is more ductile. The precipitation region is epoxy-rich region, which is more brittle. Within these two regions, the long chain TP entangle with the crosslinked TS structure. When the crack approaches to the interface, the crack tip yield zone will shrink due to the high strength fiber and epoxy. The diffusion and precipitation region will arrest the crack within it. Thus the crack will need to break the semi-IPN to propagate, which consumes more fracture energy, as shown in Fig. 2b.

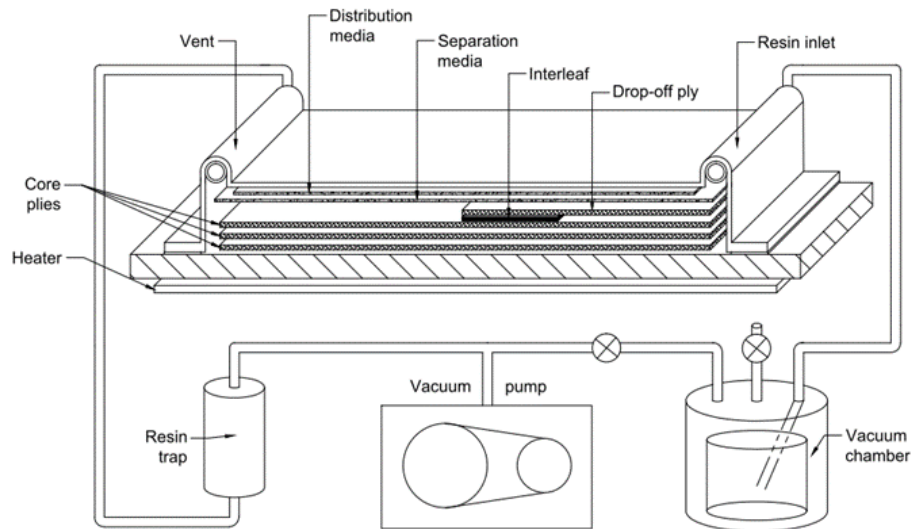


Fig.3 Vacuum assisted resin transfer molding experiment setup. The entire process is under high vacuum, which provides the lowest porosity in the final specimen.

3.3 Experiment Materials and Procedures

The epoxy resin is purchased from EPOKOTE Resin MGS RIMR 135, of which the major component is bisphenol A diglycidyl ether (DEGBA). The hardener is EPIKURE curing agent MGS RIMH 137, which contains diamine group. The PC, PSU, and PEI are the three potential TP

tested in this study and PSU was the only TP that used as a toughener. The detailed explanation of choosing PSU is in the results and discussion section. The solubility parameters of PC, PSU, and PEI are evaluated by viscometry. Methyl chloride is used to dissolve 0.2g TP with the total volume of 25ml, which produces a solution with approximately 1% weight concentration of tested polymers. For PC, dimethyl sulfoxide (DMSO) is chosen to mix with chloroform by a volume ratio from 1:4 to 4:1 but the total volume of the mixed solution is still 25ml. For PEI and PSU, ethyl acetate is mixed with methyl chloride at different ratio as the solvents. Cambridge VISCOpro 2000 is the viscometer to measure the viscosity in each case.

The specimens was produced by VARTM [23] since it was able to obtain a constant high fiber volume fraction with low thickness gradient along the infusion direction. The test specimens were fabricated using Saertex 970g/m² glass fiber fabric. The specimens consisted of three core plies of dimensions 11" by 1", as well as one drop-off ply of dimensions 5.5" by 1". A 2" by 1" polysulfone (PSU) Udel/Thermalux interleaf" was inserted between the drop-off ply and the adjacent core ply [14]. As can be seen from Fig. 3, the entire infusion of epoxy process was accomplished under vacuum environment to minimize the porosity in the final specimen. The heater is used to provide constant processing temperature during the curing. The morphology of the diffusion region was examined by optical microscopy and EDX. The current study employed mechanical tests as per ASTM-D3309 on an Instron 5569a universal testing machine. The stain gauges were mounted on the drop-off ply 0.4 in. from the drop-off. The specimens were loaded at strain rate of 1mm/min

until the drop-off layer was entirely delaminated, i.e., until the strain at the strain gauge dropped to zero [14]. Scanning electron microscopy was used to examine the fracture surfaces.

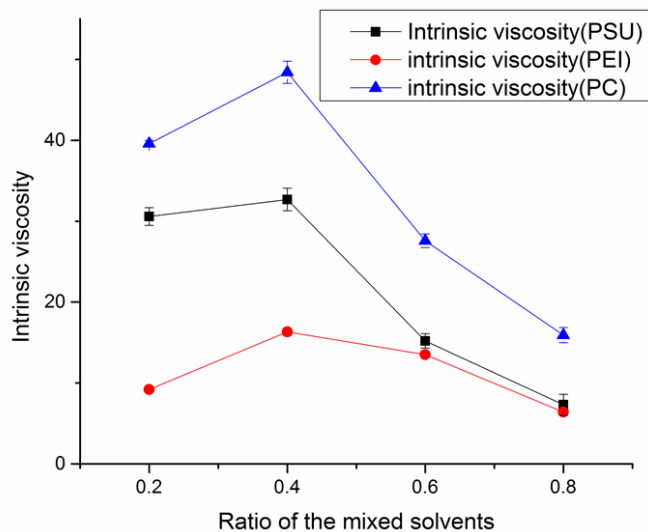


Fig.4 Experimentally determined intrinsic viscosity of PSU, PEI and PC by using eq.3.

3.4 Results & Discussion

3.4.1 Compatibility of Thermoplastics and Epoxy

In this study, the three TP materials PC, PEI, and PSU are chosen as the tested materials for potentially toughening the TS epoxy structure due to their high toughness and high glass transition temperatures.

Since the solubility parameter is generally used to determine the compatibility between polymers, it is important as a guide to choose the proper polymer. Due to the huge interaction forces between high MW polymers, traditional vaporization method is not suitable to measure the solubility

parameter. Instead, viscometry was used in this study to determine the compatibility between PC, PEI, PSU and RIMR 135 epoxy.

Fig. 4 shows the experimental determined solubility parameters of PC, PSU and PEI by using viscometry. The x-axis represents the ratios of the two mixed solvents. The y-axis represents the intrinsic viscosity of the solution calculated from Eq.3. All three trends increased at the beginning and then leveled off at some point. The mechanism of solution viscosity of polymers is similar to that of swelling: with a good solvent, polymer was likely to interact with the solvent, the molecular chain of the polymer was able to extend, leading to a retractive force, which is similar to the process that happened during the swelling process [15]. Thus, the most compatible solvent is the one can swell the polymer most, making the solution of highest intrinsic viscosity. Since the solubility parameter of the dissolved polymer was equal to the solubility parameter of the solution when the intrinsic viscosity approached the maximum value, for the PSU solution the highest intrinsic viscosity is around 34. By using the equation 2 in the background section, the average solubility parameter for PSU was 21.800. For the PEI, the highest intrinsic viscosity is around 17 and the average solubility parameter of PEI was 23.114. For PC, the highest intrinsic viscosity is around 46, the solubility parameter of PC was determined as 22.465.

The major component of RIMR 135 epoxy is DGBEA, of which the solubility parameter was 20.000. Compared with the solubility parameters of PEI, PSU and PC, it was obvious that PSU was of the closest solubility parameter to that of the epoxy. Thus, PSU should be the most

compatible polymer of the three to the epoxy and was expected to achieve significant diffusion region with the thermoset epoxy as the toughener of the epoxy system.

3.4.2 Temperature and Additive Concentration Dependent Diffusion/precipitation Process

The PSU interleaf was cured with non-modified epoxy and PS modified epoxy from 0% to 5% under various curing temperatures from room temperature to 120°C. The cured samples were polished to mirror surface for optical observation.

Fig.5a shows the diffusion depths with various curing temperatures at 0 and 5 wt% concentrations of PS. The non-modified epoxy (0% PS) is the lower black line in the figure. It shows no observable diffusion region until the curing temperature reached to 80°C. The diffusion depth reached to 25 microns into PSU at 120°C. Compared to the non-modified epoxy, with the addition of PS, the diffusion depths into PSU were improved with the increasing concentration of PS dissolved in the epoxy. With 5% PS modified epoxy, the diffusion depths under 120°C reached to more than 80 microns into PSU, which were almost 4 times than the non-modified epoxy. The main reason that both curve shows a jump of the diffusion depths above 60°C was that the diffusivity of the polymer was extremely small at low curing temperature but much higher at elevated curing temperature. The diffusivity of polymer is highly sensitive to the processing temperatures. Under low curing temperatures, the limited mobility

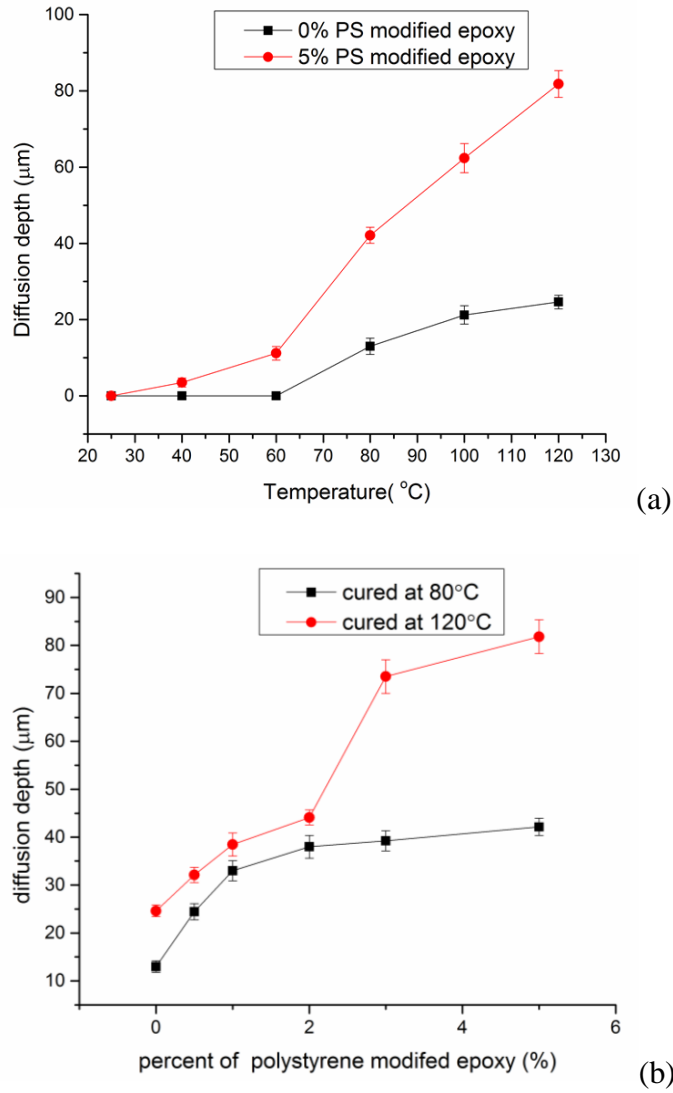


Fig.5 Average diffusion depths of the specimens (a) with 0% and 5% polystyrene modified epoxy cured from room temperature to 120 $^{\circ}\text{C}$ (b) with 0% to 5% polystyrene modified epoxy cured at 80 $^{\circ}\text{C}$ and 120 $^{\circ}\text{C}$.

and high viscosity of the TP polymers made the TS difficult to penetrate into the PSU-rich region before the diffusion process ceased due to the curing kinetics. Under high curing temperatures, the significantly reduced viscosity increased the diffusivity of the polymers and made the TS able to transport deep into the PSU region within the decreased time frame for diffusion process. With the

PS additive, the curing reaction rate was lower than that without the PS additive. Thus, the curing epoxy required more time to reach gelation point at which the diffusion process would stop, and diffusion process was longer than that of non-modified epoxy.

Fig.5b shows the diffusion depths with different concentration of PS additives from 0 to 5 wt% cured at 80°C and 120°C. Under 80°C, the diffusion depths gradually increased with concentration of PS from 0 wt% to 2 wt%, and leveled off from 2 wt% to 5 wt%. Under 120°C, the diffusion depths kept increasing. This was mainly due to significant reduction of polymer viscosity and curing reaction rate at elevated temperature, which led to increasing polymer chain mobility.

Fig.5b also showed that with the same concentration of PS additive, the specimens had deeper diffusion depth under higher curing temperatures. The difference between the specimens with same PS concentration cured at different temperatures were small at low PS concentration and became larger as the concentration rose to 5%.

Fig.6 shows the diffusion and precipitation morphology under 5% PS modified epoxy cured at 120°C. The bright area represents the PSU region and the dark area represents the epoxy region. The islands shaped gradient interphase due to the diffusion from the epoxy to the TP region can be clearly observed. The average diffusion depth in this case was 83.7 microns. Within the gradient interphase region, the size of islands decreased with deeper diffusion depth. This decrease in size was due to the reduced concentration of epoxy with deeper diffusion. As a result, when the liquid epoxy phase started to turn to gelation, it separated out from the solution and formed smaller sizes of clusters along the diffusion direction due to the reduction of epoxy concentration. In the epoxy

region, there were small bright dots. These dots were PSU-rich region in the epoxy due to the precipitation process. The precipitation depths in this case was around 32 microns.

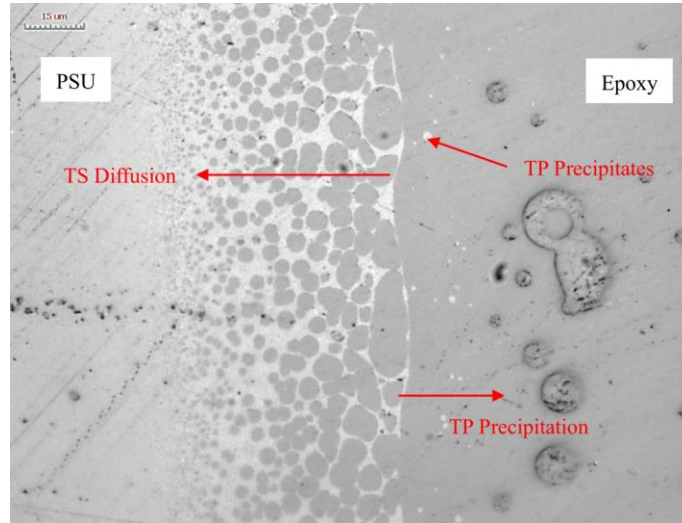


Fig.6 Polysulfone (PSU) thermoplastic diffusion and precipitation region with 5% PS modified epoxy cured at 120°C

is measured from optical microscopy imaging of the thermoplastic (TP)- thermoset (TS) interface. The thermoset diffusion into thermoplastic is characterized by a gradient island-shaped phases and the thermoplastic precipitation region is characterized by the dispersed PSU in the epoxy after curing.

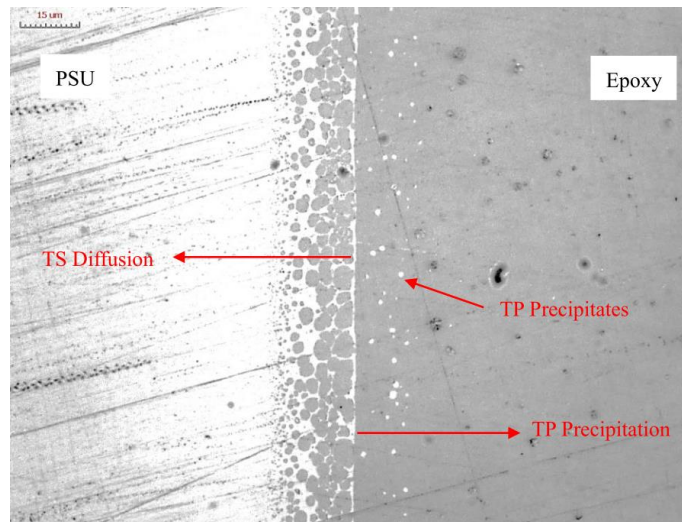


Fig.7 Polysulfone (PSU) thermoplastic diffusion and precipitation region with 5% PS modified epoxy cured at 80°C

is measured from optical microscopy imaging of the thermoplastic (TP)- thermoset (TS) interface.

As a comparison, Fig. 7 shows the diffusion and precipitation morphology under 5% PS modified epoxy but cured at 80°C. The average diffusion depth in this case was 37.1 microns and the average precipitation depth was 25 microns. The reason for the reduced diffusion and precipitation depths was that the diffusivity was highly temperature dependent. The diffusivity was expected to increase significantly with evaluated curing temperatures even though the curing reaction rate also increased. Fig.8 showed the diffusion and precipitation morphology with non-modified epoxy under 120°C. Compared with Fig. 6, the diffusion depth reduced to around 25 microns and the precipitation depth to around 15 microns. With the modified epoxy, significantly improved diffusion and precipitation region can be realized compared to the non-modified epoxy.

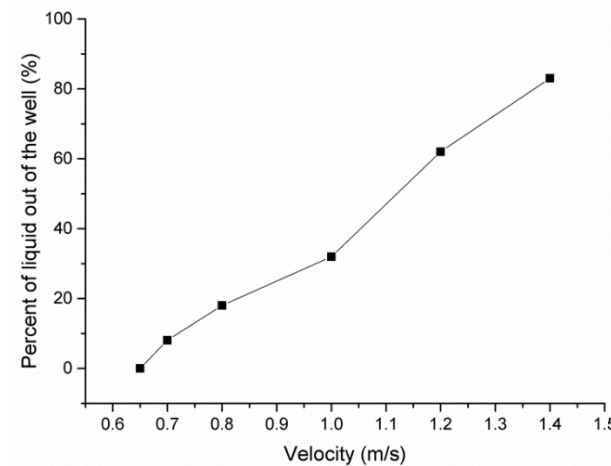


Fig.8 Polysulfone (PSU) thermoplastic diffusion and precipitation region with non-modified epoxy cured at 120°C is measured from optical microscopy imaging of the thermoplastic (TP)- thermoset (TS) interface.

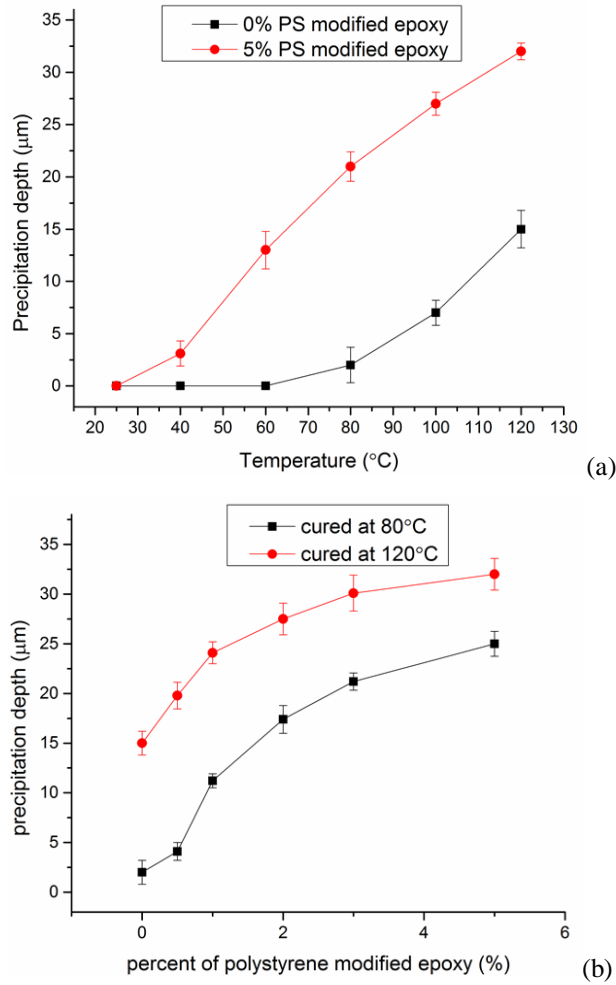


Fig.9 Average precipitation depths of the specimens (a) with 0% and 5% polystyrene modified epoxy cured from room temperature to 120°C . (b) with 0% to 5% polystyrene modified epoxy cured at 80°C and 120°C .

Fig.9a shows average precipitation depths with 0% and 5% PS modified epoxy cured from room temperature to 120°C . Fig.9b shows average precipitation depths with 0% to 5% PS modified epoxy cured at 80°C and 120°C . The precipitation depth was determined by the deepest observable precipitates from the interface between PSU and epoxy. Both curves increased with the elevated temperatures. Compared to Fig.5, the precipitation depths was normally smaller than diffusion

region. The reason for this phenomenon was that the mobility of the long chain TP molecules was smaller compared to the mobility of low molar weight uncrosslinked TS

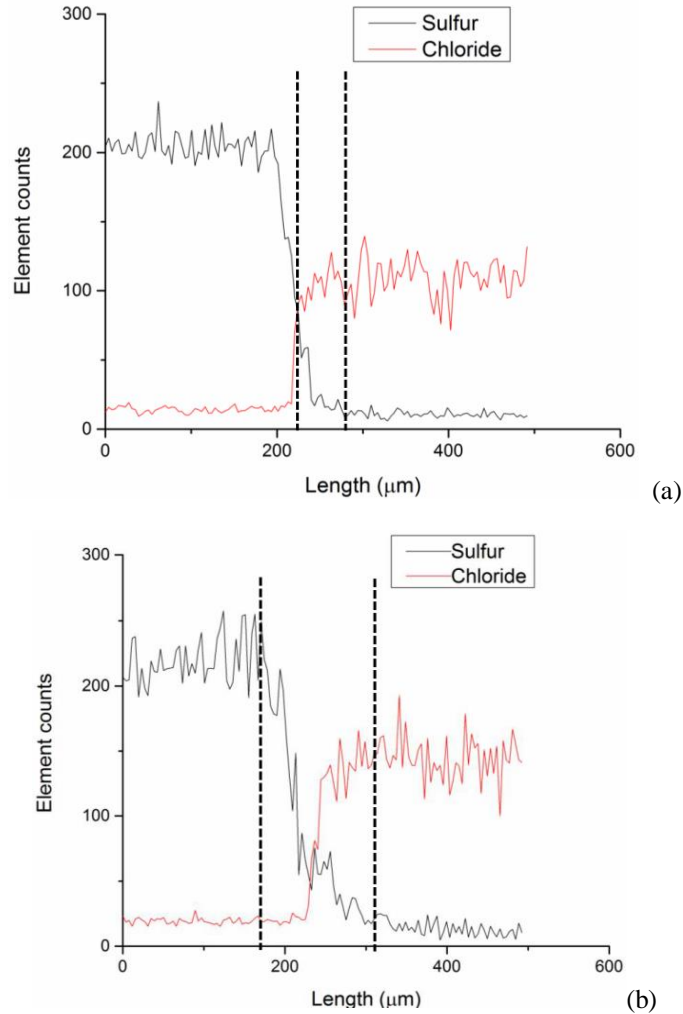


Fig.10 EDX line scan across TS-TP interface of the specimen (a) under 5% PS modified epoxy cured at 80°C.

(b) under 5% PS modified epoxy cured at 120°C. The dash lines indicate the diffusion and precipitation region.

molecules. Fig. 10 shows the EDX line scan of the specimen across the interface between the PSU and epoxy matrix. Sulfur element was traced along the line which only existed in the PSU and chloride element was traced to represent the existence of epoxy. From Fig. 10, it can be known

that at high temperature, low MW TS diffused much faster than the high MW TP, leading to sharp reduction of sulfur element counts in Fig. 10b but gradual reduction of sulfur elements in Fig. 10a. The existence of sulfur elements in the precipitation region indicated that only part of the PSU precipitated out, the rest was mixed with epoxy matrix due to the limited mobility of long chain structure after the gelation of curing epoxy.

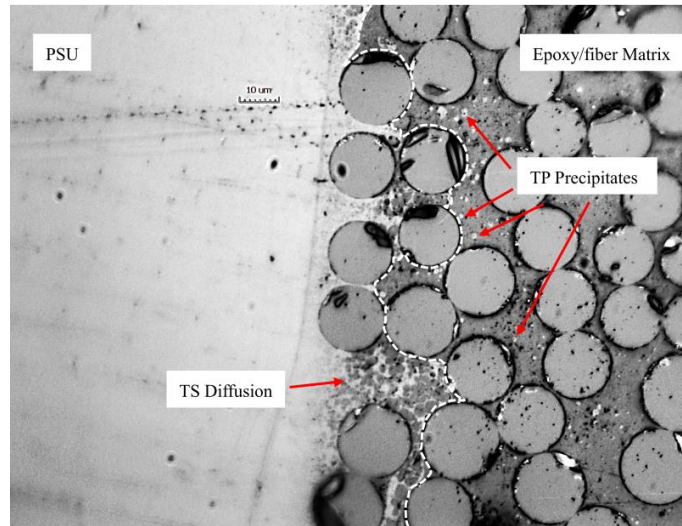


Fig.11 Polysulfone (PSU) thermoplastic diffusion and precipitation region in the fiber matrix with 5% PS modified epoxy curing at 120°C. The dash line represents the boundary of TS-TP interface. Arrows represent the locations where there are precipitates.

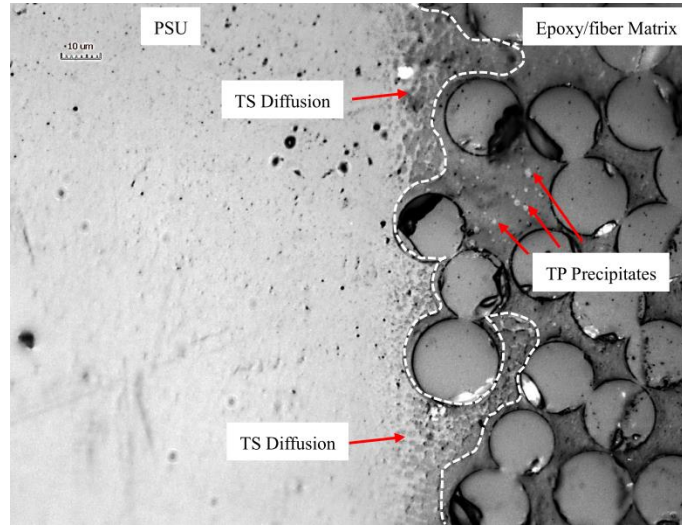


Fig.12 Polysulfone (PSU) thermoplastic diffusion and precipitation region in the fiber matrix with 5% PS modified epoxy curing at 80°C. The dash line represents the boundary of TS-TP interface. Arrows represent the locations where there are precipitates.

3.4.3 Geometry Influence on the Diffusion and Precipitation Process

The geometry factor also influenced the diffusion and precipitation process. The PSU film was embedded between the fiber plies and co-cured with the epoxy. Fig. 11 shows the diffusion and precipitation region of the 5% PS modified epoxy cured at 120°C. The arrows were used to highlight the TS diffusion and TP precipitates in the epoxy matrix and the white line was used to distinguish the interface between the TP and epoxy. Compared with the case under the same condition but without fiber structures, the diffusion and precipitation regions both reduced significantly. In this condition, the diffusion depth was around 45 microns and the precipitation depth was around 30 microns. The reason for the reduction of diffusion and precipitation region was that the existence of the fiber bundles acted as obstacles in the direction of PSU diffusing into

epoxy. The small gaps between the fibers generated great resistance for PSU to pass through and increase the length of the path that TP need to travel, which led to the reduced precipitation region. On the other hand, since less PSU was transferred into epoxy-rich region, there were less free space in PSU-rich region, and the existence of the fiber beams reduced the amount of epoxy in the unit region that was able to swell the TP. Both reasons led to significant reduced diffusion depth. Fig. 12 shows the diffusion and precipitation region of 5% PS modified epoxy with fiber structure under 80°C. The average diffusion region was 19 microns and precipitation region was 10 microns. Since the fibers were not uniformly distributed in the local area, the region with less fibers showed more diffusion and precipitation. On the other hand, the region where the fiber came into contact with PSU, almost no diffusion and precipitation was observed. Fig. 13 shows the diffusion and precipitation with non-modified epoxy curing at 120°C. Very limited diffusion and almost no obvious precipitation can be observed under this condition. The impermeable fiber beams reduced the diffusivity of both curing epoxy and PSU with or without PS additive. The diffusion and precipitation depth decreased under all conditions but the specimen with 5% PS still showed relatively large diffusion and precipitation region.

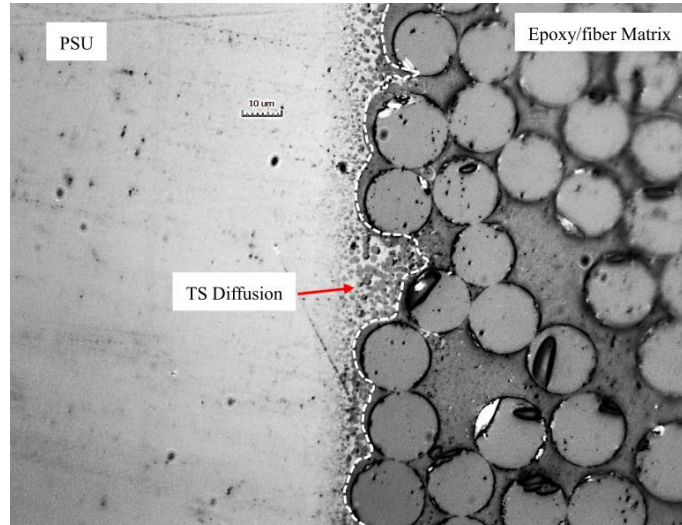


Fig.13 Polysulfone (PSU) thermoplastic diffusion and precipitation region in the fiber matrix with non-modified epoxy curing at 120°C. The dash line represents the boundary of TS-TP interface.

3.4.4 Stress-strain and Toughness Behavior

Uniaxial tensile tests were carried out. The drop-off specimen used in the test was to simulated the mixed mode loading conditions in reality [14]. The specimens were loaded until the drop-off region was totally delaminated by cracking through the intelaminar region and the value of the strain gauge returned to zero, which were mounted on the surface of drop-off layer 0.4 in. away from the drop-off. Fig.14 shows the stress and strain curves of the drop-off layer under three conditions. The curve marked “reference” referred to the case where no interleaf was introduced. As a result, the reference specimen began to fail at a low strain (about 0.35%). The curves whose slopes were similar to the reference specimen were the specimens with 5% PS cured at 120°C and 80°C. As Fig.14 shows, because of the inserted interleaf, the interlaminar layer connecting the drop

off layer to the core plies became much tougher. For the curve marked 120°C, it did not fail until the strain reached almost 0.8% due to its increased diffusion and precipitation depth (Fig. 11).

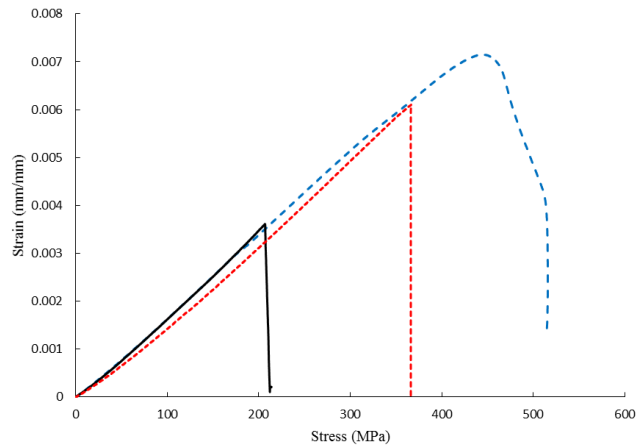


Fig.14 Representative strain-stress curves obtained from the strain gauge mounted on the drop-off layer in uniaxial tensile tests: reference specimen (without interleaf), interleaved specimens with 5% PS modified epoxy cured at 80°C and 120°C.

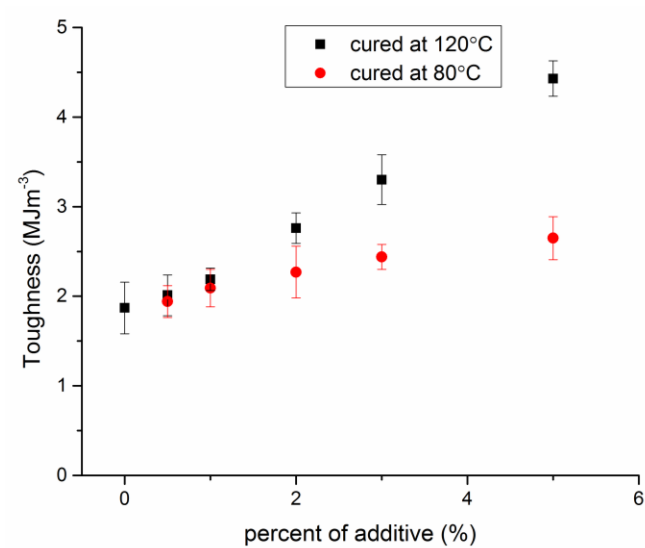


Fig.15 Toughness of PSU interleaved specimens from 0.5 to 5% PS modified epoxy cured at 80°C and 120°C. The error bars represent standard errors.

The toughness, which represents the energy required for a crack to initiate and propagate, was calculated by integrating the area under the stress strain curve. In Fig. 16, for each curing temperature, three specimens were tested to validate the data repeatability under different concentrations of PS. Each average toughness and their standard errors were represented by a symbol and an error bar. As shown in the figure, the toughness of the specimens had a gradual increase and a peak at 5% PS modified epoxy cured at 120°C. The trend resembled that of the diffusion and precipitation depths seen in Fig.10 and provided strong evidence that deep semi-IPN of the interleaf into the matrix led to increased toughness and improved delamination resistance. At its peak, the toughness was almost three times as high as the reference specimen which had no interleaf.

3.4.5 Crack Propagation Location and Toughening Mechanism

Fracture surfaces of the specimens after mechanical tensile tests were observed via scanning electron microscopy. The toughness of reference specimen was obtained from Chapter 2. Since the Weibull modulus of the brittle reference calculated in Chapter 2 was high, it indicated that the reference specimens showed similar failure performance. Fig.16a shows the fracture surface of the reference specimen. It was clean where fewer broken fiber beams were found on the surface.

Individual fiber beams were seen with very few particles on their surfaces. Clean and clear river lines between the fibers indicated there was no plastic shear deformation. The crack of this kind mainly went through the interface between epoxy and fiber, which led to adhesion failure. For the PSU interleaved specimens cured with 5% PS modified epoxy cured at 120°C (Fig. 16b), more residues were observed on the fibers throughout the fracture surface. Most fibers were not clean and had a veil attached on the surface, which indicated large plastic deformation. Fig. 16c shows the fracture surface of fiber beam under high magnification (5K). On the surface of the fiber beam, a spongy veil can be observed throughout the entire fracture surface. The porous residue was the diffusion and precipitation region, which matched the morphology in Fig. 10. Thus, the crack was located at the generated semi-IPN region and propagated by breaking the network, which required much more energy due to the plastic shear deformation of the diffusion and precipitation region. The results indicated that high toughness interleaf and deep diffusion and precipitation region were both the key factors to improve the toughness of the composites by avoiding the traditional adhesion failure along the interface between epoxy and fiber.

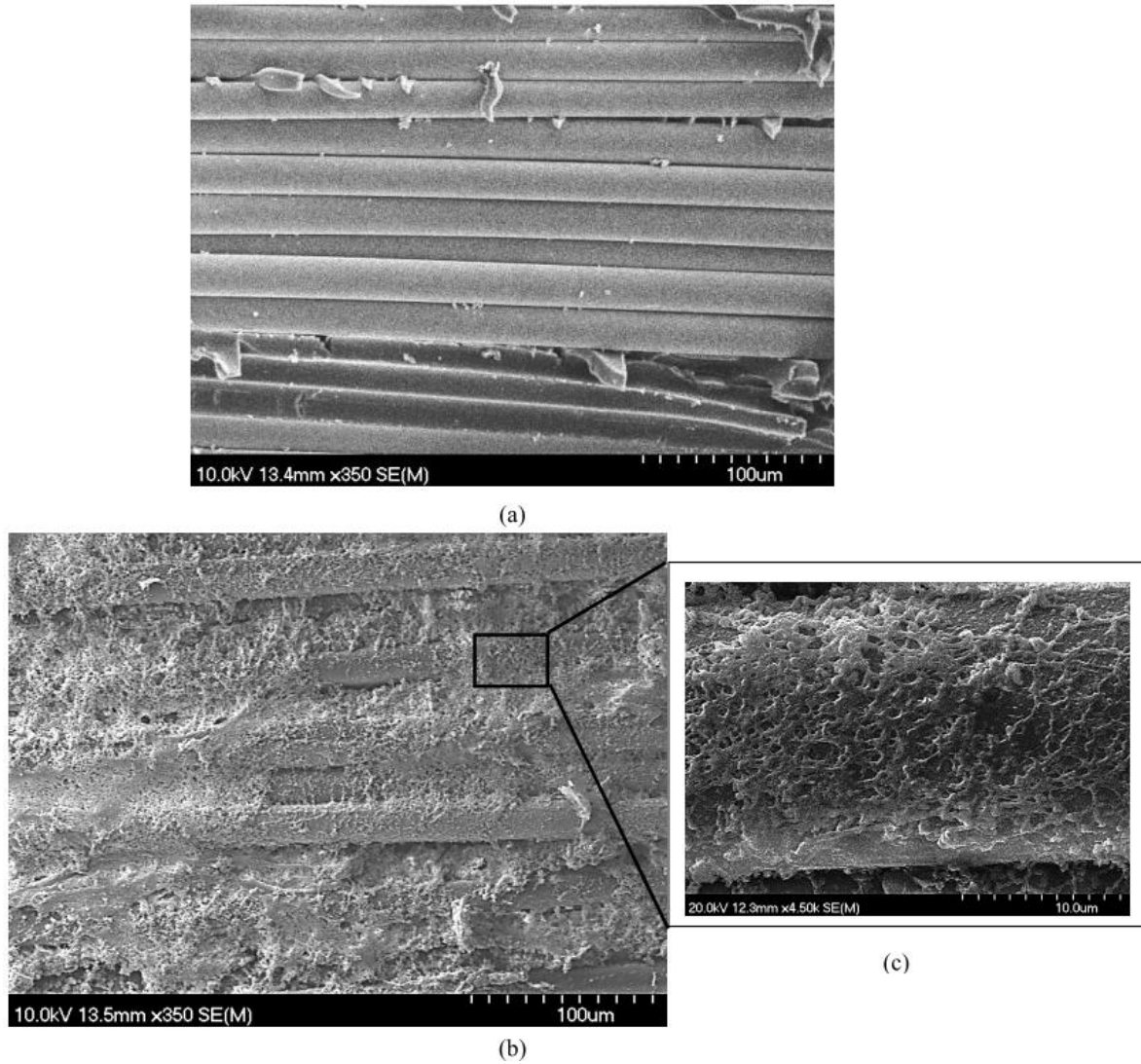


Fig.16 SEM image of the fracture surface of (a) the reference specimen without interleaf. (b) the interleaved specimen with diffusion and precipitation. (c) High resolution close up of the fracture surface.

3.5 Conclusion

The effect of the interleaf deep diffusion and precipitation on the delamination resistance was investigated for the PSU interleaved GFRP. PSU was chosen due to its close solubility to the epoxy

system. The diffusion and precipitation depth increased with the curing temperature and concentration of the PS additive. The improved diffusion and precipitation depth is mainly due to the increased mobility of the molecules at high temperature and increased time for diffusion and precipitation process due to the addition of PS. As compared with the GFRP without interleaf, the fracture toughness increased by a factor of three with the 5% PS modified epoxy cured at 120°C. This is mainly because the deep diffusion and precipitation zone of improved ductility confines the plastic zone ahead of the crack tip within its boundaries and thus requires more fracture energy for the crack to propagate. Spongy veil covered the entire fracture surface, indicating the crack propagated through the generated semi-IPN, which was the key factor for the improved delamination resistance.

3.6 Acknowledgement

This research was supported by National Science Foundation under a GOALI award CMMI-1363328. Authors would also like to thank Ming Gao from Columbia University for providing us viscometry equipment.

Chapter 4: Interlaminar Toughening of GFRP, Part 2: Characterization and Numerical Simulation of Curing Kinetics

4.1 Introduction

The methods to toughen the fiber reinforced polymer have been studied in the past decades. Thermoplastic (TP) materials have been considered as potential materials because the ductile behavior of TP can absorb more energy when the crack propagates. Many industries used high performance TP like polycarbonate, polymethylmethacrylate, polyetherimide, polysulfone and polyethersulfone, which have been studied as a modifier to the epoxy [1-4]. Results indicate that even though TP has high strength and toughness, the adhesion failure can still occur if the TP cannot bond well with the thermoset (TS) epoxy.

Thus, choosing a compatible TP to the epoxy is vital to improve the bonding quality because a semi-interpenetration network (semi-IPN) region can be generated between the TP and epoxy [5-6]. The long chain of compatible TPs can relax and increase the free space inside, which let the low molar mass curing epoxy diffuse into these spaces. On the other hand, the relaxed TPs disentangle and flow into the curing epoxy out from the solid TPs region. Finally, the long chain TPs entangle with the crosslinked cured epoxy, which is semi-IPN. This network is the key to improve better bonding between TPs and TSs and avoid the adhesion failure.

For polymers, diffusion is dependent on many factors. Compatible polymer-polymer systems need to be chosen based on the solubility theory: the closer the solubility parameters of the two polymer are to each other, the more likely they will have diffusion [7]. Typically TP is of high molecular

weight and high viscosity. Thus TP often cannot diffuse easily within the acceptable time regime of the bonding operations like the curing process of epoxy. Improved adhesion due to diffusion and precipitation of molecules is hard to realize except by significantly increasing the mobility of the molecular chains of the two polymers by applying heat or solvent [8-10]. Diffusing molecules would also need to find their way around impermeable particles such as fibers in the matrix, increasing path lengths and reducing mass transport rates [11].

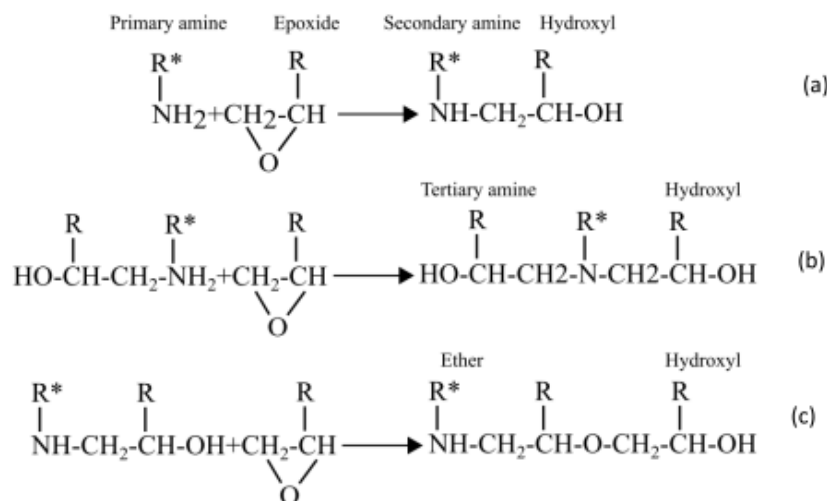


Fig.1 The three main chemical reactions during curing process of the epoxy. a) Primary amine from hardener has open-ring reaction with epoxide group and generates secondary amine. b) Secondary amine reacts with the epoxide group and generates tertiary amine. c) Etherification reaction [15].

The mechanical behavior of PS modified epoxy and the morphology of improved diffusion and precipitation region was studied in Part 1 of this paper [12]. The results indicated that deep diffusion and precipitation was critical to the high toughness. Thus, in this study, diffusivity of

polymers and curing kinetics of the system were characterized by using ATR-FTIR technique. The changing peaks of curing epoxy system were monitored to quantify the diffusivity of species at different curing temperatures. Numerical methods were used to predict and optimize the experiment results with and without the existence of the glass fiber reinforced polymer. The dependence of diffusivity and curing kinetics as well as diffusion and precipitation mechanism at the interface between TP and TS were investigated and discussed.

4.2 Background

4.2.1 Chemical Reactions of the Curing Process

The cure of epoxy resin with amine cross-linking agents proceeds primarily through the addition reaction between the epoxide ring and amine hydrogen as shown in Fig. 1. Fig.1a shows that during the reaction with primary amine, the epoxide ring opens, bond formation occurs between the terminal carbon of the epoxy and amine nitrogen. In Fig.1b reaction of the resultant secondary amine with another epoxy molecule results in a tertiary amine which acts as a branch point. The repetitions of this reaction scheme leads to the construction of a highly branched, high molecular weight network structure. Since the cure reaction produces hydroxyl groups, the reaction should be autocatalytic, which means the hydrogen in the hydroxyl group bonds to the epoxide ring, as shown in Fig.1c. The weakened bond of the hydrogen-bonded epoxy then reacts with the unreacted epoxide ring and leads to etherification. The three chemical reactions happen simultaneously in the curing epoxy, but the primary amine reaction dominates most of the reactions in the system [13].

4.2.2 Diffusion and Precipitation Process Considering the Curing Kinetics

The interaction between TS and TP was complex because it depended on various factors such as temperature, degree of curing, and phase change of the TS.

The starting state of the process was the liquid phase of TS epoxy, which was mixed with the curing agent, coming into contact with the TP. On the molecular level, since TP had close solubility parameter as the epoxy system, their molecular interaction forces were similar. The more similar the intermolecular forces, the more compatible the solvent and solute. Thus, TS molecules swelled the long chain structure of the TP, and the relaxation of the TP long chains increased the free volume in the TP region. In this TP region, the TS molecules started to fill in the spaces and long chains started to flow into the uncured TS region. However, with increasing time there was a curing process between the epoxy and curing agent, which the epoxide ring of the epoxy opened and connected to the amine group of the curing agent. With more epoxy ring opening and reconnecting, the molecular weights of the TS significantly increased and cross-linked structure formed, which meant the liquid phase changed to gelation and finally to a solid phase. Considered the curing reactions in the TS region, the diffusion and precipitation ceased when the degree of curing reached about 0.6, because the viscosity of the gel-phase TS was too high and the solubility parameters changed when TS phase changed. Thus, when the degree of curing was approaching 0.6, the compatibility of TP and TS reduced and the solute started to separate from the solution leading to a two phase morphology. Since it took time to fully cure, the separated solute could have enough time to gather together and form clusters. As a result, islands shaped cured epoxy would be likely

to form in the TS rich region and the islands shaped TP would be likely to form in the TS rich region.

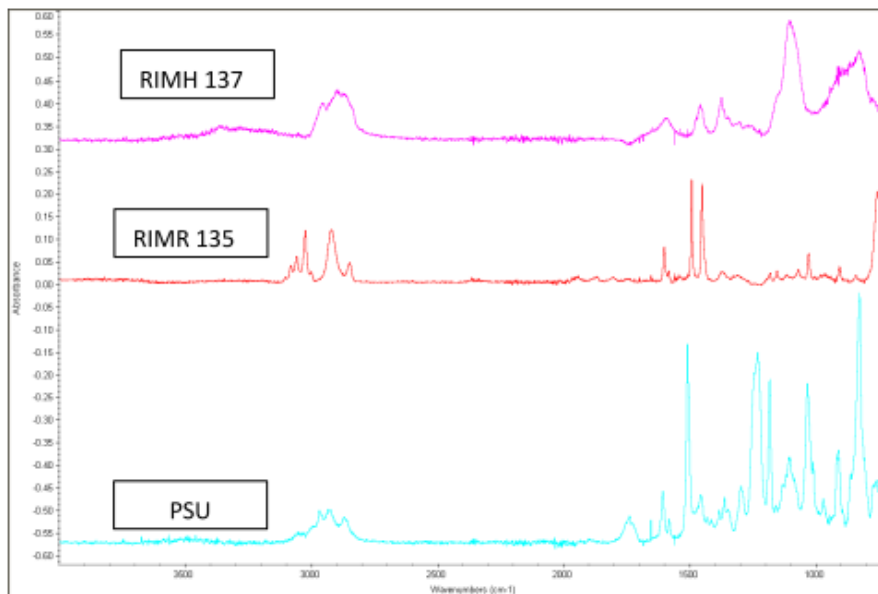


Fig.2 ATR-FTIR spectra of RIMH 137 curing agent, RIMR 135 resin and PSU. Peaks monitored during diffusion experiments: 915 cm^{-1} (epoxide deformation) and 1036 cm^{-1} (aromatic deformation) in RIMR 135; 2916 cm^{-1} (C-H stretching of diamine) for RIMH 137; 1151 cm^{-1} (S=O stretching) for PSU

4.2.3 Attenuated Total Reflectance – Fourier Transform Infrared Spectroscopy

Fourier Transform Infrared Spectroscopy-Attenuated Total Reflectance is an internal reflection technique in which an optically dense medium (the internal reflection element, IRE) is used to obtain an infrared spectrum. Due to the sensitivity of the detection, the ATR-FTIR can monitor

the diffusion process in real time by measuring the changing absorbance of one or two characteristic bands of the sample [13].

Since the IRE has larger refractive index, IR totally reflected above the critical angle at the crystal/sample interface. An evanescent wave form at interface, decaying exponentially from the surface through the penetration depth. The penetration depth is defined as the distance at which the electric field formed by the evanescent wave diminishes by a factor of 1/e

$$d_p = \frac{\lambda}{2\pi n_2 (\sin^2 \theta - (\frac{n_1}{n_2})^2)^{0.5}} \quad (1)$$

where λ is the wavelength of light in vacuum, θ is the angle of incidence, n_1 and n_2 are the refractive indices of the IR crystal and the sample respectively. If the sample absorbs in the inferred, the wave interacts with the material causing the attenuation of the total reflection of the propagating beam inside the IR crystal

$$A = \int_0^\infty aSC(z)\exp(-\frac{2z}{d_p})dz \quad (2)$$

where A is the absorbance, z is the distance from the surface, a is the oscillator strength, $C(z)$ is the concentration, S is the cross sectional area. This expression represents a weighted average of the concentration of the absorbing species.

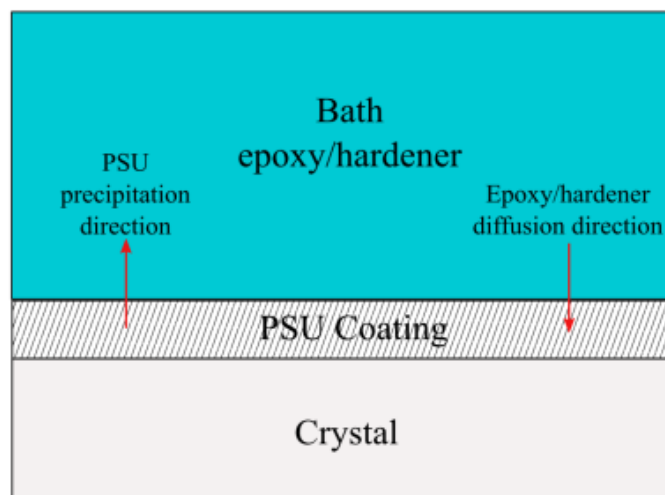


Fig.3 FTIR experiment setup for determination of diffusivity and curing kinetics.

4.3 Experiment Materials and Procedures

The ATR-FTIR experiments were accomplished on MKII Golden Gate Single Reflection ATR system with a heating accessory. The objectives of ATR-FTIR experiments are to obtain the diffusivity of single component into PSU, the diffusivity of PSU into epoxy or hardener, and curing kinetics of the epoxy system. The ATR-FTIR spectra of the PSU and the epoxy system are shown in Fig. 2. For the first objective, the IR crystal is coated with a thin PSU film. The PSU was dissolved in the methyl chloride solution with an approximately 5% weight concentration. One coat at 500 rpm for 10 seconds by using spin coating consistently produced 5 micron film, of which the thickness is suitable so that the results are not sensitive to variations in the penetration depth of the infrared [14]. RIMR 135 epoxy resin (modified and non-modified) and RIMH 137 hardener were dropped on the thin film at different temperatures separately. Since FTIR provided

information through the change in peak height or peak area with time and the peaks presented specific chemical groups in the molecules, some characteristic peaks such as 915 cm⁻¹ (epoxide ring deformation), 1151 cm⁻¹ (S=O bond) and 2915 cm⁻¹ (C-H stretching in the hardener spectra) were monitored. Spectra were taken every few minutes early in the diffusion and several times an hour at longer time. For the second objective, there was no film on the IR crystal, epoxy resin (modified and non-modified) and hardener were pre-mixed and dropped directly on the surface of the IR crystal under different temperatures. Peaks that represented epoxide ring were monitored at various times.

4.4 Numerical Simulation

4.4.1 Diffusivity of Species in the Epoxy System

By assuming Fickian diffusion kinetics, ATR-FTIR technique was used to study the individual diffusion of epoxy and amine monomers into PSU and PSU into the epoxy or hardener bath. The model geometry is showed in Fig. 3. The general Fickian and Fick's second law is

$$\frac{\partial c_p}{\partial t} = D_p \frac{\partial^2 c_p}{\partial x^2} \quad (3)$$

where p represents penetrant, either epoxy or amine. Assuming the concentration of amine or epoxy in the film is zero at the beginning, the solution to the diffusion equation is [15]

$$\frac{A(t) - A_\infty}{A_0 - A_\infty} = \frac{\sum_{n=0}^{\infty} F_n \exp(-(\frac{(2n+1)\pi}{2l})^2 D t)}{\sum_{n=0}^{\infty} F_n} \quad (4)$$

$$F_n = \left[\frac{(-1)^n}{2n+1} \frac{l}{d_p} + \frac{\pi}{4} \exp(-2 \frac{l}{d_p}) \right] * \left\{ [(2n+1)\pi]^2 + 16(\frac{l}{d_p})^2 \right\}^{-1} \quad (5)$$

where A is the absorbance, D is the diffusivity of the penetrant at current temperature, l is the film thickness and d_p is the penetration depth of the infrared at specific wavelength. In this expression, the diffusivity is the only fitting parameter and is of the Arrhenius diffusivity relationship with temperature:

$$D_p(T) = C \exp\left(-\frac{D}{RT}\right) \quad (6)$$

where p represents the penetrant, C and D are constant coefficients.

4.4.2 Curing Kinetics of the Epoxy System

The curing kinetics is assumed to be proportional to the rate of heat generation, which can be defined by two separable parameters: K and α [16]. The simplest model corresponds to an n th-order kinetic expression:

$$\frac{d\alpha}{dt} = K(1 - \alpha)^n \quad (7)$$

where α is the degree of cure in the system

$$\alpha = 1 - \frac{c_e}{c_{e0}} = 1 - \frac{c_a}{c_{a0}} \quad (8)$$

where c_e and c_a are the epoxide and amine hydrogen concentrations at any time, 0 indicates the initial condition, n is the reaction order and K is the rate constant given by an Arrhenius temperature dependence.

Assumed that the secondary amine group formed in the reaction show the same degree of reactivity toward epoxy groups as the primary amine groups, the total rate of consumption of epoxides

$$\frac{d\alpha}{dt} = (k_1 + k_2\alpha)(1 - \alpha)^2 \quad (9)$$

$$k_1 = A_1 \exp\left(-\frac{E_1}{RT}\right) \quad (10)$$

$$k_2 = A_2 \exp\left(-\frac{E_2}{RT}\right) \quad (11)$$

where A_1 , A_2 are pre-exponential constants; E_1 , E_2 are the activation energies; R is the ideal gas constant; T is temperature. These equations represent the intrinsic kinetics, and they only depend on the chemical nature of the reacting species.

The glass transition temperature reflects the amount of free volume in the curing TS available for diffusion or precipitation. As the glass transition temperature increases, the mobility of the molecules decreases and the system becomes rigid. The DiBenedetto model is used to provide a reliable relation between the glass transition temperature of the curing epoxy and the degree of curing [17]. By relating DiBenedetto equation and free volume theory [18], the diffusivity expression becomes

$$D = D_p \exp\left(B\left(1 - \frac{1}{0.025 + \beta(T - T_g(\alpha(t)))}\right)\right) \quad (12)$$

for most cases, B is 0.9~1.2.

Thus, the general governing equation for epoxy and curing agent transport in the TP is [18-19]:

$$\frac{\partial C_p(\alpha)}{\partial t} = \frac{\partial}{\partial x} \left(\frac{\partial C_p(\alpha)}{\partial x} \right) D_p(\alpha) - R_r(\alpha) \quad (13)$$

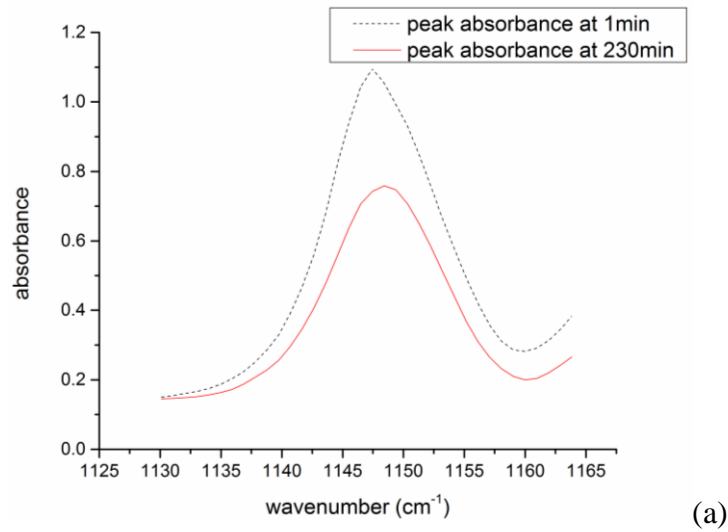
where C_p is the concentration of the species, $R_r(\alpha)$ represents the reaction rate, which is Eq. 9.

Since the TP do not have the curing reaction, the governing equation for TP transport in the epoxy-rich region is:

$$\frac{\partial C_p(\alpha)}{\partial t} = \frac{\partial}{\partial x} \left(\frac{\partial C_p(\alpha)}{\partial x} \right) D_p(\alpha) \quad (14)$$

4.5 Results & Discussion

ATR-FTIR technology was used to determine the diffusivity between the epoxy system and PSU experimentally. Since the entire process was the superposition of the diffusion and precipitation process, and the curing process, it was important to simplify the complexity of the problem. It was assumed that the diffusivity was dependent of temperature, degree of curing and free space in the diffusion direction, which meant the entire process could be experimentally determined from three aspects: single component diffusivity (D_p in Eq. 12), curing kinetics (α in Eq. 9) and structure factor.



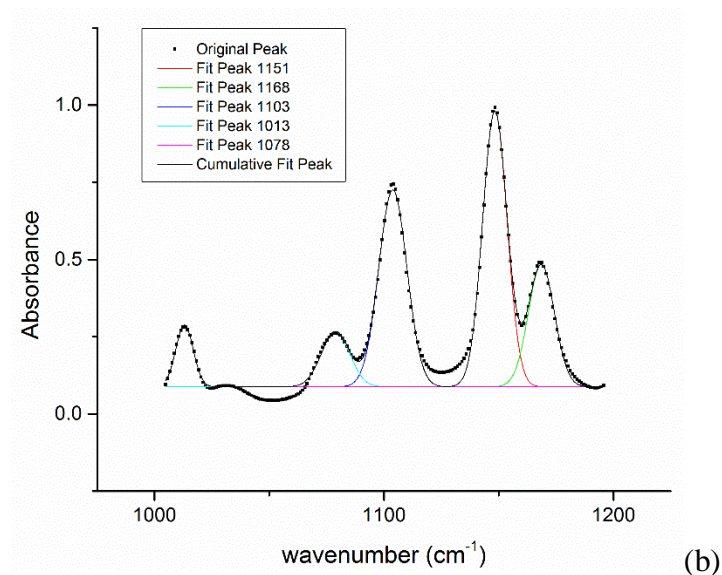


Fig.4 (a) Typical FTIR spectra of 1151 cm^{-1} peak (S=O stretching) decreases with the increasing time observed in the experiment. The diffusivity and reaction rate are both obtained by monitoring the absorbance changes of characteristic peaks with time. (b) Multiple peaks fit around 1151 cm^{-1} peak during diffusivity determination experiment.

4.5.1 Diffusivity Determination of the Epoxy System

By monitoring the absorbance change of the FTIR spectra, the concentration of species was determined at the specific time. As can be seen from Fig. 4a, it showed the FTIR spectra of 1151 cm^{-1} peak (S=O stretching in the PSU) decreased with the increasing time, which indicated that from 1min to 230min, in the infrared penetration region, diffusion and precipitation process was happening that reduced the concentration of the PSU. The PSU film coated on the crystal shown in Fig. 3 was initially thicker than the penetration depth of infrared lights. As the diffusion

and precipitation proceeded, epoxy/hardener began to penetrate into the PSU film and PSU molecules began to flow into the bath. Thus, the reduced concentration of PSU and increased concentration of epoxy/hardener in the infrared penetration region led to the reduction of PSU peak intensity and increment of penetrant peak intensity. During diffusivity determination, the mass transportation process due to diffusion reduced the amount of PSU in the infrared detected region, leading to the decreasing of 1151cm^{-1} peak. However, since the monitored peaks were medium or strong peaks in the materials, influences of surrounding peaks were small enough to ignore, which was shown in Fig. 4b that after decomposition of spectra, the original 1151cm^{-1} peak had almost the same absorbance intensity as the decomposed 1151cm^{-1} peak. Based on this principal, the different characteristic peaks were monitored during the experiments for diffusivity determination or curing kinetics.

The experiment setup for determination of the diffusivity was that a thin PSU film was first spin-coated on the infrared crystal element and 1 ml of epoxy or hardener was dropped on the film surface at various temperatures. The infrared crystal was made of Germanium, of which the refractive index was 4. Fig.5 shows the experimental results of PSU into epoxy at 4 processing temperatures. The dots represented the normalized absorbance of the 1151cm^{-1} peaks at the moment of measurement. The 1151cm^{-1} peak was for the S=O stretching in the PSU. From the figure, the peak reduced rapidly in the beginning at high processing temperatures but reduced slowly at low temperatures. The reason for the concentration drop was that the absorbance of the peak represented the concentration of the species with this specific chemical bond. When the

hardener started to contact with the PSU surface, it swelled the long-chain TP. The relaxation of the long chain structure produced more free space in between, where the epoxy began to diffuse into and fill the free space and PSU began to flow into the epoxy bath in the opposite direction, which led to the reduction of the concentration of the PSU. After a period of time, the concentration of two species approached to steady state, which led to the level off of the data points. The processing temperature significantly influenced the diffusivity. At 120°C, the normalized absorbance of PSU dropped to less than 0.1 in 30 seconds. However at 60°C, it took almost 10000 seconds to drop to 0.1. By using the relationship between absorbance and diffusivity shown in Eq. 4, least square fitting curves were plotted in Fig. 5 for each conditions. From 60°C to 120°C, the diffusivity of PSU into epoxy at each conditions were 1.31×10^{-11} , 1.03×10^{-10} , 5.611×10^{-10} and 1.01×10^{-7} m²/s. The corresponding experimental results of epoxy into PSU is shown in Fig. 6. From 60°C to 120°C, the diffusivity of epoxy into PSU at each conditions were 1.71×10^{-11} , 2.05×10^{-10} , 9.991×10^{-10} and 2.23×10^{-7} m²/s. The results were reasonable since the diffusivity was highly dependent on the processing temperatures and the difference between 60 to 120°C was 4 orders of magnitude. Based on the diffusivity of epoxy into PSU, it was about one time larger than that of PSU into epoxy under each processing temperature, which means the diffusion process was easier than the precipitation process due to the limited mobility of large molar weight and amorphous long- chain PSU.

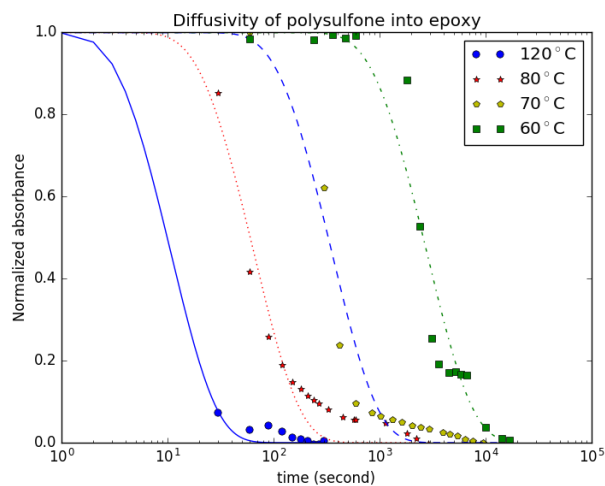


Fig.5 Diffusivity determination of PSU into epoxy from 60°C to 120°C. Normalized absorbance data were obtained from ATR-FTIR experiments. Least square fitting curves were based on Eq.4 for each conditions.

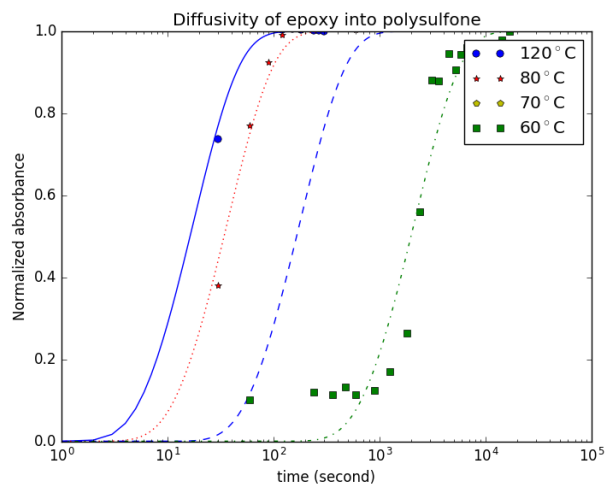


Fig.6 Diffusivity determination of epoxy into PSU from 60°C to 120°C. Normalized absorbance data were obtained from ATR-FTIR experiments. Least square fitting curves were based on Eq.4 for each conditions.

Fig. 7 and Fig.8 show the experimental results of PSU into hardener and hardener into PSU. The monitored peaks in this case was 2916cm^{-1} for C-H stretching in the hardener. From 60°C to 120°C,

the diffusivity of PSU into hardener at each conditions were 1.97×10^{-11} , 4.6×10^{-11} , 4.571×10^{-10} and 1.31×10^{-7} m²/s. The diffusivity of hardener into PSU at each conditions were 1.011×10^{-10} , 1.201×10^{-10} , 8.341×10^{-10} and 1.71×10^{-7} m²/s.

Fig. 9 shows the experimental results of 5% PS modified epoxy to PSU. The effect of low concentration PS additive on the diffusivity of the epoxy into PSU was not significant. For example, the corresponding diffusivities of modified epoxy into PSU were 1.9×10^{-11} m²/s at 60°C and 1×10^{-10} m²/s at 70°C. Compared the diffusivity data between the non-modified and modified epoxy, they were at the same order of magnitude and the values were close to each other, which indicated that the addition of PS did not influence the diffusivity of the epoxy to the PSU.

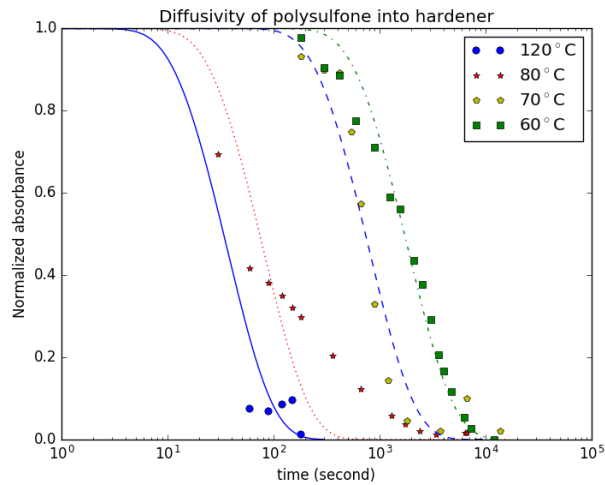


Fig.7 Diffusivity determination of PSU to hardener from 60°C to 120°C. Normalized absorbance data were obtained from ATR-FTIR experiments. Least square fitting curves were based on Eq.4 for each conditions.

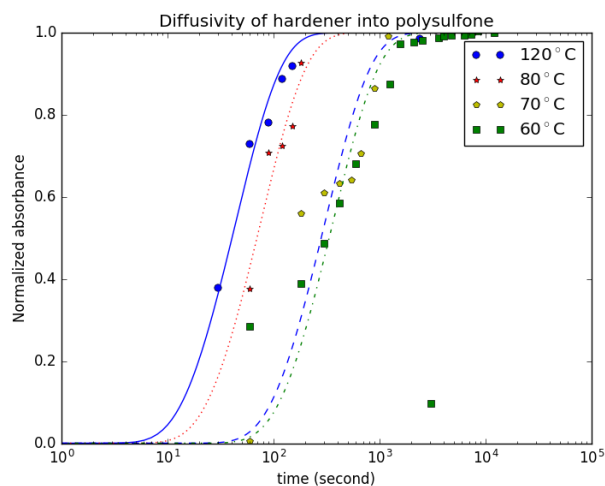


Fig.8 Diffusivity determination of hardener to PSU from 60°C to 120°C. Normalized absorbance data were obtained from ATR-FTIR experiments. Least square fitting curves were based on Eq.4 for each conditions.

4.5.2 Curing Kinetics of Epoxy System

In the ATR-FTIR experiment, the infrared element crystal disk was pre-heated to the desired processing temperature. The epoxy was premixed with the hardener and glass pipet was used to transfer the epoxy onto the crystal surface. The change of the 915 cm^{-1} and 1187 cm^{-1} peaks were monitored during the experiments. The processing temperatures used in the experiments were 80°C and 120°C.

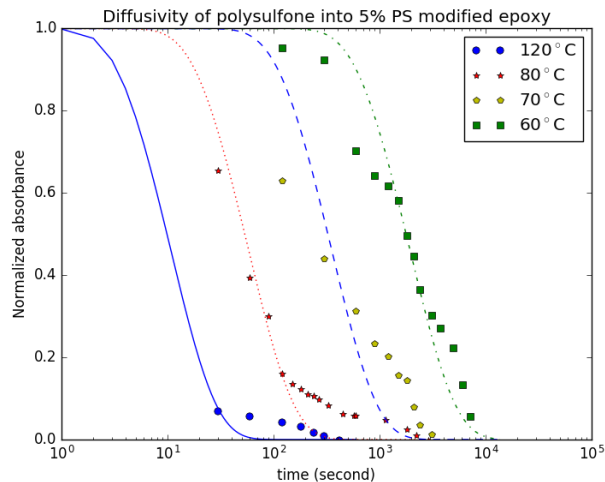


Fig.9 Diffusivity determination of PSU into 5% PS modified epoxy from 60°C to 120°C. Normalized absorbance data were obtained from ATR-FTIR experiments. Least square fitting curves were based on Eq.4 for each conditions.

Fig.10 shows the curing kinetics of epoxy with and without 5% PS additives cured at 80°C and 120°C. The y-axis represents the degree of cure, which is calculated based on the reduction of the uncured epoxy concentration measured in the experiment through monitoring 915 cm^{-1} peak. During the curing process, the epoxide ring opened, branched and crosslinked with the hardener and other open epoxide rings. Thus, the low molecular weight epoxy began to turn to high molecular weight molecules, which led to gelation and finally turned into solid cured epoxy. The increasing molecular weight and crosslinking epoxy reduced its mobility in the system and changed its solubility. Thus, the curing kinetics played an important role in the diffusion and precipitation process. In order to improve the diffusion and precipitation depth, the curing kinetics must be modified to make the diffusion and precipitation process longer. The low concentration of additive PS has shown the ability to reduce the curing reaction rate of the epoxy system without

significantly reducing the glass transition temperature and increasing viscosity of the epoxy, which corresponds to the high crosslinked density and feasibility of resin infusion by vacuum assisted resin transfer molding.

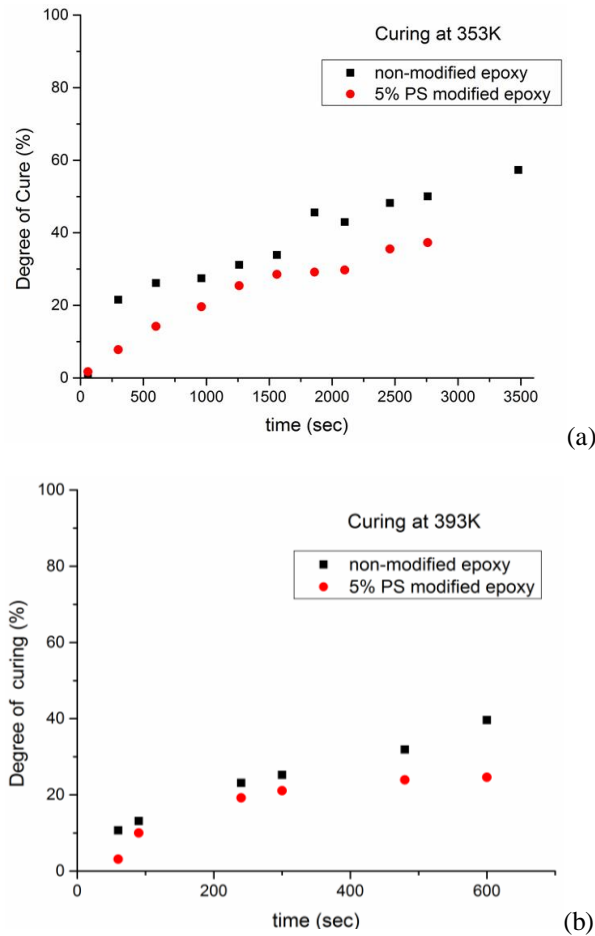


Fig.10 Degree of curing vs curing time of modified and non-modified epoxy curing at a) 80°C b) 120°C

From Fig. 10a, it shows the curing kinetics of non-modified epoxy and 5% PS modified epoxy cured at 80°C. Both trends increases gradually with the increasing curing time. However, the 5% PS modified epoxy showed less degree of cure at the same time compared to the non-modified epoxy. For example, when time reached 3000 seconds, the degree of cure of non-modified epoxy

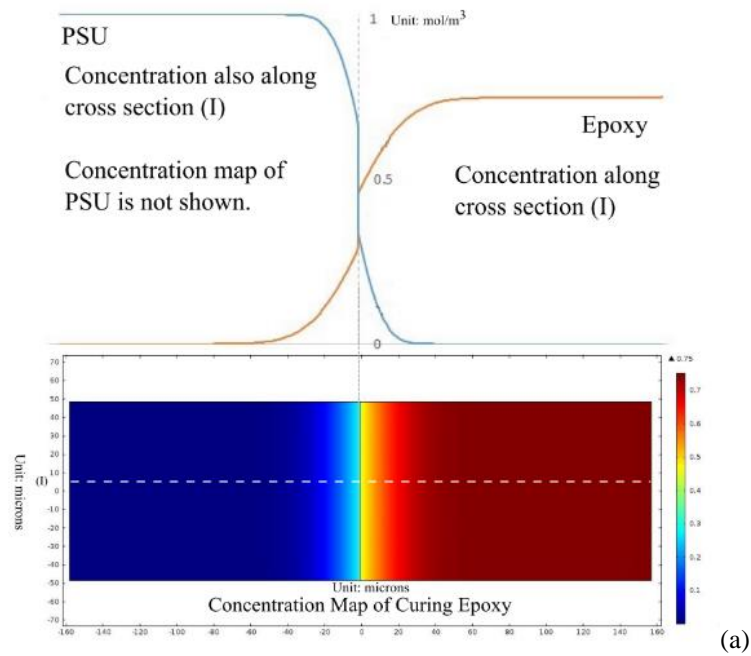
was above 50% but that of 5% PS modified epoxy only reached 35%. The experiment data was a strong evidence that with the PS additives, the curing reaction rate was reduced. This was mainly due to the dilute effect and non-chemical reactive PS to the curing epoxy. From Fig.10b, the curing temperature was risen to 120°C. Based on the Eq.8 and Eq.9, the reaction coefficient k_1 was 5.308×10^{-6} and k_2 was 0. At the elevated processing temperature, the curing reaction rate increased significantly. Compared to the case under 80°C, the degree of cure of non-modified epoxy reached to 40% in 600 seconds at 120°C but almost took 2000 seconds at 80°C. The degree of cure of 5% PS modified epoxy was also lower than that of the non-modified case and showed leveling off after 300 seconds. By using Eq.8 and Eq.9, the reaction coefficient k_1 was 1.647×10^{-5} and k_2 was 0.

4.5.3 Diffusion and Precipitation Process Simulation without Fibers

The geometry used in the simulation was a rectangular with 320 microns in length and 100 microns in width. At the initial stage, the right half was filled with epoxy and hardener with the concentration ratio of 0.75:0.25, and the left half was filled with PSU with the concentration of 1. The vertical line in the middle is the initial interface between PSU and curing epoxy. The upper and lower boundaries were set as no flux was able to pass through. The left boundary was set as a constant concentration of PSU as 1. The right boundary was set as a constant concentration of epoxy and hardener as 0.75 and 0.25. Since the diffusivities of curing epoxy was higher than that of PSU, the model used corresponding diffusivity for each species. The input diffusivities of the

epoxy, hardener, and PSU were obtained experimentally from FTIR, which were also coupled with the curing reaction as shown in Eq.13 and 14.

Fig.11 shows the diffusion and precipitation process simulation coupled with curing kinetics of 5% PS modified epoxy curing at 80°C and 120°C. The determination of the diffusion depth was to trace the concentration of the epoxy after the interface into the PSU-rich region and reduce to 1% of the initial value. The determination of the precipitation depth was based on tracing the concentration of the PSU into the epoxy-rich region and reducing to 1% of the initial value. Fig.



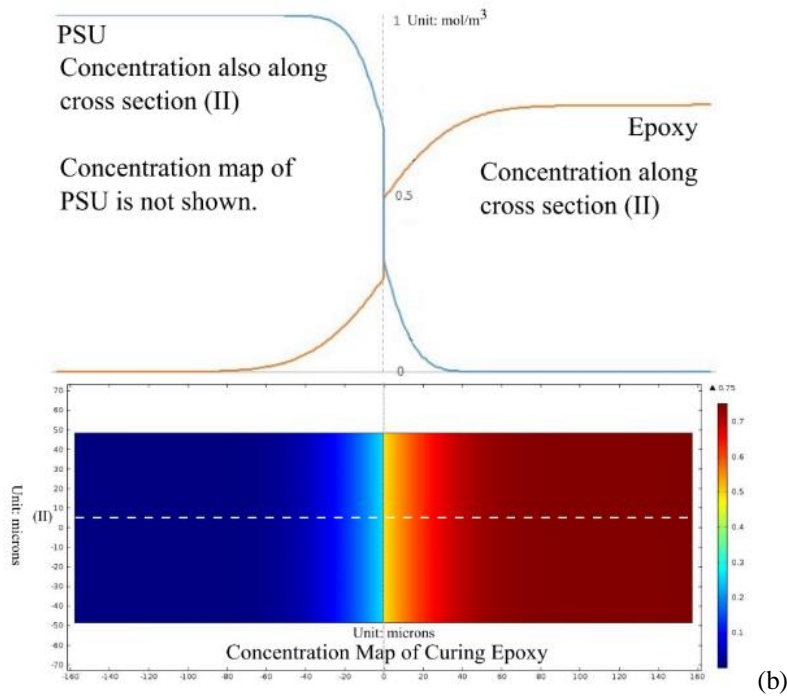


Fig.11 Diffusion and precipitation process simulation of the 5% PS modified epoxy cured at a) 80°C b) 120°C.

Concentration map of PSU is not shown. The line plots represent the concentration of epoxy and PSU along the dash line (I).

11a shows the concentration map of epoxy and PSU across the interface at 80°C. The diffusion depth was 61 microns and the precipitation depth was 32 microns. Fig.11b shows the concentration map of epoxy and PSU across the interface at 120°C. The diffusion depth was 109 microns and the precipitation was 42 microns. From the concentration along dashed line (I) and (II), there was drop of the concentrations in both cases at the interface. The reason was due to the limited mobility of the swollen TP. For example, the mechanism of PSU precipitating into epoxy-rich region was due to being swollen by the compatible curing epoxy molecules and chain relaxation. The interface was considered as the boundary of the swollen PSU and the generated retractive forces due the

swelling effect made the swollen region still consist of high concentration of the PSU [20]. However, due to the chain relaxation, part of the long chain was able to escape from the swollen region and flow into the epoxy-rich and be quickly distributed in it due to the increased mobility of PSU in the low molecular weight epoxy. As a result, the concentration of PSU had a drop across the interface. The optical observation was shown in the Part 1 of the paper [12]. Fig. 12 shows the EDX line scan across the interface of the specimens modified with 5% PS cured at 80°C and 120°C. The sulfur and the chloride was to represent the PSU and curing epoxy. The dashed lines were used to indicate the diffusion and precipitation region. The line profiles showed the same trends as in the simulation and the simulated diffusion and precipitation depths was in the same order of magnitude as those measured in the experiments.

Fig. 13 shows the diffusion and precipitation depth of the specimen modified with 5% PS obtained from the simulation and experiment. The experimental results were represented by the square and round dots with standard deviation bars on them and indicated that there were no observable diffusion and precipitation if the specimens were cured at room temperatures. When the curing temperature increased to 40°C and 60°C, it began to show slight diffusion and precipitation observed from optical microscopy. However, during this temperature range, the difference between diffusion depth and precipitation depth was not significant. The possible reason for this was that the diffusivities of each species at low curing temperature were small and the mobility of the molecules were limited. Thus, each species were not able to move deep into the other side and both precipitation depth and diffusion depth were small and close to each other. As the

temperatures rose above 80°C, the diffusion and precipitation region largely increased. The elevated curing temperatures influenced the increasing diffusivities of the species and the curing reaction rate. However, the change of curing reaction reaching to the same degree of curing from 80°C to 120°C was one order of magnitude as can be seen from Fig. 10, and the change of diffusivities of species from 80°C to 120°C was several orders of magnitude. This indicated that the high curing temperature influenced more on diffusivity than curing reaction rate, which made the species able to move much larger distances compared to the case under low curing temperatures, especially for the low molar weight curing epoxy. The simulation results showed trends close to the experiment results. The simulated diffusion depths were slightly larger than the diffusion depths observed in the experiment and the simulated precipitation depths were almost the same as the precipitation depths at the beginning but larger than those at the higher curing temperatures. Both simulated depth curves were at the same order of magnitude as the experimental results. The reason that the simulation results were slightly larger than the experiment results was that the cease of the diffusion and precipitation process was not exactly when the degree of curing reached 0.6, it was some point before 0.6 [13]. Thus, the time window for the diffusion and precipitation process to carry out was smaller than the time window used in the simulation, which led to the difference between the simulation results and experiment observations.

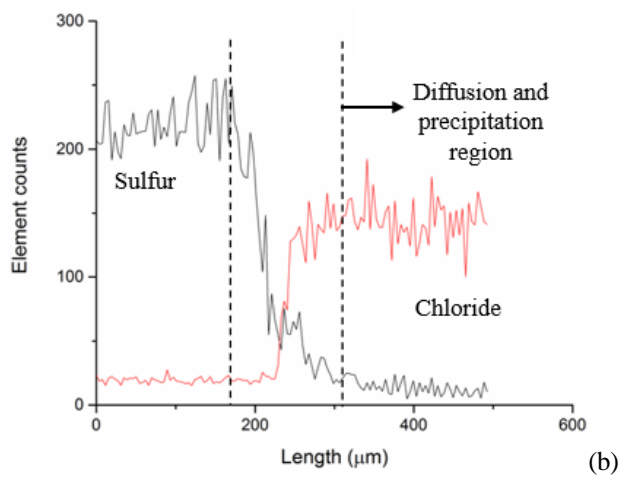
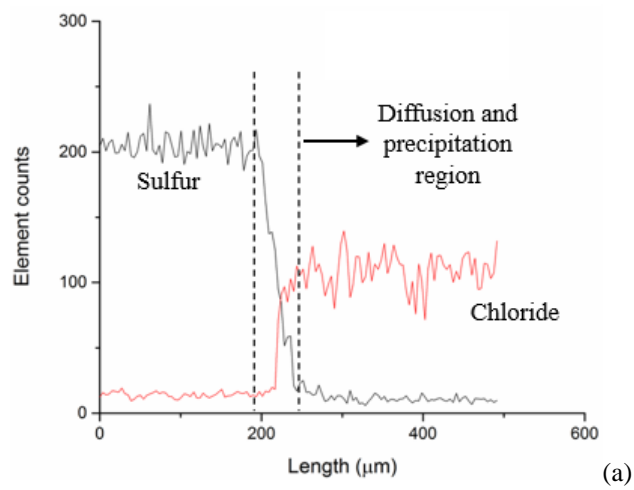


Fig.12 EDX line scan across the interface of 5% PS modified specimen without fibers cured at a) 80°C b) 120°C.

The dash lines represent the width of the diffusion and precipitation region.

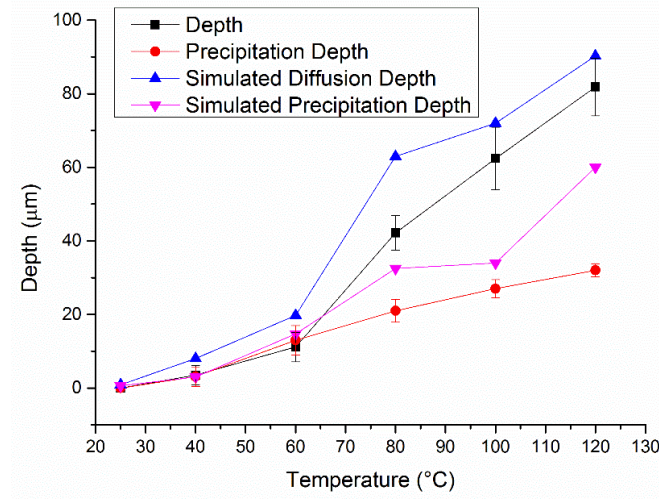


Fig.13 Diffusion and precipitation depth results from experiments and simulations from 25°C to 120°C. The error bars represent standard deviation.

4.5.4 Diffusion and Precipitation Process Including Fibers

In this case, the geometry was rectangular with the same size as that in the simulation without considering fibers. However, there were white circles in the epoxy-rich region, which represented the fiber beams. The diameter of the circles was 15 microns, which was the same as the actual size of one fiber beam. The surfaces of the fiber beams were set as impermeable for PSU, epoxy and hardener in both diffusion and precipitation directions in the simulation.

Fig. 14 shows the simulation results of the typical concentration profile of curing epoxy with fiber structures cured at 80°C. The corresponding concentration map of PSU was not shown here. Line (I) was the line met with the fiber beams at the first column. Line (II) was the line through the center of the geometry, which went through the small gap between the fiber beams at the first

column. The line plots of the epoxy and PSU concentration along line (I) and (II) were superimposed on the top and bottom of the concentration map. In the line plots, concentration of curing epoxy was constant high at the far field away from the interface and reduced to zero after passing through the interface. The corresponding concentration of PSU had the opposite trend compared to the curing epoxy. The gaps between the lines were indicated that these region were fiber beams, where there were no curing epoxy nor PSU. In the center line (II), both PSU and curing epoxy concentrations reduced sharply after the interface and the concentration drop at the interface was smaller compared to the simulation results without the existence of fibers. In the line (I), after the interface, due to existence of the fibers, the slope of the PSU concentration reduced and approved to zero before discontinued. The reason was that the fiber beams acted as obstacles and hedged the flow motion of the curing epoxy and PSU, which was shown in the magnified interface region.

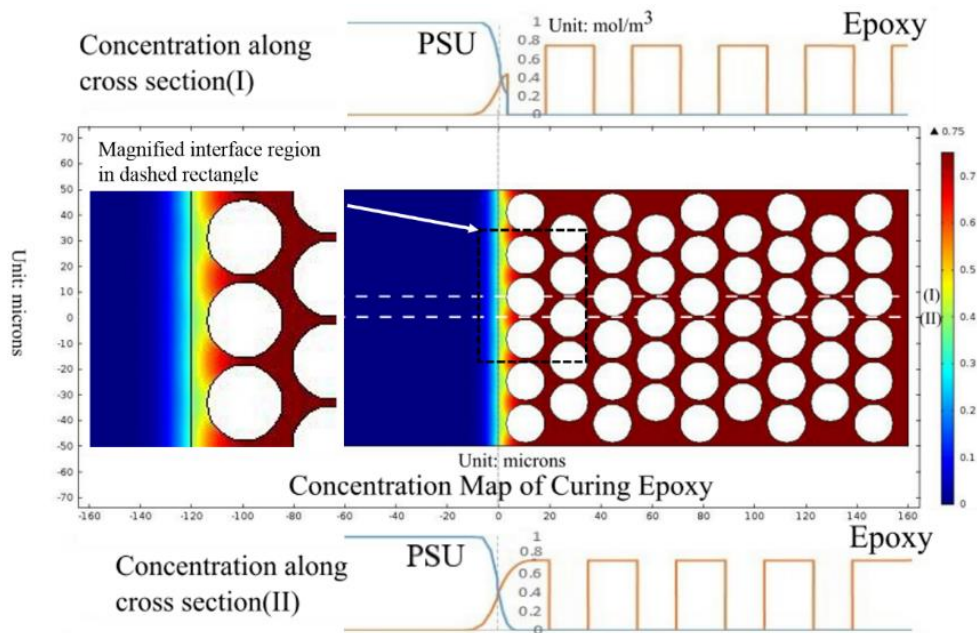


Fig.14 Diffusion and precipitation simulation of the 5% PS modified epoxy with fibers cured at 80°C. Concentration map of PSU is not shown. Line plots represents the concentration along line (I) and line (II) in the concentration map.

As a comparison, Fig.15 shows the simulation concentration map of curing epoxy and line plot of curing epoxy and PSU at 120°C. The corresponding concentration map of PSU was not shown here. The upper and lower line plots represented the concentration changes along line (I) and line (II). Compared to Fig. 14, at high curing temperature, the diffusion depth (the distance curing epoxy into PSU-rich region) and the precipitation depth (the distance PSU into epoxy-rich region) were both larger than those at 80°C. From the center line (II), the concentration changes in the fiber matrix were not uniform: the slope of the curing epoxy was almost flat at the tip of the first contacted fiber beam, increased and reduced again when reached the small gaps between the

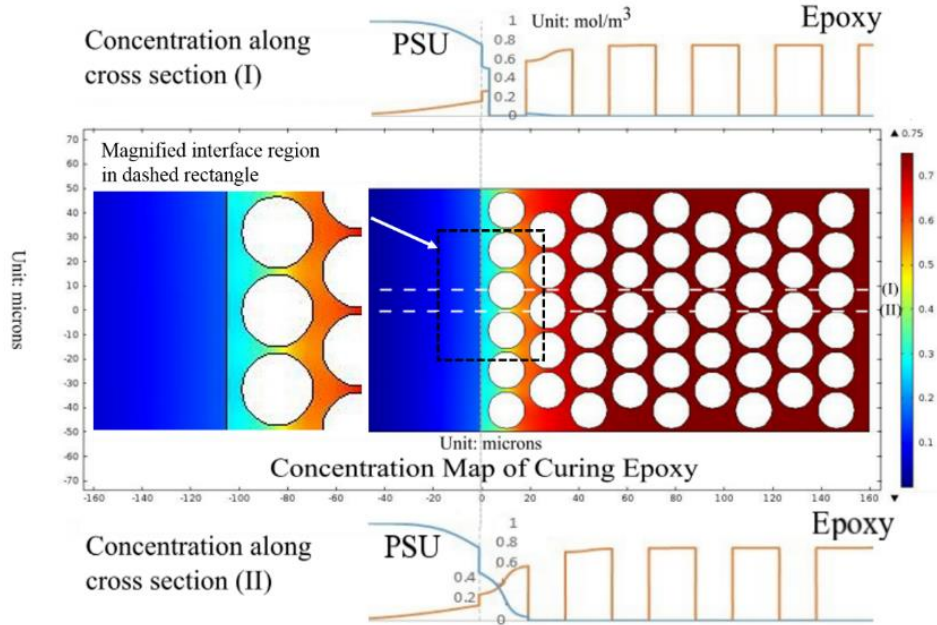


Fig.15 Diffusion and precipitation simulation of the 5% PS modified epoxy with fibers cured at 120°C. Concentration map of PSU is not shown. Line plots represents the concentration along line (I) and line (II) in the concentration map.

fibers. The precipitation depth in this case was less than three fiber beam diameters. From line (I), the existence of the fiber beams directly stopped the flow movement of the curing epoxy and PSU before the interface, which represented by the flat curve at the tip of the fiber. After first column of fiber beams, the concentration of PSU was zero, which indicated that the precipitation depth along this line was less than two fiber beam diameters. Both diffusion and precipitation depths were smaller than the case without fiber structures. However, as seen in the magnified interface region, due to the higher curing temperature, there were still significant diffusion and precipitation region.

Fig. 16 shows the EDX element mapping of 5% PS modified specimen cured at 120°C. The element mapping of sulfur (green), nitrogen (pink) and silicon (blue), which represent PSU, cured epoxy and fiber beams correspondingly. High density of PSU shows a concentration gradient starting from the middle to the right. The cured epoxy shows the opposite behavior to PSU. The uneven distributed low concentration PSU in fiber matrix indicated that only part of the PSU separated out from the unstable homogeneous solution during the late stage of the curing process. Other dissolved PSU entangled with the crosslinked epoxy and stayed homogenous as one phase. This evidence matched the optical microscopy observation shown in the part 1 of the paper [12] that there showed more epoxy diffusing into the PSU-rich region but only a few of PSU precipitates were found in the epoxy-rich region because other PSU did not separate from the solution during the phase separation process. As a comparison, Fig. 17 shows the EDX element mapping of 5% PS modified specimen cured at 80°C. Due to the low curing temperature, there was a sharp interface and limited diffusion and precipitation was observed.

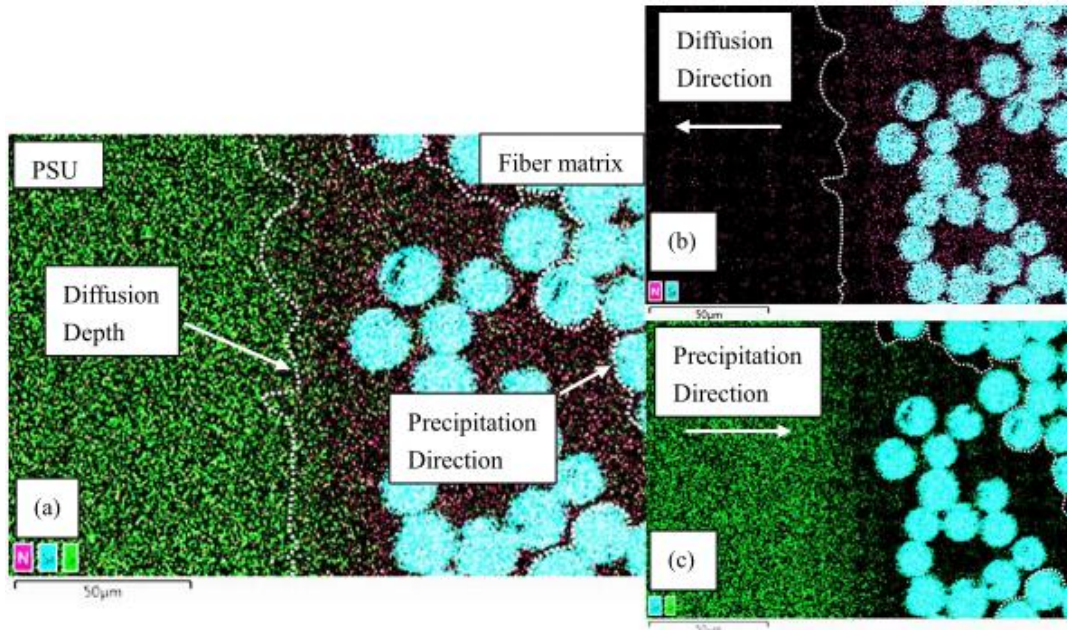


Fig.16 EDX element mapping of the 5% PS modified specimen cured at 120°C. Sulfur, nitrogen and silicon were traced to represent PSU, cured epoxy and fibers.

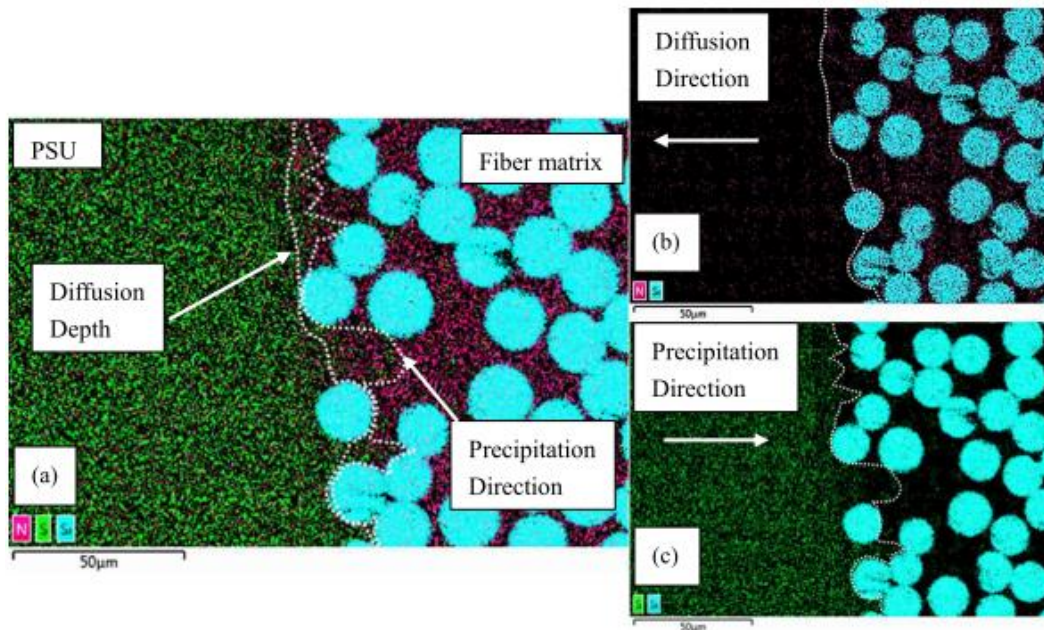


Fig.17 EDX element mapping of the 5% PS modified specimen cured at 80°C. Sulfur, nitrogen and silicon were traced to represent PSU, cured epoxy and fibers.

4.6 Conclusion

The diffusivities of curing epoxy and hardener into PSU were close, and both are higher than the diffusivities of PSU into epoxy or hardener due to the low molecular weight and high mobility of small molecules. Low concentration of PS additive did not influence the diffusivity of the epoxy. However, the PS modified epoxy showed reduced reaction rate compared to the non-modified epoxy, providing more time for diffusion and precipitation to happen and leading to deep semi-IPN. The diffusivity model coupled with curing kinetics simulation results captured the trends of diffusion and precipitation depths at various curing temperatures. The small gaps between the fiber beams generated large resistance for the TS and TP to pass through and hedged the movement of diffusion and precipitation. From both simulation and experiment results, 5% PS modified specimen cured at 120°C showed significant diffusion and precipitation region even with the existence of the fiber structures.

4.7 Acknowledgement

This research was supported by National Science Foundation under a GOALI award CMMI-1363328. Authors would also like to thank Ming Gao from Columbia University for providing us ATR-FTIR equipment.

Chapter 5: Interlaminar toughening of fiber reinforced polymers by synergistic modification of resin and fiber

5.1 Introduction

Many methods have been used to study and improve the delamination resistance of fiber reinforced polymers. However, the synergistic effect of modification methods was rarely investigated.

Many researchers tried to add two or more modifiers in the same epoxy system to overcome and compensate the loss of strength due to the ductile toughener. Caccavale et al. [1] studied the epoxy resin using polyamine hardener. In his study, 7.3 wt% rubber modification only partially compensated in its loss of strength by the addition of 3.7 wt% nanosilica but the toughness was still 6% lower than that of nonmodified epoxy system and the glass transition temperature was dropped by 19°C. Tsau et al. [2] studied the liquid reactive rubber acrylonitrile and used isophorone diamine as the hardener. The modulus of the unmodified system was lowered by 10 wt% of rubber from 3.25 GPa to 2.63 GPa, and the addition of 10 wt% nanosilica brought the modulus back up to 3.18 GPa. Gic was increased by 516% (1170J/m) but the hybrid system achieved only 930J/m, thus there was no synergistic effect. Sun et al. [3] studied SC-79 epoxy resin system and used nanosilica and alumina or carbon nanofibers as the third modifier. The modulus of the matrix improved by 40% with 10 wt% nanosilica, however, alumina or carbon nanofibers showed no further improvements. Carboxy-terminated polyurethane-co-polyether block copolymer was also used as an elastomer toughener with nanosilica. It showed that 9 wt% elastomer and 9 wt% nanosilica was the best mixture but there was no synergistic effect of the two modifiers [4]. In

another study, amino-functional reactive liquid rubbers showed synergistic improvement. The long flexible rubber molecules randomly crosslinked into polymer matrix was concluded as the major reason causing the toughening [5, 6]. Core-shell elastomers was another widely studied modifier used to toughen the epoxy matrix, but the Core-shell hybrid system with nanosilica indicated the behavior is not synergistic effect [7-9]. The main disadvantages of this method were the reduced strength and modulus due to rubber molecules and lower glass transition temperature of the cured epoxy system resulting from low crosslinking density. The results indicated that physical or chemical interaction between different modifiers must exist to potentially obtain the synergistic effect.

Besides using additive modifiers, other researchers attempted to find methods to toughen the resins through chemical bonding process. Rajasekaran et al. [10] chemically grafted POSS and tetraethylenepentamine onto the carbon fibers and studied the interfacial properties and impact toughness of methylphenylsilicone resin composites. Wu et al. [11] used amino end-capped aromatic liquid crystalline copolyesteramide to react with the epoxy group. Alessi et al. used hydroxyl terminated polyethersulfone on the epoxy system [12]; Mutua et al. used bismaleimides modified polysulfone to react and dissolve in the epoxy matrices [13]; Perez et al. proposed a method to produce polysulfone with amino group, which can react with the epoxy [14]. However, the increased viscosity makes it difficult to use in the vacuum assist resin transfer molding and the strong oxidant treatment may influence the mechanical behavior.

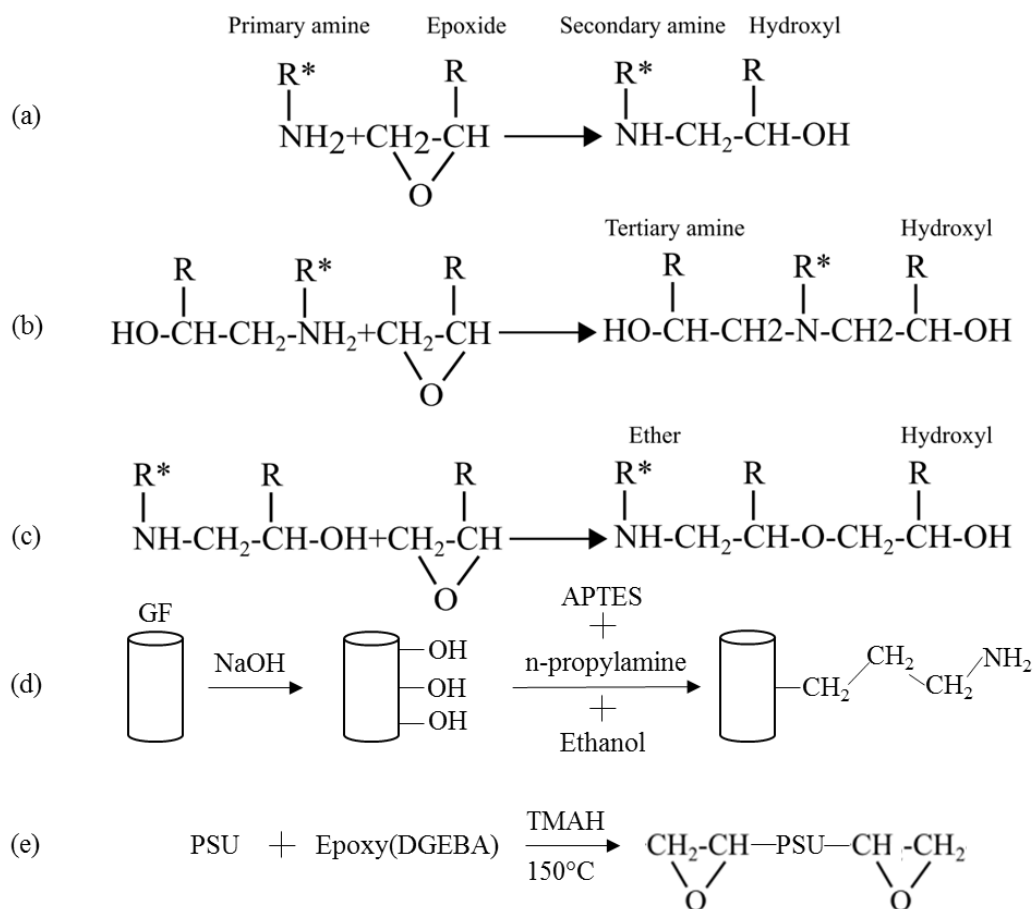


Fig.1 Chemical reactions in epoxy curing [17] and modification process [10] [13]. a) Primary amine from hardener has open-ring reaction with epoxide group from epoxy and generates secondary amine. b) Secondary amine reacts with the epoxide group. c) Etherification reaction. d) Amino-group grafting onto glass fiber surface. e) Epoxide group end-capped PSU.

From the previous study, PSU has shown compatibility with the epoxy [15-16]. In this study, an interactive modification method is used to obtain the synergistic effect. Epoxide end-capped PSU is dissolved in the epoxy to chemically react with the amine hardener and the amino group which is grafted on the fiber surface. Consequently, PSU is able to chemically bond to the crosslinked epoxy structure and fiber surface, which compensates the reduction of the glass transition temperature of the epoxy. At the same time, due to the compatibility of the PSU to the

epoxy, the long chain of the thermoplastic is deeply entangled with the crosslinked epoxy, which results in the improved matrix toughness; the veil-shaped amino-functionalized fiber surface increases the contact area with the curing epoxy and generates the micromechanical interlocks and strong chemical bonding to the epoxy, which further lead to improved interfacial strength.

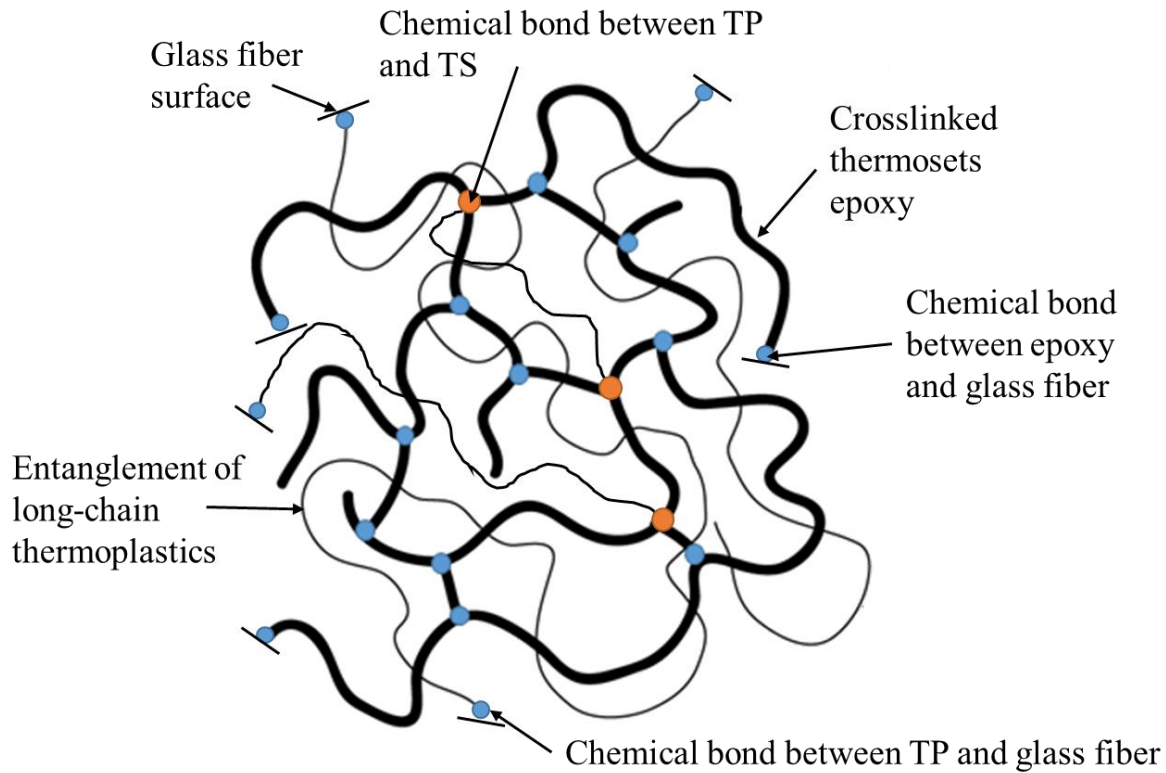


Fig. 2 Bonding in the cured epoxy matrix. The physical bonding here is due to the entanglement of long-chain thermoplastics with the crosslinked thermosets epoxy, which is known as semi-interpenetration network. The chemical bonding due to the modifications are among glass fiber surface to PSU, glass fiber surface to curing epoxy, and PSU to curing epoxy.

5.2 Background

5.2.1 Chemical reactions between curing epoxy, polysulfone and glass fiber

The proposed modification method includes both chemical and physical bonding in the epoxy system. In order to understand what factors lead to the synergistic effect, the chemical reaction

process in the epoxy system should be clearly explained first. In this study, chemical reactions mostly occur in the curing epoxy, epoxide end-capped PSU and amino group functionalized fiber surface. Fig. 1 shows the chemical reactions and modifications in this study. Fig. 1a, b and c represent the curing reactions in the epoxy system [17]: the primary amine from the curing agent opens the epoxide rings and forms a chemical bond between the carbon and amine nitrogen, leading to the secondary amine and hydroxyl group; the secondary amine repeats the epoxide ring opening reaction and forms tertiary amine and hydroxyl group; the hydroxyl groups can also react with the unreacted epoxy ring. The repetition of these three chemical reactions leads to the crosslinked network structures. The glass fiber (GF) surface is chemically treated in order to graft the amino functional group on the surface. Sodium hydroxide (NaOH) solution is first used to generate hydroxyl groups on the fiber surface, then with the help of (3-aminopropyl) triethoxysilane (APTES) and n-propylamine in the ethanol solution, the amino functional groups replace the hydroxyl groups [13]. PSU is known as a thermoplastic compatible with the epoxy system, which means the epoxy monomers can swell the PSU [10]. Thus, with a tetramethylammonium catalyst, PSU can dissolve into the epoxy solution at high temperature, and the two ends of the PSU long chain are capped with the epoxide ring groups. The proposed chemical modification methods lead to the interactions among the PSU, glass fiber and epoxy system through the bond formation between epoxide ring to amino function groups. The generated chemical bonds not only improve the semi-interpenetration networks between thermoplastics and thermosets but also enhance the interface strength between glass fiber and matrix materials, which are expected to compensate for the reduction of the crosslinked density due to the additive and to

further improve toughness and interface strength.

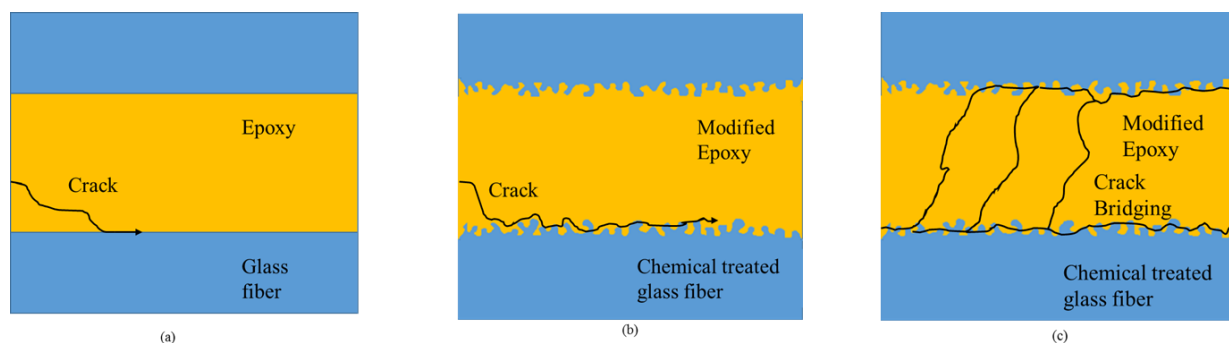


Fig. 3 Schematic of crack propagation between glass fiber surface and cured epoxy under different conditions. (a) With no modifications, the crack lies on the interface between non-treated glass fiber surface and epoxy. Weak intermolecular forces are the only major factors holding two materials together. (b) Under Mode I fracture, the crack propagates through the interface between chemical treated glass fiber and modified epoxy. The surface of treated glass fiber becomes rough. The increased contact area not only improves the adhesion strength but also generates micromechanical interlocks. (c) Under Mode II fracture, the crack propagates through the interlaminar region with crack bridging phenomenon.

5.2.2 Potential synergistic effect

With the previous chemical modifications, the fibers, PSU and epoxy can generate strong bonding among one another. Furthermore, the potential synergistic effect may exist due to of the interaction between individual modification methods.

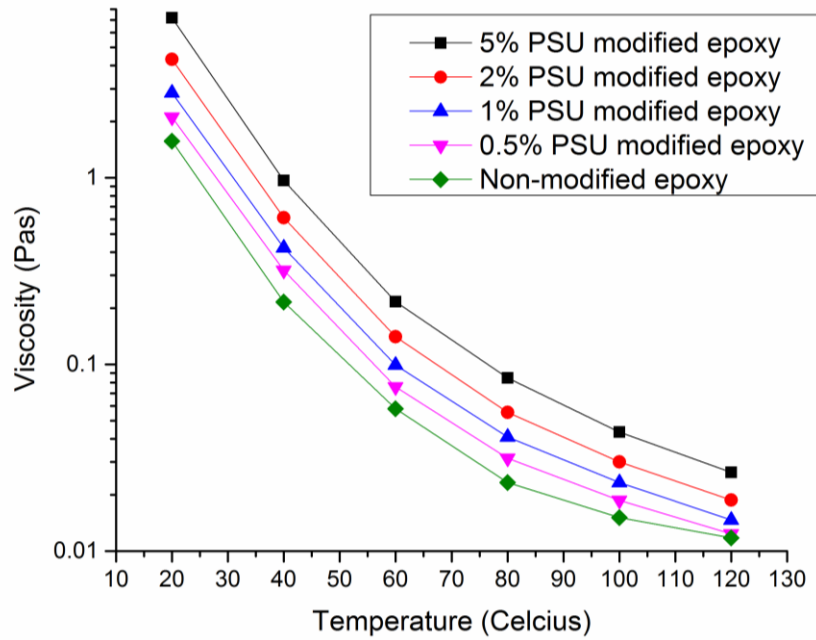
The first potential synergistic effect may be induced by the epoxide end-capped PSU. With the help of the tetramethylammonium hydroxide (TMAH) and high temperatures, PSU is grafted with epoxide ring groups, which are chemically reactive with the amino groups in curing agent and on the surface of glass fiber. Thus, strong chemical bond forms to link these three species. Besides this chemical bond, since the PSU is also a compatible thermoplastic to the epoxy, it creates semi-interpenetration networks with cured epoxy as shown in Fig. 2, which means the long

chain thermoplastic molecules entangle into the crosslinked thermoset epoxy networks. This physical bonding is considered as a strong bonding. In our case, the entangled thermoplastic PSU molecules are also able to form the strong chemical bond in the crosslinked networks and connect to the glass fiber surface. This kind of modified semi-interpenetration network is expected to have high toughness without losing the crosslinking density and strong interface strength between network to glass fiber leads to high load transfer capability.

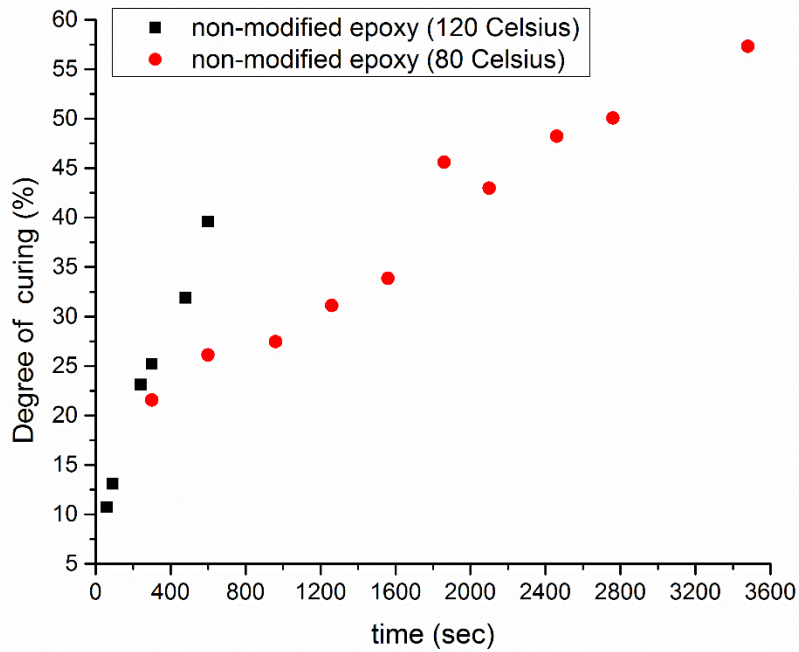
Second potential synergistic effect may be induced by the functionalized glass fiber. As described in the previous section, the amino function groups are grafted onto the glass fiber surface through the hydroxyl replacement reactions, which make the glass fiber able to bond into the crosslinked networks, generating the bonding between amino groups and epoxide group from both modified PSU and epoxy. Besides this consequence, the strong oxidant NaOH solution also generates a micron-size rough surface on the glass fiber. The original glass fiber surface is clean and smooth, as shown in Fig. 3a. In this case, the forces holding fiber and epoxy together are mainly the weak intermolecular forces. Compared to the non-modified case, after oxidization, the rough surface works as mechanical interlocks to further improve the interface bonding as shown in Fig. 3b.

Fracture mechanism in the laminate structure also influences the synergy of different modifications. The delamination in the laminate structures always starts in the interlaminar region near the interface between fiber matrix and interlaminar epoxy resin, since the epoxy is weaker than the fiber matrix. When the crack initiates, it generates a crack tip yield zone ahead of the crack tip, where the material yields and undergoes plastic deformation, and the crack tends to propagate

to the weakest region within the yield zone. The size of the crack tip yield zone is typically one to several hundred microns in epoxy [18], which is almost always larger than the interlaminar thickness in real applications since the weak interlaminar region is reduced as much as possible. Thus, the crack is considered to always approach the interface between epoxy resin and fiber matrix as shown in Fig. 3. In Mode I fracture, shown in Fig. 3a, the interface between glass fiber and the epoxy is only due to the intermolecular forces in the case without any modifications. The smooth interface is a weak region in the structure and when crack propagates, it essentially grows along the weak interface. By comparison, as shown in Fig. 3b, the rough glass fiber surface will generate more resistance for the crack to propagate, and the formation of chemical bond between glass fiber and modified epoxy (not shown in the figure) also consumes more fracture energy because the crack needs to break both the ductile thermoplastic and brittle thermosets, which would not happen if individual modification method is used. In the case of Mode II fracture, the crack will undergo a crack bridging phenomenon, in which the crack will jump through the upper and bottom interface by passing the interlaminar region (Fig.3c). In this case, more modified epoxy will participate in plastic deformation compared to the case with Mode I fracture.



(a)



(b)

Fig.4 (a) Viscosity for epoxy with various concentrations of modified PSU from room temperature to 120°C. (b) Curing kinetics of neat epoxy under 80 and 120°C.

5.3 Numerical simulation

The way in which crack propagates through the interlaminar region is considered the major

contribution to the delamination resistance in both Mode I and II fracture as described in the previous section. A numerical method is proposed to simulate the crack growth in the interlaminar region to predict the crack propagation and to investigate the effect of the modifications to the interface and interlaminar regions.

5.3.1 Simulating crack growth in composites using XFEM

The conventional ways to simulate the crack growth in the composites are using cohesive zone model (CZM) [19] or virtual crack closure technique (VCCT) [20]. The limitation of these two modelling methods are the pre-defined crack path: the propagation of the crack location is considered as known and the crack is only able to propagate along this path. The extended finite element method (XFEM) is developed to overcome this limitation by enriching the shape function with additional displacement functions according to the partition of unity [21]:

$$\mathbf{u} = \sum_{I=1}^N N_I(x) [u_I + H(x)a_I + \sum_{\alpha=1}^4 F_{\alpha}(x)b_I^{\alpha}] \quad (1)$$

Where \mathbf{u} is the displacement vector; $N_I(x)$ is the usual nodal shape functions; the first term on the right-hand side of the above equation, u_I , is the usual nodal displacement vector associated with the continuous part of the finite element solution; the second term is the product of the nodal enriched degree of freedom vector a_I , and the associated discontinuous jump function $H(x)$ across the crack surfaces; and the third term is the product of the nodal enriched degree of freedom vector, b_I^{α} , and the associated elastic asymptotic crack-tip functions, $F_{\alpha}(x)$ [22]. The XFEM does not require the mesh to match the geometry of discontinuity, thus the crack propagation and initiation along arbitrary path can be more realistically simulated.

In order to simulate a moving crack, a traction-separation behavior of the crack model is used

[23]:

$$\mathbf{t} = \begin{Bmatrix} t_n \\ t_s \end{Bmatrix} = \begin{bmatrix} K_{nn} & 0 \\ 0 & K_{ss} \end{bmatrix} \begin{Bmatrix} \delta_n \\ \delta_s \end{Bmatrix} = K \delta \quad (2)$$

Where \mathbf{t} is the traction stress vector in normal direction (n) and shear direction (s), δ is the corresponding separation in normal and shear directions; K is the stiffness of the enriched element.

The crack propagation direction is determined by J-integral around the crack tip [24]:

$$J = \lim_{\Gamma \rightarrow 0} \int_{\Gamma} \mathbf{n} \cdot \left(W \mathbf{I} - \sigma \frac{d\mathbf{u}}{dx} \right) \cdot \mathbf{q} d\Gamma \quad (3)$$

Where Γ is the contour around crack tip, \mathbf{n} is normal to the contour, \mathbf{q} is the unit vector of virtual displacement direction of the crack and W is elastic and plastic strain energy, \mathbf{I} is identity tensor, σ is stress field related to stress intensity factor and yield zone functions for loaded crack, and \mathbf{u} is displacement. J represents the rate of change of net potential energy with respect to crack advance and a measure of the singularity strength at the crack tip for the case of elastic-plastic material response. The value of J around the crack tip indicates the difficulty level, at which the crack propagates in that direction, meaning the crack prefers to propagate in the direction where less energy is required to generate a new crack surface [24]. J integral is assumed to use in small scale yielding in elastic-plastic materials, which means the load level is sufficiently small so that the yield zone forms near the tip is small compared to the crack length [25].

5.3.2 Interface modeling

From previous section, the crack is likely to propagate near the interface between interlaminar and fiber matrix regions. Therefore, the way to model the region near this interface becomes important. The geometry of the model is treated as one body with different regions on it. The epoxy resin in the interlaminar region is considered as isotropic materials, the material properties are

collected and modified according to the concentration of PSU [26]. The fiber matrix region is treated as anisotropic material since its material properties are dependent on the orientation of the fibers. The material properties of unidirectional fiber matrix used in this study are obtained and modified from the literature [27]. The micromechanical interlocks and formed chemical bonding on the fiber surface are treated as two exceedingly thin layers between fiber matrix and interlaminar epoxy resin, of which the thickness is chosen based on the experiment observation in a later section. The critical energy release rate of the interface region and epoxy resin for fracture criteria is determined experimentally from Mode I and II tests, because the formed chemical bonding on the fiber surface is the same as the one in the epoxy thermosets.

5.4 Experiment materials and procedures

The fiber fabric is Saertax unidirectional fiber preform. The epoxy resin is purchased from EPOKOTE Resin MGS RIMR 135, of which the major component is bisphenol A diglycidyl ether (DEGBA). The hardener is EPIKURE curing agent MGS RIMH 137. The 0~5 wt% polysulfone (Udel 1700) is dissolved in epoxy at 140°C with TMAH (Sigma-Aldrich) catalyst for 2 hours to generate a homogeneous solution and to form epoxide end-capped polysulfone [10]. 0.5 mol/L NaOH (Sigma-Aldrich) aqueous solution is prepared and fiber fabric is submerged into the solution at 60°C for 1 hour to generate hydroxyl group. APTES (Sigma-Aldrich) in 200ml ethanol with 0.2g n-propylamine (Sigma-Aldrich) catalyst solution is to replace the hydroxyl group by amino group [13]. The specimens were produced by vacuum assisted resin transfer molding (VARTM). A Teflon sheet is inserted as a pre-crack. The VARTM produced glass FRP panel is cut and trimmed to the Mode I and Mode II specimens according to ASTM D5528 and ASTM D7905

test methods. The viscosity of the modified epoxy is measured by Haake Mars III Rheometer from room temperature to 120°C. Netzsch STA 449 F3 Jupiter TGA-DSC is used to determine the change of glass transition temperature of the specimens under different modifications. Renishaw inVia Raman microscopy is used to characterize the formation of functionalized groups on the glass fiber surface. Instron 5569A mechanical testing machine is used to perform mode I and end notched flexure test. Zeiss Scanning Electron Microscopy is used to examine the morphology and fracture surface.

5.5 Results and discussion

5.5.1 Viscosity behavior of the epoxy system

Viscosity changes due to the modification were examined from room temperature to 120°C with the concentration of PSU from 0 to 5 wt% (Fig. 4a). The diamond symbols represented the non-modified epoxy, showing that the epoxy with a viscosity of 1.571 Pas was considered as a reference value that the viscosity of the epoxy was not too high to infuse into the fiber fabrics. With increasing concentration of PSU in the modified epoxy, at 20°C the viscosity of the modified epoxy significantly increased from 1.57 to 7.2 Pas. This result indicated that the modified epoxy may not be suitable for resin infusion method at room temperature. Fig. 4b showed the curing kinetics of the epoxy under 80 and 120°C. Under high curing temperature, the curing process was much faster than that at low temperature. Thus, it is important to study the viscosity behavior of the curing epoxy. The viscosity rose significantly with increasing degree of curing. The degree of curing influences the viscosity of the curing epoxy [28]

$$\alpha = mK(T)\ln\left(\frac{\eta-\eta_0}{\eta_0}\right) \quad (4)$$

α is the degree of curing, m is the coefficient, $K(T)$ is the reaction rate coefficient shown in Eq. 5, η is the current viscosity, η_0 is the initial viscosity [28]

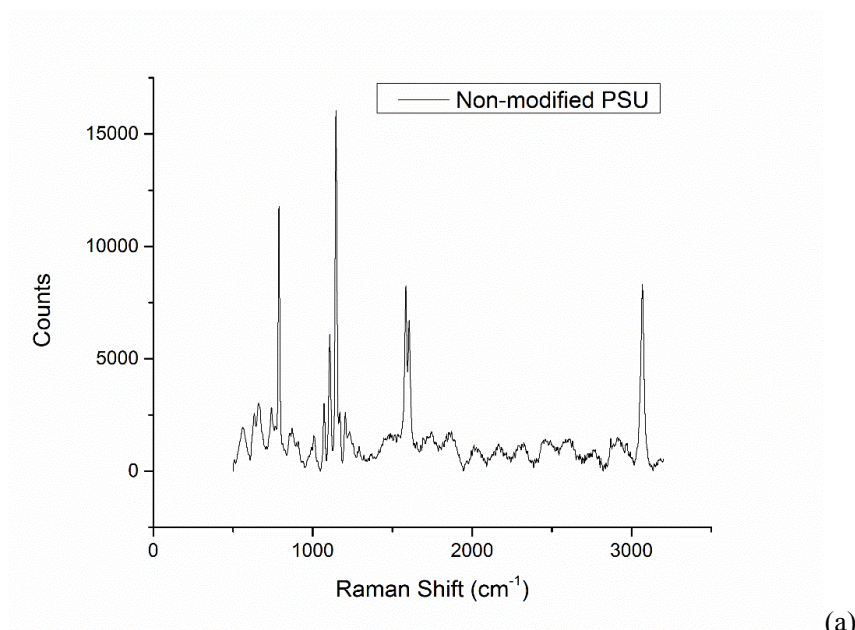
$$K(T) = K_0 \exp\left(-\frac{E_o}{RT}\right) \quad (5)$$

E_o is the activation energy related to K , R is the constant.

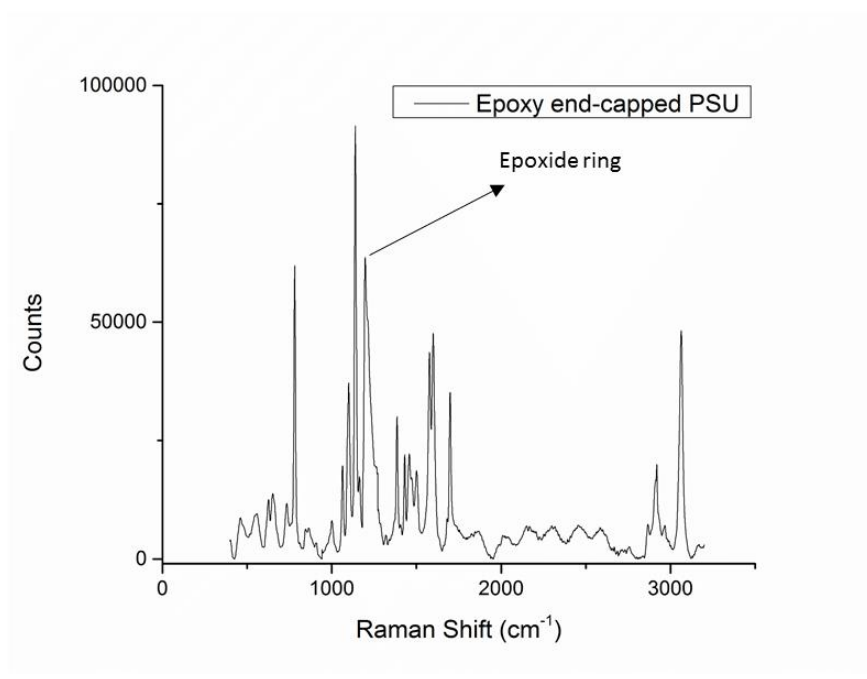
The curing process was assumed to follow the 1st order kinetics law. By fitting the data from two different temperatures, the following constants were obtained: $K_0=46.94$ [1/sec] and $E_o=35.73$ [kJ/mol] and $mK(120^\circ\text{C}) \approx 0.082$. Considering the reference as neat epoxy, if epoxy cannot flow when viscosity is higher than 1.57118, at 120°C , then the neat epoxy would take around 10 mins to reach this viscosity and the degree of curing is 0.41. On the other hand, the PSU modified epoxy would only take less than 4.5mins to finish the infusion. Thus, the proposed toughening method could apply in the resin transfer molding [15, 16].

5.5.2 Chemical and morphology determination of modified epoxy system

Fig. 5 showed the Raman spectra of PSU before and after TMAH treatment. Fig. 5a showed the non-modified PSU spectra, and some typical peaks represent the specific chemical structures in the polymer. 788 cm^{-1} is C-H deformation and was used to measure the PSU concentration; 1073 and 1108.3 cm^{-1} are attributed to symmetric and antisymmetric SO_2 stretching; 1148 cm^{-1} is C-O-C asymmetric vibration; 1587 and 1606 cm^{-1} represent phenyl ring vibration; 3070 cm^{-1} is C-H vibration; 790 , 1140 , 1580 and 3065 cm^{-1} correlate to the asymmetric C-S-C, asymmetric C-O-C vibration, aromatic ring chain vibrations, and C-H vibration. [29-30]. Fig. 5b showed the PSU after the chemical treatment. The new peak appeared around 1240 cm^{-1} and is the evidence



(a)



(b)

Fig. 5 Raman spectroscopy for (a) PSU and (b) Epoxide end-capped PSU. The new peak appeared $\sim 1240 \text{ cm}^{-1}$ was the evidence of the epoxide ring grafting onto the polymer chain

of the epoxide ring grafting onto the polymer chain; 1112 and 1186 cm^{-1} associated with phenyl and gem-dimethyl resin backbone vibration, do not change, and use as reference [31-32]. Fig. 6

showed the Raman spectra of glass fiber before and after APTES treatment. Fig. 6a showed the spectra of original glass fiber. The broad Raman bands at around 500, 604, and 810 cm^{-1} originate from the SiO_2 support. Several samples exhibit broad bands at around 1077 cm^{-1} which are characteristic of $\text{Si}(-\text{O}-)_2$ and $\text{Si}-\text{O}-$ functionalities. 487 cm^{-1} and around 800 cm^{-1} represent the Si-O-Si stretching, around 1060 cm^{-1} is the longitudinal optical stretching of the silica network [33]. Fig. 6b showed the spectra after the chemical treatment. The rising peak around 996 cm^{-1} is attributed to the vibration of the aromatic ring carrying the amine group in m-position [34], which indicated the grafting of amino functional group on the fiber surface. As described in the previous section, the amino group was expected to react with the epoxide group and form the bond between carbon and nitrogen, of which the bond energy is from 276 to 615 kJ/mol. As comparison, for the intermolecular forces, for example, of hydrogen bond, the bond energy is from 6-30 kJ/mol. Thus, the formed bonds were strong covalent bonding.

The surface morphology of glass fiber was also examined before and after the chemical treatment. From Fig. 7a, it showed the original glass fiber before the chemical treatment. The surface was clean and smooth. As a comparison, Fig. 7b showed the glass fiber surface changed to a thin layer of spongy veil. The high magnification image (Fig. 7c) showed that the chemical treatment made the glass fiber surface covered with veil-shaped residues. As known from the Raman spectra results, the treated glass fiber surface was formed amino groups and they were detected from this rough and veil-shape surface. The rough and chemically active surface was expected to improve the interfacial strength by increasing the contact area between the glass fiber and epoxy, generating the mechanical interlocks. The amino functional groups grafted on the glass

fiber were also chemically active with the epoxide groups in the epoxy and modified PSU, which simultaneously made the glass fiber chemically bond to the matrix.

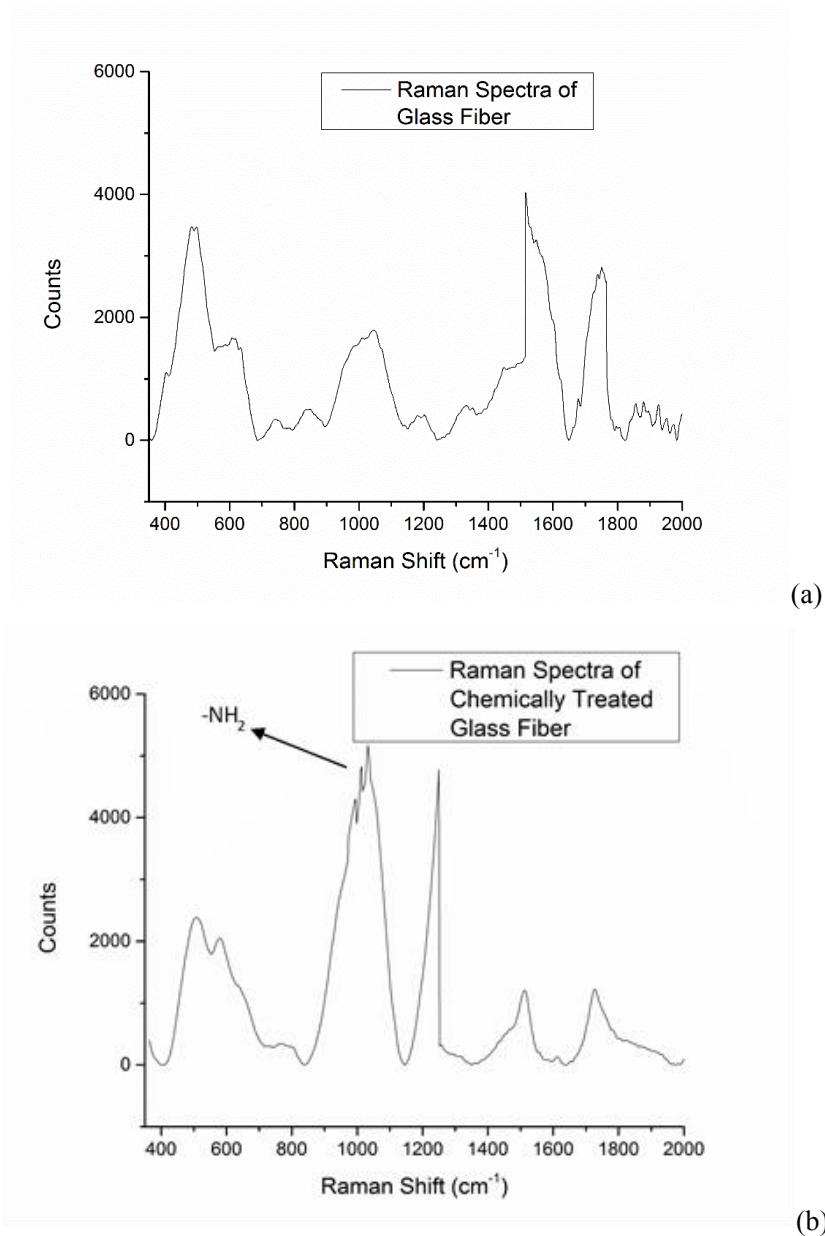


Fig. 6 Raman spectroscopy for (a) non-modified glass fiber surface and (b) chemically treated glass fiber surface. The peak appeared $\sim 995 \text{ cm}^{-1}$ is the evidence of the amino functionality group.

5.5.3 Glass transition temperatures of the epoxy system

The glass transition temperature was an important property of a thermosetting polymer system because it represents the crosslinking density, which influences the mechanical behavior of the cured epoxy system. Generally, with the existence of the additives, the degree of cure is limited and the crosslinking density is lower due to the incomplete formation of crosslinking networks. In this paper, the epoxide end-capped PSU was the additive to the epoxy system. Fig. 8 showed the glass transition temperatures of cured epoxy with different concentrations of modified PSU. The trend increased with PSU concentration before leveled off. The additive normally reduces the glass transition temperature; however, in this study the glass transition temperatures of cured epoxy with 0-5wt% modified PSU were higher than that of the cured epoxy with no additive. The main reason was that the covalent bonds formed between the epoxide ring from the modified PSU to the curing agent made the additive chemically bond to the epoxy network during the curing. The chemical bonding between the additives and the epoxy limited the movement of molecule chains, the bonding also compensated for the influence of enlarged free volume by PSU which provided more space for polymer chain to move at low temperature [35]. With the increasing concentration of modified PSU, the trend started to level off, which indicated that the advantage of bonding between additives and epoxy can only compensate the negative effect at low concentration. It was believed that if the concentration of modified PSU kept increasing, the glass transition of cured epoxy would be lower.

5.5.4 Phase separation of PSU in the cured epoxy system

The modified PSU was able to dissolve in the uncured epoxy before mixing with the curing agent because of the high compatibility between PSU and epoxy at elevated temperatures. The

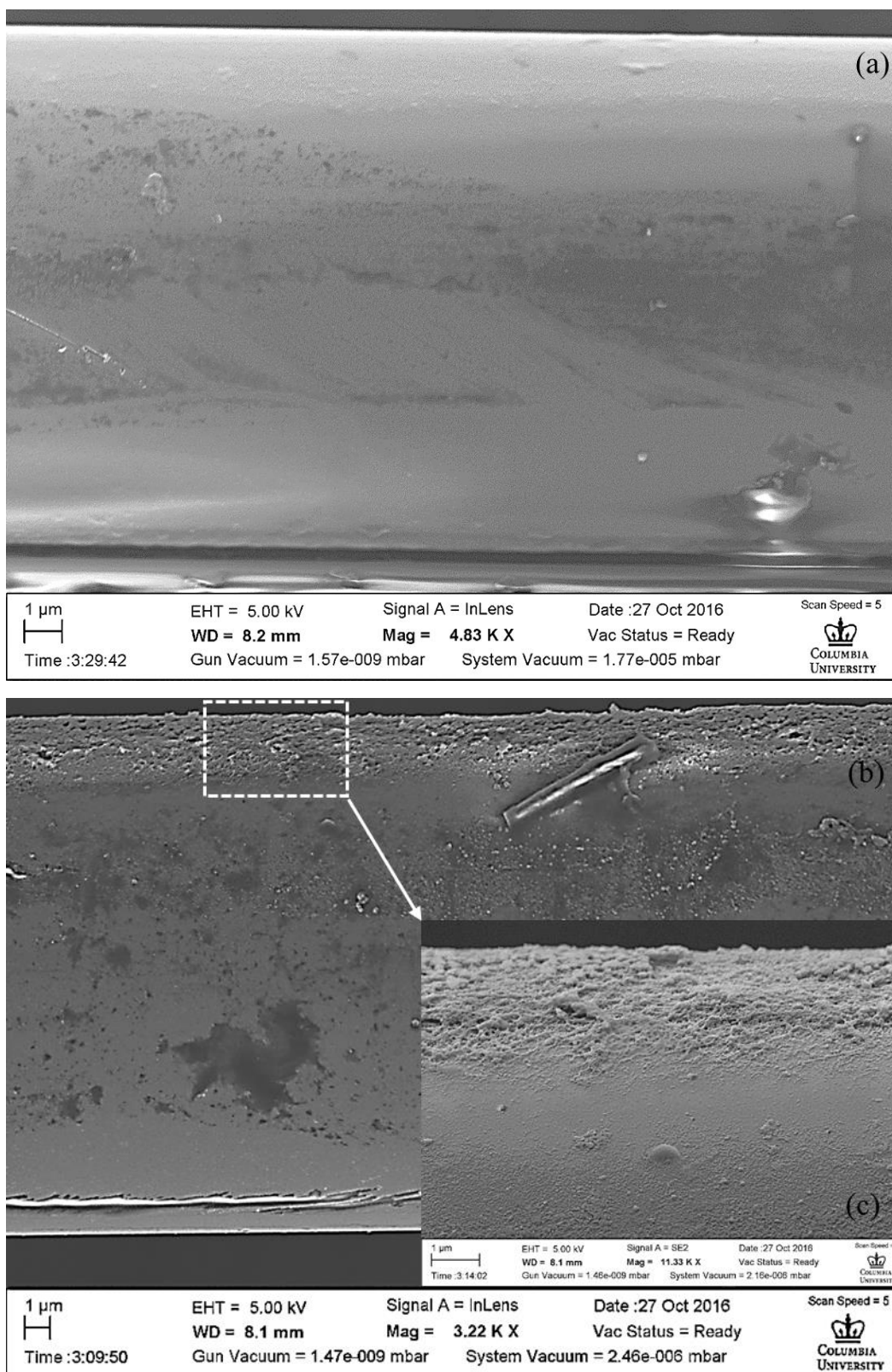


Fig. 7 SEM images of glass fiber surface morphology (a) before chemical treatment, (b) after chemical treatment, and (c) after chemical treatment at high magnification

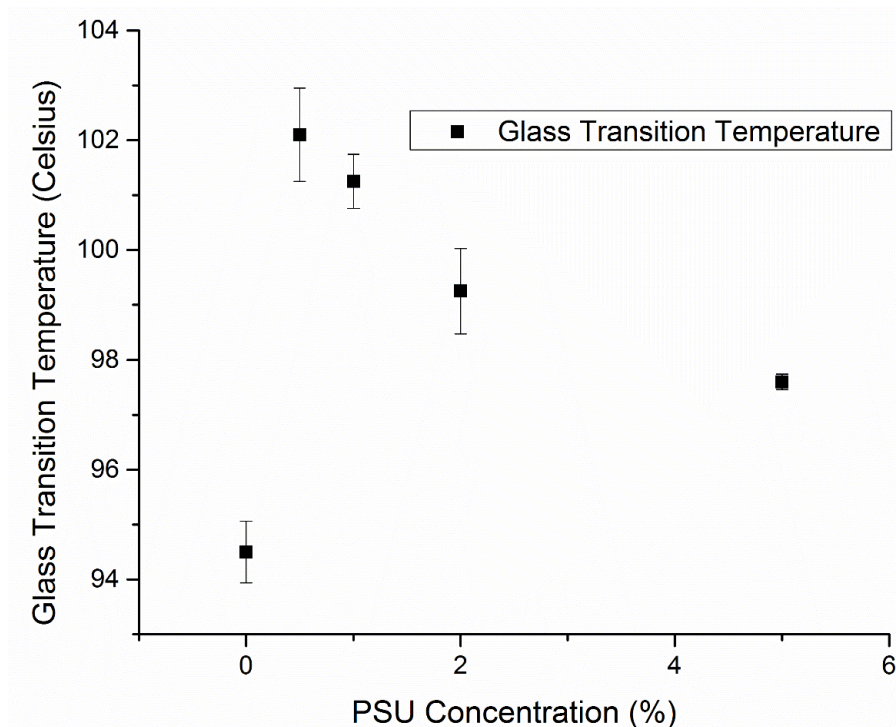


Fig. 8 Glass transition temperatures of cured epoxy with different concentrations of modified polysulfone. Error bars represent the standard errors. The advantage of bonding between additives and epoxy can compensate for the influence of additive at low additive concentration, leading to increased glass transition temperature.

final mixture before curing was homogeneous. When the liquid phase epoxy started to cure, it turned into gel and then into cured epoxy. Since the crosslinked structures were gradually generated during the curing process, it reduced the mobility of the species, and decreased the compatibility between PSU and the curing epoxy. Part of PSU started to separate out, and the other part of PSU was still entangled in the crosslinked epoxy. PSU molecules were chemically bonded to the cured epoxy due to the end-capped epoxide group reacting with the amino group in the curing agent. Figure 9 showed the phase morphology of modified PSU in the cured epoxy at different concentrations after chemical etching. At low concentration of modified PSU, small amount of PSU separated out and formed submicron size clusters (Fig. 9a). They were well

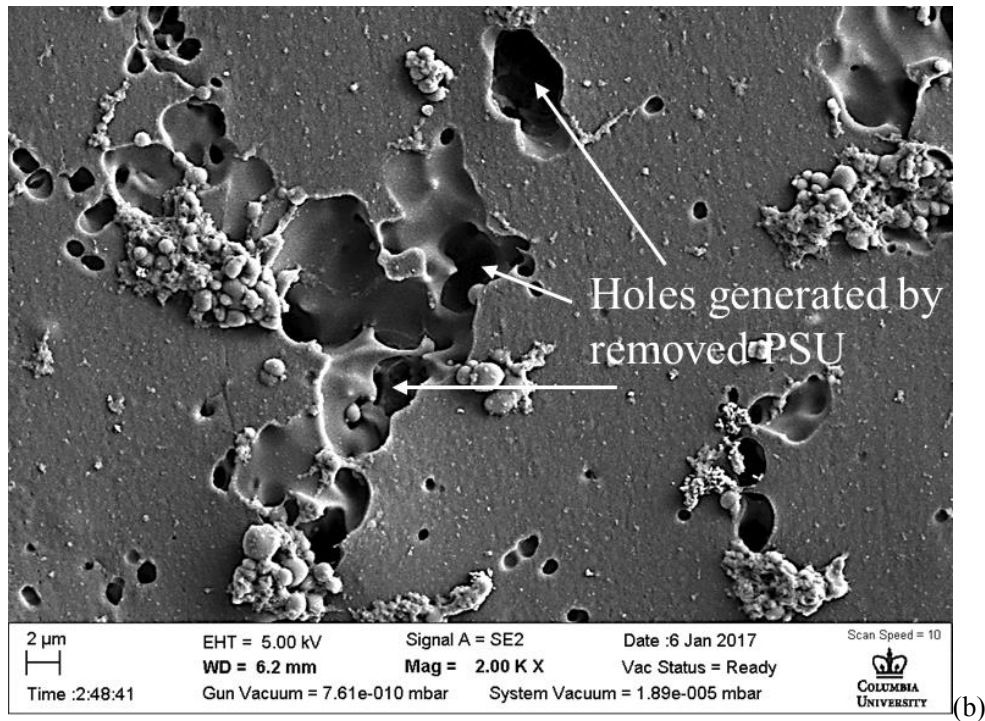
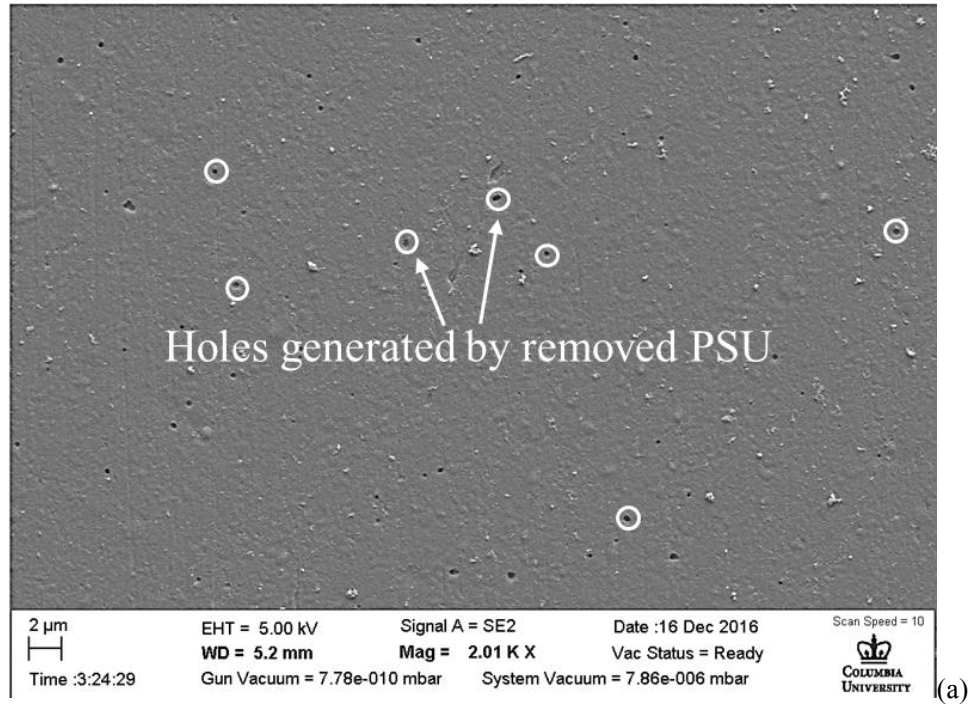


Fig. 9 Optical microscopy of phase morphology in the cured epoxy etched by methyl chloride to remove the PSU-rich region (a) with 0.5 wt% PSU, and (b) with 5 wt% PSU. The holes on the surface were due to the removal of PSU, which were highlighted with arrows.

distributed in the epoxy matrix. At high concentration of modified PSU, more irregular shaped

clusters were formed and the size of the clusters was much larger (Fig. 9b). Also, the distribution of the PSU was not even. Supported by the DSC results to be presented later, it can be shown that at high concentration, the advantage of the additive started diminishing and the crosslinking density of the epoxy matrix was reduced. The phase morphology also supported the trend of glass transition temperatures of cured epoxy with different concentrations of modified PSU.

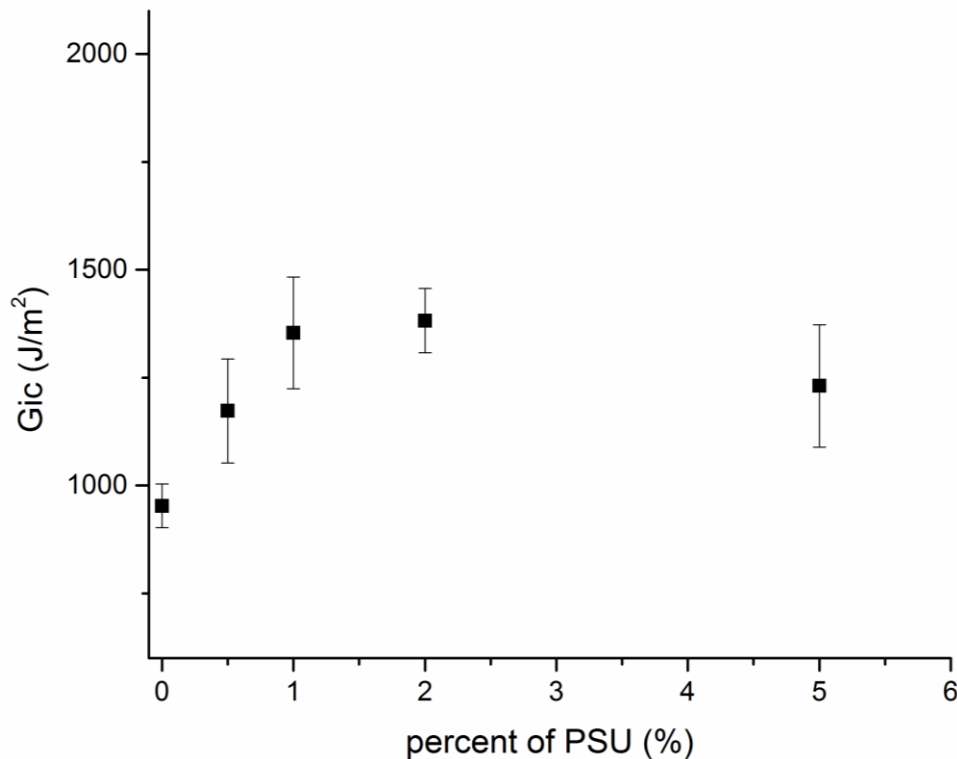


Fig. 10 Mode I critical energy release rate of the specimen with different concentrations of modified PSU. Error bars represent the standard errors.

5.5.5 Mode I fracture test

Specimens were prepared with both modification methods or individual modification method to examine the potential synergistic effect on delamination resistance.

Fig 10 showed the Mode I critical energy release rate of the specimen with both

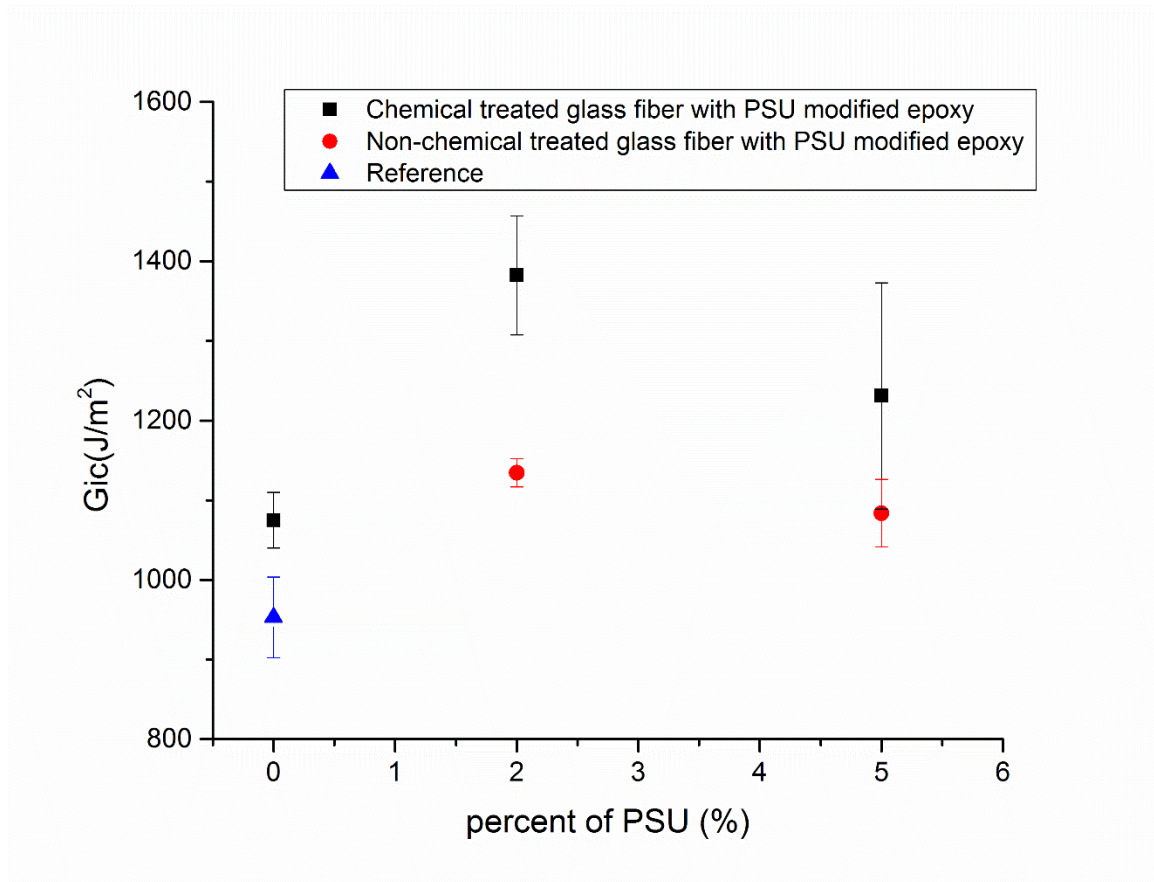


Fig. 11 Synergistic study of Mode I fracture test. Specimens with individual modification method were compared to the specimens with combined modification methods. Slight synergistic effect from two individual modifications methods were found in Mode I fracture test.

modifications under different concentrations of modified PSU. The average toughness and standard error were represented by a symbol and an error bar. The toughness of the specimen increased rapidly from non-modified specimen to 1 wt% PSU modified specimen. The toughness reached its maximum in specimens between 1 wt% to 2 wt% PSU. The trend levelled off towards 5 wt% PSU modified specimen. The toughness results showed a strong evidence that with the physical and chemical bonding in the system, Mode I delamination resistance of the specimen was improved. To examine the synergistic effect, three more conditions were used: 0%

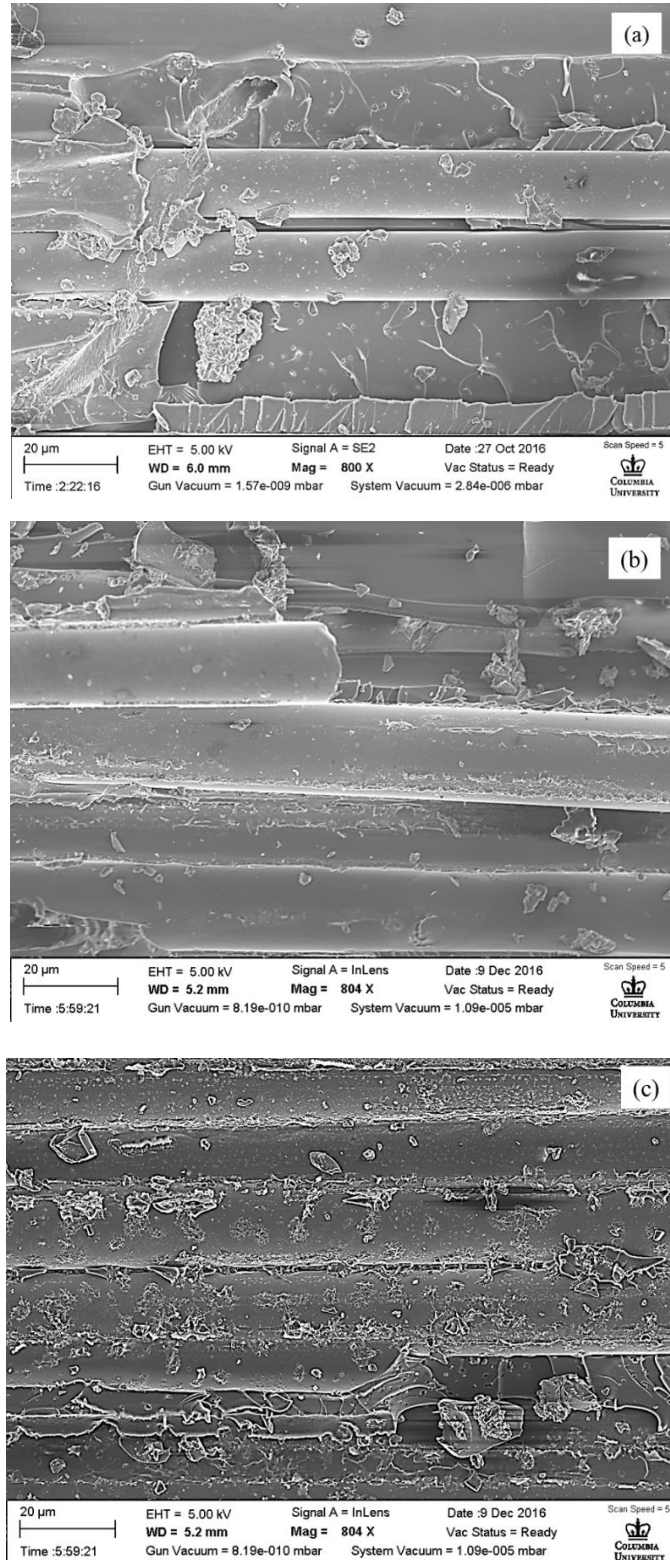


Fig. 12 SEM images of mode I fracture surface morphology of (a) 2% PSU with non-modified glass fiber, (b) 0% PSU with modified glass fiber and (c) 2% PSU with modified glass fiber.

PSU modified epoxy with chemical treated glass fiber surface, 2% PSU modified epoxy with non-chemical treated glass fiber surface, and 5% PSU modified epoxy with non-chemical treated glass fiber surface. The results were shown in Fig. 11. Compared to the reference specimen, under the condition of 0% PSU modified epoxy with chemical treated glass fiber surface, the critical energy release rate G_{ic} was improved by 12.8%. Under the condition of 2% PSU modified epoxy with non-chemical treated glass fiber, the G_{ic} was improved by 19.05%. With 2% PSU modified epoxy with chemical treated glass fiber, the G_{ic} was improved by 45.1%, which was 13% higher than the summation of the two individual modifications. However, the G_{ic} of the specimen with 5% PSU modified epoxy with chemical treated glass fiber was only 3% larger than the summation of the two modifications. The similar G_{ic} with different PSU concentrations confirmed previous hypothesis stating that the major contributions to G_{ic} was micromechanical interlocks and interfacial strength. Limited matrix deformation at high PSU concentration leads to levelling off and thus very limited synergistic effect.

Besides the toughness results, the experimental evidences from fracture surface morphology also supported the synergistic mechanism for Mode I test. Fig. 12a showed the fracture surface of the specimen only with 2% PSU modified epoxy. The glass fiber surfaces were clean and with few residue particles. As described in the background section, the fracture mainly propagated through the interface between the fiber and interlaminar region in Mode I fracture. The clean fiber surface indicated the poor adhesion between the fiber and epoxy. However, the modified epoxy showed large plastic deformation due to pull-out fibers, which increased the toughness. As a comparison, Fig. 12b showed the specimen only with chemical treated glass fiber surface. The fractured epoxy

showed smaller deformation in this case, indicating the brittle fracture. Part of the fiber surface covered with the pike-shaped residues, which were due to the formed chemical bond and mechanical interlocks. The brittle resin was of low toughness, which was not able to transfer the loads into the surrounding materials to make more resin enrolled in consuming the fracture energy. With both modifications, in Fig. 12c, the fracture surface was rough and the entire glass fiber surface was covered with a layer of residue epoxy. The strong chemical bonds and interlocks between glass fiber and modified epoxy prevented the crack from propagating through this interface, and the chemical bond between modified epoxy and the glass fiber led to more ductile epoxy participating in consuming fracture energy, which resulted in the further improvement of the fracture toughness.

5.5.6 Mode II fracture test

Fig. 13 showed the mode II critical energy release rate of the specimens with combined modification methods under different concentrations of modified PSU. The average toughness and its standard error were represented by a symbol and an error bar. The toughness of the specimen increased rapidly from non-modified specimen to 1 wt% PSU modified specimen, then it kept an small increment from 1 wt% to 2 wt% PSU specimen. The trend reached its maximum for the 5 wt% PSU modified specimen compared to the trend in Mode I test. The modified specimen showed greater resistance to Mode II fracture.

Fig. 14 showed the synergistic study of Mode II fracture tests. Compared to the reference specimen, under the condition of 0% PSU modified epoxy with chemical treated glass fiber surface, the critical energy release rate G_{IIC} was improved by 22.84%. Under the condition of 2% PSU

modified epoxy with non-chemical treated glass fiber, the G_{IIC} was improved by 29.18%, as a comparison, with 2% PSU modified epoxy and chemical treated glass fiber, the G_{IIC} was improved by 74.974%, which was 23% larger than the summation of the two individual modifications. Furthermore, the G_{IIC} of the specimen with 5% PSU modified epoxy with chemical treated glass fiber was 24% larger than the summation of the two modifications. The significant increasing G_{IIC} with different PSU concentrations confirmed previous hypothesis stating that the major contributions to G_{IIC} were both matrix deformation and high interfacial strength. Thus, more synergistic effect from two modifications was found in Mode II fracture tests.

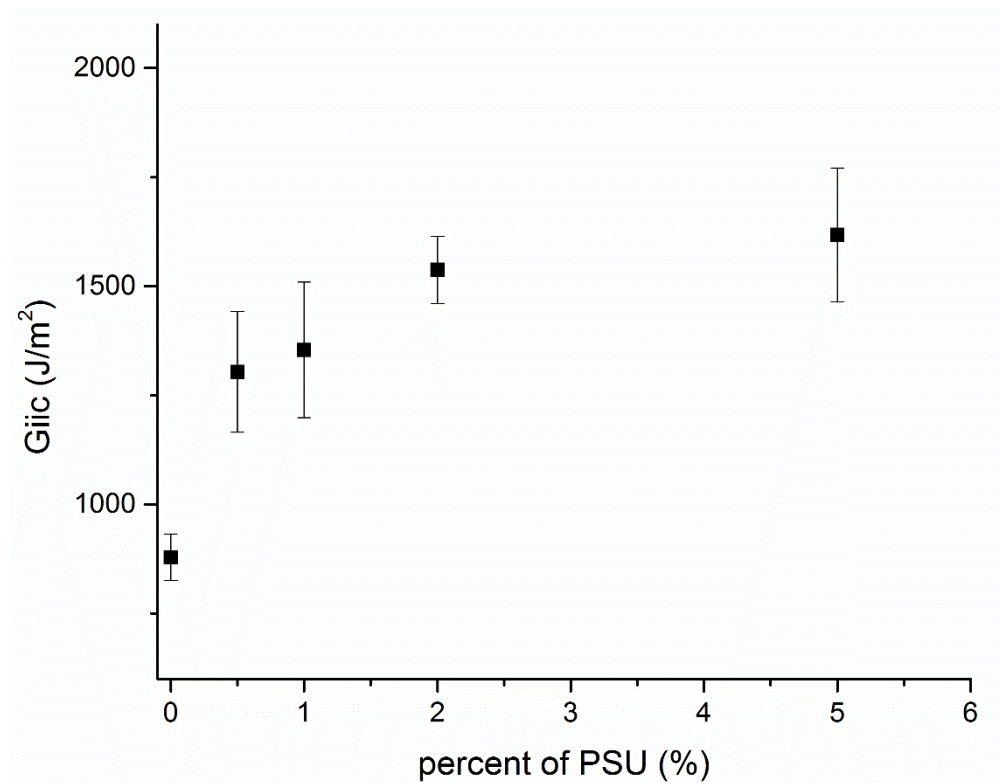


Fig. 13 Mode II critical energy release rate of the specimen with different concentrations of modified PSU. Error bars represent the standard errors.

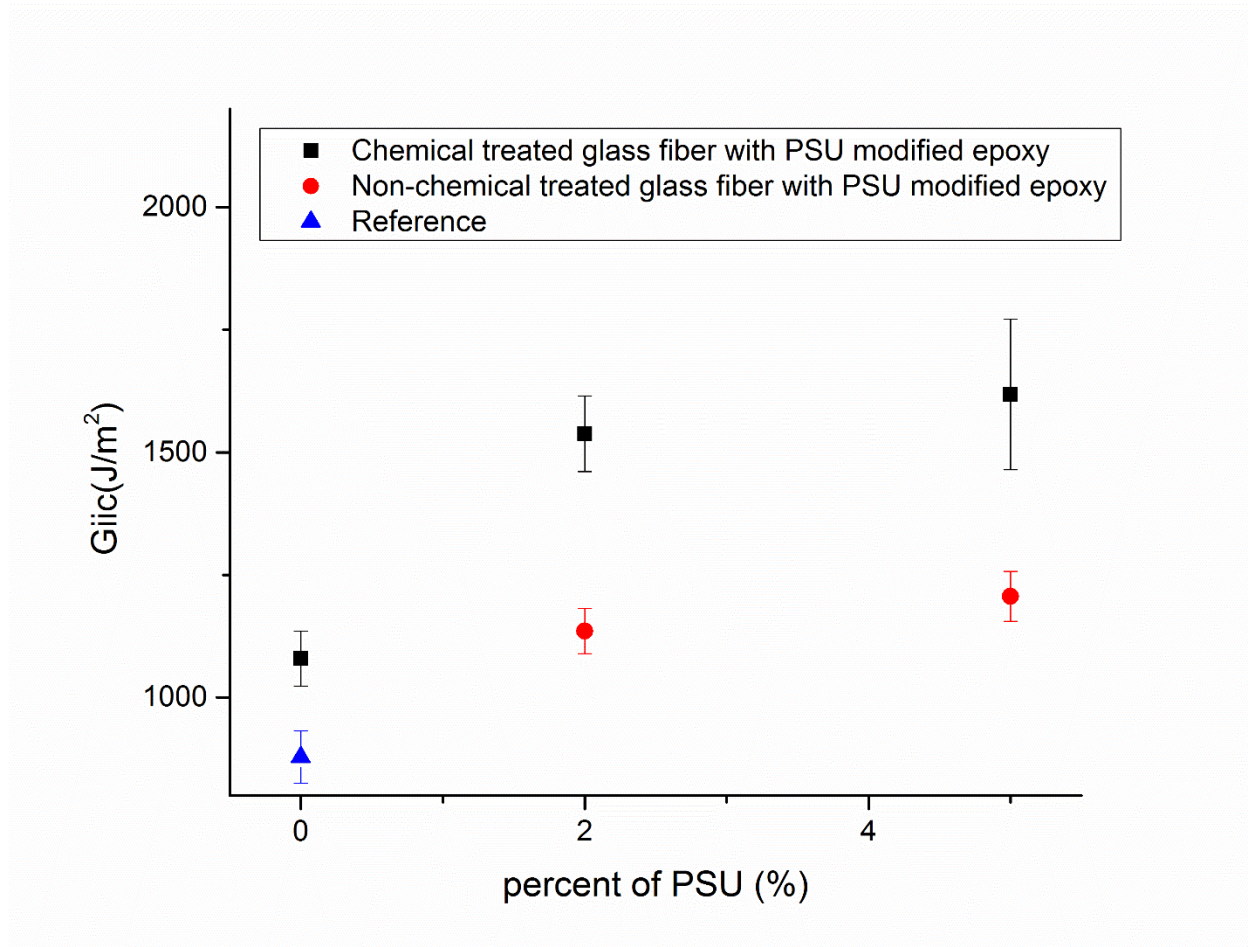


Fig. 14 Synergistic study of Mode II fracture test. Specimens with individual modification methods were compared to the ones with combined modification methods. The further improvement of delamination in Mode II was considered due to the more modified epoxy resin participating in the plastic deformation.

By examining the surface morphology of the specimen, synergistic improvement of fracture toughness can be better explained. From the previous background section, the crack in Mode II fracture propagates through the interface between the fiber and interlaminar region and jumps within the interlaminar region (crack bridging phenomenon). Fig. 15a showed the fracture surface of the specimen only with chemical treated glass fibers. The glass fiber surfaces contained a few residue particles on it. Small blocks of epoxy resin indicated that the brittle

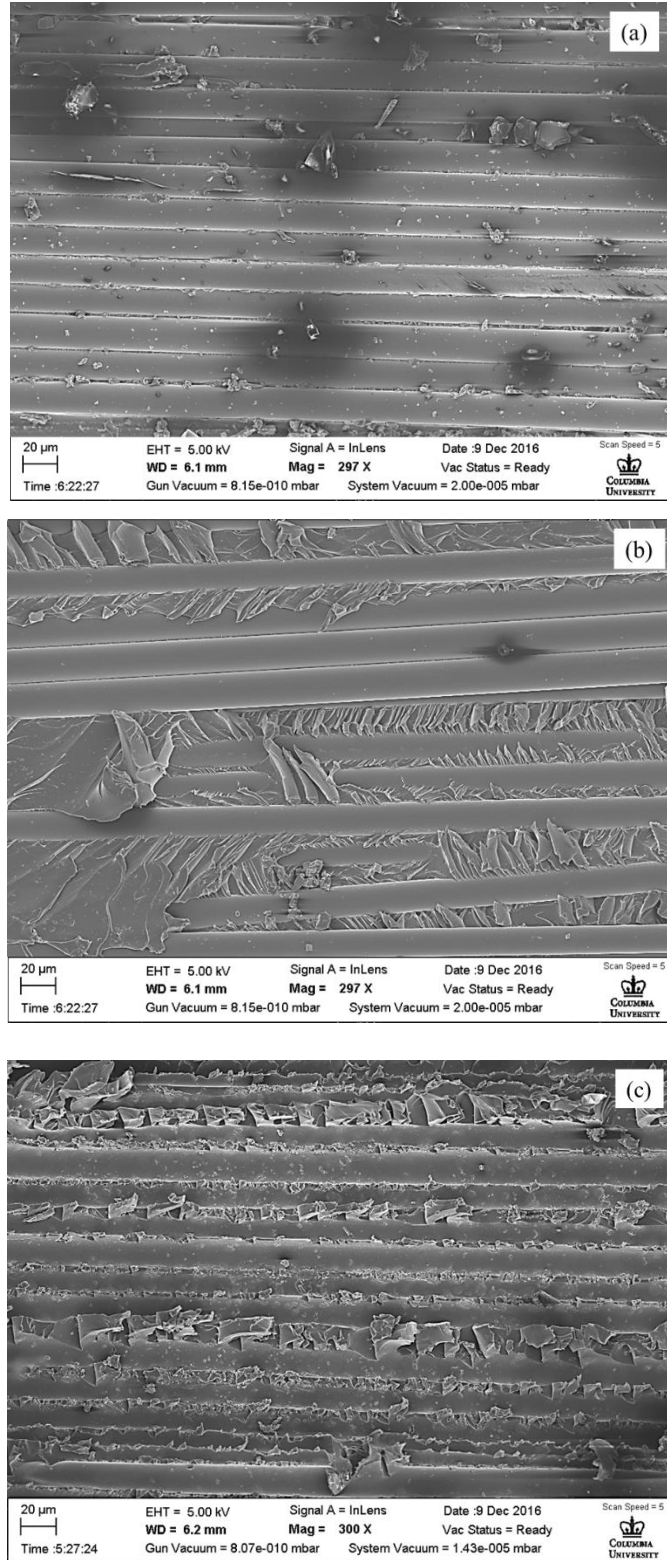


Fig. 15 SEM images of mode II fracture surface morphology of (a) 0% PSU with modified glass fiber, (b) 2% PSU with non-modified glass fiber and (c) 2% PSU with modified glass fiber

epoxy did not undergo large plastic deformation. The limited improvement of delamination resistance was due to the enhanced interface between epoxy and fiber. Fig. 15b showed the specimen only with the modified PSU epoxy. Compared to Fig. 15a, the fiber surfaces were extremely clean, almost no residues on them, which means the bonding between the fiber and epoxy was poor. The poor adhesion led to the low toughness, however, and the modified epoxy between the fibers were of higher toughness, which compensated the loss of toughness. Since the existence of the poor interface, a smaller amount of modified epoxy played a role in consuming the energy. For the specimens with both modifications (Fig. 15c), besides the residues on the fibers throughout the fracture surface, the epoxy matrix showed large regions where the torn epoxy peeled from the matrix. The torn epoxy showed fish scale shaped deformation, which indicated it underwent large shear deformation during Mode II test. This kind of deformation provided a strong evidence that the modified epoxy was tougher and was the major reason for Mode II delamination resistance improvement. Unlike Mode I, in Mode II, crack propagated through both the interface at epoxy/fiber matrix and interlaminar region. Thus, both the physical and chemical bonds played important roles in the delamination resistance. It was noted that the crack bridging due to the shear deformation led to a large amount of epoxy enrolled in crack propagation. Epoxy properties were the major contributions to the improved toughness, which was reflected in the increasing trends in Fig. 14.

5.5.7 Mode I and Mode II simulation

Both Mode I and II fracture tests were simulated to examine the improvement of the interlaminar delamination resistance by the modification methods. The model used the same

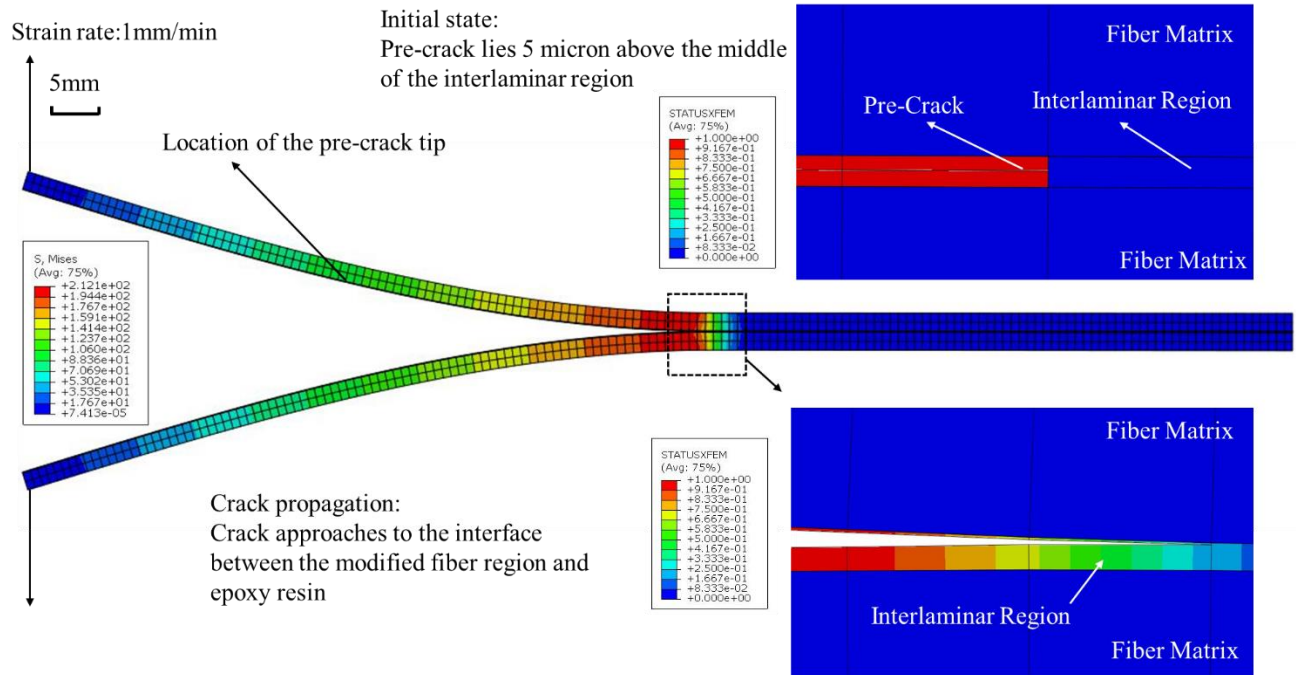


Fig. 16 Simulation of Mode I fracture. Specimen was 160mm in length, 4.15mm in thickness. The left end was under a displacement loading. Initially the pre-crack was 60mm in length and placed 5 microns above the middle of the interlaminar region. The contour map in magnified regions represented the status of crack. Value of 1(red) in that element represented total fracture and value of 0 (blue) in that element represented zero fracture. The value in between indicated there still existed traction on the crack surface, which were considered as partial fracture. The crack growth matched the previous crack propagation analysis for Mode I in Fig. 3b.

geometry as in the experiment according to ASTM D5529 and D7905 test methods. The specimen was 160mm in length, 4.15mm in thickness. The pre-crack is 60mm long from the edge of the specimen and initially placed 5 microns above the middle of the interlaminar region. Between the interlaminar and fiber matrix region, there were two one-micron thick layers to represent chemical bonding and mechanical interlocks. The layer thickness was based on the experiment observation. Fig. 16 showed the simulation results of the Mode I fracture. The contour map of the entire specimen showed the stress states when the specimen was loaded. It was clear that at the crack tip region, the stress reached its peak, which was high enough to form

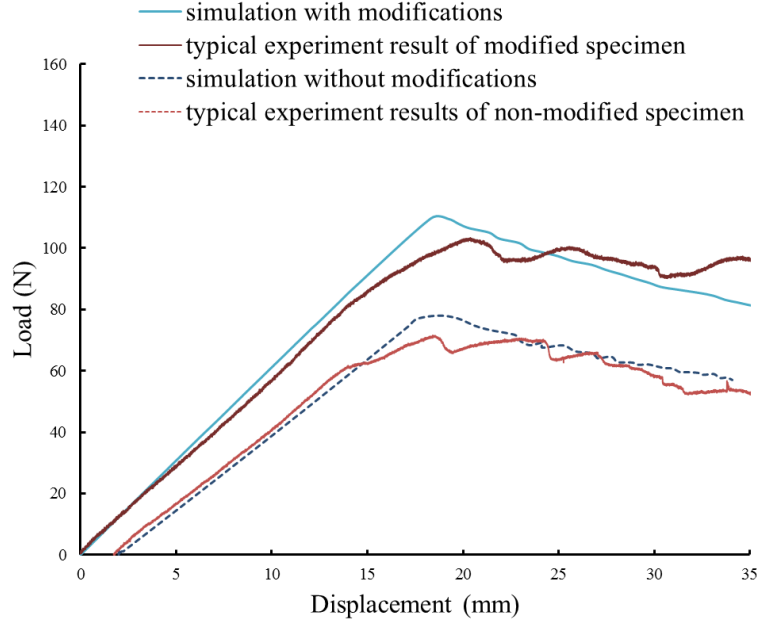


Fig. 17 Mode I simulation results vs experiment results.

new crack ahead. After the crack propagated for a certain distance, it approached the interface between the modified fiber region and epoxy resin, which confirmed our previous experiment observation in Fig. 12, where the crack path located above the rough glass fiber surface in the toughened epoxy resin region was shown. The color contour in the magnified region represented the value of XFEM status, in which 0 meant no fracture and 1 meant total fracture. The in-between value of this status along the crack tip path was because there still existed tractions on the crack surface, considered as partially fractured. By extracting the reaction force and displacement at the point where the displacement loading was applied, the simulation results compare to the experimental results in Fig. 17 and they are largely in agreement. The load and displacement curves increased then leveled off in both simulation and experiments. For the non-modification specimen, the load reached 80N then the crack initiated and propagated. As a

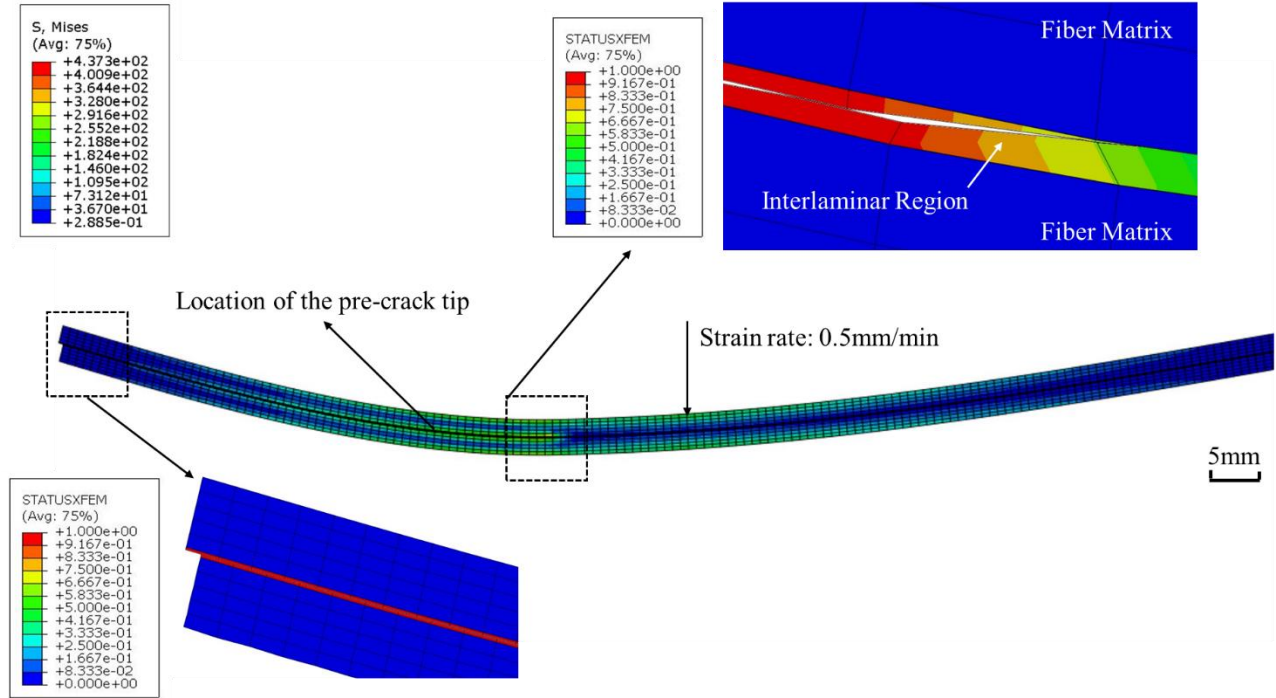


Fig. 18 Simulation of Mode II fracture. The shear deformation was represented by the misalignment of the cells along the pre-defined interlaminar region. The contour map in magnified region represented the status of crack.

comparison, for the specimen with modification, the maximum loads reached 108N, as in the simulation, the yield strength was increased by nearly 40%. Also, the higher slope of the curve indicated that the specimen with modifications showed higher mechanical stiffness, which confirmed previous conclusion drawn from glass transition temperatures that with the epoxide end-capped PSU, the crosslinking density even increased at low additive concentration, leading to higher mechanical performance.

Fig. 18 showed the simulation results for Mode II fracture. Due to the shear forces, the specimens showed a sliding phenomenon. The layer above the crack region extended beyond the layer below the crack and this deformation led to the shear force concentrated at the crack tip region. The crack in Mode II also approached the interface between the modified fiber surface and

epoxy resin. The simulation results were in good agreement with the experimental results at the beginning as shown in Fig. 19. In this case, the yield strength was 80% higher than the reference specimen. The simulation results had overestimation after the crack initiation in both reference and modification cases. This was mainly because in Mode II, the crack underwent a bridging phenomenon, which also helped to dissipate the energy. However, in XFEM, the crack was not able to branch, leading to the overestimated load and displacement curves when crack propagated.

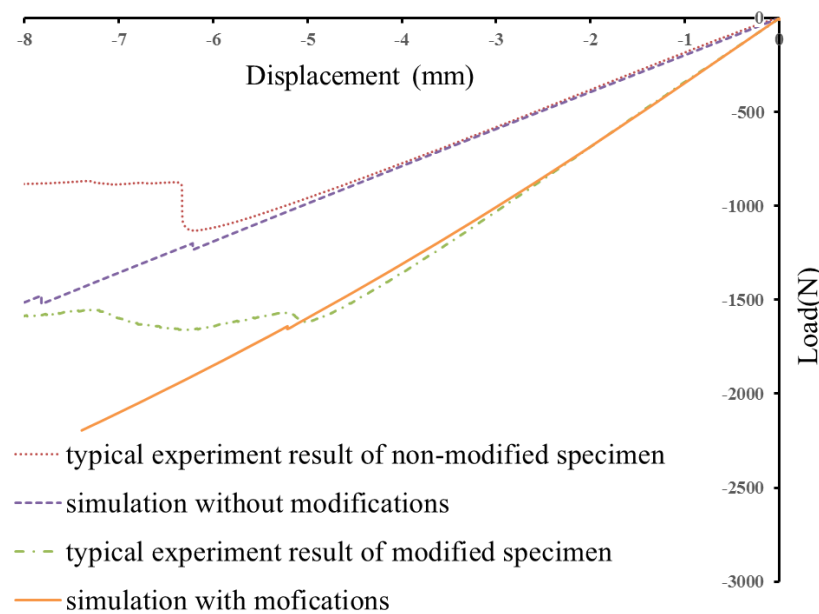


Fig. 19 Mode II simulation results vs experiments results. The overestimation of the simulation results after the crack initiation was mainly because the crack bridging phenomenon dissipated more energy than single crack growth modelled in the simulation.

5.6 Conclusion

Lower concentration of PSU modified epoxy showed slightly higher viscosity than non-modified epoxy. Despite of the increased viscosity, PSU modified epoxy can still be implemented into the vacuum assisted resin transfer molding process. Lower concentration of PSU led to an increased glass transition temperatures of the cured epoxy modified by PSU because of the

chemical bonding between thermoplastic and crosslinked thermoset structure. Higher concentration of PSU modified epoxy showed large PSU clusters, and the glass transition temperature increase leveled off because the dilute effect became dominant. The reported synergistic modification scheme showed more significant toughness improvement on both Mode I and Mode II fractures than the sum of improvements due to PSU modified epoxy and glass fiber grafting alone. Toughness was improved because cracks need more energy to propagate through the physical bonding of micromechanical interlocks and semi-interpenetration networks, cracks also require more energy to overcome the chemical bonding among epoxy, glass fiber and polysulfone. The large shear deformation of the cured epoxy matrix, pulled out fibers, and residues on the fiber surface indicated strong interlaminar strength due to the formed chemical and physical bonding. Numerical simulation of Mode I and II tests agreed with mechanical testing results and crack growth observations in the interlaminar region.

5.7 Acknowledgement

This research was supported by National Science Foundation under a GOALI award CMMI-1363328. Authors would also like to thank Shuoxun Wang and Daniel Eida in Prof. Robert Farrauto's lab to provide us DSC equipment and Siwei Ma in Prof. Shiho Kawashima's lab to provide us Haake Mars III Rheometer.

Chapter 6: Conclusions

In this study, the knowledge of toughening the fiber reinforced polymers (FRP) as structure composites materials have been advanced. Hot melt bonding and diffusion bonding (dual bonding) processes have been conducted to increase the interaction between epoxy resin and thermoplastic interleaf and to arrest the crack within the toughened region. Furthermore, the modified epoxy system with epoxide end-capped polysulfone and functionalized fiber surface has been utilized to toughen the FRP synergistically through both chemical and physical bonding without the interleaf. Both methods shows significant improvement on the delamination resistance and fracture toughness. Major findings and contributions of this study are summarized as follows. Suggestions for future work are also listed.

6.1 Effect of deep interleaf penetration on delamination resistance

It has been systematically demonstrated that the penetration depth of thermoplastic interleaf into the fiber depend on the hot melt bonding temperatures. The hot melt bonding process increases the thermoplastic polymer chain mobility, leading to significant reduction of viscosity after the temperature is heated above the glass transition temperature of the thermoplastic polymer. The original thermoplastic is amorphous and molecular chains are entangled. With the elevated temperatures, the molecular chains of the thermoplastics undergo relaxation and increase the mobility. Optical microscopy and chemical etching technology have been conducted for the detailed investigation of the process effected and resulted penetration morphologies. The deep penetration depths are observed under high hot melting temperatures, which is mainly due to the viscosity reduction of the thermoplastics and the ability of the molecules to move more freely.

Specimens with external drop-offs have been used to simulate the structures under mixed-mode failure in reality such as wind turbine blade. Stress analysis on the drop-off region indicates the crack initiation and propagation locations, which are confirmed by the optical microscopy of cross-sectioned fractured specimens. In the case with low interleaf penetration region, the crack propagates essentially through the weak interface between the epoxy/fiber and thermoplastics interleaf. With deep penetration region, the crack propagates within the penetration depth and does not reach the weak boundary. High strength fibers confine the crack in the toughened region due to the shrinking size of the crack tip yield zone. Uniaxial tensile tests have been performed and toughness is improved by a factor of two. Scanning electron microscopy has been used to characterize the fracture mode and toughening mechanism. The specimen with low penetration shows clean and clear fracture surface morphology, indicating the dominant fracture type is brittle adhesive failure. The specimen with high penetration shows rougher fracture surface: pulled out fibers and blocks of residues indicating large plastic deformation. The major reasons for the improved toughness are breaking of the entangled thermoplastic molecular chains and the intermolecular forces between thermoplastics and fibers. The deep penetration zone of improved ductility confines the plastic zone ahead of the crack tip within its boundaries and thus requires more fracture energy for the crack to propagate. The detailed investigation advances the knowledge of toughening fiber reinforced polymers. The advanced knowledge of the process potentially can be implemented in various composites structures where the drop-off will create stress concentrations such as wind turbine blade, airplane wings, and automotive body.

6.2 Interlaminar toughening by diffusion and precipitation

The interleaving method is used to locally toughen the drop-off region, while using interleaf introduces new problem that bonding between interleaf material and epoxy resin must be strong. Proper interleaf can form semi-interpenetration networks between the inserted thermoplastic interleaf and epoxy resin through diffusion and precipitation process, which is expected in the dual bonding process. A low concentrated polystyrene (PS) modified epoxy system has been shown to improve the degree of diffusion and precipitation. It has been experimentally determined that polysulfone (PSU) is the most compatible thermoplastic of the three high performance thermoplastics (polycarbonate, polysulfone and polyetherimide) to the current epoxy system by using the viscometry method. The degree of diffusion and precipitation region has been shown to be a relationship with curing temperatures and additive concentrations. Higher curing temperatures lead to lower viscosity and larger chain mobility. Higher concentration of additive increase the dilute effect and lead to wider diffusion and precipitation region. The fiber structure has also shown to influence the diffusion and precipitation degree under all the conditions. With the modified epoxy system, even considering the fiber structures, the diffusion and precipitation region still reaches almost three times larger than the case with neat epoxy system. As compared with the FRP without interleaf, the fracture toughness increased by a factor of three with the 5% PS modified epoxy cured at 120°C. The enhanced bonding within the diffusion and precipitation region is mainly due to the entanglement of epoxy networks and thermoplastics, since the interaction between them is mechanical interlocks and intermolecular forces, this bonding is considered as chemical reaction induced physical bonding. The scanning electron microscopy of the fracture morphology indicates that the crack propagation locates in the diffusion and precipitation region

and the large plastic deformation of this region during fracture leads to the improved delamination resistance.

Since the diffusion and precipitation between epoxy resin and interleaf thermoplastic occurs during the infusion process, it simplifies the modification process. Therefore, interlaminar toughening through diffusion and precipitation further provides a potential method to improve the composites toughness with less complicated production procedure.

6.3 Effect of curing kinetics on interlaminar toughening

The addition of polystyrene into the epoxy system modifies the diffusion and precipitation process in many ways, including changing chain mobility, and reducing the curing reaction rate. The combined effects determine the degree of diffusion and precipitation. In this study, detailed investigation of the additive influence on diffusion and precipitation has been carried out as a function of degree of cure, temperature and diffusivity of epoxy, hardener and PSU thermoplastic. The diffusivity of epoxy, hardener and PSU in both diffusion and precipitation direction are characterized by attenuated total reflection-Fourier transform infrared spectroscopy (ATR-FTIR). The diffusivities of curing epoxy and hardener into PSU were close, and both are higher than the diffusivities of PSU into epoxy or hardener due to the low molecular weight and high mobility of small molecules. Low concentration of PS additive does not influence the diffusivity of the epoxy. The chemical reactions during curing is the epoxide ring open and branching reactions, of which the curing reaction rate coefficients are quantified based on the consumption of the epoxide rings monitored by ATR-FTIR. The PS additives are compatible to the epoxy but incompatible to the curing hardener, thus the chemical inactive PS particles prevents the curing reaction by absorb

epoxy molecules in PS rich region, resulting in that the PS modified epoxy shows reduced reaction rate compared to the non-modified epoxy, providing more time for diffusion and precipitation to happen and leading to deep semi-IPN. A physical based numerical model coupled with curing kinetics has been developed to simulate the diffusion and precipitation under various conditions for optimizing the experiment conditions and reducing trial and error of the tests. The numerical model well captures the trends of diffusion and precipitation depths at various curing temperatures.

6.4 Interlaminar toughening by synergistic modification of resin and fiber

As described above, the interlaminar toughening through interleaving methods is limited to locally toughen the laminate structure and the entire thermoplastic does not fully participate in absorbing more fracture energy since the crack propagates in diffusion and precipitation region or interleaf penetration region while local stiffness is reduced. To address this limitation, a new modification methods was developed which utilizes a synergistic modification to form both strong chemical and physical bonding in the epoxy and at the interface between fiber and epoxy. The interface between epoxy and fibers are usually considered as the weak interface, which is investigated through chemical modifications and interactions to the epoxy resin. Low concentration of epoxide end capped PSU modified epoxy system shows slightly higher viscosity than non-modified epoxy but it is still capable to implement onto the vacuum assisted resin transfer molding, which is conventional technique to produce the large-scale laminate composites product. Raman spectroscopy confirms the formation of desired functional groups grafting on fiber surface and polysulfone, which can crosslink into the thermosets networks. It is demonstrated that the glass transition temperatures of the modified cured epoxy increased at low concentration of PSU because

the formed chemical bonding between thermoplastic and crosslinked thermoset structure compensates the effect of additives based on the results from differential scanning calorimetry (DSC). High concentration of PSU modified epoxy shows large PSU clusters and reduces the glass transition temperature because the dilute effect is dominant based on the observation from the scanning electron microscopy. The novel FRP system showed significant synergistic toughness improvement on both Mode I and Mode II fractures. Crack needs more energy to propagate through the physical bonding (the micromechanical interlocks and semi-interpenetration networks) and chemical bonding among epoxy, glass fiber and PSU. The large shear deformation of the modified epoxy matrix, pulled out fibers and residues on the fiber surface indicate strong interlaminar strength due to the formed chemical and physical bonding. Extended finite element methods (xFEM) has been used to simulate the crack propagation in Mode I and Mode II fractures. The simulation results indicate significantly improved interlaminar material properties by matching the experiment results.

6.5 Future work

The major contributions outlined above, in both physical-chemical modification and interleaving or non-interleaving methods, form a foundation on which further developments can be based.

In terms of the surface functionalization of glass fiber, the results have shown the significant improvement of interfacial bonding between the modified epoxy resin and fiber matrix, which is mainly due to the formed chemical bonding between carbon from epoxide groups in modified epoxy system and nitrogen from amino groups on fiber surface. This modification process is worth

further investigation because the amount of amino functional groups grafted onto the fiber surface directly influences the number of the strong chemical bonds generated between the modified epoxy and fiber matrix. Raman spectroscopy would enable characterization of the chemical modification quantitatively, the concentration of the interested chemical peak can be determined by the change of the specific chemical peak under various experiment conditions.

The geometry used in the interleaving methods is external drop-off structure. The reason for choosing this type of geometry is that captures the delamination phenomenon of laminate composites. As an example, wind turbines' tapered blades introduce drop-off layers. During the operation, the blade experiences both the flapping forces due to the wind and centrifugal forces due to the rotation. These forces cause mixed mode failure at the drop-off region, the crack will propagate through the interlaminar region between the drop-off layer and the layer beneath the drop-off layer. In this thesis, the external drop-off structure also fractures due to mixed mode failure and the crack grows into the drop-off layer. Using this type of geometry has the advantages of severer stress concentration around the drop-off region compared to the internal drop-off structures and simpler stress state at the edge of the drop-off. In practical applications, drop-offs are mostly likely embedded into the entire structure, also known as internal drop-off layers. Although the stress concentration effect on internal drop-off layer is reduced, it is still worth studying since it is more similar to real world applications. ASTM D3039M test may potentially be modified to obtain the stress and strain state at the crack initiation and propagation. The position of the embedded drop-off layer, the taper angle of the drop-off region, the size of the resin-rich pocket ahead of the drop off and the position of the interleaf should be considered as factors that

may influence the results.

In the current regime, all the specimens produced by the vacuum assisted resin transfer molding are cured at a constant elevated temperature or room temperature, which is also the method used in industry. From the current study, the degree of diffusion and precipitation has shown effects on the fracture toughness of the specimen. Since the initial stage of curing and final cured morphology between thermoplastic and epoxy have been examined in current work, future study could be done on the transient process of diffusion and precipitation between epoxy and PSU. FTIR with transmission microscopy may enable monitoring the diffusion and precipitation process from the start to end of the curing process, potentially providing information about polymer swelling, phase separation, gelation point at specific time, and the degree of curing. Study on the transient processes of diffusion and precipitation may help in understanding the mechanism of diffusion and precipitation processes and provide more information such as gelation time. With better understanding, the current simulation model can be improved and its prediction capability of diffusion and precipitation process increased.

References

Chapter 1

1. Smallman, R. E., Bishop, R.J., “Modern Physical Metallurgy and Materials Engineering,” Oxford: Butterworth-Heinemann, 6th ed., 1999.
2. Erhard, G., “Designing with Plastics,” *Trans. Martin Thompson*, Munich: Hanser Publishers, 2006.
3. “Magyar Archery (1),” Magyar Archery (1). [Online]. Available: http://www.atarn.org/magyar/magyar_1.htm. [Accessed: 09-Apr-2017].
4. “Tim Palucka and Bernadette Bensaude-Vincent:” History of composites - overview. [Online]. Available: http://authors.library.caltech.edu/5456/1/hrst.mit.edu/hrs/materials/public/composites/Composites_Overview.htm. [Accessed: 09-Apr-2017].
5. “History of Composite Materials,” Corrosion, Composites, Pipe Supports Blog. [Online]. Available: <http://blog.appinc.co/history-of-composite-materials>. [Accessed: 09-Apr-2017].
6. “Learning Center - About Prepregs,” Fibre Glast. [Online]. Available: http://www.fibreglast.com/product/about-prepregs/Learning_Center. [Accessed: 12-Apr-2017].

7. Niggemann, C., Young, S. S., Gillespie, J. W., and Heider, D., 2008, “Experimental Investigation of the Controlled Atmospheric Pressure Resin Infusion (CAPRI) Process,” *Journal of Composite Materials*, 42(11), pp. 1049-061.
8. “Fabrication methods,” *CompositesWorld*, 31-Dec-2013. [Online]. Available: <http://www.compositesworld.com/blog/post/fabrication-methods>. [Accessed: 12-Apr-2017].
9. “Composites Manufacturing Processes,” *CompositesLab*. [Online]. Available: <http://compositeslab.com/composites-manufacturing-processes/>. [Accessed: 09-Apr-2017].
10. “MTorres,” Automated Tape Layer machine | Torreslayup. [Online]. Available: <http://www.mtorres.es/en/aeronautics/products/carbon-fiber/torreslayup>. [Accessed: 12-Apr-2017].
11. “Continuous Fiber Composite Part Cost Vs Production Volume By Manufacturing Process And Material” [Online]. Available: <http://www.iceaaonline.com/ready/wp-content/uploads/2015/01/Chris-Rush-SoCal-ICEAA-Dec-2014.pdf> [Accessed: 12-Apr-2017].
12. “Tooling up for large wind turbine blades,” *Tooling up for large wind turbine blades - Renewable Energy Focus*, 01-Oct-2007. [Online]. Available: <http://www.renewableenergyfocus.com/view/1149/tooling-up-for-large-wind-turbine-blades/>. [Accessed: 12-Apr-2017].

13. J. A. Grande, "Wind Power Blades Energize Composites Manufacturing," *Plastics Technology*, 30-Sep-2008. [Online]. Available: <http://www.ptonline.com/articles/wind-power-blades-energize-composites-manufacturing>. [Accessed: 12-Apr-2017].
8. "WINDFORCE 12: A Blueprint to Achieve 12% of the World's Electricity from Wind Power by 2020," *European Wind Energy Association*, 2003.
9. Rasmussen, F., Madsen, P.H., "Current Direction of Danish Wind Energy Research," *Journal of Solar Energy Engineering*, 126(4), pp. 1105-1109, 2004.
10. de Vries, E., "Thinking Bigger," *Renewable Energy World*, 3, pp. 42-55, 2005.
11. Joosse, P.A., Van Delft, D.R.V., Kensche, C., Hahn, F., Jacobsen, T.K., Van den Berg, R.M., "Economic Use of Carbon Fibers in Large Wind Turbine Blades?," *19th ASME Wind Energy Symposium*, Reno, pp. 10-13, 2000.
12. Brøndsted, P., Lilholt, H., Lystrup, A., "Composite Materials for Wind Power Turbine Blades," *Annual Review of Materials Research*, 35, pp. 505-538, 2005.
13. "Wind Turbine Blades," *Eco Chunk*, [Online], Available: <http://www.ecochunk.com/tag/wind-turbine-blades/>, [Accessed: 06-Apr-2017].
14. Wu, G., Ma, L., Wang, Y., Liu, L., Huang, Y., "Interfacial properties and impact toughness of methylphenylsilicone resin composites by chemically grafting POSS and tetraethylenepentamine onto carbon fibers," *Composites Part A: Applied Science and Manufacturing*, 84, pp. 1-8, 2016.

15. Sinh, L. H., Son, B. T., Trung, N. N., Lim, D.-G., Shin, S., Bae, J.-Y., “Improvements in thermal, mechanical, and dielectric properties of epoxy resin by chemical modification with a novel amino-terminated liquid-crystalline copoly(ester amide),” *Reactive and Functional Polymers*, 72(8), pp. 542–548, 2012.
16. Rajasekaran, R., “Effect of polyethersulfone and N,N'-bismaleimido-4,4'-diphenyl methane on the mechanical and thermal properties of epoxy systems,” *eXPRESS Polymer Letters*, 2(5), pp. 339–348, 2008.
17. Perez, R., Sandler, J., Altstädt, V., Hoffmann, T., Pospiech, D., Ciesielski, M., Döring, M., Braun, U., Balabanovich, A., Schartel, B., “Novel phosphorus-modified polysulfone as a combined flame retardant and toughness modifier for epoxy resins,” *Polymer*, 48(3), pp. 778–790, 2007.
18. Rajasekaran, R., Alagar, M., “Mechanical Properties of Bismaleimides Modified Polysulfone Epoxy Matrices,” *International Journal of Polymeric Materials*, 56(9), pp. 911–927, 2007.
19. Patra, A., Bisoyi, D. K., Manda, P. K., Singh, A. K., “Electrical and mechanical properties of the potassium permanganate treated short sisal fiber reinforced epoxy composite in correlation to the macromolecular structure of the reinforced fiber,” *Journal of Applied Polymer Science*, 128(2), pp. 1011–1019, 2012.
20. Sprenger, S., Kinloch, A.J., Taylor, A.C., Mohammed, R.D., “Rubber-toughened GFRCs optimised by nanoparticles,” *JEC Composites*, 21, pp. 66-69, 2005.

21. Kinloch, A. J., “Toughening Epoxy Adhesives to Meet Today's Challenges,” *MRS Bulletin*, 28(6), pp. 445–448, 2003.
22. Caccavale, V., “Master of Science Thesis,” University of Padova, Italy, 2007.
23. Tsai, J.-L., Huang, B.-H., Cheng, Y.-L., “Enhancing Fracture Toughness of Glass/Epoxy Composites by Using Rubber Particles Together with Silica Nanoparticles,” *Journal of Composite Materials*, 43(25), pp. 3107–3123, 2009.
24. Uddin, M., Sun, C., “Improved dispersion and mechanical properties of hybrid nanocomposites,” *Composites Science and Technology*, 70(2), pp. 223–230, 2010.
25. Tang, L.-C., Zhang, H., Sprenger, S., Ye, L., Zhang, Z., “Fracture mechanisms of epoxy-based ternary composites filled with rigid-soft particles,” *Composites Science and Technology*, 72(5), pp. 558–565, 2012.
26. Carolan, D., Ivankovic, A., Kinloch, A., Sprenger, S., Taylor, A., “Toughening of epoxy-based hybrid nanocomposites,” *Polymer*, 97, pp. 179–190, 2016.
27. Sprenger, S., Kinloch, A.J., Taylor, A.C., Mohammed, R.D., “Rubber-toughened GFRCs optimised by nanoparticles,” *JEC Composites*, 21, pp. 66-69, 2005.
28. Wang, G.-T., Liu, H.-Y., Saintier, N., Mai, Y.-W., “Cyclic fatigue of polymer nanocomposites,” *Engineering Failure Analysis*, 16(8), pp. 2635–2645, 2009.

29. Liu, H.-Y., Wang, G.-T., Mai, Y.-W., Zeng, Y., “On fracture toughness of nano-particle modified epoxy,” *Composites Part B: Engineering*, 42(8), pp. 2170–2175, 2011.
30. Liu, H.-Y., Wang, G.-T., Mai, Y.-W., “Cyclic fatigue crack propagation of nanoparticle modified epoxy,” *Composites Science and Technology*, 72(13), pp. 1530–1538, 2012.
31. Heijden, S. V. D., Daelemans, L., Schoenmaker, B. D., Baere, I. D., Rahier, H., Paepegem, W. V., Clerck, K. D., “Interlaminar toughening of resin transfer moulded glass fibre epoxy laminates by polycaprolactone electrospun nanofibres,” *Composites Science and Technology*, 104, pp. 66–73, 2014.
32. Li, G., Li, P., Zhang, C., Yu, Y., Liu, H., Zhang, S., Jia, X., Yang, X., Xue, Z., Ryu, S., “Inhomogeneous toughening of carbon fiber/epoxy composite using electrospun polysulfone nanofibrous membranes by in situ phase separation,” *Composites Science and Technology*, 68(3-4), pp. 987–994, 2008.
33. Villoria, R. G. D., Hallander, P., Ydrefors, L., Nordin, P., Wardle, B., “In-plane strength enhancement of laminated composites via aligned carbon nanotube interlaminar reinforcement,” *Composites Science and Technology*, 133, pp. 33–39, 2016.
34. Li, P., Liu, D., Zhu, B., Li, B., Jia, X., Wang, L., Li, G., Yang, X., “Synchronous effects of multiscale reinforced and toughened CFRP composites by MWNTs-EP/PSF hybrid nanofibers with preferred orientation,” *Composites Part A: Applied Science and Manufacturing*, 68, pp. 72–80, 2015.

35. D. Cairns, J. Mandell, M. Scott, and J. Maccagnano, "Design and manufacturing considerations for ply drops in composite structures," *Composites Part B: Engineering*, vol. 30, no. 5, pp. 523–534, 1999.
36. M. Grassi, B. Cox, and X. Zhang, "Simulation of pin-reinforced single-lap composite joints," *Composites Science and Technology*, vol. 66, no. 11-12, pp. 1623–1638, 2006.
37. Ozdil, F., and Carlsson, L. A., "Mode I Interlaminar Fracture of Interleaved Graphite/Epoxy," *J. Comp. Mater.*, 26(3), pp. 433-59, 1992.
38. Matsuda, S., Hojo, M., Ochiai, S. A., Murakami, Akimoto, H., and Ando, M., "Effect of Ionomer Thickness on Mode I Interlaminar Fracture Toughness for Ionomer Toughened CFRP," *Composites Part A: Applied Science and Manufacturing*, 30(11), pp. 1311-319, 1999.
39. Hojo, M., Matsuda, S., Tanaka, M., Ochiai, S., and Murakami, A., "Mode I Delamination Fatigue Properties of Interleaf-toughened CF/Epoxy Laminates," *Composites Science and Technology*, 66(5), pp. 665-75, 2006.
40. Hojo, M., Matsuda, S., Ochiai, S., Marukami, A., and Akimoto, H., "The Role of Interleaf/Base Lamina Interphase in Toughening Mechanism of Interleaf-Toughened CFRP", *ICCM12 Conference Paris*, pp. 410.
41. Wu, S., "Polymer interface and adhesion," Basel: Marcel Dekker, 1982.
42. Kinloch, A. J., "Adhesion and adhesives," Chapman and Hall, London, 1987.

43. Deryaguin, B.V., and V.P. Smillgaa, “Adhesion, Fundamentals and Practice,” McLaren and Son, London, 1969.
44. Russell, T.P., “The Characterization of Polymer Interface,” *Annual Review Materials Science*, 21, 249-68, 1991.
45. Voyutskii, S.S., “Autoadhesion and adhesion of High Polymers,” Wiley Interscience, New York, 1963.
46. Wool, R. P., “Polymer entanglements,” *Macromolecules*, 26(7), pp. 1564–1569, 1993.
47. Wu, W.L., “Neutron Reflectivity Study of Diffusion in Crosslinked Polymer Networks,” Presented to CCM interphase and Bonding Focus Group, Center for Composite Materials, Newark, DE 19716, 1995.
48. “Adhesives, glues and sealants,” Adhesives, glues and sealants - All about adhesives. [Online]. Available: <http://www.adhesiveandglue.com/>. [Accessed: 05-Apr-2017].
49. Erickson P. W., Plueddemann, E. P., “Mechanics of Load Transfer at the Interface,” New York: Academic Press, 1974.
50. Cooper G. A., Kelley, A., “Role of the Interface in the Fracture of Fiber-Composite Materials,” *Interfaces in Composites*, Philadelphia: ASTM, 91, 1968.
51. Sottos, N. R., “The Influence of Interphase on Local Thermal Stresses and Deformations in

Composites,” Ph. D. Dissertation, University of Delaware, Newark, Delaware, 1990.

52. Palmese, G. R., “Interphases in Thermosetting Composites,” Ph. D. Dissertation, University of Delaware, Newark, Delaware, 1990.

53. P. E. Rouse, “*A Theory of the Linear Viscoelastic Properties of Dilute Solution of Coiling Polymers*,” J. Chem. Phys., 21(1272), 1953.

54. de Gennes, P.-G., “Scaling Concepts in Polymer Physics,” Cornell University Press: Ithaca, NY, 1979.

55. Doi, M., Edwards, S. F., “The Theory of Polymer Dynamics,” Clarendon Press, Oxford, 1986.

56. de Gennes, P.-G., “Reptation of a Polymer Chain in the Presence of Fixed Obstacles,” J. Chem. Phys., 55(572), 1971.

57. Wool, R. P., “Polymer Interfaces: Structure and Strength,” Hanser Gardner Publishers Inc., Cincinnati, 1995.

58. Helfand, E., Tagami, Y., “Theory of the Interface between Immiscible Polymers. II,” J. Chem. Phys., 56(3592), 1972.

59. Denison, P., Jones F. R., Watts, J. F., Interfaces in Polymer, Ceramic, Metal Matrix Composites, Ed. H. Ishida, Elsevier, 77-85, 1988.

60. Drzal, L.T., Rich, M.J., Floyd, P.F., "Adhesion of Graphite Fibers to Epoxy Matrices, I The Role of Fiber Surface Treatment," *J. of Adhesion*, 16, pp. 1-30, 1982.
61. Drzal, L.T., Rich, M.J., Koenig, M. F., Floyd, P.F., "Adhesion of graphite fibers to epoxy matrices: II. The effect of fiber finish," *J. Adhesion*, 16, pp. 133-152, 1982.
62. Pangelinan, A. B., "Surface Induced Molecular Weight Segregation in Thermoplastic Composites," Ph. D. Dissertation, University of Delaware, Newark, Delaware, 1991.
63. ASTM D5528-13, Standard Test Method for Mode I Interlaminar Fracture Toughness of Unidirectional Fiber-Reinforced Polymer Matrix Composites, ASTM International, West Conshohocken, PA, 2013
64. ASTM D7905 / D7905M-14, Standard Test Method for Determination of the Mode II Interlaminar Fracture Toughness of Unidirectional Fiber-Reinforced Polymer Matrix Composites, ASTM International, West Conshohocken, PA, 2014
65. Catherine A. Rees, John L. Provis, Grant C. Lukey, and Jannie S. J. van Deventer. In Situ ATR-FTIR Study of the Early Stages of Fly Ash Geopolymer Gel Formation. *Langmuir* , 2007, 23: 9076 —9082.
66. G. Rajagopalan, "Diffusion and reaction of epoxy and amine in polysulfone studied using Fourier transform infrared spectroscopy: experimental results," *Polymer*, vol. 41, no. 7, pp. 2591–2602, 2000.

67. Mangaraj, D., Bhatnagar, S. K., Rath, S. B., 1963, "Cohesive-Energy-Density of High Polymers Part III: Estimation of C.E.D by Viscosity Measurement," *Macromolecular Chemistry and Physics*, 67(1), pp.75-83.

Chapter 2

1. Leach, D. C., and Moore, D. R., 1985, "Toughness of Aromatic Polymer Composites Reinforced with Carbon Fibers," *Compos. Sci. Tech.*, **23**, pp. 131-161.
2. Takashi, I., and Masamichi, M., 1997, "Compression After Impact (CAI) Properties of Hat Stiffened CF/PEEK Panels Fabricated Through A Route Without Autoclave," *Proceedings of ICCM-11.*, **2**(1).
3. Cairns, D. S., Mandell, J. F., Scott, M. E., and Maccagnano, J. Z., 1999, "Design and Manufacturing Considerations for Ply Drops in Composite Structures," *Composites Part B: Engineering*, **30**(5), pp. 523-34.
4. Ozdil, F., and Carlsson, L. A., 1992, "Mode I Interlaminar Fracture of Interleaved Graphite/Epoxy," *J. Comp. Mater.*, **26**(3), pp. 433-59.
5. Groleau, M. R., Shi, Y. B., Yee, A. F., Bertram, J. L., Sue, H. J., and Yang, P. C., 1996, "Mode II Fracture of Composites Interleafed with Nylon Particles," *Composites Science and Technology*, **56**, pp. 1223-40.
6. Hillermeier, R. W., and Sefeis, J. C., 2001, "Interleaf Toughening of Resin Transfer Molding Composites," *Composites: Part A*, **32**, pp. 721-29.
7. Li, G., Li, P., Zhang, C., Yu, Y. H., Liu, H. Y., Zhang, S., Jia, X. L., Yang, X. P., Xue, Z. M., and Ryu, S. K., 2008, "Inhomogeneous Toughening of Carbon Fiber/Epoxy Composite Using Electrospun Polysulfone Nanofibrous Membranes by in Situ Phase Separation," *Composites Science and Technology*, **68**, pp. 987-94.

8. Magniez, K., Chaffraix, T., and Fox, B., 2011, "Toughening of a Carbon-Fibre Composite Using Electrospun Poly(Hydroxyether of Bisphenol A) Nanofibrous Membranes Through Inverse Phase Separation and Inter-Domain Etherification," *Materials*, **4**, pp. 1967-84.
9. Zhang, J., Yang, T., Lin, T., and Wang, C. H., 2012, "Phase Morphology of Nanofibre Interleaves: Critical Factor for Toughening Carbon/Epoxy Composites," *Composites Science and Technology*, **72**, pp. 256-62.
10. Wu, X. F., Rahman, A., Zhou, Z. P., Pelot, D. D., Sinha-Ray, S., Chen, B., Payne, S., and Yarin, A. L., 2012, "Electrospinning Core-Shell Nanofibers for Interfacial Toughening and Self-Healing of Carbon-Fiber/Epoxy Composites," *Journal of Applied Polymer Science*, **129**(3), pp.1383-93.
11. Kuwata, W., and Hogg, P. J., 2011, "Interlaminar Toughness of Interleaved CFRP Using Non-woven Veils," *Composites: Part A*, **42**, pp. 1551-70.
12. Matsuda, S., Hojo, M., Ochiai, S. A., Murakami, Akimoto, H., and Ando, M., 1999, "Effect of Ionomer Thickness on Mode I Interlaminar Fracture Toughness for Ionomer Toughened CFRP," *Composites Part A: Applied Science and Manufacturing*, **30**(11), pp. 1311-319.
13. Hojo, M., Matsuda, S., Tanaka, M., Ochiai, S., and Murakami, A., 2006, "Mode I Delamination Fatigue Properties of Interleaf-toughened CF/Epoxy Laminates," *Composites Science and Technology*, **66**(5), pp. 665-75.
14. Hojo, M., Matsuda, S., Ochiai, S., Marukami, A., and Akimoto, H., "The Role of Interleaf/Base Lamina Interphase in Toughening Mechanism of Interleaf-Toughened CFRP", *ICCM12 Conference Paris*, pp. 410.

15. 2010, "Upsizing blade test regimes," Composites Technology, <http://www.compositesworld.com/articles/upsizing-blade-test-regimes> (accessed Sep 15, 2015)
16. Jensen, F. M., Falzon, B. G., Ankersen, J., and Stang, H., 2006, "Structural Testing and Numerical Simulation of a 34m Composite Wind Turbine Blade," Composites Structures, **76**, pp. 52-61.
17. Shim, D. J., and Lagace, P. A., 2006, "Mechanisms and Structural Parameters Affecting the Interlaminar Stress Field in Laminates with Ply Drop-offs," Journal of Composite Materials, **40**, pp. 345-69.
18. Shim, D. J., 2002, "Role of Delamination and Interlaminar Fatigue in the Failure of Laminates with Ply Dropoffs," Massachusetts Institute of Technology.
19. Chen, S. F., and Zhang, B. Z., 1991, "Fracture Behavior of Interleaved Fiber-Resin Composites," Composites Science and Technology, **41**, pp. 77-97.
20. Brewer, J. C., and Lagece, P. A., 1988, "Quadratic Stress Criterion for Initiation of Delamination," Journal of Composite Materials, **22**, pp. 1141-55.
21. Aksoy, A., and Carlsson, L. A., 1991, "Crack Tip Yield Zone Estimates in Mode II Interlaminar Fracture of Interleaved Composites," Engineering Fracture Mechanics, **39**(3), pp. 525-534.
22. Smiley, A. J., Chao, M., and Gillespie, J. W., 1991, "Influence and Control of Bondline Thickness in Fusion Bonded Joints of Thermoplastic Composites," Composites Manufacturing, **2**, pp. 223-31.
23. SolvayPlastic, "Udel@PSU Design Guide," pp.55.

24. Woods, J., Modin, A. E., Hawkins, R. D. and Hanks, D. J., 2002, "Controlled Atmospheric Pressure Infusion Process", International Patent WO 03/101708 A1.
25. Niggemann, C., Young, S. S., Gillespie, J. W., and Heider, D., 2008, "Experimental Investigation of the Controlled Atmospheric Pressure Resin Infusion (CAPRI) Process," *Journal of Composite Materials*, **42**(11), pp. 1049-061.
26. Mandell, J. F., Samborsky, D. D., Agastra, P., Sears, A. T., and Wilson, T. J., 2010, "Analysis of SNL/MSU/DOE Fatigue Database Trends for Wind Turbine Blade Materials," Contractor Report SAND2010-7052, Sandia National Laboratories.
27. Ou, Y.F., Zhang, H., Huang, L., Yao, Y., Li, G., and Mobasher, B. 2016, "Mechanical Characterization of the Tensile Properties of Glass Fiber and Its Reinforced Polymer (GFRP) Composites under Varying Strain Rates and Temperatures", *Polymers*, 8, pp. 195-211.

Chapter 3

1. Shetty, R. R., Pavithra, G. K., Rai, S. K., 2013, "Studies on Mechanical and Fractographic Behavior of Polycarbonate-Toughened Epoxy-Granite Particle Hybrid Composites," *Polymer-Plastics Technology and Engineering*, 52(11), pp. 1122-1126.
2. Jin, Zhang, Tong, Lin, Xungai, Wang, 2010, "Electrospun nanofiber toughened carbon/epoxy composites: effects of polyetherketone cardo (PEK-C) nanofiber diameter and interlayer thickness," *Composites Sciences and Technology*, 70, pp.1660-1666.
3. Xu, Y., Liao, G., Gu, T., Zheng, L., Jian, X., 2008, "Mechanical and Morphological properties of Epoxy Resins Modified by Poly(phthalazinone ether sulfone ketone)," *Journal of Applied Polymer Science*, 110, pp. 2253-2260.
4. Martines, I., Martin, M. D., Eceiza, A., Oyanguren, P., Mondragon, I., 2000, "Phase separation in polysulfone-modified epoxy mixtures. Relationships between curing conditions, morphology and ultimate behavior," *Polymer* 41(3), pp.1027-35.
5. Blanco, I., Cicala, G., Faro, C. L., 2003, "Improvement of thermomechanical properties of a DGEBS/DDS system blended with a novel thermoplastic copolymer by realization of a semi-IPN network," *Journal of Applied Polymer Science*, 88(13), pp.3021-3025.

6. Heitzmann, M. T., Hou, M., Verdt, V. M., Vandi, L., Paton, R., 2013, "Morphology of an interface between polyetherimide and epoxy prepreg," Trans Tech Publications.
7. Tan, H., Yao, Y. L., 2013, "Laser Joining of Continuous Glass Fiber Composite Preforms," ASME J. Manuf. Sci. Eng., 135(1), 011010.
8. Bian, D. K., Satoh, G., Yao, Y. L., 2015, "The laser interlaminar reinforcement of continuous glass fiber composites," Journal of Manufacturing Science and Technology, 136(6), 061001.
9. Groleau, M. R., Shi, Y. B., Yee, A. F., Bertram, J. L., Sue, H. J., Yang, P. C., 1996, "Mode II Fracture of Composites Interleafed with Nylon Particles," Composites Science and Technology, 56, pp.1223-40.
10. Hillermeier, R. W., Sefeis, J. C., 2001, "Interleaf Toughening of Resin Transfer Molding Composites," Composites: Part A, 32, pp.721-29.
11. Li, G., Li, P., Zhang, C., Liu, Y. H., Zhang, H.Y., Jia, X. L., Yang, X. P., Xue, Z. M., Ryu, S. K., 2008, "Inhomogeneous Toughening of Carbon Fiber/Epoxy Composite Using Electrospun Polysulfone Nanofibrous Membranes by in Situ Phase Separation," Composites Science and Technology, 68, pp.987-94.
12. Kuwata, W., Hogg, P. J., 2011, "Interlaminar Toughness of Interleaved CFRP Using Non-woven Veils," Composites: Part A, 42, pp.1551-70.
13. Tan, H., Yao, Y. L., 2013, "Feasibility Analysis of Inter-Laminar Toughening for Improving

- Delamination Resistance,” *Manuf. Lett.*, 1(1), pp.33–37.
14. Bian, D. K., Bucher, T., Shim, D. J., Jones, M., Yao, Y. L., 2016, “Effect of deep penetration of interleaf on delamination resistance in GFRP,” *Journal of Manufacturing Science and Technology*, 138(7), 071011.
 15. Mangaraj, D., Bhatnagar, S. K., Rath, S. B., 1963, “Cohesive-Energy-Density of High Polymers Part III: Estimation of C.E.D by Viscosity Measurement,” *Macromolecular Chemistry and Physics*, 67(1), pp.75-83.
 16. Bernard, L., Chapel, J. P., Gernard, J. F., 2001, “Gradient interphase between reactive epoxy and glassy thermoplastic from precipitation process, reaction kinetics and phase separation thermodynamics,” *Macromolecules* 34, pp.1204-1213.
 17. Gyun, N., Yong, Y., Won, G., Kim, S. C., 2004, “Toughening of epoxy composite by dispersing polysulfone particle to form morphology spectrum,” *Polymer Bulletin*, 52, pp.365-372.
 18. Gyun, N., Yong, Y., Won, G., Kim, S. C., 2004, “Toughening of carbon fiber/ epoxy composite by inserting polysulfone film to form morphology spectrum,” *Polymer*, 45, pp.6953-6958.
 19. Gan, W. J., Yu, Y. F., Liu, X. Y., 2009, “Kinetics of phase separation at the early stage of spinodal decomposition in epoxy resin modified with PEI blends,” *Colloid Polymer Science*,

287, pp.23-28.

20. Rico, J. L., Montero, B., Diez, J., Ramirez, C., 2009, "Polymer blends based on an epoxy-amine thermoset and a thermoplastic: Effect of thermoplastic on cure reaction and thermal stability of the system," *Journal of Thermal Analysis and Calorimetry*, 95(2), pp.369-376.
21. Brewer, J. C., Lagece, P. A., 1988, "Quadratic Stress Criterion for Initiation of Delamination," *Journal of Composite Materials*, 22, pp.1141-55.
22. Aksoy, A., Carlsson, L. A., 1991, "Crack Tip Yield Zone Estimates in Mode II Interlaminar Fracture of Interleaved Composites," *Engineering Fracture Mechanics*, 39(3), pp.525-534.
23. Woods, J., Modin, A. E., Hawkins, R. D., Hanks, D. J., 2002, "Controlled Atmospheric Pressure Infusion Process," *International Patent WO 03/101708 A1*.

Chapter 4

1. Shetty, R. R., Pavithra, G. K., Rai, S. K., 2013, “Studies on Mechanical and Fractographic Behavior of Polycarbonate-Toughened Epoxy-Granite Particle Hybrid Composites,” *Polymer-Plastics Technology and Engineering*, 52(11), pp.1122-1126.
2. Pena, G., Eceiza, A., Valea, A., Remiro, P., Oyanguren, P., Mondragon, I., 2003, “Control of morphologies and mechanical properties of thermoplastic-modified epoxy matrices by addition of a second thermoplastic,” *Polymer International*, 52, pp.1444-1453.
3. Xu, Y., Liao, G., Gu, T., Zheng, L., Jian, X., 2008, “Mechanical and Morphological properties of Epoxy Resins Modified by Poly(phthalazinone ether sulfone ketone),” *Journal of Applied Polymer Science*, 110, pp. 2253-2260.
4. Martines, I., Martin, M. D., Eceiza, A., Oyanguren, P., Mondragon, I., 2000, “Phase separation in polysulfone-modified epoxy mixtures. Relationships between curing conditions, morphology and ultimate behavior,” *Polymer*, 41(3), pp.1027-35.
5. Blanco, I., Cicala, G., Faro, C. L., 2003, “Improvement of thermomechanical properties of a DGEBS/DDS system blended with a novel thermoplastic copolymer by realization of a semi-IPN network,” *Journal of Applied Polymer Science*, 88(13), pp.3021-3025.

6. Heitzmann, M. T., Hou, M., Verdt, M., Vandi, L., Paton, R., 2013, "Morphology of an interface between polyetherimide and epoxy prepreg," Trans Tech Publications.
7. Milliman, H. W., Boris, D., Schiraldi, D. A., 2012, "Experimental Determination of Hansen Solubility Parameters for Select POSS and Polymer Compounds as a Guide to POSS – Polymer Interaction Potentials," *Macromolecules*, 45(4), pp.1931-1936.
8. Yun, N. G., Won, Y. G., Kim, S. C., 2004, "Toughening of epoxy composite by dispersing polysulfone particle to form morphology spectrum," *Polymer Bulletin*, 52, pp.365-372.
9. Vandi, L. J., Hou, M., Veidt, M., Truss, R., Heitzmann, M., Paton, R., 2012, "Interface diffusion and morphology of aerospace grade epoxy co-cured with thermoplastic polymers," 28th International Congress of the Aeronautical Science.
10. Bulter, C. A., McCullough, R. L., Pitchumani, R., Gillespie, J. W., 1998, "An analysis of mechanisms governing fusion bonding of thermoplastic composites," *Journal of Thermoplastic Composite Materials*, 11, pp.338-363.
11. Sorrentino, A., Gorrasi, G., Tortora, M., Vittoria, V., 2006, "Barrier properties of polymer/clay nanocomposites," *Polymer Nanocomposites*, 11, pp.273-292.
12. Bian, D., Beeksma, B. R., Shim, D. J., Jones, M., Yao, Y. L., "Interlaminar Toughening of GFRP, Part 1: Improved Diffusion and Precipitation," [unpublished]
13. Sanford, W. M., 1987, "Curing behavior of thermosetting resin composites," PhD Thesis,

University of Delaware.

14. Skourlis, T. P., McCullough, R. L., 1994, "Measurement of Diffusivity of a Liquid Diamine in Solid Epoxies using Attenuated Total Reflectance Infrared Spectroscopy," *Journal of Applied Polymer Science*, 52, pp.1241-1248.
15. Rajagopalan, G., Immordino, K. M., Gillespie, J. W., and McKnight, S. H., 2000, "Diffusion and reaction of epoxy and amine in polysulfone studied using Fourier transfer infrared spectroscopy: experimental results," *Polymer*, 41, pp.2591-2602.
16. Hardis, R., 2012, "Cure Kinetics characterization and monitoring of an epoxy resin for thick composite structures," *Graduate Thesis and Dissertations*, Iowa State University.
17. Dibenedetto, A. T., 1987, "Prediction of the glass transition temperature of polymers: A model based on the principle of corresponding states," *Journal of Polymer Science*, 25(9), pp.1949-1969.
18. Rajagopalan, G., Gillespie, J. W., McKnight, S. H., 2000, "Diffusion of reacting epoxy and amine monomers in polysulfone: a diffusivity model," *Polymer*, 41, pp.7723-7733.
19. Rajagopalan, G., Narayanan, C., Gillespie, J. W., McKnight, S. H., 2000, "Diffusion and reaction of epoxy and amine in polysulfone – transport modeling and experimental validation," *Polymer* 2000, 41, pp.8532-8556.
20. Mangaraj, D., Bhatnagar, S. K., Rath, S. B., 1963, "Cohesive-Energy-Density of High

Polymers Part III: Estimation of C.E.D by Viscosity Measurement,” *Macromolecular Chemistry and Physics*, 67(1), pp.75-83.

Chapter 5

1. S. Sprenger, A.J. Kinloch, A.C. Taylor, R.D. Mohammed, “Rubber-toughened GFRCs optimised by nanoparticles,” *JEC Composites*, vol.21, pp. 66-69, 2005.
2. J.-L. Tsai, B.-H. Huang, and Y.-L. Cheng, “Enhancing Fracture Toughness of Glass/Epoxy Composites by Using Rubber Particles Together with Silica Nanoparticles,” *Journal of Composite Materials*, vol. 43, no. 25, pp. 3107–3123, Sep. 2009.
3. M. Uddin and C. Sun, “Improved dispersion and mechanical properties of hybrid nanocomposites,” *Composites Science and Technology*, vol. 70, no. 2, pp. 223–230, 2010.
4. Heijden, S. V. D., Daelemans, L., Schoenmaker, B. D., Baere, I. D., Rahier, H., Paepegem, W. V., Clerck, K. D., “Interlaminar toughening of resin transfer moulded glass fibre epoxy laminates by polycaprolactone electrospun nanofibres,” *Composites Science and Technology*, 104, pp. 66–73, 2014.
5. Li, G., Li, P., Zhang, C., Yu, Y., Liu, H., Zhang, S., Jia, X., Yang, X., Xue, Z., Ryu, S., “Inhomogeneous toughening of carbon fiber/epoxy composite using electrospun polysulfone nanofibrous membranes by in situ phase separation,” *Composites Science and Technology*, 68(3-4), pp. 987–994, 2008.
6. Villoria, R. G. D., Hallander, P., Ydrefors, L., Nordin, P., Wardle, B., “In-plane strength enhancement of laminated composites via aligned carbon nanotube interlaminar

- reinforcement,” *Composites Science and Technology*, 133, pp. 33–39, 2016.
7. Li, P., Liu, D., Zhu, B., Li, B., Jia, X., Wang, L., Li, G., Yang, X., “Synchronous effects of multiscale reinforced and toughened CFRP composites by MWNTs-EP/PSF hybrid nanofibers with preferred orientation,” *Composites Part A: Applied Science and Manufacturing*, 68, pp. 72–80, 2015.
 8. D. Cairns, J. Mandell, M. Scott, and J. Maccagnano, “Design and manufacturing considerations for ply drops in composite structures,” *Composites Part B: Engineering*, vol. 30, no. 5, pp. 523–534, 1999.
 9. M. Grassi, B. Cox, and X. Zhang, “Simulation of pin-reinforced single-lap composite joints,” *Composites Science and Technology*, vol. 66, no. 11-12, pp. 1623–1638, 2006.
 10. R. Rajasekaran and M. Alagar, “Mechanical Properties of Bismaleimides Modified Polysulfone Epoxy Matrices,” *International Journal of Polymeric Materials*, vol. 56, no. 9, pp. 911–927, 2007.
 11. G. Wu, L. Ma, Y. Wang, L. Liu, and Y. Huang, “Interfacial properties and impact toughness of methylphenylsilicone resin composites by chemically grafting POSS and tetraethylenepentamine onto carbon fibers,” *Composites Part A: Applied Science and Manufacturing*, vol. 84, pp. 1–8, 2016.
 12. S. Alessi, D. Conduruta, G. Pitarresi, C. Dispenza, and G. Spadaro, “Hydrothermal ageing of radiation cured epoxy resin-polyether sulfone blends as matrices for structural composites,” *Polymer Degradation and Stability*, vol. 95, no. 4, pp. 677–683, 2010.

13. F. N. Mutua, P. Lin, J. K. Koech, and Y. Wang, "Surface Modification of Hollow Glass Microspheres," *MSA Materials Sciences and Applications*, vol. 03, no. 12, pp. 856–860, 2012.
14. R. Perez, J. Sandler, V. Altstädt, T. Hoffmann, D. Pospiech, M. Ciesielski, M. Döring, U. Braun, A. Balabanovich, and B. Schartel, "Novel phosphorus-modified polysulfone as a combined flame retardant and toughness modifier for epoxy resins," *Polymer*, vol. 48, no. 3, pp. 778–790, 2007.
15. D. Bian, B. Beeksma, D. J. Shim, M. Jones, and Y. L. Yao, "Interlaminar Toughening of GFRP, Part 1: Bonding Improvement through Diffusion and Precipitation," *Journal of Manufacturing Science and Engineering* [Accepted].
16. D. Bian, B. Beeksma, D. J. Shim, M. Jones, and Y. L. Yao, "Interlaminar Toughening of GFRP, Part 2: Characterization and Numerical Simulation of Curing Kinetics," *Journal of Manufacturing Science and Engineering* [Accepted].
17. Rajagopalan, G., Immordino, K. M., Gillespie, J. W., and McKnight, S. H., 2000, "Diffusion and reaction of epoxy and amine in polysulfone studied using Fourier transfer infrared spectroscopy: experimental results," *Polymer*, 41, pp.2591-2602.
18. A. Aksoy and L. Carlsson, "Crack tip yield zone estimates in mode II interlaminar fracture of interleaved composites," *Engineering Fracture Mechanics*, vol. 39, no. 3, pp. 525–534, 1991.
19. M. Alfano, F. Furguele, A. Leonardi, C. Maletta, and G. H. Paulino, "Cohesive Zone Modeling of Mode I Fracture in Adhesive Bonded Joints," *Advances in Fracture and Damage Mechanics VI Key Engineering Materials*, pp. 13–16, 2007.
20. D. Xie and S. B. Biggers, "Strain energy release rate calculation for a moving delamination

- front of arbitrary shape based on the virtual crack closure technique. Part I: Formulation and validation,” *Engineering Fracture Mechanics*, vol. 73, no. 6, pp. 771–785, 2006.
21. Libin Zhao, Jie Zhi, Jianyu Zhang, Zhanli Liu, Ning Hu, “XFEM simulation of delamination in composite laminates”, *Composites Part A: Applied Science and Manufacturing*, Vol. 80, pp. 61-71, 2016.
22. N. Moës, J. Dolbow, and T. Belytschko, “A finite element method for crack growth without remeshing,” *International Journal for Numerical Methods in Engineering*, vol. 46, no. 1, pp. 131–150, Oct. 1999.
23. Abaqus User Manual, Section 36.1.0: Surface-based cohesive behavior.
24. J. Wang, S. Seah, E. Wong, and D. Cadge, “Fracture mechanics study of fatigue crack growth in solder joints under drop impact,” 2008 58th Electronic Components and Technology Conference, 2008.
25. J. R. Rice, “A Path Independent Integral and the Approximate Analysis of Strain Concentration by Notches and Cracks”, *Journal of Applied Mechanics*, vol. 35, pp. 379-386.
26. Ansys Engineer Data Source, Composite Materials, Epoxy_Eglass_UD and Resin_Epoxy.
27. W. Yu, M. Qian, and H. Li, “Elastic and plastic properties of epoxy resin syntactic foams filled with hollow glass microspheres and glass fibers,” *Journal of Applied Polymer Science*, vol. 133, no. 46, Aug. 2016.
28. F. Lapique and K. Redford, “Curing effects on viscosity and mechanical properties of a commercial epoxy resin adhesive,” *International Journal of Adhesion and Adhesives*, vol. 22, no. 4, pp. 337–346, 2002.

29. R. E. Lyon, K. E. Chike, and S. M. Angel, "In situ cure monitoring of epoxy resins using fiber-optic Raman spectroscopy," *Journal of Applied Polymer Science J. Appl. Polym. Sci.*, vol. 53, no. 13, pp. 1805–1812, 1994.
30. H. Miyagawa, M. J. Rich, and L. T. Drzal, "Amine-cured epoxy/clay nanocomposites. I. Processing and chemical characterization," *J. Polym. Sci. B Polym. Phys. Journal of Polymer Science Part B: Polymer Physics*, vol. 42, no. 23, pp. 4384–4390, 2004.
31. C. A. Carrero, C. J. Keturakis, A. Orrego, R. Schomäcker, and I. E. Wachs, "Anomalous reactivity of supported V₂O₅ nanoparticles for propane oxidative dehydrogenation: influence of the vanadium oxide precursor," *Dalton Transactions*, vol. 42, no. 35, p. 12644, 2013.
32. E. L. Lee and I. E. Wachs, "In Situ Raman Spectroscopy of SiO₂-Supported Transition Metal Oxide Catalysts: An Isotopic ¹⁸O–¹⁶O Exchange Study," *J. Phys. Chem.*, vol. 112, no. 16, pp. 6487–6498, 2008.
33. E. Vanoverbeke, V. Carlier, J. Devaux, J. Carter, P. McGrail, and R. Legras, "The use of Raman spectroscopy to study the reaction between an amine-terminated thermoplastic and epoxy resins," *Polymer*, vol. 41, no. 23, pp. 8241–8245, 2000.
34. S. Gupta, P. C. Ramamurthy, and G. Madras, "Synthesis and characterization of flexible epoxy nanocomposites reinforced with amine functionalized aluminan nanoparticles: a potential encapsulant for organic devices," *Polym. Chem.*, vol. 2, no. 1, pp. 221–228, 2011.
35. X. Zhang, X. Yan, J. Guo, Z. Liu, D. Jiang, Q. He, H. Wei, H. Gu, H. A. Colorado, X. Zhang, S. Wei, and Z. Guo, "Polypyrrole doped epoxy resin nanocomposites with enhanced mechanical properties and reduced flammability," *J. Mater. Chem. C*, vol. 3, no. 1, pp. 162–

176, 2015.

Appendix

This appendix section works in conjunction with the archived files, and is for the purpose of describing the attached data as well as practical requirements in order to run the numerical simulation that were developed for this thesis. A folder corresponding to each body chapter has been created: effect of deep interleaf penetration on delamination resistance is found in “\Chap2,” interlaminar toughening of GFRP is found in “\Chap3” and “\Chap4” corresponding to part 1 and part 2, interlaminar toughening of fiber reinforced polymers by synergistic modification of resin and fiber is found in “\Chapter 5”. Relevant information for each chapter, as well as some additional data which was not included in the described results, will now be individually provided. Furthermore, slides for the corresponding presentations of each chapter are found in “\Presentation,” as well as the Thesis Defense presentation slides.

Chapter 2: Effect of Deep Penetration of Interleaf on Delamination Resistance in GFRP

The folder “\optical microscopy” contains additional crack path microscopy obtained from the experiments for different samples. The files were named with the format of *MaterialMeltbondingtemperature-Direction-Samplenumber*, using to examine the fractured samples. The folder “\mechanical tests” contains both raw data and some complied chars from the MTS testing. Strain stress data for different melt bonding temperatures were summarized in the file *strain stress and toughness.xlsx*, with corresponding calculated toughness by integrating the area below the strain-stress curves. The raw data for each sample are in the folder “\mechanical test\tensile test dakai”. Additional SEM images for the fractured surface morphology are contained

in the folder “\sem”.

Chapter 3: Interlaminar Toughening of GFRP, Part 1: Bonding Improvement through Diffusion and Precipitation

The folder “\solubility” contains the raw data obtained from the viscometry experiments. The solvents used are listed in “\solubility\chemicals”. The solubility parameters of solvents are collected from literatures and materials data sheets. The calculated solubility parameters for different organic solvents and dissolved polymers are listed in *HSP for organic solvents and solute.xlsx*. The folder “\microscopy” contains additional images for diffusion and precipitation morphology and fracture surface morphology observations. The folder “\microscopy\fine polish” contains the optical microscopy images for the diffusion and precipitation with 5% polystyrene modified epoxy. The folder “\microscopy\fracture surface” contains all the SEM images for the fractured surface morphology. Besides the SEM images used in Chapter 3, images for the samples after chemical etching process are kept in the subfolder. The folder “\tensile test” contains both raw data and some complied chars from the MTS testing. Strain stress data are summarized in the file *tensile.opj*, with corresponding calculated toughness by integrating the area below the strain-stress curves. The raw data for each sample are in the subfolder.

Chapter 4: Interlaminar Toughening of GFRP, Part 2: Characterization and Numerical Simulation of Curing Kinetics

The folder “\FTIR” contains both the raw data from the FTIR experiments and program scripts

used to obtain the coefficients required in the coupled diffusion rate and curing rate equation in Chapter 4. The Fourier Transformed Infrared Spectroscopy equipment was provided by Prof. Ah-Hyung Park in Earth and Environmental Engineering department in Columbia University. The detailed experiment plan and procedure for diffusivity and curing rate determination is in *FTIR experiment plan.docx* and *reaction rate experiment plan.docx*. The folder “\FTIR\FTIR raw data” contains all the experiment results. In each subfolder, *readme.txt* contains the experiment conditions for the data in corresponding folder. The experiment data is saved as *CSV* format. The names of the files are the time at which the spectra was collected.

.py files under the folder “\FTIR” are the program scripts to fit the experiment data and generate the figures in Chapter 4. The *.py* files require to install the Python 2.7 and libraries such as *matplotlib*, *numpy* and *sys* must be pre-installed to run the program.

The program is mainly consisted of two parts: fit *D* in the Dibenditto equation and plot the fit curve with experiment data points. For example, in *psu-amine-4lines-2916.py*,

```
x = np.array([60,90,120,150,180])
```

```
y_standard=np.array([0.03940617,0.047682944,0.04810830263,0.049314932169,0.0532018163])
```

represents the time and corresponding absorbance of specific peak obtained from experiments.

```
A_0 = 0.03
```

```
A_inf = 0.055
```

represents the initial absorbance and final absorbance.

```
fit_min = 10 ** -13
```

$$fit_max = 10 ** -8$$

$$step = 10 ** -12$$

represents the min value of fit D and max value of fit D with the specific step size. The larger difference between min and max value, the smaller the step size lead to the longer program running times.

$$D = fit(fit_min, fit_max, step, x, A_inf, y_standard)$$

represents the main fitting functions in the program, which has six inputs: minimum value of D, maximum value of D, step size between min and max, time, final absorbance and absorbance at each time.

The working principle of this program is that by given the initial guess of D (fit_min). the program starts to recalculate the absorbance at each time and compare the difference between calculated values and experiment determined values. Thus, the D with minimum difference would be the D used in the Dibenditto Equation.

The folder “*diffusion and precipitation simulation*” contains the simulation .mph files under different curing temperatures with and without consideration the fibers. Comsol 4.2 is required to open .mph files. The .mph files contain both the simulation model and data obtained from the simulation. The physical system used here is *Transport of Dilute Species*. The *Transport of Diluted Species* simulates chemical species transport through diffusion, convection (if coupled to fluid flow), and migration. The three dependent variables used in the model is *ce*, *ca* and *cp*, which represent the concentration of epoxy, amine hardener and polysulfone. In the model, since there is no velocity field applied on the computational region, the *u* in the convection and diffusion

equation is set to 0. The diffusivity for three species is set as isotropic. The surrounding boundaries and fiber surfaces are set as *No Flux* boundary conditions. Only epoxy and amine hardener have the term of reaction rate equation because polysulfone does not reaction during the diffusion and precipitation process. A thin diffusion barrier is set in the model to simulation the interface between diffusion region and precipitation region. The interface observed in the experiment in Chapter 4 mainly depends on whether the governing phase separation mechanism is spinodal decomposition or nucleation and growth in the current region.

Chapter 5: Interlaminar Toughening of Fiber Reinforced Polymers by Synergistic Modification of Resin and Fiber

The folder “*\glass transition temperature*” contains the experiment raw data from differential scanning calorimetry. DSC is provided by Prof. Robert Farrauto from Earth and Environmental Engineering department. The DSC is Netzsch STA 449 F3 Jupiter TGA-DSC. The glass transition temperatures of samples are identified through the change of the heat flow, with the help of Netzsch Proteus software. The working principle, experiment procedures and summarized experiment results is listed in dsc experiment summary.docx. Subfolder “*\glass transition temperature\DSC RAW DATA*” contains the experiment raw data. The folder “*\psu morphology*” contains the additional SEM images for the polysulfone modified epoxy system after chemical etching away the PSU-rich region. The folder “*\viscometer*” contains the raw data from the viscosity determination experiment. Haake Mars III Rheometer is provided by Prof. Ah-Hyung Park in Earth and Environmental Engineering department in Columbia University. The raw data were saved as .xml file which can be opened by Excel. The folders “*\mode 1*” and “*\mode2*” contains the

summarized mechanical tests results. The folder “\SEM” contains additional fracture surface morphology for mode 1 and mode 2 tests. The folder “\xfem” contains the input files for mode 1 and mode 2. Abaqus 6.17 is required to run the program. Element type is set as XFEM element, which means the crack propagation path is independent of the element boundaries. Field outputs are set as *statusxfem*, *philsm*, *RF*, *U*, *S*. *statusxfem* is a scalar variable that shows the extent of damage or “cracking” inside an element. *Philsm* is used to define/show the location of crack inside a body. *RF*, *U* and *S* are the reaction forces, displacement and stress at the nodes.

The folder “\raman” contains the raw data from the Raman spectroscopy and program script to remove the background noise. The program script *one_single_run.m* is to remove the background fluorescence from the signal. The raw signal obtained from the Raman spectra consists of Raman bands and background fluorescence. Polynomial curve fitting is done to separate fluorescence from the Raman bands. In essence Raman bands are sitting on top of the fluorescence halo. Procedure is the following: the bands are flattened and reminder of the signal is fitted via polynomial curve fit. The curve fit is then subtracted from the original signal. If the procedure is done properly noise will be removed and only Raman bands will remain.

```
raw_data=xlsread('raw.xlsx',loop);
```

represents the raw data from Raman must be saved in an excel file, in which first column is Raman shift and second column is signal intensity. Then *xlsread* command let Matlab to read these data as matrix.

Function *polyfit* is used to fit and curve and remove the fluorescence halo by dividing the original signal *Y* to the *polyfit* results, shown in $f_res = Y_f_fit$


```
xlswrite('adjusted.xlsx',R,loop);
```

In the end, R is a matrix containing the Raman shifted and adjusted signal intensity, and *xlswrite* command let Matlab to generate an excel file and save R . *loop* is the number of round of fitting process. Here, *loop* equals 1.

Publications Under Candidature

- **D. Bian**, J. Tsui, R. Kydd, D. J. Shim, M. Jones, and Y. L. Yao, “Interlaminar Toughening of Fiber Reinforced Polymers by Synergistic Modification of Resin and Fiber” [To be submitted]
- **D. Bian**, B. Beeksma, D. J. Shim, M. Jones, and Y. L. Yao, “Interlaminar Toughening of GFRP, Part 1: Bonding Improvement through Diffusion and Precipitation,” *Journal of Manufacturing Science and Engineering*, vol. 139, no. 7, p. 071011, July. 2017.
Also presented at ASME International Conference on Manufacturing Science & Engineering (MSEC), June 4th -8th, 2017, Los Angeles, CA.
- **D. Bian**, B. Beeksma, D. J. Shim, M. Jones, and Y. L. Yao, “Interlaminar Toughening of GFRP, Part 2: Characterization and Numerical Simulation of Curing Kinetics,” *Journal of Manufacturing Science and Engineering* vol. 139, no. 7, p. 071012, July. 2017.
Also presented at ASME International Conference on Manufacturing Science & Engineering (MSEC), June 4th -8th, 2017, Los Angeles, CA.
- **D. Bian**, T. Bucher, D. J. Shim, M. Jones, and Y. L. Yao, “Effect of Deep Penetration of Interleaf on Delamination Resistance in GFRP,” *Journal of Manufacturing Science and Engineering*, vol. 138, no. 7, p. 071011, Oct. 2016.
Also presented at the 43rd SME North America Manufacturing Research Conference (NAMRC), June 8th-12th, 2015, Charlotte, NC.
- **D. Bian**, J. C. Tsui, M. Repin, G. Garty, H. Turner, Y. L. Yao, and D. J. Brenner, “Liquid Handling Optimization in High-Throughput Biodosimetry Tool,” *Journal of Medical Devices*, vol. 10, no. 4, p. 041007, 2016.
Also presented at ASME International Conference on Manufacturing Science & Engineering (MSEC), June 27th -July 1st, 2016, Blacksburg, VA.
- **D. Bian**, G. Satoh, and Y. L. Yao, “The Laser Interlaminar Reinforcement of Continuous Glass Fiber Composites,” *Journal of Manufacturing Science and Engineering*, vol. 137, no. 6, p. 061001, Sept. 2015.
- M. Zhang, C. J. Chen, G. Brandal, **D. Bian**, and Y. L. Yao, “Experimental and Numerical Investigation of Laser Forming of Closed-Cell Aluminum Foam,” *Journal of Manufacturing Science and Engineering*, vol. 138, no. 2, p. 021006, Sept. 2015.
- C. J., Chen, M., Zhang, P., Kongsuwan, G., Brandal, **D. Bian**, Y. L., Yao, “Effects of Laser Radiation on the Wetting and Diffusion Characteristics of Kovar Alloy on Borosilicate Glass.” *Proceedings of the 33rd International Congress on Applications of Lasers & Electro-Optics*. San Diego, CA, Oct 19-23, 2014.
- G., Garty, H. C., Turner, A., Salerno, A., Bertucci, J. Zhang, Y., Chen, A., Dutta, P., Sharma, **D. Bian**, M., Taveras, H., Wang, A., Bhatla, A., Balajee, A. W., Bigelow, M., Repin, O. V., Lyulko, N., Simaan, Y. L., Yao, D. J., Brenner, “The decade of the RABiT”, *Radiat Prot Dosimetry*, vol.172, no.1-3, page. 201-206,2016.

- G., Garty, A. W., Bigelow, M., Repin, H. C., Turner, **D. Bian**, A. S., Balajee, O. V., Lyulko, M., Taveras, Y. L., Yao, D. J., Brenner, "An automated imaging system for radiation biodosimetry", *Microsc Res Tech*, vol. 78, no. 7, page. 587-98, 2015.